

Hybrid hydrogels for load-bearing implants

Présentée le 8 février 2021

à la Faculté des sciences et techniques de l'ingénieur
Laboratoire de biomécanique en orthopédie
Programme doctoral en science et génie des matériaux

pour l'obtention du grade de Docteur ès Sciences

par

Céline Samira WYSS

Acceptée sur proposition du jury

Prof. A. Fontcuberta i Morral, présidente du jury
Prof. D. Pioletti, Dr P.-E. Bourban, directeurs de thèse
Prof. C. Creton, rapporteur
Prof. T. Hoare, rapporteur
Prof. E. Amstad, rapporteuse

Acknowledgements

The present work was carried out at Ecole Polytechnique Fédérale de Lausanne (EPFL, Switzerland) in the Laboratory for Processing of Advanced Composites (LPAC) and the Laboratory of Biomechanical Orthopedics (LBO). I would like to sincerely thank the Swiss National Foundation for financing this research project with grant CR 2312-137743.

For the last years, I have learned what it means to be a scientific researcher, undertaking new experiments every day. Most of the time, difficulties have to be overtaken on your own, but I was hopefully surrounded by fantastic colleagues. I would like to express my deepest gratitude to everyone who helped me and participated in this research.

First of all, I would like to thank Professor Véronique Michaud, head of LPAC, for offering me a position as a Ph.D. student at LPAC. I admire her energy and constant positive attitude, which strongly contributed to the laboratory's wonderful atmosphere. I would like to particularly thank my dear supervisor, Dr. Pierre-Etienne Bourban. He constantly found some time to discuss and develop new ideas around coffee, chocolates, or caramels. His caring nature and our numerous engaging discussions helped me take a step away from my project and re-evaluate the work from another perspective. Special thanks to Professor Dominique Pioletti, head of LBO. He always guided me on the right path and frequently provided valuable advice with his strong biomedical experience. Dominique was very active in participating and organizing various events, which was always very much appreciated by the whole LBO's team.

Many thanks to my colleague Peyman Karami and former Ph.D. Dr. Azadeh Khoushabi for many brainstorming sessions and collaborations that composed some parts of the thesis. I was particularly fortunate to pursue the work previously undertaken by Azadeh. She transmitted me a lot of knowledge with a lot of enthusiasm. I also would like to express my gratitude to Dr. Christopher Plummer and Professor Christophe Moser for providing guidance and new ideas during my PEXs, and to Professor Esther Amstad and Michael Kessler for helping me to synthesize microgels.

Many thanks to Cécile Chariatte and Virginie Kokocinski. They regularly helped me with administration questions. I am also very thankful to Raphaël Charvet for his assistance and IT support.

I sincerely acknowledge all the scientists and laboratory technicians of LPAC and LBO, Yves, Sandra, Adrien, Baris, Oriane, and Yasmine, for providing practical and precious advice on different aspects of my project. In particular, I want to thank Josiane Smith-Clerc for her support with the TP, the equipment of DLL, and the lovely time we spent together. Additionally, I appreciated the patience of Dr. Adrian Demongeot when he helped me with the FTIR analysis. And of course, many thanks to my office-mate and friend, Helena Teixido, for all the intense discussions, surrounded by our wonderful flowers and green plants.

Thanks to the BIOP team for making the invisible visible with cutting-edge imaging machines, and to all my semester students, Baptiste Guyon, Hubert Taïeb, Clémont Gremion, Morgan Binggeli, and Yann Müller, who contributed to the research. I also would like to express my gratitude to Professor Benjamin Gantenbein from the Department for BioMedical Research (DBMR, University of Bern), for providing us the swiss-made silk and to Dr. Daniel Görl, from the laboratory of macromolecular and organic materials (LMOM, EPFL) for helping me with the synthesis of PEGDM.

I have been very honored that Professor Ether Amstad, Professor Costantino Creton, and Professor Todd Hoare agreed to review and evaluate my thesis. I especially thank them for the time and advice.

Finally, I gratefully thank my cherished partner, Romain, for his constant encouragement and feedback during my Ph.D., as well as my parents and my sister for their comforting thought and support.

Abstract

Load-bearing tissues such as articular cartilage, meniscus, or intervertebral discs have highly organized microstructures for optimal stress transmission. However, like other materials, load-bearing tissues are not infallible and might deteriorate due to trauma, over-solicitations, or diseases, which could subsequently alter the mobility of the patient. Repairing these damaged tissues in a minimally invasive way is nowadays widely studied.

Generally composed of more than 80% of water, hydrogels are promising biocompatible materials for repairing soft tissues, and they can be injected directly into the human body. However, trying to reproduce the highly hierarchical microstructures of load-bearing tissues is extremely complicated. In fact, conceiving hydrogels with optimal properties for specific applications is challenging as most of the hydrogel's properties are interrelated, such as toughness, stiffness, swelling, or deformability. The improvement of one property usually comes at the cost of another. Moreover, the requirement for an ideal customized implant depends on the patient and the exact part of the tissue to treat.

The objective of the thesis is to develop different hydrogel microstructures and evaluate their potential for load-bearing implants. In particular, the study focuses on (i) designing tough and fatigue resistant hydrogels, (ii) establishing a methodology to control the stiffness and the swelling of hydrogels independently, and (iii) considering processing ease by tailoring each hydrogel precursor viscosity.

An extensive parametric study on hydrogels' structure and composition allowed establishing complete property charts for mechanical, swelling, and rheological properties. Seven different hydrogel structures based on poly(ethylene glycol) dimethacrylate were developed: neat, double network, composite, double network composite, granular, hybrid granular, and silk granular hydrogels. The precursors of neat hydrogels had the lowest viscosity, suited for confined applications such as replacing the nucleus pulposus, the core of intervertebral discs. Microgels of similar composition were added to the precursor to adapt and increase its viscosity for unconfined applications like repairing focal cartilage defects without using a membrane or 3D print complex structures. In parallel, adding nano-fibrillated cellulose fibers was an effective way of increasing toughness. This method was more efficient than creating a double network with alginate. Indeed, while the results were promising at the *as-prepared state*, alginate had lost almost all its benefits in the *swollen state*. Moreover, high-cycles fatigue tests revealed that hydrogel composites successfully survive 10 million loading cycles at 20% applied strain.

However, it became softer after the first loading cycles and behaved similarly to the *Mullins effect*. Subsequently, we assessed how cyclic loading affects fracture behavior, distribution of strain fields, and microstructure. The study demonstrated that cyclic loading on hydrogel composites re-arrange the fiber network without seriously deteriorating the mechanical properties. The small preloading strain was actually beneficial for reducing residual stresses. Additionally, we demonstrated that combining composite and microgel effectively tailored hydrogels' swelling and viscosity without significantly affecting elastic modulus, fracture energy, and deformability. Those hybrid granular hydrogels would, therefore, be appropriated for replacing the superficial layer of articular cartilages, where toughness is essential for limiting the propagation of cracks in the more deeper and stiffer layers. Finally, the microgels were swollen in silk fibroin solution for forming self-reinforced silk granular hydrogels, where around 50% of the secondary structures could be assigned to strong silk β -sheets. Those hydrogels exhibited considerably higher stiffness. Despite their lower elongation performance, silk granular hydrogel represents a potential candidate for repairing focal cartilage defects.

Following the evaluation of various hydrogel microstructures, hybrid hydrogels, composed of stacked hydrogels, were developed for better targeting local properties or mimicking the morphology of native tissues. First, mechanical gradients were successively processed through a sequential layering of silk or hybrid granular hydrogels. Subsequently, a hydrogel composite and a silk granular hydrogel, based this time on gelatin hydrogels, were synthesized. The experiment validated the potentials of studied structures, even when using other hydrogels and microgels.

We demonstrated that hydrogels' mechanical and physical properties could be effectively controlled with the microstructure and composition of well-known biomaterials. The analyzed material systems can be combined to obtain local or gradient properties that address specific biomedical applications, soft robotics, sensing applications, or even food packaging.

Keywords: hydrogel, composite, granular, microgels, PEGDM, cellulose, silk fibroin, swelling, elastic modulus, Mullins effect, fracture, gradient, digital image correlation, confocal microscopy.

Resumé

Les tissus conjonctifs tels que le cartilage articulaire, le ménisque et les disques intervertébraux disposent de microstructures très organisées pour une transmission optimale des contraintes. Néanmoins, ils ne sont pas infailibles et peuvent se détériorer en raison de traumatismes, de sollicitations excessives ou de maladies, au dépens de la mobilité du patient. De ce fait, le traitement de ces tissus endommagés de manière peu invasive est aujourd’hui largement étudié.

Constitués généralement de plus de 80% d’eau, les hydrogels sont des biomatériaux prometteurs pour réparer ou remplacer des tissus mous, et peuvent être injectés directement dans le corps humain. Cependant, il est extrêmement compliqué de reproduire les microstructures hautement hiérarchisées des tissus conjonctifs. En effet, développer des hydrogels aux propriétés optimales pour des applications spécifiques reste un défi. La plupart des propriétés sont liées entre elles, comme la ténacité, la rigidité, le gonflement ou la déformabilité. L’amélioration d’une propriété se fait généralement au détriment d’autres. De plus, les critères d’un implant personnalisé dépendent du patient et de la partie exacte du tissu à traiter.

L’objectif de la thèse est de développer différentes microstructures d’hydrogel et d’évaluer leur potentiel afin d’être utilisées en tant qu’implant porteur. L’étude se concentre sur (i) la conception d’hydrogels résistants à la fatigue, (ii) l’établissement d’une méthodologie pour contrôler la rigidité et le gonflement des hydrogels de manière indépendante, et (iii) la mise en œuvre des hydrogels en adaptant la viscosité de chaque précurseur.

Une étude paramétrique approfondie sur la composition et la structure des hydrogels a permis d’établir des diagrammes qui résument les propriétés mécaniques, de gonflement et rhéologiques. Basées sur le poly(éthylène glycol) diméthacrylate, sept structures d’hydrogel différentes ont été développées: simple réseau, double réseaux, composite, composite à double réseaux, granulaire, granulaire hybride et granulaire de soie. Les précurseurs d’hydrogels munis d’un unique réseau de polymère avaient la plus faible viscosité. Une caractéristique adaptée pour des applications confinées telles que le remplacement de la partie interne gélatineuse des disques intervertébraux. Des microgels de composition similaire ont été ajoutés au précurseur pour adapter et augmenter la viscosité. Ainsi ces matériaux granulaires peuvent être employés pour des applications non-confinées telles que la réparation de défauts localisés du cartilage sans l’utilisation d’une membrane ou de créer des structures complexes en impression

3D. En parallèle, l'ajout de fibres de cellulose est un moyen efficace d'augmenter la ténacité. Cette méthode était plus efficace que la création d'un double réseau avec de l'alginate. En effet, alors que les résultats étaient prometteurs à l'état juste *après synthèse*, l'alginate a perdu presque tous ses avantages à l'état *gonflé*, saturé de liquide. De plus, des tests de fatigue de longue durée ont révélé que les hydrogels composites ont survécu avec succès à 10 millions de cycles de chargement à 20% de déformation. Cependant, cet hydrogel s'est affaibli après les premiers cycles et s'est comporté de manière similaire à l'*effet Mullins*. Par la suite, nous avons évalué comment les charges cycliques affectent le comportement à la rupture, la distribution des champs de déformation et la microstructure. L'étude a montré que les charges cycliques sur les hydrogels composites ont réarrangé le réseau de fibres sans sérieusement détériorer les propriétés mécaniques. En effet, un pré-chargement à faible déformation était bénéfique pour réduire les contraintes résiduelles. Il a également été démontré que la combinaison d'une approche composite et microgel permettait d'adapter efficacement le gonflement des hydrogels sans affecter de manière significative le module d'élasticité, l'énergie de rupture et la déformabilité. Ces hydrogels granulaires hybrides seraient donc appropriés pour remplacer la couche superficielle des cartilages articulaires, où la ténacité est essentielle pour limiter la propagation des fissures dans les couches inférieures et plus rigides. Finalement, les microgels ont été gonflés dans une solution de fibroïne de soie pour former des hydrogels granulaires de soie auto-renforcés, où environ 50% des structures secondaires ont pu être assignées à des β -*sheets* résistants. Ces hydrogels présentaient une rigidité considérablement plus élevée. Malgré leurs performances d'élongation plus faibles, ils sont des candidats potentiels pour traiter des défauts locaux internes du cartilage.

Suite à l'évaluation de diverses microstructures, des hydrogels hybrides, composés de plusieurs hydrogels, ont été conçus pour mieux cibler les propriétés locales ou imiter la morphologie hiérarchique des tissus natifs. Dans un premier temps, des gradients mécaniques ont été créés en superposant successivement des hydrogels granulaires hybrides ou de soie. Ensuite, un hydrogel composite et un hydrogel granulaire de soie ont été synthétisés cette fois avec une gélatine au lieu du polyéthylène glycol. L'expérience a permis de valider le potentiel des structures étudiées, en utilisant d'autres hydrogels et microgels.

Nous avons démontré que les propriétés mécaniques et physiques des hydrogels pouvaient être contrôlées efficacement avec les microstructures et les compositions de biomatériaux bien connus. De plus, les systèmes de matériaux analysés peuvent être combinés pour obtenir des propriétés locales ou de gradient, pour répondre à des applications spécifiques dans le milieu biomédical, de la robotique, des senseurs, ou même de l'alimentation.

Mots-clés: hydrogel, composite, granulaire, microgels, PEGDM, cellulose, fibroïne de soie, gonflement, module élastique, effet Mullins, fracture, gradient, corrélation d'images numériques, microscopie confocale.

Contents

Acknowledgment	ii
Abstract	iv
Resumé	vi
List of Figures	xiii
List of Tables	xviii
Abbreviations	xx
Glossary	xxii
1 Introduction	1
1.1 Motivation	1
1.2 Objectives	4
1.3 Structure and approach	4
2 State of the art	7
2.1 Biocompatible hydrogels	8
2.2 Hydrogel processability	9
2.2.1 Photopolymerization	9
2.3 Mechanical properties	14
2.3.1 Hydrogel composites	15
2.4 Gradient and anisotropic properties	20
2.5 Biological properties	23
2.5.1 Mesh size	23
2.5.2 Cell adhesion	23
2.5.3 Open microporosity	23
2.6 Swelling properties	24
2.7 Adhesion properties	26
2.7.1 Influencing parameters in adhesion	26
2.7.2 Adhesion in biomedical applications	27
2.7.3 Clinical needs	28
2.7.4 Hydrogel based adhesive	28

2.8	Reliability	32
2.8.1	Fatigue resistance	32
2.8.2	Degradation	34
2.9	Characterization methods	36
2.10	Conclusions	38
3	Materials and methods	39
3.1	Hydrogel structures and materials	39
3.2	Synthesis and processing	40
3.2.1	Raw materials	40
3.2.2	Sub-component synthesis	42
3.2.3	Hydrogel synthesis	43
3.2.4	Casting	45
3.3	Sampling plan	46
3.4	Material characterization methods	47
3.4.1	Imaging the morphology of fibers	48
3.4.2	Swelling ratio	48
3.4.3	Rheology	50
3.4.4	Compression test	50
3.4.5	Tensile test	52
3.4.6	Single notch edge test	52
3.4.7	Digital image correlation analysis	54
3.4.8	Adhesion test	56
3.4.9	Interfacial fracture test	56
3.4.10	Fourier-transform infrared spectroscopy	57
3.4.11	Cytocompatibility test	57
4	Single and double network hydrogels and their composites	59
4.1	Introduction	60
4.2	Materials and methods	61
4.2.1	Materials	61
4.2.2	Hydrogel synthesis	61
4.2.3	Methods	62
4.3	Results and discussion	64
4.3.1	Processability - rheology	64
4.3.2	Physical properties - swelling	65
4.3.3	Mechanical properties	66
4.3.4	Adhesion and interfacial fracture strength	72
4.3.5	Biological properties - cytocompatibility	73
4.3.6	Long-term reliability	75

4.4	Conclusions	78
5	Fracture properties of preloaded hydrogel composites	79
5.1	Introduction	80
5.2	Materials and methods	81
5.2.1	Materials	81
5.2.2	Hydrogel synthesis	81
5.2.3	Cyclic tensile loading	82
5.2.4	Preloading of hydrogels	82
5.2.5	Tensile loading under optical microscope	82
5.2.6	Single edge notch test	82
5.2.7	Digital image correlation analysis	83
5.2.8	Fluorescence confocal microscopy	83
5.3	Results and discussion	83
5.3.1	Cyclic tensile loading and Mullins effect	83
5.3.2	Single edge notch test on hydrogels with and without preloading	84
5.3.3	Distribution of strain fields at macroscopic scale	86
5.3.4	Distribution of the strain fields at microscopic scale	86
5.3.5	Direct observation of the NFC morphology	88
5.4	Conclusions	91
6	Hybrid granular hydrogels	92
6.1	Introduction	93
6.2	Materials and methods	94
6.2.1	Materials	94
6.2.2	Synthesis of hydrogels	95
6.2.3	Swelling ratios	96
6.2.4	Mechanical properties	96
6.2.5	Digital image correlation analysis	97
6.2.6	Microstructures	97
6.2.7	Rheology	97
6.2.8	Direct contact test	98
6.3	Results and discussions	98
6.3.1	Swelling and mechanical properties	98
6.3.2	Effect of pre-swollen PEGDM microgels	103
6.3.3	Effect of cellulose fibers	105
6.3.4	Processing	107
6.3.5	Direct contact test	109
6.4	Conclusions	110

7	Self-reinforced granular hydrogel with silk fibroin fibers	111
7.1	Introduction	112
7.2	Materials and methods	113
7.2.1	Materials	113
7.2.2	Synthesis of microgels	113
7.2.3	Synthesis of silk fibroin	114
7.2.4	Synthesis of self-reinforced silk fibroin granular hydrogel	114
7.2.5	Swelling ratios	115
7.2.6	Mechanical properties	115
7.2.7	Digital image correlation analysis	116
7.2.8	Microstructures	116
7.2.9	Crystallinity	116
7.2.10	Direct contact test	117
7.3	Results and discussion	117
7.3.1	Swelling and mechanical properties	117
7.3.2	Microstructure and crystallinity of silk fibroin	123
7.3.3	Processing	128
7.4	Conclusions	132
8	Tailoring hybrid hydrogels for load-bearing applications	133
8.1	Introduction	134
8.2	Materials and methods	137
8.2.1	Materials	137
8.2.2	Synthesis of microgels	137
8.2.3	Synthesis of silk fibroin	137
8.2.4	Synthesis of hydrogels	137
8.2.5	Swelling ratios	138
8.2.6	Compression and tensile test	138
8.2.7	Digital image correlation analysis	138
8.2.8	Microstructures	139
8.3	Gradient in hydrogels	139
8.3.1	Hybrid granular hydrogels	140
8.3.2	Silk granular hydrogels	143
8.4	Gelatin based hydrogels	144
8.4.1	Hydrogel composites	144
8.4.2	Silk granular hydrogel	145
8.5	Conclusions	149

9	Conclusions and perspectives	150
9.1	Conclusions	150
9.2	Perspectives	153
9.2.1	Hybrid granular hydrogels	153
9.2.2	Silk granular hydrogels	153
9.2.3	Hybrid silk granular hydrogels	154
9.2.4	Additive manufacturing	154
10	Annexes	157
10.1	Annexes - State of the art	157
10.1.1	Adhesion theories	157
10.1.2	Photopolymerization	159
10.2	Annexes - Equipment	159
	Bibliography	161

List of Figures

1.1	Anatomy of human knee composed of several tissues with highly organized and hierarchical microstructures	1
1.2	Important characteristics of load-bearing hydrogel implants.	2
1.3	Thesis charter.	6
2.1	Absorption spectra of Irgacure 2959.	13
2.2	Scattering effect of nano-cellulose fibers.	14
2.3	Example of silk fibroin versatile structures.	18
2.4	Effect of the degumming and the concentration of CaCl_2 on silk fiber dissolution.	19
2.5	Techniques for developing gradient in hydrogels.	20
2.6	Influence of crosslinking density on different hydrogel properties.	23
2.7	Swelling ratios and elastic moduli of PEGDM, 6 kDa and 20 kDa, hydrogels with/out NFC fibers.	25
2.8	Bio-inspired microneedle adhesive.	29
2.9	A Gecko-inspired surface coated with DOPA molecule.	30
2.10	Insect captured by the natural adhesive secreted from sundew.	31
2.11	Protective shelters of caddisfly larvae composed of debris stitched together with its secreted silk.	31
2.12	Representative <i>Mullins effect</i> in filled rubber.	33
2.13	Example of adhesion tests according to standard ASTM.	36
3.1	Hydrogel structures.	39
3.2	Microgels synthesis.	42
3.3	Silk fibroin solution preparation.	42
3.4	Synthesis of neat hydrogels.	43
3.5	Synthesis of hydrogels composite.	43
3.6	Synthesis of double network hydrogels.	43
3.7	Synthesis of composite double network hydrogels.	44
3.8	Granular hydrogel synthesis.	44
3.9	Self-assembled silk granular hydrogel synthesis.	44
3.10	Representative hydrogel samples for compression test.	45
3.11	Casting molds of tensile and single notch edge tests.	45
3.12	Representative hydrogel composite prepared for fluorescence microscopy.	48
3.13	<i>Archimedes'</i> setup for the determination of the swelling ratio.	49
3.14	Tensile machine <i>Zwicky</i>	51
3.15	Definition of elastic modulus and dissipation of energy.	52

3.16	Calibration of dog-bone samples.	53
3.17	Definition of fracture strength and crack initiation energy of notched samples.	53
3.18	Speckle pattern on the surface of hydrogel for digital image correlation.	54
3.19	Setup for digital image correlation in 3D.	55
3.20	Adhesion setup.	56
3.21	Interfacial fracture test setup.	56
4.1	Structure and composition of neat, composite, double network, and double network hydrogels. . .	60
4.2	Rheology measurement on the elastic modulus of neat, composite, double network, and double network hydrogels.	64
4.3	Swelling ratios of neat, composite, double network, and double network hydrogels.	66
4.4	Elastic moduli and dissipated energies in compression and tensile loadings of neat, composite, double network, and double network hydrogels.	67
4.5	Effect of swelling on the compressive elastic modulus of neat, composite, double network, and double network hydrogels.	68
4.6	Property chart showing the compressive modulus in function of the swelling ratio of neat, composite, double network, and double network hydrogels.	69
4.7	Z-stack projection of NFC fibers in a swollen composite hydrogel.	70
4.8	Fracture strength of neat, composite, double network, and double network hydrogels.	71
4.9	Adhesion test and fracture test on bovine cartilage with neat, composite, double network, and double network hydrogels.	72
4.10	Digital image correlation analysis showing the strains of hydrogel composites during fracture and interfacial fracture test.	73
4.11	Cytocompatibility of composite double network hydrogels in the swollen state.	74
4.12	High cycle fatigue of neat hydrogel and hydrogel composite.	75
4.13	Representative cyclic stress-strain curves, cyclic evolution of the elastic modulus and the energy dissipation of swollen neat hydrogel and hydrogel composite.	76
4.14	Representative cyclic loading/unloading stress-strain curves of swollen composite hydrogels. . . .	77
5.1	Structures and compositions of neat hydrogel and hydrogel composite.	80
5.2	Effect of cyclic preloading on the fracture strength of pre-notched samples, the microstructure and the elastic modulus of hydrogel composites.	81
5.3	Representative cyclic tensile loadings and single notch edge test of swollen neat hydrogels and hydrogel composites.	84
5.4	Fracture properties of hydrogel composites.	85
5.5	Digital image correlation analysis showing the strain field of swollen hydrogel composites during a single notch test.	86
5.6	Digital image correlation analysis showing the microscopic strain field of swollen hydrogel composites during tensile loading.	87
5.7	Effect of cyclic loading on the morphology of the cellulose fibers in swollen hydrogel composites. . .	88
5.8	Fiber bridging in a swollen hydrogel composite.	89
6.1	Swelling behavior of neat, composite, granular, and hybrid granular hydrogels.	94
6.2	Size distribution and morphologies of microgels.	95

6.3	Property chart the compressive modulus as a function of the swelling ratio of swollen neat, composite, granular, and hybrid granular hydrogels.	99
6.4	Representative cyclic compression loadings of swollen neat, composite, granular, and hybrid granular hydrogels.	100
6.5	Deformation to rupture of a representative broken hybrid granular hydrogel and the failure mechanisms at the surface of rupture.	101
6.6	Property chart showing tensile properties of swollen neat, composite, granular, and hybrid granular hydrogels.	102
6.7	Fracture properties of swollen neat, composite, granular, and hybrid granular hydrogels.	103
6.8	Swelling behavior of granular hydrogels.	104
6.9	Effect of the fibers in swollen granular hydrogels on compressive elastic modulus and the swelling ratio.	106
6.10	Property chart showing the elastic modulus in compression as a function of the complex viscosity of neat, composite, granular, and hybrid granular hydrogels.	108
6.11	Representative behavior of precursors' complex viscosities.	109
6.12	Direct contact test of hybrid granular hydrogel.	109
7.1	Regeneration silk fibroin fibers <i>in situ</i> with microgels swelling.	112
7.2	Nomenclature designing structures and compositions of silk granular hydrogels.	114
7.3	General nomenclature designing structures and compositions of studied hydrogels.	115
7.4	Property chart showing the compressive modulus as a function of the swelling ratio of silk granular hydrogels.	117
7.5	Influence of the microgel and silk fibroin content on swelling and mechanical performances.	118
7.6	Estimation of the water content of microgels.	119
7.7	Property chart showing the tensile modulus as a function of the strain at failure of swollen silk granular hydrogels.	120
7.8	Representative cyclic loadings in compression and tensile of a silk granular hydrogel.	121
7.9	Fracture properties of silk granular hydrogels.	122
7.10	Synthesis method for creating an optimal silk granular hydrogel.	123
7.11	Microstructure of silk granular hydrogels.	124
7.12	FTIR of microgels, regenerated silk fibroin, and silk granular hydrogel.	126
7.13	Secondary structures of silk fibroin regenerate in silk granular hydrogel.	127
7.14	FTIR of silk fibroin fibers regenerated <i>in situ</i> in silk granular hydrogels.	128
7.15	Illustration showing how silk fibroin regenerates around agglomerates of dry microgels.	129
7.16	Sample quality of larger samples of silk granular hydrogels.	130
7.17	Injectability of a representative silk granular precursor.	130
7.18	Direct contact test of silk granular hydrogels.	131
8.1	Examples of requirements for the ideal implant according to applications and the location.	134
8.2	Components of studied hydrogel structures.	135
8.3	Range of properties of studied hydrogel structures.	136
8.4	Requirements for developing mechanical gradients in hydrogels through sequential layering.	140
8.5	Gradient in hybrid hydrogels through sequential layering of hybrid granular hydrogels.	141
8.6	Layering of hydrogels with different swelling ratios.	142

8.7	Gradient in hybrid hydrogels through sequential layering of silk granular hydrogels.	143
8.8	Property chart of neat and hydrogel composites based on gelatin.	145
8.9	Microstructure of granular hydrogel based on gelatin reinforced with silk fibroin fibers.	146
8.10	Property chart of silk granular hydrogel based on gelatin showing the compressive modulus as a function of the swelling ratio.	147
8.11	Property chart of silk granular hydrogel based on gelatin showing the tensile modulus as a function of the maximum deformation.	148
9.1	Hybrid granular hydrogel reinforced with self-assembled silk fibroin.	155
9.2	Potential 3D printing of anisotropic silk granular hydrogels.	156

List of Tables

2.1	Conventional biocompatible hydrogels.	8
2.2	Characteristics describing the processability of hydrogels.	10
2.3	Requirements for injectable photopolymerizable hydrogels.	11
2.4	Examples of photoinitiators for biomedical applications.	12
2.5	Natural reinforcements.	16
2.6	Techniques for developing gradient in hydrogels and their limitations.	21
2.7	Influencing parameters for adhesion.	26
2.8	Required properties for hydrogel-based adhesive.	27
2.9	Commercial available surgical adhesives.	28
2.10	Fatigue behavior according to different hydrogel structures.	35
2.11	Example of tests for evaluating load-bearing hydrogel implants.	37
3.1	Raw materials for hydrogel synthesis.	40
3.2	Test equipment used for the characterization of hydrogels.	47
3.3	Mechanical test parameters.	50
3.4	3D digital image correlation parameters.	55
4.1	Material approach.	61
4.2	Sample geometries.	62
4.3	Characterization methods.	63
6.1	Sample geometries.	96
7.1	Absorbance peaks of secondary structures of silk fibroin.	125
7.2	Assigned secondary structures of silk granular hydrogel.	128
8.1	Selection of hybrid granular hydrogels for creating gradients through sequential layering.	141
8.2	Selection of hybrid granular hydrogels with different swelling ratios.	142
8.3	Selection of silk granular hydrogels for creating gradients through sequential layering.	143
10.1	Common adhesion theories.	157
10.2	Photopolymerization steps	159
10.3	Equipment for the material characterization.	160

Abbreviations

ϵ	Strain	GelMa	Gelatin methacryloy
λ	Stretch	GeS	Silk granular hydrogel based on gelatin microgels
σ	Stress	H	Hybrid granular hydrogel based on PEGDM
A	Area of sample	h	Height of sample
C	Hydrogel composite based on PEGDM	IPN	Interpenetrating polymer network
CDN	Composite double network hydrogel	IWC	Initial water content
DIC	Digital image correlation	N	Neat hydrogel based on PEGDM
DN	Double network hydrogel	NFC	Nano-fibrillated cellulose
E	Elastic modulus	PBS	Phosphate buffered saline
EWC	Equilibrium water content	PEG	Poly(ethylene glycol)
FTIR	Fourier transform infrared spectroscopy	PEGDM	Poly(ethylene glycol) dimethacrylate
G	Granular hydrogel based on PEGDM	S	Silk granular hydrogel based on PEGDM microgels
Gc	Fracture energy	SR	Swelling ratio
Ge	Neat hydrogel based on gelatin	UV	Ultraviolet
GeC	Hydrogel composite based on gelatin		

Glossary

Adhesion	Attraction between two substances.
Anisotropy	Property that changes according to the direction.
Biocompatibility	Material property describing the host's response when the material is implanted or in contact with the body. A biocompatible material manifests no or low toxic or immunological response.
Cohesion	Attraction between molecules or particles inside one same substance.
Composite	Material constituted of different immiscible materials (that do not form a homogeneous mixture).
Compressive modulus	Elastic modulus measured in compression loading (intrinsic property).
Deformability/ Elongation	Ability to deform before breaking.
Double network hydrogel	Hydrogel containing two polymer networks (with a molar chain length ratio of 20-30x).
Energy dissipation	Release or loss of energy during a mechanical solicitation.
Elastic modulus	Resistance of a material to being deformed (intrinsic property).
Fatigue resistance	Resistance of material to weakening under repeated cyclic loading.
Gradient	A continuous and progressive variation of a property along one or several axes.
Granular hydrogel	Hydrogel composed of microgels only or microgels embedded in another hydrogel.
Hierarchical structure	Presence of defined material structures at different length scales.
Hybrid granular hydrogel	Granular hydrogel reinforced with fibers.
Hydrogel	Gel constitute of a 3D network of hydrophilic polymers and water.

Hydrogel composite	Hydrogel reinforced with particles or fibers.
Interface	Contact area between the two materials also called boundary layer.
Interphase	Region around the interface, which has different chemical and physical characteristics as the bulk material.
Load-bearing material	Material able to carry a load.
Microgels	Hydrogels the micro-size, which are often spherical.
Microstructure	Structure of the material at the microscopic scale.
Neat hydrogel	Conventional hydrogel containing a single polymer network.
Precursor	Substance before being formed in the final material.
Preloading	Cyclic loading on the material before being evaluated.
Processability	Ability of the precursor to be manipulated into the final material.
Rheology	Study of material flows, properties in shear or tracking gelation.
Self-reinforced granular hydrogel	Granular hydrogel reinforced with fibers self-assembled <i>in situ</i> .
Stiffness	Resistance of a material with a specific geometry to being deformed in tensile loading.
Swelling ratio	Volume or weight increase of a hydrogel due to water absorption.
Tensile modulus	Elastic modulus measured in tensile loading (intrinsic property).
Toughness	Amount of energy that a material can absorb before a crack starts to propagate in it.
Viscosity	Consistency of a fluid (<i>i.e.</i> thick, fluid, sticky).

Chapter 1

Introduction

1.1 Motivation

Load-bearing tissues are fascinating materials. With their high water content between 60% and 95%, tissues show remarkable mechanical properties^[1–4]. As illustrated in Fig. 1.1, tissues such as articular cartilage, meniscus, or annulus fibrosus have a highly organized microstructure for optimally transmitting stress^[5,6]. Nevertheless, like other materials, load-bearing tissues are not infallible. They might fail due to trauma, over-solicitations, or diseases, which subsequently alter the host’s mobility. Therefore, repairing those damaged tissues in a minimally invasive way is nowadays widely studied.

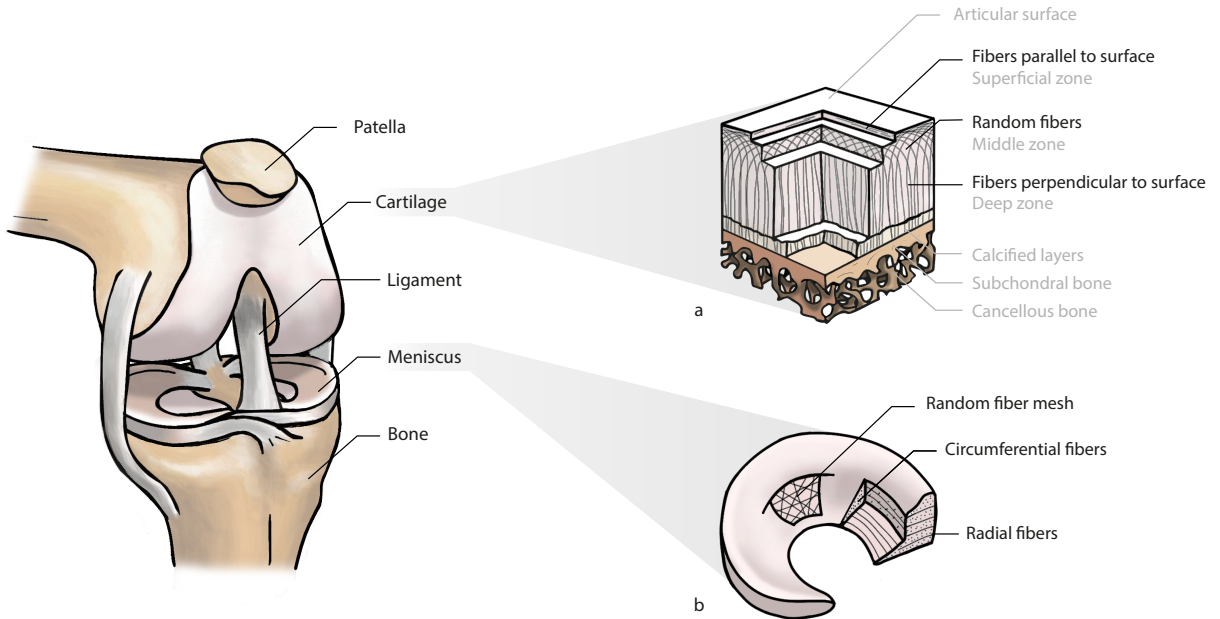


Figure 1.1: Anatomy of human knee composed of several tissues with highly organized and hierarchical microstructures such as (a) articular knee cartilage (osteocondral tissues) and (b) meniscus^[5,6].

Hydrogels are promising biomaterials for repairing soft tissues^[7]. Like living tissues, their high water content, typically more than 80% of water, is suitable for encapsulating cells and transporting nutrient^[8]. Moreover, surgeons can inject the hydrogel precursor in the human body and cure it *in situ* in a minimally invasive way without damaging the surrounding tissue. These last years, load-bearing

hydrogels have gained attention^[9] because the tough hydrogels can discharge some functions of the tissue by sustaining load and subsequently promote new ones^[10–13]. Furthermore, the patient could rapidly put weight on the implant after its implementation validating then what has been defined as functional tissue engineering^[14].

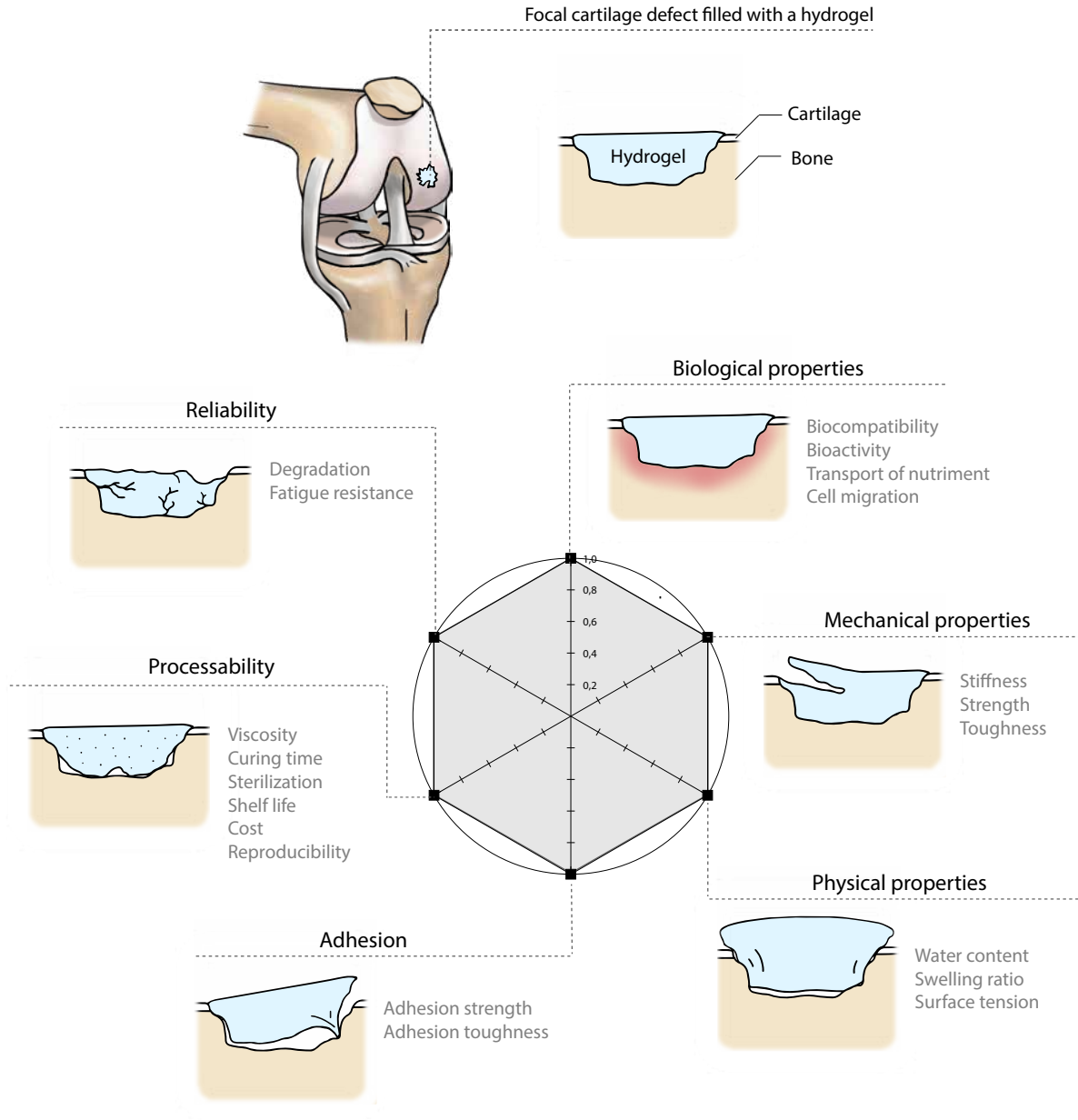


Figure 1.2: Important characteristics of load-bearing hydrogel implants. The example illustrates a hydrogel used to repair a focal cartilage defect.

For their application, load-bearing hydrogels should satisfy a demanding list of critical requirements that are illustrated in Fig.1.2. One of the most challenging requirements is to reach similar mechanical properties to the native tissue. Indeed, the mechanical performance of conventional hydrogels composed of a single polymer network (*i.e.* neat hydrogel) is known to be relatively low^[15]. More

complex hydrogel structures such as dual crosslink hydrogels^[16,17], double network^[18,19], or hydrogel composites^[20,21] are employed to significantly improve their stiffness and toughness. However, those hydrogels can currently not compete with some load-bearing tissues, such as meniscus or articular cartilage, mainly because it is extremely difficult to mimic their highly hierarchical microstructures. Therefore, several procedures such as additive manufacturing or redistribution of the component were established these last years for better replicating physiological microstructures or gradients in hydrogels^[22]. Another challenge in hydrogel development is better controlling the swelling performance while minimally affecting other properties, such as stiffness or deformation performance. Different strategies have been investigated, including changing the crosslinking type, crosslinking density, the polymer content, the polymer chain length, or the polymer's hydrophilicity. These approaches are efficient but often at the expense of other properties such as biocompatibility, stiffness, toughness, or processability^[23–25]. Moreover, as the human body is continually subjected to cyclic loading, reliable fatigue resistance is crucial for their application. In particular, many hydrogels become softer and lose their toughness after the first loading cycles^[26–30].

Therefore, this work focuses on developing and assessing different hydrogels structures, including neat, double network, composite, and granular structures according to the load-bearing characteristics illustrated in Fig. 1.2. An extensive parametric study on hydrogels' composition and structure enabled establishing complete property charts that summarize mechanical, swelling, and rheological properties. In a second step, different hydrogel structures were combined for better mimicking the morphology and functions of living tissues.

Tissues incorporate numerous spatially organized components and can be viewed as multi-functional composites themselves. Therefore, composite and granular approaches are proposed for better replicating native tissues. Adding fibers or particles in hydrogels is an effective way to increase stiffness and toughness as well to control swelling^[28,31]. In parallel, granular hydrogels belong to a new promising group offering an extended range of material properties for biomedical applications^[32–39] or 3D printing^[37–39]. For example, their precursors, mainly composed of microgels, exhibit inherent stability due to friction and cohesive forces between microgels, ideal for unconfined applications. Furthermore, microgels can be tailored in composition to explore additional biological, physical, and mechanical properties^[33]. Accordingly, combining both composite and granular structures open new doors for designing multi-functional hydrogel implants with gradient and anisotropic properties.

1.2 Objectives

The goal of the thesis is to develop different hydrogel microstructures and evaluate their potential for load-bearing implants. Based on the requirements illustrated in Fig. 1.2, the study focuses on (i) designing tough and fatigue resistant hydrogels and (ii) establishing a methodology to control the stiffness and the swelling of hydrogels independently, and (iii) considering processing ease by tailoring each hydrogel precursor's viscosity.

The main objectives are thus defined as followed:

1. Tailor and extend hydrogel properties by investigating different hydrogel structures of known biomaterials. Heavy chemical modifications, leading to new full assessment, in particular regarding biocompatibility, should be avoided.
2. Assess single and double network hydrogels and their composites according to load-bearing characteristics such as swelling ratio, adhesion, elastic modulus, toughness, or fatigue resistance.
3. Study the effect of cyclic loadings on the fracture behavior and the microstructures of hydrogel composites.
4. Perform an extensive parametric study on compositions and microstructures in varying the concentrations of polymers, fibers, and microgels to control swelling ratio, elastic modulus, and viscosity independently.
5. Investigate the feasibility of self-reinforced hydrogels and explore the range of achievable properties.
6. Design hybrid hydrogels for better mimicking the microstructures and functions of living tissues.

1.3 Structure and approach

Fig.1.3 presents the general approach adopted for the research. The thesis, divided into nine chapters, evaluates several hydrogel structures and addresses several questions tightly related to the development of load-bearing hydrogels, such as:

Which hydrogel structure is suitable for load-bearing applications?

How cyclic loading affects mechanical properties and microstructures?

How to decouple hydrogel properties?

How to process self-reinforced hydrogels?

How to select and combine hydrogels to better mimic the microstructures and functions of living tissues?

Before answering those pertinent questions, the *Chapter 2. State of the art* provides a thoroughgoing review of the research done behind the main characteristics to consider for developing load-bearing hydrogels implants.

The methods used for processing and analyzing the properties of the studied materials are presented in *Chapter 3. Materials and methods*.

The *Chapter 4. Single and double network hydrogels and their composites* highlights the strengths and weaknesses of four hydrogel structures: neat, composite, double network, and composite double network. In particular, the study investigates the effect of swelling and fatigue loading on mechanical properties and how the hydrogel's dissipative capability can enhance the adhesion to tissues.

The next *Chapter 5. Fracture properties of preloaded hydrogel composites* focuses on how cyclic loading affects the fracture behavior of hydrogel composites reinforced with nano-fibrillated cellulose fibers. In this chapter, the strain field around the crack tip and the evolution of the morphology of cellulose fibers according to the preloading strain are observed.

The following *Chapter 6. Hybrid granular hydrogels* explains how combining composite and microgels approaches can decouple physical and mechanical properties. An extensive parametric study on different hydrogel compositions is performed for creating complete property charts. Those charts summarize mechanical, swelling, and rheological properties and help to target hydrogel properties for specific applications. Moreover, we discuss how the compositions of the precursors affect the swelling degree of microgels.

The *Chapter 7. Self-reinforced granular hydrogel with silk fibroin fibers* introduces a novel self-reinforced silk granular hydrogel composed of microgels and silk fibroin fibers regenerated *in situ*. The underlying principle is to locally concentrate and regenerate silk fibroin *in situ* using microgel swelling. To our knowledge, the approach is unique in the field of hydrogels.

Since the requirement for an ideal customized implant depends on the patient and the exact part of the tissue to treat, hybrid hydrogels composed of stacked hydrogels are processed in *Chapter 8. Tailoring hybrid hydrogels for load-bearing applications*. It is discussed how the analyzed materials can be combined to create local or mechanical gradient properties through a sequential layering. Additionally, the knowledge acquired from the previous chapters will be validated with other hydrogels and microgels.

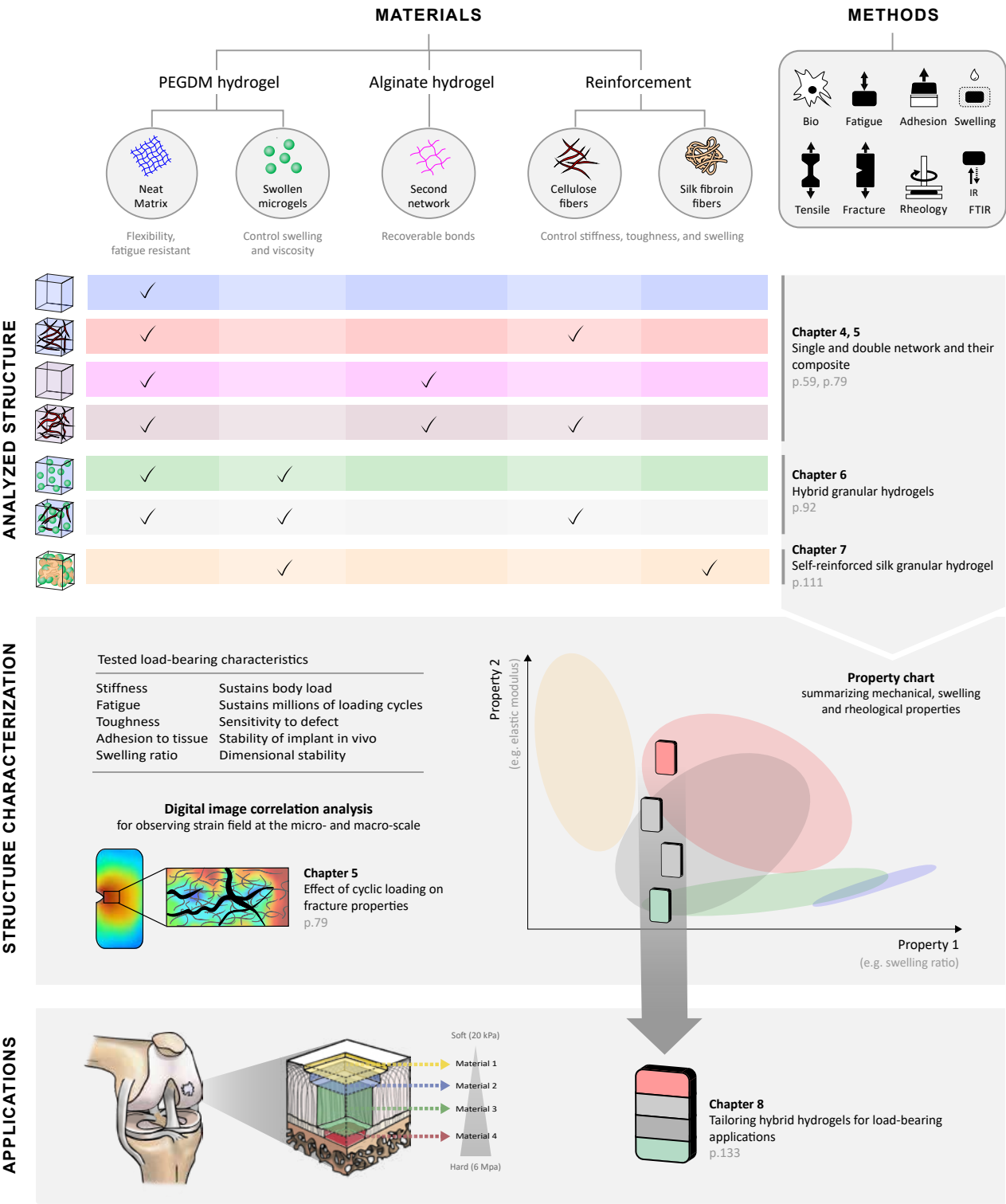


Figure 1.3: Thesis charter.

Chapter 2

State of the art

Soft contact lenses, jam, or gelatin desserts are some examples of common hydrogels processed by humans. Hydrogels are composed of a 3-dimensional polymer network filled with a lot of water, typically more than 80%, which confers their soft consistency. Those unique characteristics are suitable for a wide range of applications, as tissue engineering^[40,41], tissue repair^[7,42] or drug delivery^[43–45], but also for soft robotics^[46–48], sensing applications^[49,50] or food packaging^[51]. Nevertheless, to use hydrogels as load-bearing implants, they have to fulfill a demanding list of requirements illustrated in Fig. 1.2, where biocompatibility is substantial. Naturally, the requirements will differ depending on the tissue to repair or replace. For example, repairing a focal cartilage defect would necessitate an injectable fast curing hydrogel that adheres strongly to the surrounding tissue, while replacing a meniscus would need a robust anisotropic hydrogel able to damp energy. Nevertheless, both must have dimensional stability and sustain millions of loading cycles.

This chapter provides a review of the research done so far behind the following characteristics:

- 2.1 Biocompatible hydrogels
- 2.2 Hydrogel processability
- 2.3 Mechanical properties
- 2.4 Gradient and anisotropic properties
- 2.5 Biological properties
- 2.6 Swelling properties
- 2.7 Adhesion properties
- 2.8 Reliability

2.1 Biocompatible hydrogels

Biocompatibility is crucial for any biomedical applications. Indeed, every material implanted in a living being or exposed to bodily fluids will generate a response from the host. Accordingly, a bio-compatible implant represents manifests no or low toxic or immunological response.

The commonly used biocompatible hydrogels are summarized in Table 2.1. Only a limited range of materials and synthesis processes are available. The most prominent choice would be to mimic the native composition of the damaged tissues, such as collagen, which is abundantly present in cartilaginous tissues. However, those materials are not easily accessible. For example, collagen can currently not be synthesized, and its extraction is complicated, and time-consuming^[52].

Table 2.1: Conventional biocompatible hydrogels.

Description	Type	Crosslinking	Characteristics
Agarose	Natural Polysaccharide	Physical	Biodegradable, bioactive, temperature-sensitive ^[53]
Alginate	Natural Polysaccharide	Ionic	Biodegradable, bioactive, injectable, viscoelastic, strain-stiffening behavior, pH and temperature sensitive ^[8,53–56]
Chitosan	Natural Polysaccharide	Physical	Biodegradable, bioactive, pH-sensitive ^[8,57–61]
Collagen	Natural Protein	Physical	Biodegradable, cell recognition ability, self-assembling, injectable, viscoelastic, strain-stiffening behavior ^[53,62–64]
Hyaluronic acid HA	Natural Polysaccharide	Physical	Biodegradable, bioactive, injectable, viscoelastic ^[8,53,55,64–66]
Fibrin	Natural Protein	Physical	Biodegradable, cell recognition ability, viscoelastic, strain-stiffening behavior ^[53,62,63]
Silk fibroin SF	Natural Protein	Physical	Biodegradable, bioactive, self-assembling, pH and temperature sensitive ^[67] [68–72]
Poly(ethylene glycol) PEG	Synthetic	Covalent	Possibility to be biodegradable, inert, injectable, elastic, strain-stiffening behavior ^[53,55,73,74]
Poly(vinyl alcohol) PVA	Synthetic	Covalent or physical	Possibility to be biodegradable, inert, elastic ^[73,74]
Poly(2-hydroxyethyl-methacrylate) pHEMA	Synthetic	Covalent	Possibility to be biodegradable, inert, elastic ^[53]
Poly(acrylamide) PAAm	Synthetic	Covalent	Possibility to be biodegradable, inert, elastic ^[55,75,76]

The commonly used hydrogels, summarized in Table 2.1, can be classified into two main categories: natural or synthetic hydrogels. Natural polymers, such as proteins or polysaccharides, resemble more the molecules constituting tissues and are often highly biocompatible. Moreover, most natural polymers are degradable, implying that the damaged tissues must repair and replace the implant in the long-term. In contrast, synthetic polymers are considered to have better reproducibility and stability. Therefore, many synthetic implants are non-degradable and aim to replace the damaged tissues permanently.^[53,54,73]

Many processing factors can alter the biocompatibility of the hydrogels described in Table 2.1, such as sterilization or the crosslinking mechanisms. In particular, when the material requires to be cured *in situ*, it strongly restricts the choice of the synthesis process. Indeed, if the hydrogel is injected and fixed inside the human body, no exothermic reactions or toxic compounds are allowed. For example, free radical polymerization generates heat, which might cause damage, stress, or even kill the surrounding cells^[77]. Also, many solvents (*e.g.* n-hexane) or strongly alkaline hardener are harmful to the human body and can significantly damage the contacting living tissues^[78,79].

2.2 Hydrogel processability

The translational potential of new material from academic research to the industry is strongly linked to the processability. In particular, hydrogels' synthesis and sterilization targeted for biomedical applications require to be simple, fast, and reproducible mainly for safety and cost reasons. Each minute of surgery is extremely costly, regarding the renting of the operating room and the involved personnel. Moreover, the risk for complications is increasing with the duration of surgery. The characteristics summarized in Table 2.2 enable evaluating the processability of hydrogels.

2.2.1 Photopolymerization

Stimuli-sensitive hydrogels have increasingly gained attention because the surgeon is able to control curing *in situ* without significantly releasing heat^[82,83]. The stimuli can be issued from the body environment (*e.g.* change in pH or temperature) or by external stimuli (*e.g.* light, ultrasound, magnetic field^[84]).

In particular, photopolymerization via visible or UV light irradiation is an attractive curing method to obtain fast and controlled covalent crosslinking of hydrogel under ambient or physiological conditions^[8,85,86]. Indeed, the surgeon acquires not only a temporal but also a special control over polymerization^[1,8,87].

Photopolymerization is usually classified into three categories: radical, anionic, and cationic. Nevertheless, only radical photopolymerization is suitable for biomedical applications because of its lower reactivity and better control over polymerization. Indeed the presence of water will necessarily terminate ionic photopolymerization^[88].

Table 2.2: Characteristics describing the processability of hydrogels.

Characteristic	Description
Viscosity of the precursor	<p>Low viscosity reduces the risk of defects by limiting the formation of close porosity in the bulk hydrogel and filling all pores and asperities on the tissues' surface. It also favors the injectability of the hydrogel, which allows minimally invasive treatments^[77].</p> <p>High viscosity makes the hydrogels more malleable and sticky, which might be advantageous for unconfined applications such as 3D printing or to stick two parts together. However, the risk of defects due to trapped bubbles during mixing is higher, which may reduce mechanical properties.</p>
Wettability of the precursor	Related to the surface tension, good wettability to the tissue is essential for fast implementation and high adhesion strength: it ensures intimate contact between implant and tissue or between hydrogel layers ^[80] .
Curing time	Curing of hydrogels needs to be safe, controlled, and fast because the patient cannot wait several hours in an operating room for cost and safety reasons ^[77] .
Number of synthesis steps	The more complicated the synthesis is, the higher the risk of contamination and the production cost.
Sterilization	Since hydrogels are made of polymers, the sterilization is not straight forwards. Indeed, many polymers such as chitosan start to degrade and release potentially toxic compounds under gamma or beta ionization irradiation. Nevertheless, it resists the high temperature (121°C) and pressure (15 lbs) of an incubator ^[81] .
Shelf-life	Hydrogel implants or precursors need to have at least 18 months of shelf-life to ensure the product's quality. It means that the product could be stored and used safely during this time. Any preliminary deterioration could lead to critical postoperative complications.

Photopolymerizable hydrogels are composed of at least three elements: water, photosensitive polymer, and a photoinitiator. All three elements should be compatible with each other and not be toxic to the host. Nevertheless, there are some limitations in order to keep the surrounding tissue intact. In particular, the viability of cells strongly depends on the photoinitiator, the number of free radicals in the system, and the used wavelength^[89]. Table 2.3 summarizes the main requirements for injectable photopolymerizable hydrogels.

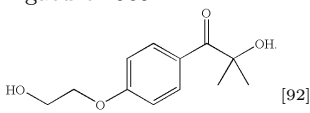
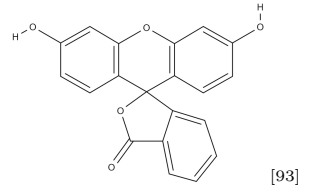
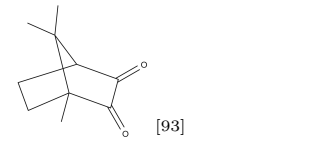
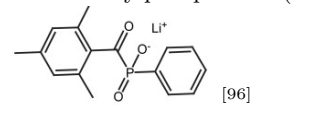
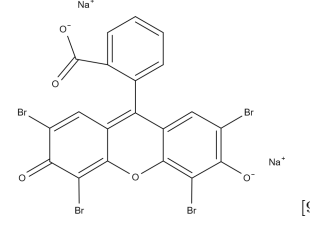
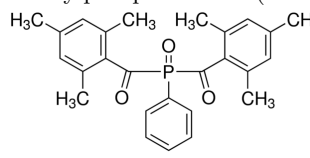
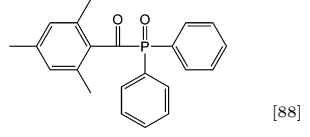
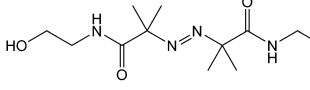
Table 2.3: Requirements for injectable photopolymerizable hydrogels.

Parameters	Description	Comments
Toxicity of components	No or very low cytotoxicity	No harmful reactions should occur between the components and the human body ^[77,86,90] .
Wavelength	Over 365 nm	Ultraviolet (UV) light, in particular below 320 nm (UVB) may damage DNA, which can induce mutations or even develop tumors ^[89] . In contrast, when the protein absorbs the used wavelength (<i>e.g.</i> 515 nm), it can lead to a slight temperature increase ^[88] .
Light intensity	Less than 10 mW/cm ²	The intensity of light should be sufficient to initiate the polymerization but not to lead to a local temperature increase ^[8,40,41,86,91] .
Type of photopolymerization	Radical	Only radical photopolymerization is suitable for biomedical applications because of its lower reactivity and better control over polymerization. Besides, the presence of water will necessarily terminate ionic photopolymerization ^[91] .
Solubility of the components	High	The polymerization rate is tightly related to the solubility and mobility of radicals and monomers ^[83] .
Conversion degree	Close to 100%	Radical polymerization generates free radicals that can potentially react with tissues. Therefore, the fewer radicals in the system, the better it is accepted by the human body ^[89–91] . Moreover, the mechanical properties highly depend on the conversion degree ^[8] .
Gelation kinetics	Fast	Gelation have to be feasible under physiological conditions and start within seconds to a few minutes after injection. The cost and the risks of surgery significantly increase with its duration ^[77] .

Photoinitiators

Radical polymerization is, in turn, categorized in Type I and Type II. Type I systems decompose the photoinitiator molecule, while Type II absorbs hydrogen from a donor co-initiator such as a tertiary amine (*e.g.* triethanolamine)^[88]. Table 2.4 presents the current Type I or II photoinitiators proposed for biomedical applications. Most water-soluble photoinitiators are Type I. Despite their lower solubility than Type II, Type I photoinitiator usually exhibit higher reactivity and lower cytotoxicity^[88].

Table 2.4: Examples of photoinitiators for biomedical applications.

Description	Type Maximum absorption	Comments
Irgacure 2959  [92]	Type I 275 nm	Irgacure 2959 is only poorly effective at a wavelength higher than 365 nm ^[88] (see Fig. 2.1).
Fluorescein (FR)  [93]	Type II 495 nm	Fluorescein is usually used as a fluorescent tracer. However, this dye shows promising properties as a photoinitiator (high conversion rate, low cytotoxicity) ^[94]
Camphorquinone (CQ)  [93]	Type II 468 nm	Camphorquinone becomes yellowish with time, which causes problems in dentistry ^[95] and exhibits some cytotoxicity effect. However, as a photo-bleaching initiator, it allows the polymerization of thicker samples.
Lithium acylphosphinate (LAP)  [96]	Type I 375 nm (local maximum)	LAP has better solubility and reactivity at long-wavelength than Irgacure 2959 but shows some cytotoxicity issues ^[89,96] .
Eosin Y  [93]	Type II 515 nm	The used wavelength of 515 nm is absorbed by some proteins, leading to slight temperature increases ^[88] .
Bisacylphosphineoxide (BAPO)  [97]	Type I 371 nm	BAPO is highly reactive ^[95] .
Monoacylphosphineoxide (MAPO)  [88]	Type I 381 nm	MAPO is similar to BAPO but it is a bit less effective ^[98,99] .
VA-086  [88]	Type I 375 nm	VA-086 may generate some nitrogen bubbles that are harmful to living tissue ^[88] .

Nowadays, only a few water-soluble photoinitiators are FDA approved. Irgacure 2959 is commonly used for UV irradiation in the biomedical field because of its reasonable water solubility and its low cytotoxicity at concentrations used for crosslinking (0.050-0.1% w/v)^[89]. However, it is only poorly effective at a wavelength higher than 365 nm^[88]. As shown in Fig. 2.1, its maximal absorption peak is located around 295 nm. Consequently, a larger concentration of initiator is required to polymerize the hydrogel at 365 nm, which implies a higher risk of toxicity^[86,91]. Therefore, for safety and efficiency reasons, current research aims to develop new photoinitiators that are more effective at a longer wavelength, typically over 400 nm^[88].

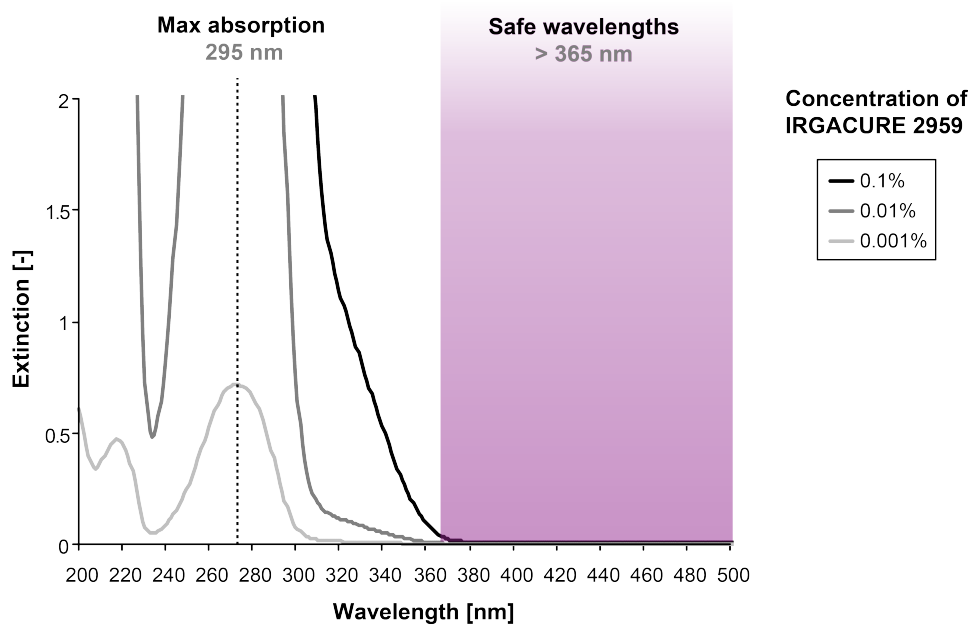


Figure 2.1: Absorption spectra of Irgacure 2959 (modified from^[92]).

Photopolymerizable hydrogels

A common approach to synthesize photopolymerizable and biocompatible polymer is to add acrylate or diacrylate group to a polymer backbone through an available amine (NH_3), carboxylic acids (COOH), and hydroxyl groups (OH)^[8]. Methacrylation can be performed on several water-soluble biopolymers, such as polyethylene glycol (PEG), polyvinyl alcohol (PVA), dextran, hyaluronic acid (HA), chondroitin sulfate (CS), chitosan, and alginate^[8]. Table 10.2 in *Chapter 10, Annexes* presents the main steps of a radical photopolymerization. Dimethacrylate groups are usually preferred over methacrylate groups in the biomedical field because of its lower reactivity^[100].

Thick hydrogel polymerization

The polymerization of thick hydrogels or hydrogels constrained between two tissues is challenging. Although the mobility of the reactive components is better in a highly aqueous medium^[83], the light intensity is gradually attenuated with increasing depth^[101]. Photo-bleaching initiators, such as cam-

phorquinone (CQ)^[102], that absorbs light at a different wavelength^[8] can minimize the attenuation of light. In parallel, adding some scattering agents in the hydrogel precursor can improve the homogeneity of the conversion degree of thick samples^[103]. Fig. 2.2 shows the scattering effect of nano-cellulose fibers. The shapes of polymerized poly(ethylene glycol) dimethacrylate (PEGDM) after being illuminated with a 600 nm fiber at a wavelength of 365 nm change when nano-fibrillated cellulose (NFC) fibers are present in the hydrogel. The spherical shapes showed in Fig. 2.2b indicates a homogenous polymerization^[103].

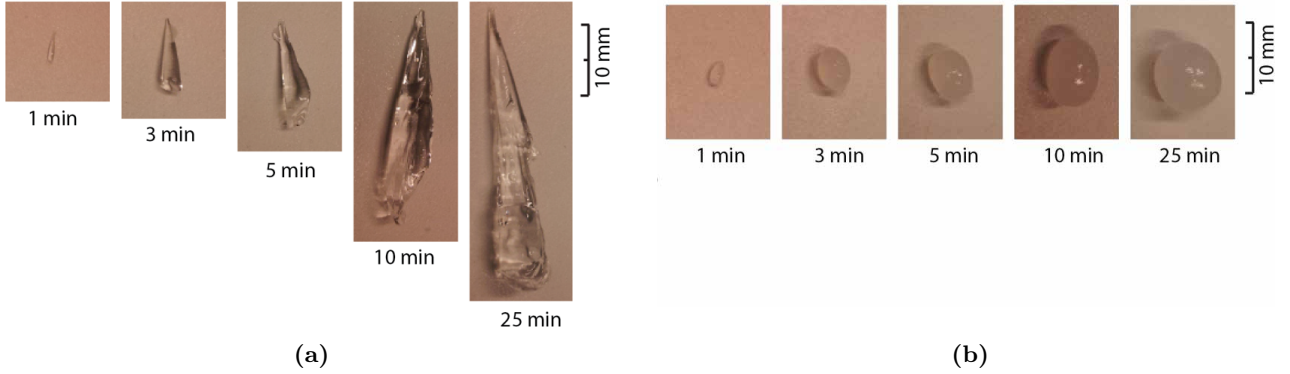


Figure 2.2: Scattering effect of nano-cellulose fibers (reproduced with permission from^[103]). The resulting shape of polymerized poly(ethylene glycol) dimethacrylate (PEGDM) (a) with (b) without nano-fibrillated cellulose (NFC) fibers after being illuminated with a 600 nm fiber at a wavelength of 365 nm.

2.3 Mechanical properties

Commonly used hydrogels described in Table 2.1 are known for their low mechanical properties^[15] due to their high water content and soft consistency. Many efforts were made to understand why hydrogels are lacking in mechanical properties and how to improve them. In particular, hydrogels' mechanical performance cannot compete with native tissues such as meniscus or articular cartilage nowadays^[18].

The conventional hydrogel, also called neat hydrogel, is composed of one single network. This network is often heterogeneous, which leads to early failure. When the network is under load, the stress is concentrated around the shortest chains, which can break at a very low force^[18]. Pre-formed polymer chain or coupling "click" reaction has been proposed to create a homogeneous network^[104]. This structure can also be reached with some polyampholyte hydrogels^[105,106], which are composed of a random copolymerization chain of oppositely charged ionic monomers, forming pairwise ionic crosslinks.

Another reason for the poor mechanical properties of conventional hydrogels is the polymer chain length and the lack of dissipative mechanisms^[18]. Some researchers are focusing on optimizing these parameters by employing longer polymer chain lengths to enhance their deformability (*e.g.* macromolecular hydrogels^[16,107]) or by mixing two or more polymer networks to increase the internal friction. The common name for the multiple network hydrogels is interpenetrating polymer network (IPN) hy-

drogels^[28,108–110]. Other techniques were developed to improve the damping properties. In particular, it was shown that using a sacrificial network, especially in double network (DN) hydrogel, significantly increases the energy dissipation mechanism^[27,30,105,111–113]. Double network hydrogels are a subgroup of interpenetrating polymer network hydrogels where the first network increases the elastic modulus and serves as sacrificial bonds that fracture at relatively low stress. The second aims to sustain stress at larger extension and thus increase the hydrogel's deformability of the hydrogel^[18,111].

A different way to enhance the mechanical properties, including dissipative mechanisms without compromising the flexibility, is to reinforce the hydrogel locally. That can be achieved by adding reinforcements in the hydrogel, which forms hydrogel composites^[28,29,112,114–116] or in creating some rigid crystalline domains inside the hydrogel^[26]. The apparent stiffness of the locally reinforced hydrogels will increase simply by the rule of mixtures. Moreover, the additional interfaces between reinforcement and matrix help to stop or deflect crack propagation. Accordingly, the quality of the matrix/reinforcement interfaces affects the efficiency to load transfer, or dissipative energy^[117].

2.3.1 Hydrogel composites

Tissues incorporate many spatially organized components, and can be viewed as multi-functional composites themselves. Therefore, composite approaches are very attractive for replicating native tissues. In particular, adding reinforcement reveals many advantages to enhance mechanical properties as listed hereafter:

- Reinforcement can be easily added to the hydrogel precursor^[23].
- Stiffness can effectively be tuned without significantly compromising the water content, or the failure strain^[1].
- Damping properties are improved due to better energy dissipation, for example, induced by friction between fibers with the matrix^[28,112,115,116].
- The number of bonding sites is multiplied^[118].
- Anisotropic or gradient properties can be achieved to better mimic living tissue^[119–121].
- Stimuli-responsive particles can be added for creating externally addressable hydrogels^[122].

Different forms of reinforcement are available such as fibers, fibrils, crystals, whiskers, clays, or particles, while the size varied from the nanometer to a few millimeters. When using reinforcement at the nanoscale, (i) the hydrogel keeps the optical transparency^[123] and (ii) the large specific surface of the reinforcement offers suitable mechanical and physical properties, like better cell adhesion^[124].

In biomedical applications, natural fibers are preferred over synthetic fibers because of their abundance, high biocompatibility, biodegradability, high specific strength and modulus, low density, high surface-to-volume ratio as well as non-abrasive properties^[123]. Table 2.5 presents an overview of important natural fibers.

Table 2.5: Natural reinforcements.

Reinforcement	Type	Form	Characteristics
Cellulose	Polysaccharide	Nanowiskers, nano/micro-fibrils, nano-crystals	Most abundant biopolymer, excellent mechanical properties, low density, large aspect ratio and specific surface area, large size distribution, gas barrier properties, (poor biodegradability), many (six per mer) hydroxygroups allowing chemical functionalization, polymorphic ^[123,125–129] .
Chitin and chitosan	Polysaccharide	Nanowisker, nano/micro-fiber	Second most abundant biopolymer, biodegradable, very limited solubility in water but can be solved with chemical fictionalization, high specific surface area, polymorphic ^[60,123,130–133] .
Starch	Polysaccharide	Nanocrystals, colloidal starch nanoparticle	Abundant, odorless, low cost, biodegradable, versatile, functional attributes, brittle ^[80] .
Collagen	Protein	Fibers	Hierarchical structure, stiff and hard polymer ^[80,123] .
Silk fibroin	Protein	Fibers	Very high toughness, extensible and high tensile strength, organized crystalline β -structure ^[123,134,135] .

Fibrillated cellulose fibers

Cellulose attracts rapidly attention for packaging, automotive, or biomedical application^[123,125–129,136]. The natural fiber is widely used because of its several advantages as described hereafter:

- Availability: cellulose is the most abundant biopolymer.
- Versatile structures: it can be processed into fibers, crystals, foam, film, fibrous tissues, or even hydrogels.
- Excellent mechanical and physical properties: cellulose crystals or fibers at the nano- or microscopic scale have, in particular, remarkable mechanical properties, low density, large aspect ratio, and specific surface area.
- Stimuli-responsive: cellulose crystals or fibers can be oriented through external electrical and magnetic fields^[126,137–140].

Nevertheless, there is still some confusion concerning their nomenclature, especially with the term *nano*. For example, nano-fibrillated cellulose fibers are hierarchical structured, where *nano* refers to the fibrils only, while the fibers are in the microscale^[123,125–129].

Cellulose is commonly extracted from wood, such as spruce, beech, or directly produced by bacteria or fungi^[127]. Wood-based cellulose, fibrillated at the nano- or microscopic scale, are obtained by mechanically treatment (*e.g.* high-shear disintegration, high pressure homogenization, grinding, refining, microfluidization, high-intensity ultra-sonication, cryo-crushing or steam explosion)^[141,142], which are sometimes combined with chemical and enzymatic pretreatment (*e.g.* oxidation, alkaline extraction, carboxymethylation)^[142].

For the development of membranes or bio-hydrogels, bacterial cellulose is often preferred over wood-based cellulose because of its purity. Additionally, often no pretreatment is required^[143,144]. Nevertheless, wood-based cellulose fibers are larger and more flexible. These characteristics are more suitable for reinforcing hydrogels^[23].

Regenerated silk fibroin fibers

Bombyx mori silk is composed mainly of two proteins: silk fibroin (70-75%) and sericin (25-30%). The water-soluble sericin is usually removed because it is often associated with an immune response such as inflammation. Nevertheless, recent findings suggest that sericin used as isolated material shows low biocompatibility concerns and even good antibacterial properties^[145]^[146]. In contrast, silk fibroin fibers have already commercial applications in biomedicine such as surgical mesh, sutures or garment^[146,147] and are widely studied because it offers many additional advantages as described hereafter:

- Self-assembling material^[68].
- Good biocompatibility^[147].
- Good cell adhesion^[147].
- Slow in vivo degradation^[148].
- High stiffness^[68].
- Low swelling ratio^[149].
- Versatile structures: fibers, sponge, hydrogel, film, tube, microspheres^[150].
- Convenient for chemical modification^[151].

In particular, silk fibroin fibers can be used in their native form or being dissolved and regenerated in various morphologies, such as illustrated in Fig 2.3^[145,152]. These versatile structures raise up new

applications opportunities for drug delivery, artificial skin, contact lenses, gene delivery system, cartilage repair, or bone graft^[145]. Moreover, the gel transition of silk fibroin solution can be achieved with different methods such as (i) time, (ii) temperature increase, (iii) sonication/ultrasound, (iv) non-solvent induced phase separation, (v) pH, or (vi) osmotic stress induced by poly(ethylene glycol)^[71,146,149,153–156].

Silk fibroin solution preparation

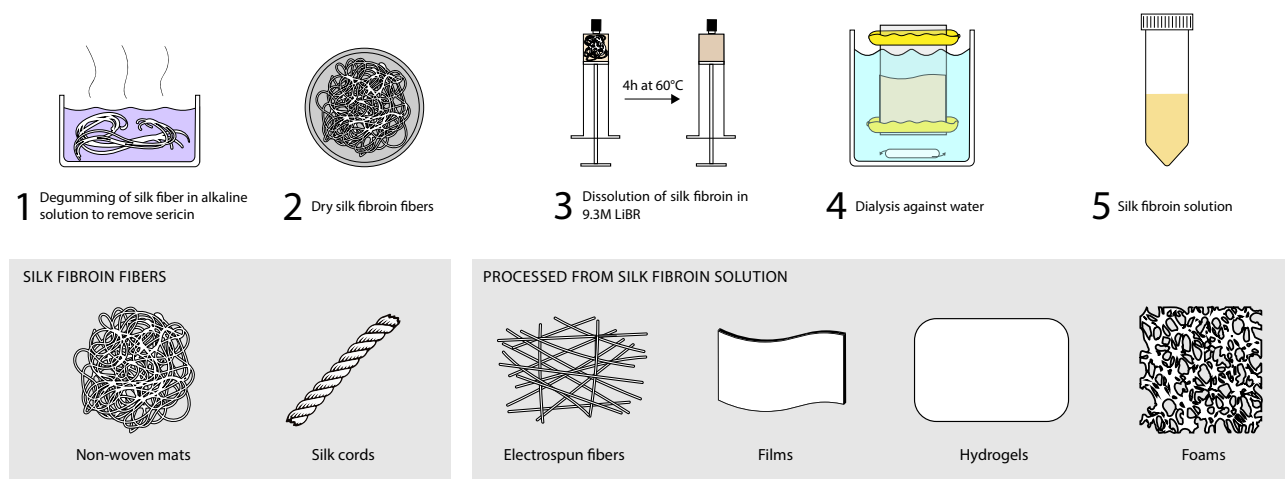


Figure 2.3: Example of silk fibroin versatile structures.

Silk fibroin is usually extracted from silkworms. In the classical extraction protocol, illustrated in Fig 2.3, silk cocoons or fibers follow first an alkaline treatment to remove sericin, where the raw material is boiled in water containing 0.02-0.1M sodium carbonate (Na_2CO_3) and washed three times with pure water. The remaining silk is dissolved in 80 wt.% 9.3M lithium bromide (LiBr) for 4h at 60°C before being dialyzed for three days against pure water^[150]. This process dissolves the protein at the molecular level and gives a metastable silk fibroin solution based on water.

Nevertheless, in other protocols 1-15 wt.% silk fibroin is dissolved in 1-10 wt.% calcium chloride - formic acid (CaCl_2 -FA)^[157–159]. The dissolution of degummed silk fibroin is more efficient in CaCl_2 -FA than LiBr solution and occurs at the fibrils levels preserving nanofibers' structure, as shown in Fig 2.4a^[158]. The boiling time or concentration of Na_2CO_3 during the degumming process highly influences the dissolution rate, the morphology, and the size of silk nanofibers (Fig 2.4a). However, the solution can not be dialyzed against pure water. As soon as CaCl_2 /FA starts to be substitute by water, silk fibroin forms a gel, which becomes progressively stiffer with time (*own experience*). Therefore, this dissolution method is usually used for electrospinning processes^[160] and cannot be injectable due to toxicity concerns.

Some researchers proposed, therefore, either a combined LiBr/ CaCl_2 /FA^{[158][161]} or two-step methods that consist first a dissolution with CaCl_2 /FA then in LiBr solution^[153]. The two-step dissolution generates a fibrous hydrogel structure, while the classical dissolution produces a porous hydrogel structure.

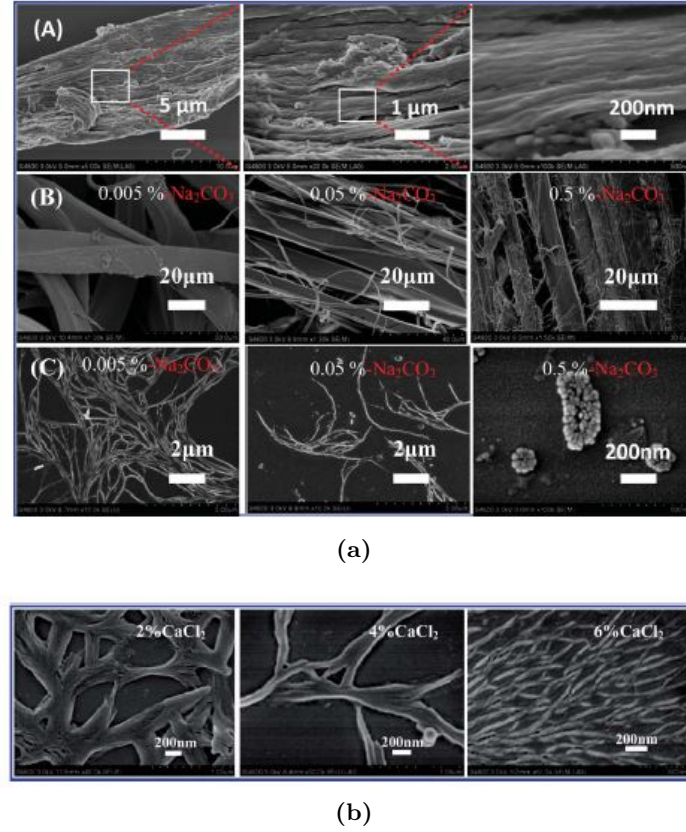


Figure 2.4: (a) Effect of the degumming and (b) the concentration of CaCl₂ in formic acid on the dissolution and morphology of silk fiber (reproduced with permission from [158]).

Fiber-matrix interface

The quality of the interface between fiber and matrix significantly impacts the distribution of load and mechanical properties. Strong interfaces lead to good load transfer into the fibers, where most dissipative mechanisms are originated from the bulk of the fibers. The accumulated stress inside the fiber might result in the brittle scission of the fiber itself^[117]. In contrast, weak interfaces promote pull-out mechanisms, where dissipation is mainly issued from friction at the interface^[117].

The interface strength can be tailored by chemical modification of the fiber surface^[162]. For example, it was observed that grafting methylmethacrylate on cellulosic polymer improves interface strength and stability against moisture and significantly increases the tensile strength properties of the composite material^[163].

Natural fibers incorporate many hydroxyl groups making them sensitive to water, which generally ends up in weakened interfaces and agglomerates. Subsequently, good dispersion is essential to obtain efficient reinforcement^[127,164]. It was shown that dispersion could be enhanced by adding polar groups on fiber surface^[60,62].

2.4 Gradient and anisotropic properties

When approaching the sea on a sunny day, the sand gradually changes from dry to wet, from hot to cold, from soft to hard, and from pale to dark-colored. This simple example shows that gradients are omnipresent. It is a continuous and progressive variation of a property along one or several axes. In natural tissues such as tendon, bone, or cartilage, the interfaces are rarely abrupt. The transition from one medium to another is progressive. Variation in density, microstructure, or composition usually lead to mechanical gradients, which are essential to efficiently transfer stress^[5,6,22,165,166]. Articular cartilage exhibits multiple mechanical gradients, for example. The stiffness progressively increases when approaching the subchondral bone and regions, which sustain and transfer higher loads.

In tissue engineering, gradients are usually ignored mainly for practical reasons, despite their role in physiological functions. Creating gradients, especially multiple gradients, remains challenging and often requires special equipment and a complex synthesis process. Nevertheless, these last years, many techniques were established to create layered or continuous gradients in hydrogels as illustrated in Fig. 2.5 and described in Table 2.6^[22]. The choice of the synthesis process is based on different criteria such as the type of gradients (*i.e.* continuous or layered), type of precursors (*i.e.* low or high viscosity), freedom of geometries, or number of gradients (*i.e.* gradient along multiple axes).

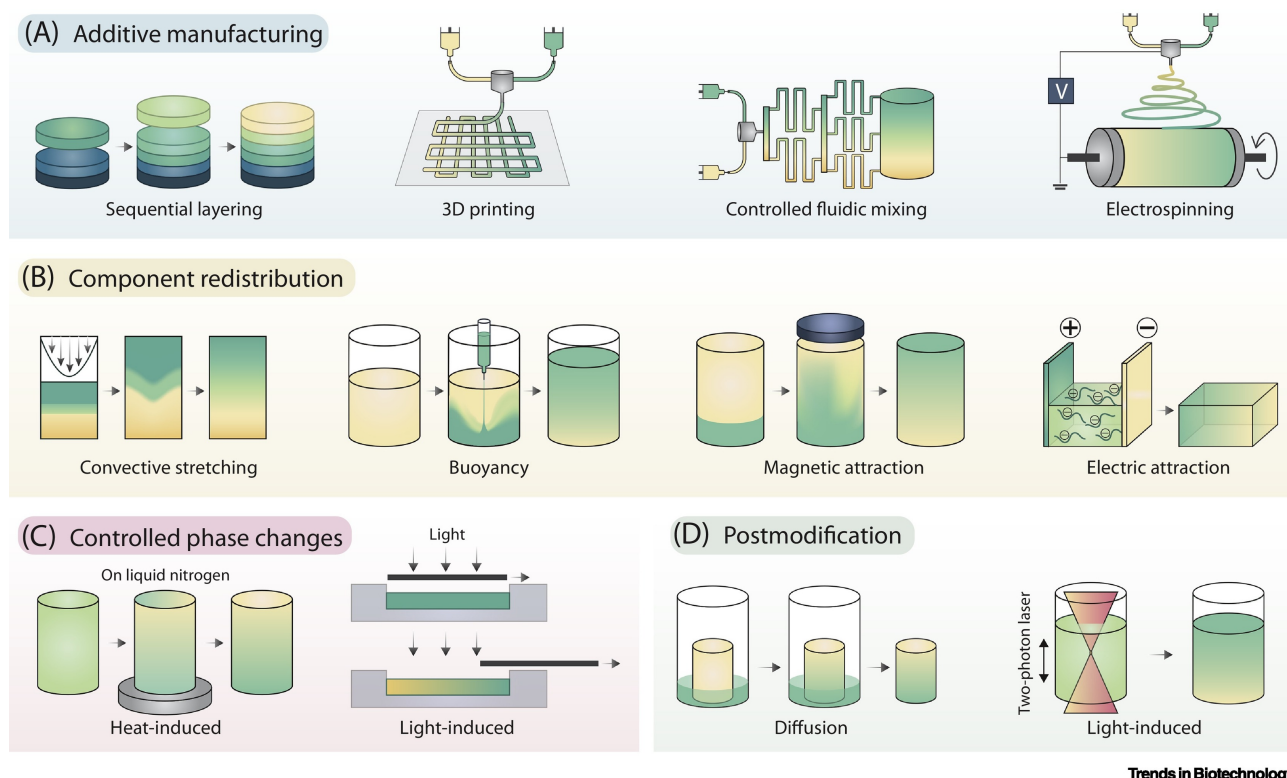


Figure 2.5: Techniques for developing gradient in hydrogels (reproduced with permission from^[22]).

Table 2.6: Techniques for developing gradient in hydrogels and their limitations.

Techniques	Procedure	Type of gradient	Limitations
Sequential layering ^[22,167]	<ul style="list-style-type: none"> • Layers of hydrogels glued together. • Layers of hydrogel cured on top of each other. • Successive layers of viscous precursor before curing. 	Layered, multi-directional.	No continuous gradient.
3D printing ^[22,168]	<ul style="list-style-type: none"> • Impregnation of a scaffold with structural or density gradient. • Successive deposition of viscous bioink. 	Layered or continuous, multi-directional.	Requires 3D (bio)printer.
Controlled fluid mixing ^[22,169,170]	Controlled deposition of <ul style="list-style-type: none"> • precursors with low viscosity before curing. • microgels before annealing. 	Continuous, mono-directional.	<ul style="list-style-type: none"> • Requires gradient maker or microfluidic device and pump. • Restricted to a single gradient.
Electrospinning ^[22,171]	Electrospinning of precursors onto a moving collector.	Continuous, mono-directional.	<ul style="list-style-type: none"> • Requires electrospinner. • Restricted to thin sample.
Magnetic/electric field ^[22,172]	Alignment of particles through an electric or magnetic field.	Continuous, mono-directional.	<ul style="list-style-type: none"> • Requires an external electric or magnetic field. • Requires particles responding to an electric or magnetic field. • Risk of cytotoxicity.
Heat-induced ^[22,173]	Spacial controlled crosslinking/crystallization using with unidirectional freezing drying.	Continuous, mono-directional.	<ul style="list-style-type: none"> • Requires lyophilizer. • Usually requires thermoresponsive material.
Light-induced ^[22,174]	Spacial controlled crosslinking with graded light exposure using sliding photomasks for partial or full crosslinking.	Continuous, mono-directional.	<ul style="list-style-type: none"> • Requires photoresponsive material. • Presence of unreacted free radicals. • Risk of damaging cells.

As illustrated on Fig. 1.1, tissues such as articular cartilage, meniscus, tendon, or annulus fibrosus possess highly anisotropic microstructures^[5,6,168]. Anisotropy represents a property that changes according to different axis directions, which is the gradient case. The average property along the gradient direction is different from the one measured across^[175,176].

Different processes were proposed to create gradients, bilayer, patterned, or oriented structures to better replicate native tissues, such as freeze-casting or extrusion techniques^[120,175,176]. One of the most attractive techniques for inducing anisotropy is to align reinforcement in composites. In this method, the reinforcement, with an aspect ratio superior to 1, must rapidly be fixed inside the hydrogel once aligned^[177]. The magnetic or electric field was employed to orient responsive reinforcements such as cellulose fibers^[126,137–139,178] or silk nanofibers^[172]. Nevertheless, 3D (bio)printing has gained more attention this last decade because the extrusion method could successfully align reinforcement^[176,179].

Printing of hydrogel composites gave rise to 4D printing, where directional swelling is key^[119,180,181]. Hydrogel composites swell less along with the aligned reinforcement than across. Consequently, hydrogel ink of oriented fibers can be deposit in a 2D structure before curing. Then, once the hydrogel is immersed in an aqueous medium, it swells in an anisotropic way and self-folded in a complex 3D structure. Similarly, bilayer hydrogels incorporate two hydrogels with different swelling ratios. Its geometry changes according to the swelling degree of each component. This characteristic is suitable for developing biomimetic anisotropic actuators, which are employed in soft robotic and used to mimic valves or artificial muscles^[175,182].

The success of 3D/4D printing of hydrogel incorporates many processing parameters such as nozzle size, gelation time, or printing speed. Moreover, the hydrogel requires being injectable and polymerized according to stimuli such as pH, light, or temperature. Therefore, for developing a handy and stable ink, several properties have to be well controlled like hydrogel precursor's viscosity, composition, gelation procedure, and gelation rate^[53].

2.5 Biological properties

As mentioned in section 2.1, using biocompatible hydrogels is crucial. Nevertheless, the choice of polymer is not sufficient. Other parameters, like the polymer network's mesh size, the cells' ability to adhere to the polymers, or open porosity, significantly influence how the host accepts the implant.

2.5.1 Mesh size

The mesh size of the hydrogel represents the polymer network's nanoporosity and is inversely proportional to the crosslinking density. As illustrated in Fig. 2.6, many properties such as swelling ratio, permeability, or mechanical properties highly depend on crosslinking density, making it difficult to assess the influence of the mesh size on cell viability and proliferation. Nevertheless, based on different researches^[183–186], a hypothetical trend is plotted in green in Fig. 2.6b. It suggests that a minimum number of bonding sites are required for cell adhesion but that the cell proliferation, permeability, and transport of nutriment increase with the mesh size.

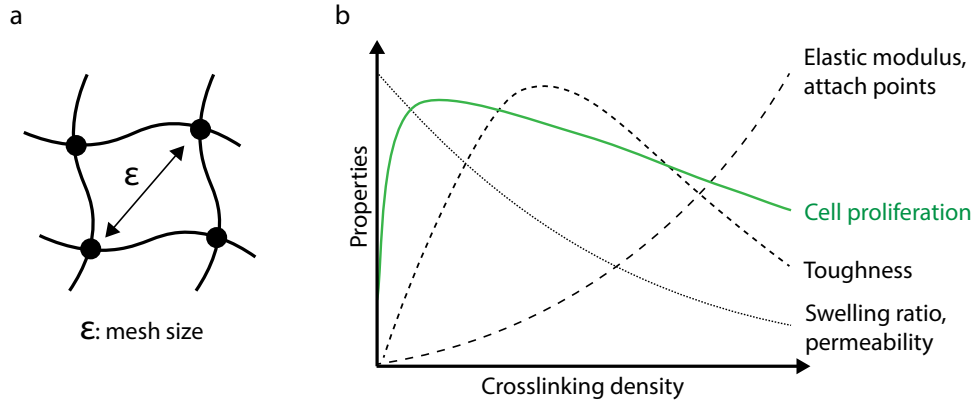


Figure 2.6: (a) Definition of the mesh size ϵ (b) illustration on how the crosslinking density influences the elastic modulus, toughness, swelling ratio, and cell proliferation^[183–186].

2.5.2 Cell adhesion

To survive and proliferate, cells have to adhere to the polymer network. Natural polymers such as collagen^[187] or silk fibroin^[147] have naturally good cell adhesion properties. Nevertheless, adhesive proteins such as arginylglycylaspartic acid (RGD) peptides can be grafted to synthetic polymers like polyethylene glycol (PEG) to improve cell adhesion^[188]. It was also shown that the surface topography^[189] and the hydrophilicity of the polymers network influence cell adhesion^[190].

2.5.3 Open microporosity

Open microporosity favors the transport of nutriment, the migration of cells and dissipation mechanisms^[191,192]. Such structures can be created with 3D printing^[193], dissolution of salt particles incorporated in the hydrogel^[194], or partial freezing^[195]. Nevertheless, those *in vitro* methods are time-consuming and can not be adapted for being used *in situ*, allowing minimally invasive treatment.

Granular hydrogels

Granular hydrogels have gained a lot of attention these last couple of years^[32–39]. Their particular microstructure composed of contacting microgels offers an extended range of material properties for biomedical applications^[32–39] or 3D printing^[37–39]. Indeed, when microgels are compacted more than 58%, the contacting force is sufficient to jam the particles and form a granular structure with inherent stability, which exhibits several advantages listed hereafter^[33]:

- The precursor of jammed microgels is injectable and shear-thinning, which is ideal for unconfined application or 3D printing.
- The contacting microgels create an *in situ* open microporosity, which promotes the transport of nutriment and migration of cells.
- The cells and the microgels can form a network independently.
- Microgels can be tailored in composition to explore additional biological, physical, and mechanical properties.
- Microgels are cured *in vitro* before injecting in the human body, limiting the risk of cytotoxicity due to unreacted elements or UV irradiation exothermic reactions.

To our knowledge, this unique combination of properties was not achieved with other hydrogel structures. Moreover, they can be tailored in composition to explore additional biological, physical, and mechanical properties^[33]. For example, the group of L. De Laporte was able to guide and align cell growths by magnetically orienting rod-shape microgels *in situ* before curing the surrounding hydrogel. Moreover, the microgels were functionalized for being cell-adhesive or bioinert^[196]. Nevertheless, their mechanical properties remain relatively low. Therefore, jammed microgels are used in confined environment or follows a post-curing, such as annealing or photopolymerization, for binding the microgels chemically^[32,39].

2.6 Swelling properties

Controlling swelling performance of hydrogel is crucial for medical applications (*e.g.* dimensional stability, interface with tissue, or mechanical properties)^[1,197,198] but also for food packaging (*e.g.* control of humidity)^[51] and soft robotic applications (*e.g.* local out of plane deformation)^[46–48]. For example, as previously mentioned, injectable hydrogels enable minimally invasive treatment because the precursor can be injected through a small needle and cured *in situ* with UV-irradiation. However, once implemented in the human body, the hydrogel is not necessary in its equilibrium swollen state. The change in volume due to swelling or shrinking might affect mechanical properties and create internal stresses in the bulk hydrogels or break the tissue interface. Nevertheless, the improvement of one property, such as swelling ratio, comes at the cost of another, as observed in many hydrogel structures, including neat, double network, or composite hydrogels^[18,19,27,31,199,200].

According to the thermodynamics of rubber elasticity, the steady swollen state is reached when the osmotic drive to dilute the polymer is balanced with the entropic resistance to strand extension of the polymer chain^[201]. Thermosensitive, ionic, or polyampholite polymers were proposed to influence the osmotic driving forces^[58,105,202–207]. As these polymers are very sensitive to temperature or pH, their swelling ratio varied significantly. A more stable manner to control swelling is to influence the maximum strand extension of the polymer chain. This can be reached by adding rigid domains. For example, self-assembled silk hydrogel forms rigid dense β -sheet-like structures, making the water up-take difficult^[208]. Recent methods employ crosslinking centers in the hydrogel, such as functionalized core-shell microgels or self-assembled micelles, to bridge the polymer chains^[197,209,210]. For example, Zhang et al. reported that their micelle-crosslinked hyaluronate hydrogel could be compressed up to 75% applied strain with an elastic modulus of 310 kPa and a swelling ratio of 9% only^[210]. Alternatively, swelling can be controlled by influencing the maximum strand extension of the polymer chain such as incorporating rigid particles or fibers^[28].

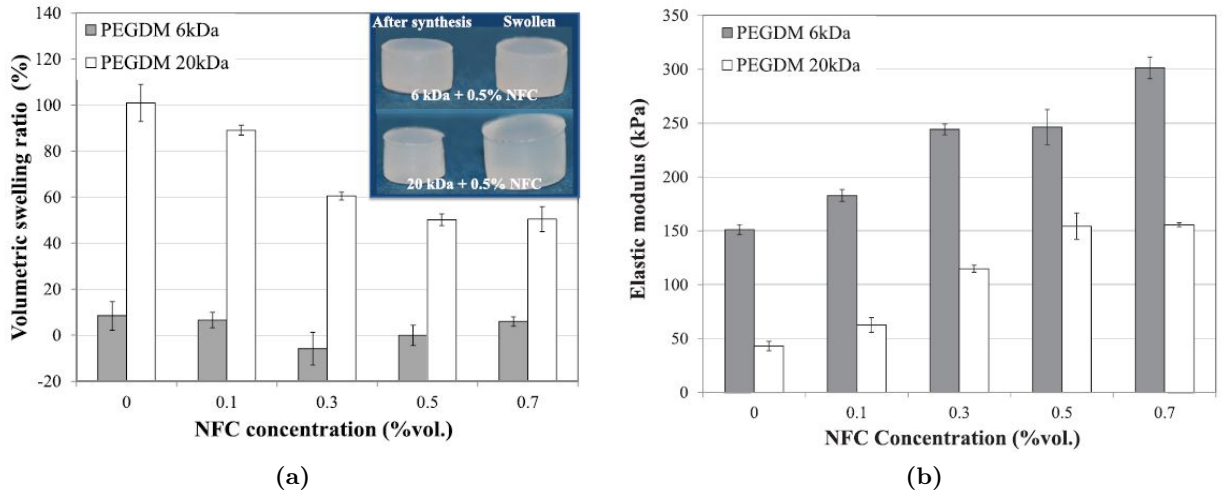


Figure 2.7: (a) Swelling ratios and (b) compressive elastic moduli of 10 wt.% PEGDM 6 kDa and 20 kDa, hydrogels reinforced at different NFC fibers concentration (reproduced with permission from^[23]).

Fig. 2.7 presents (a) the swelling ratios and (b) elastic moduli of 10 wt.% poly(ethylene glycol) dimethacrylate (PEGDM), 6 kDa and 20 kDa, hydrogels reinforced at different nano-fibrillated cellulose (NFC) fibers concentration. These results, published by Azadeh Khoushabi, the preceding Ph.D. student, in *Composite Sciences and Technology*^[23], shows clearly that the polymer chain length and the concentration of NFC fibers have a significant effect on the swelling ratios and the compressive elastic moduli. In fact, polymers with smaller chain lengths would swell less and increase the elastic modulus. For example, PEGDM 6 kDa exhibit 10% swelling only, while the compressive modulus was measured at 150 kPa. However, the increase in elastic modulus is usually accompanied by a decrease in the strain at failure and fatigue resistance, in contrast to hydrogel composite. Moreover, the swelling ratio of PEGDM hydrogel drastically decreases when NFC fibers are present in the matrix, while the elastic modulus improves.

2.7 Adhesion properties

Insects captured by spider silk or a frog tongue, mussels sticking on the hulls of boats, or frost surrounding the leaves show that adhesion is well integrated into nature. Adhesion fascinates humans for thousands of years. The first natural-based adhesives were rapidly developed, but synthetic adhesives have only been raised since the beginning of the last century^[211].

Many theories emerged trying to understand and explain how adhesion occurs. The most common ones, summarized in Table 10.1 in *Chapter 10. Annexes*, are based on energy and molecular interactions. All theories agree that high adhesion can only be achieved if the interface is strong enough to allow dissipative forms of deformation^[212–215]. Nevertheless, the link between dissipation and adhesion is not yet clear.

2.7.1 Influencing parameters in adhesion

According to the different theories described in Table 10.1 in *Chapter 10. Annexes*, the parameters that influence the most adhesion were summarized in Table 2.7.

Table 2.7: Influencing parameters for adhesion^[80].

Parameters	Function	Location	Related phenomena
Chemical interactions	Bonding strength and density at the interface.	Interface	Covalent, ionic and physical bonds.
Surface tension and energy.	Intimate contact	Interface	Wettability, contact angle.
Roughness	Contact area and number of bonding site.	Interface	Surface porosity, inclusion, hierarchical structure.
Bridging, mechanical interlocking, diffusion.	Fracture toughness at the interface/interphase.	Interphase	Diffusion length, density of bridging and mechanical interlocking, fiber orientation.
Humidity	Mechanical and bonding strength, or stress concentration at the interface due to swelling.	Bulk, interface.	Swelling, weakening of bonding strength.
Energy dissipation ability	Accommodation of energy before crack propagation.	Bulk, interphase.	Breaking of bonds, chain friction, flow, crazing or yield ^[212] , fiber fracture and pull-out.

2.7.2 Adhesion in biomedical applications

Adhesives have a decent range of uses in biomedical applications. The current applications include fixation of sutures, affix tissues, fill cavities and gaps, stop or reduce bleeding, regulate the moisture content, protect the wounds from the outside environment, and support healing^[216].

The standard ISO 10993-1 categorized surgical adhesives in three different branches, where the requirements are more or less strict according to the assigned category^[63,216]:

- **Surface-contacting adhesives:** direct contact with external tissues such as skin, mucosal membrane, breached or compromised surface.
- **External communicating adhesives:** contact with internal tissues such as blood path, tissue, bone, denting, and circulating blood.
- **Adhesives used as implants:** permanent contact with tissue, bone, or blood.

Table 2.8 exposes the requirements of surgical adhesive used as an implant.

Table 2.8: Required properties for hydrogel-based adhesive used as implant^[63,80,217].

Property	Description	Related parameters
Adhesion	High adhesion strength on the tissue (0.01-6 MPa depending on the surrounding tissue properties).	Adhesion strength in tension, torsion, peeling, and fracture energy.
Mechanical and physical properties.	Similar properties to surrounding living tissue for a good integration and load transfers.	Elastic modulus, tensile strength, water content.
Safe	Biocompatible, sterilizable and do not interfere with the healing process.	Cell viability, the effect of sterilization on mechanical and physical properties.
Stability	Resorbability: permanent or temporary implant.	Degradation rate according to external stimuli such as temperature, irradiation, and time.
Processability	Injectable, fast, and controllable curing in physiological conditions.	Precursor viscosity, polymerization time .
Reliability	Long-term performance.	Cyclic fatigue in tension, compression.

Commercially available adhesives fulfill only some of the requirements, as shown in Table 2.9. Many limitations related to safety concerns, poor adhesion and mechanical properties, excessive swelling, or low stability, make it difficult to extend the field of applications. Therefore, surgical adhesives are currently mainly used for topical applications such as wound closure, control bleeding, or stabilize sutures^[218].

Table 2.9: Commercial available surgical adhesives^[63,216,219,220].

Description	Examples	Functionalities	Advantage	Disadvantage
Fibrin & Collagen compounds	Tisseel [®] , FloSeal [®] , CoStasis [®] .	Surgical sealant.	<ul style="list-style-type: none"> • Fast curing. • Reabsorbable. • Biocompatible. 	<ul style="list-style-type: none"> • Poor mechanical properties. • Poor adhesion. • Human or bovine origin (toxicity concerns).
Cyanoacrylate	Histoacryle [®] , Dermabond [®] .	Surgical adhesive.	<ul style="list-style-type: none"> • Fast curing. • Strong adhesion. • Waterproof. 	<ul style="list-style-type: none"> • Exothermic polymerization. • Low elasticity (brittleness). • Not bioabsorbable.
Poly(ethylene glycol) polymer	FocalSeal [®] , CoSeal [®] .	Hemostat.	<ul style="list-style-type: none"> • Good adhesion. • Reabsorbable. • Biocompatible. 	<ul style="list-style-type: none"> • Short shelf-life. • Risk of swelling. • Expensive.
Glutaraldehyde products	Cardial [®] , Blueglue [®] .	Surgical sealant.	<ul style="list-style-type: none"> • Fast curing. • Good adhesion. • Flexible seal. 	<ul style="list-style-type: none"> • Safety concerns (bacterial grows). • Long absorption time.

2.7.3 Clinical needs

Several clinical needs require a highly biocompatible strong hydrogel with robust adhesion properties. In particular, often a better integration and stability of implants are desired. The recurrent issue is the attachment of soft structure to strong material, *e.g.* soft hydrogel to strong bone or cartilage. Currently, binding connective tissues such as tendons and ligaments or affix implants that have a load-bearing function like implants for replacing the *nucleus pulposus*^[1] remains challenging. Another attractive application is to use adhesive hydrogel as a sealant, like, for example, to prevent air in the lungs or fluid in the intestine leaks out^[221].

2.7.4 Hydrogel based adhesive

Hydrogel based adhesives are attractive due to their several similarities to living tissue and their high oxygen permeability^[217,222,223]. The last encourages especially *ex-vivo* wounds healing in maintaining an efficient protective barrier from the outside world.

However, many issues remain for satisfying all requirements described in Table 2.8. In particular, conventional hydrogels are significantly weaker to bear load than natural tissue such as cartilage^[18], and only a few methods are suitable for improving adhesion mainly for toxicity reasons. For example,

many solvents (*e.g.* n-hexane) or strongly alkaline hardener are toxic for the human body and can significantly damage contacting living tissues^[78,79]. Moreover, the wet environment inside the body might negatively affect adhesion: lower mechanical properties of the bulk material and stress concentration at the interface or weaker interfacial interactions (*e.g.* van der Waals forces) due to swelling.

In contrast, nature has established different strategies to overcome these performance deficiencies. For instance, mussels, barnacles, and algae can strongly adhere to wet hulls of boat^[224]. Mussels have particularly gained attention. They secrete different proteins that form robust chemical adhesion in a wet environment^[225]. Researchers especially focus on the amino acid 3,4-dihydroxyphenyl-L-alanine (DOPA) molecule. Indeed, adhesion significantly improves when the polymers of the adhesive were modified with these molecules^[224,226–229]. As a reference to Table 2.7, adhesion is here improved by modifying the nature (density of interactions and bonding strength) of the chemical interactions at the interface.

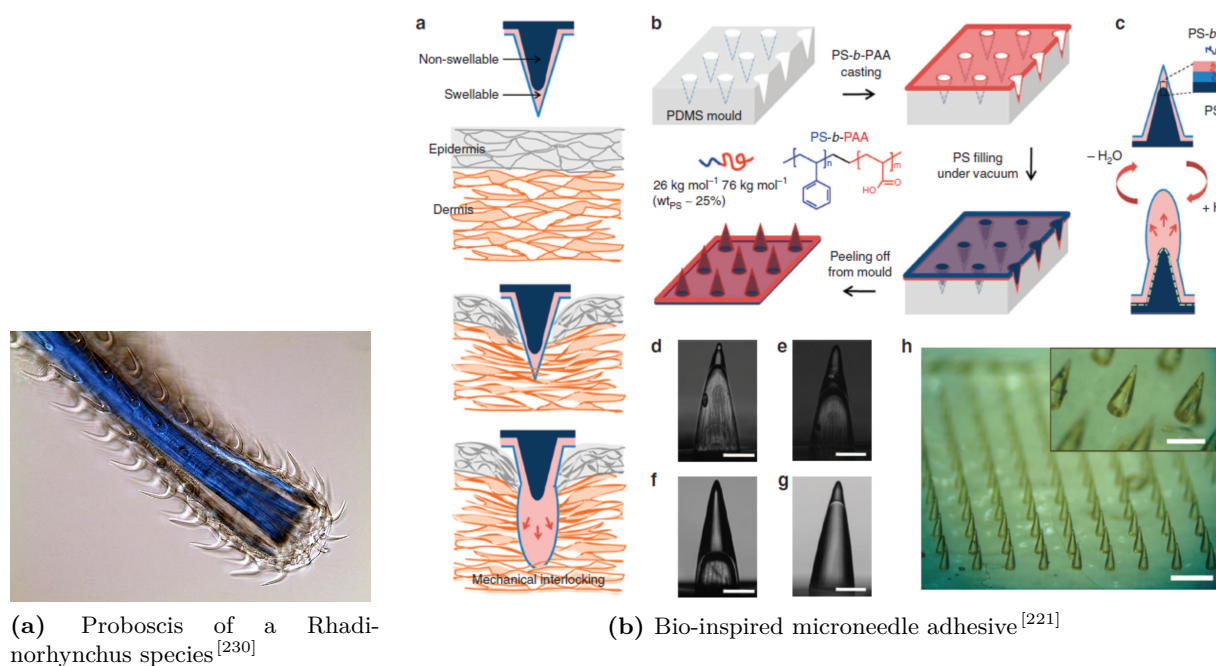


Figure 2.8: Bio-inspired microneedle adhesive (reproduced with permission from^[221]).

Another influencing parameter, namely mechanical interlocking, was explored by a group from Harvard. Inspired by the endoparasitic worms, they ingeniously use the potential of hydrogel's swelling capability in creating durable interlocking with hydrogel needles, as shown in Fig. 2.8^[221].

Some studies took the famous gecko feet as an example and evaluated the influence of the interfacial surface area. Geckos can climb nearly vertical surfaces thanks to multiple van der Waals interactions between their feet and the attaching structure. The adhesion strength strongly depends on the complex hierarchical structure of its feet: the increase of the real contacting surface area amplifies the number of interactions^[224]. Consequently, many efforts were done for imitating this structure^[231,232]. However,

the adhesion strength drastically decreases with humidity because of the supposed reduction of van der Waals interactions. To overcome this limitation, a group from Northwestern University successfully improved wet adhesion in coating a gecko-inspired surface with DOPA molecules illustrated in Fig. 2.9^[229].

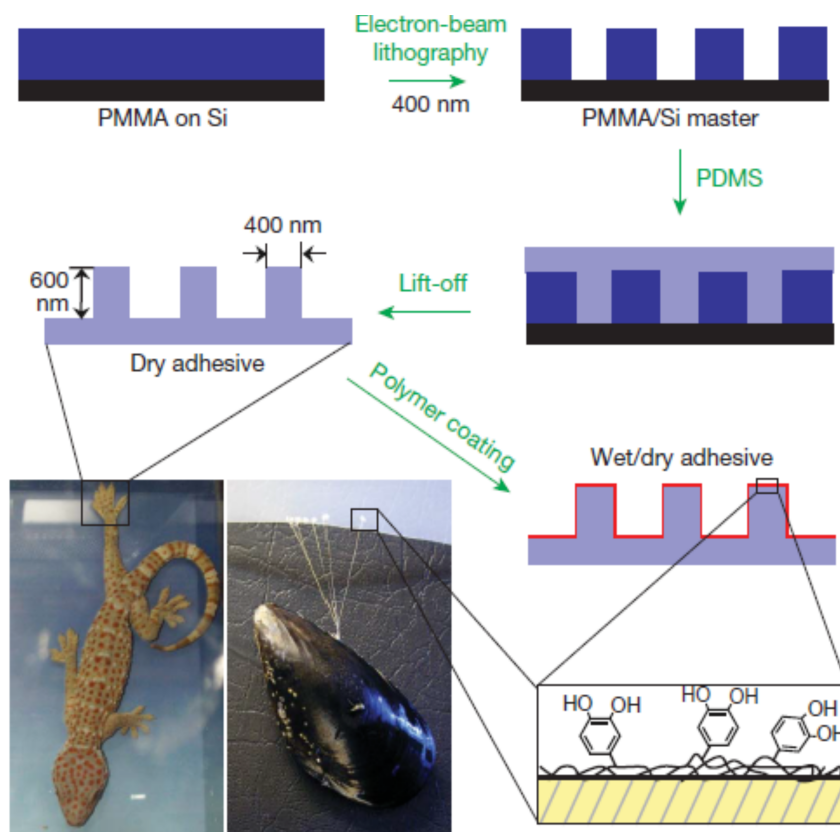


Figure 2.9: A Gecko-inspired surface coated with DOPA molecules (reproduced with permission from^[229]).

Similar results were obtained when adding nano-particles or nano-fibers to the adhesive. It permits to increase in the number of bonding sites^[118,224,233] and thus the number of potential interactions. Such an approach is employed by diverse plants like the English ivy^[224,234] or sundews^[234–236]. In particular, the function of sundews is to capture insects, as presented in Fig. 2.10. Therefore, the secreted polysaccharide adhesive reveals very interesting biological and physical properties, particularly good wettability and antibiotic properties. Also, as a natural hydrogel, its high water content represents an appropriate environment for cell cultures^[237].

A group from the University of Akron was inspired by caddisfly adhesive silk to develop a new bone adhesive^[238]. Caddisfly larvae live underwater and build an elaborate shelter protecting and hiding them from predators. To create their shelter, they secrete silk fibers with remarkable underwater adhesion and self-recovery ability to stitch debris found in their habitat together, as shown in Figure 2.11^[239]. Nevertheless, the mechanisms behind their strong adhesion and mechanical properties are still unclear^[240]. It is believed that phosphoserines and multivalent ions such as Ca^{2+} present in caddisfly adhesive silk are responsible for the extraordinary properties.



Figure 2.10: Insect captured by a sundew by the natural adhesive secreted from sundew (from Wikimedia Commons^[241]).

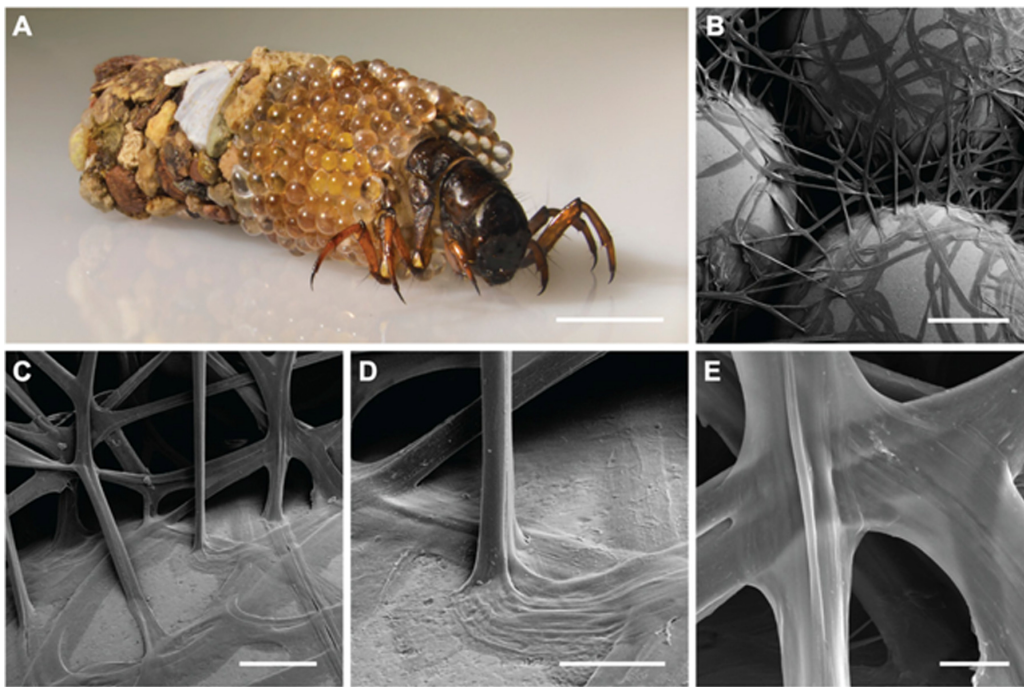


Figure 2.11: (A) Protective shelters of caddisfly larvae composed of debris stitched together with its secreted silk. (B-E) Scattering electron microscopy images showing how silk surround debris to stitch them together. Scale bars: (B) 500 μm , (C) 200 μm , (D) 50 μm , and (E) 10 μm (reproduced with permission from^[242]).

The potential of using highly dissipative hydrogel as an adhesive is not well explored in the biomedical field yet. It is generally accepted that the tougher the hydrogel is, the more energy is needed to propagate a crack and break the interface with the living tissue^[113]. Nevertheless, it is an effective way to improve adhesion without compromising methods such as adding a chemical adhesive. Indeed, depending on the reaction, chemical bonding at the interface might be exothermic and foul in the presence of blood^[221].

Likewise, physically crosslinked hydrogels are more popular for similar reasons^[74] because gelation occurs without adding potentially toxic chemical reagent^[54,73]. Most natural hydrogels are physically crosslinked and have the advantage of being highly biocompatible, cell adhesive, and biodegradable for some applications. However, compared to synthetic hydrogels, tuning their properties, such as water content, mesh size, stability, polymer length, mechanical, physical, and chemical properties, is more challenging^[74]. An overview of conventional biocompatible hydrogels can be found in Table 2.1.

2.8 Reliability

As the human body is continually subjected to cyclic loading, reliable fatigue resistance is crucial for load-bearing implants. In particular, they have to sustain millions of loading cycles. Therefore, to evaluate implants' long-term reliability, the evolution of properties must be thoroughly analyzed in time and during cyclic solicitations.

2.8.1 Fatigue resistance

The fatigue resistance of hydrogels is strongly related to the stability of bulk, interphase, and interface properties. The main characteristics are (i) the evolution of the mechanical properties, such as the stiffness or toughness during cyclic loading, (ii) how energy is dissipated, and (iii) the ability of the hydrogel to recover the initial properties.

The fatigue behavior of hydrogels can be categorized according to their microstructure. As described in Table 2.10, the major difference is observed between conventional hydrogels incorporating a single network only and the other more complex structures. The general trend can be resumed as follows:

- Single network structures exhibit constant behavior with excellent recoverability and small hysteresis of the loading-unloading cycle. Thus, they dissipate only a small amount of energy.
- Complex structures, such as double network hydrogels or hydrogel composites, are highly affected by cyclic loading. The stiffness reduces already after the first cycle outlining a large hysteresis of the loading-unloading curve. Nevertheless, a constant behavior is reached in the following cycles with significantly smaller hysteresis.

While the recoverability seems to depend mainly on the type of bonds, *e.g.* chemical, ionic or physical, the damage induced by softening mechanism is not well understood yet. Low softening might be issued from the expulsion of water during loading^[243], while larger softening is associated with damages of the polymeric network^[30,114,244]. When a load is applied, the bonds in the hydrogel are strained and break when they reach their full extension^[27]. The breaking of these bonds is related to the release of energy. Combined with other dissipative mechanisms like internal friction between the polymeric chains, the breaking of bonds results in large hysteresis in the stress-strain curve^[28,245]. In some cases, the softening behavior is described to be similar to the *Mullins effect*^[26–30] observed in unfilled and

especially in filled rubber-like material^[246].

Diani *et al.* published in 2009 an overview of the *Mullins effect*^[246] where the particularities are described and listed hereafter:

- At constant axial strain, most of the softening appears after the first loading cycles. A constant behavior is reached after about ten cycles.
- The softening appears for strain lower or equal to the maximum strain ever applied.
- The stress-strain curve has a specific appearance, as shown in Figure 2.12. When the extension exceeds the maximum extension previously applied, the material response returns on the same path as the monotonic stress-strain curve.
- Hysteresis increases with the increasing maximum strain.
- Partial to complete recovery is observed after softening over time and/or by heating^[27,246].

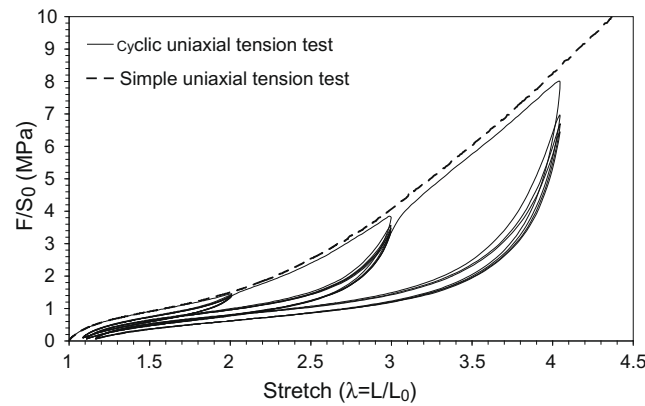


Figure 2.12: Representative with permission *Mullins effect* in carbon-black filled in styrene-butadiene rubber (SBR) (reproduced from^[246]).

While the *Mullins effect* is well-known in rubbers, the associated physical interpretation is still not well established. Several theories were proposed during the last seven decades. One of them is based on the breaking of bonds. The shorter weak bonds at the rubber-particle interface are more subjected to extend when a load is applied and break before the other stronger or longer bonds^[247,248]. Kraus *et al.*^[249] showed that the breaking of bonds at the interface could not be the main origin for the softening. He suggested that the breaking of bonds happens inside the fillers. The *Mullins effect* was also related to molecules that slip over the fillers' surface and instantly create new bonds along the chains^[250]. Finally, another more recent theory is that the disentanglement of the polymer chain causes this particular softening behavior. The chain density is still conserved, but the entanglement density is reduced, inducing anisotropy and directional softening to the system^[251].

The softening, similar to the *Mullins effect* observed in hydrogels, is essentially associated with breaking bonds^[26]. However, only a few studies have characterized softening behavior in hydrogels. The

softening behavior often does not address all particularities of the *Mullins effect*, especially recoverability, though the latter is important for long-term reliability. Therefore, the breaking of bonds is, in general, distinguished between two classes:

- Recoverable bonds: physical or ionic bonds^[28,105].
- Unrecoverable bonds: permanent chemical bonds often described as sacrificial bonds^[26,27,112].

More recent approaches replace permanent bonds with weaker but recoverable bonds to enhance fatigue resistance^[16,29,109,111]. The recoverability is evaluated by the degree of recovery, the time span as well as the environmental conditions needed to recover^[16,29,76,105,111,116].

2.8.2 Degradation

Ideally, the damaged tissue regenerates and progressively replaces the hydrogel implant. Nevertheless, hydrogels' degradation should not release toxic compounds or occur prematurely to avoid the destruction or loss of the implant. In particular, degradation is not only present *in vivo*, but it can also appear during the synthesis, the shelf-life, or the sterilization process^[83,252,253].

Degradation influences almost all properties of the hydrogels, especially mechanical properties. Nevertheless, also permeability can change, which influences the transport of nutriment or the migrations of cells^[254]. Thus many methods were proposed to evaluate degradation. Some examples are listed hereafter :

- Lost of dry weight^[255] [91].
- Evolution of the swelling ratio^[254,256].
- Evolution of mechanical properties^[256].
- Release of specific compounds^[257].
- High-pressure liquid chromatography (HPLC) evolution profile^[258].
- Ultrasound scan for *in vivo* assessment^[155].

Table 2.10: Fatigue behavior according to different hydrogel structures.

Hydrogel structure	Main characteristics	Reinforcement mechanisms	Cross-linking	Interactions	Fatigue behavior	Recovery
Conventional	Long polymer chains chemically cross-linked to another polymer.	None but dipole-dipole interaction ^[259] or a homogeneous distribution of the cross-linking ^[260] can enhance the mechanical properties.	Mainly chemical.	No ^[243] or physical ^[261] [262] interactions between the polymer chain.	Constant behavior: no ^[112,262] or low softening ^[243,261] with (almost) no hysteresis.	Instantaneous recovery.
Anisotropic	Rigid domains oriented in a soft and ductile hydrogel matrix.	Rigid domains sustain large stresses, while the softer domains give the flexibility to the hydrogel.	Chemical and/or physical.	Physical interactions between the domains which act as the reversible sacrificial bonds.	Can depend on the loading direction ^[26] : <ul style="list-style-type: none"> • Softening similar to <i>Mullins effect</i> (\parallel to the domains). • No softening with large hysteresis (\perp to the domains). 	Recover (overtime 100% after 15 min ^[29]).
Polyampholytes	Mostly homogenous network structure of random copolymerization chain of oppositely charged ionic monomers forming pairwise ionic crosslinks.	Strong permanent bonds maintain the shape of the gel and form a primary network, while the weak bonds act as sacrificial and recoverable bonds ^[105,106] .	Ionic (strong bonds and weak bonds).	n/a	Softening and large hysteresis at the first cycle then constant behavior with almost no hysteresis ^[105] .	Recovery (overtime 100% after 120 min ^[105]).
Macromolecular	Homogeneous macromolecular structure with physical and/or ionic crosslinking.	Homogenous structures distribute homogeneously stress. Ionic and/or physical bonds act as a sacrificial and recoverable bond.	Ionic and/or physical.	n/a	Softening and large hysteresis after the first cycle then constant behavior with smaller hysteresis.	Recovery (by heating 70°C ^[107] or overtime 4h ^[16]).
Interpenetrating polymer network (IPN)	Two or more entangled polymer networks.	The interpenetration of one network stretches polymer chains in the other network and reduces its chain density ^[108] and increase the internal friction at the entanglement sites.	Chemical ^[108] and/or physical and/or ionic ^[109] .	Chemical and/or physical ^[110] interactions between the polymeric network.	Softening and large hysteresis after the first cycle then constant behavior with smaller hysteresis, softening similar to <i>Mullins effect</i> ^[28] .	Partial recovery (by heating 80 °C ^[108] or overtime 53% after 80 min ^[109]).
Double network (DN)	Two (independently) cross-linked interpenetrating polymer networks with strongly asymmetric structure: <ul style="list-style-type: none"> • First network (N1) is rigid, stiff, brittle, and tightly crosslinked. • Second network (N2) is soft, ductile, and loosely cross-linked. Molar chain length ratio: N2/N1 = 20-30x ^[18] .	The first network serves as sacrificial bonds that fracture at relatively low stress and increase the elastic modulus, while the second serves as hidden length that sustains stress by large extension afterward and increase the strain ^[18,111] .	Mainly chemical.	No or physical interactions between the polymer chains.	Softening and very large hysteresis after the first cycle then constant behavior with smaller hysteresis ^[30,112] , softening similar to <i>Mullins effect</i> ^[27] .	No recovery after large deformation ^[27,105] .
Composite	Reinforced polymeric network with <i>e.g.</i> particles or fibers.	The reinforcement elements sustain most of the stress in the hydrogel system.	The network is chemically crosslinked, while the reinforcement elements are not physically or chemically crosslinked ^[115] .	Physical or ionic interaction between the reinforcement elements and the polymeric network ^[28] .	Softening and large hysteresis after the first cycle then constant behavior with smaller hysteresis ^[114] , softening similar to <i>Mullins effect</i> ^[28,112,115] .	Recovery (overtime 86.8% after 24h ^[116]).

2.9 Characterization methods

Accurate measurement of hydrogel properties might be challenging regarding the high water content, soft consistency, and often the viscoelastic behavior. For example, as presented in Fig. 2.13, only a few standards exist to measure adhesion. These methods are not optimal for adhesive hydrogels because they are exclusively conducted on glass or pork skin^[80]. Consequently, many researchers have developed their own methods, which make it difficult to compare the results. In particular, the testing mode, the loading rate, the swelling state, and the samples' size vary a lot.

Another typical example is how elastic modulus is measured. First, it can be measured in compression, tensile, or shear. Then, since many hydrogels are viscoelastic and strain-stiffening, the elastic modulus depends on the loading rate and the range of strain where it is measured. Finally, the cross-section of the sample significantly changes during tensile or compression loading. Therefore, different manners are employed for evaluating the true stress and strains, which again will induce variation.

Table 2.11 summarized different tests used to analyze the properties required for load-bearing implants, shown in Table 2.8.


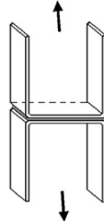


Normative designation	Glue amount (μL)	Load applied (N)	Type of solicitation
F2255-05: Standard test method for strength properties of tissue adhesives in lap-shear by tension loading	60	2	
F2258-05: Standard test method for strength properties of tissue adhesives in tension	60	2	
F 2256-05: Standard test method for strength properties of tissue adhesives in T-peel by tension loading	750	5	
F2458-05: Standard test method for wound closure strength of tissue adhesives and sealants	60	-	

Figure 2.13: Example of adhesion test according to standard ASTM adhesion tests performed on Glubran2 and Tissucol surgical glues (reproduced with permission from^[263]).

Table 2.11: Example of tests for evaluating load-bearing hydrogel implants.

Property	Specifications	Used tests
Biological properties	Biocompatibility	Live/dead test ^[264,265] , <i>in vivo</i> testing ^[255,266] , cytotoxicity ^[256,267,268] , cell encapsulation study ^[269] , according to ISO 10993-1.
	Antibacterial	Antibacterial assessment (bacteria viability) ^[270] .
Mechanical and physical properties	Tension	Tensile test ^[271] .
	Compression	Compression test ^[202,221,264,272,273] .
	Fracture	Tearing ^[274,275] , tension ^[29,214,276–282] , wire cutting test ^[283–285] , crack tip observation ^[275,278,279,281] , strain field analysis ^[282] .
	Swelling ratio	Variation in weight or volume analysis ^[202,221,255,256,266,267,273,286] .
Interface properties	Tension	Direct tension loading ^[221,256,266,270,273,287] , according to ASTM F2258 ^[263,288] , atomic force microscopy ^[233,236,237] .
	Shear	Lap-shear test in tension loading ^[118,233,264,267,272] according to ASTM F2255 ^[202,228,255,268,270,289–291] .
	T-peel	T-peel in tension loading ^[292] according to ASTM F2256 ^[263] .
	Peel-off	Peel-off in tension loading ^[271] .
	Interface quality	Histology ^[269,291] , scanning electronic microscopy (SEM) ^[269] .
	Surface energy	Contact angle ^[237] .
Processability	Viscosity	(Dynamic) oscillatory rheology ^[202,233,256,266–270,286,287,289,291] .
	Polymerization time	Inverted tube test ^[267] , vial tilting method ^[268] , stir bar method ^[269] , (dynamic) oscillatory rheology ^[270] .
	Sterilization	Mechanical properties, morphology and cytotoxicity investigation ^[293] .
Long-term reliability	Fatigue resistance	Uniaxial tension loading ^[279,286] , uniaxial unconfined compression loading ^[26–28,30,105,112,114,115,243,261,262,286] , recoverability ^[16,29,76,105,111,116,286] and (Dynamic) oscillatory rheology ^[256] .
	Resorption	Material weight loss according to time ^[228,256,270] , cytotoxicity investigation ^[73] .

2.10 Conclusions

Improving the mechanical properties of hydrogels is widely studied. However, synthesized hydrogels can currently not compete with some load-bearing tissues, such as meniscus or articular cartilage, mainly because it is extremely complicated to reproduce their highly hierarchical microstructures. However, despite their role in physiological functions, hierarchical microstructures or gradients are usually ignored in tissue engineering mainly for practical reasons. Creating gradients, especially multiple gradients, remains challenging and often requires special equipment, a complex synthesis process, and excellent control over mechanical and physical properties. Nevertheless, most of these properties, such as stiffness, swelling, or viscosity, are interrelated. Improving one property usually comes at another's cost, as observed in many hydrogel structures, including neat, double network, or composite hydrogels. Therefore, more effort is required to decouple the interdependence between these properties and extend the range of material properties for hydrogels without affecting biocompatibility. Indeed, heavy chemical modifications should be avoided during the processing of bio-hydrogels because it involves a full and time-consuming assessment.

Moreover, the field of applications of load-bearing hydrogels is often limited by (i) the lack of adhesion to biological tissue and (ii) the drastic decrease in stiffness and toughness after the first loading cycle, which shows similar characteristic to the *Mullins effect*. Subsequently, the mechanisms behind the adhesion to biological tissues and the energy dissipation have to be better understood to overcome the current limitations.

Finally, swelling properties are often placed in the background despite their importance. Indeed, swelling might not only induce major dimensional changes but also significantly alter mechanical properties. Thus, more research on controlling swelling while minimally affecting other properties, such as stiffness or deformation performance, would be needed for novel applications.

Chapter 3

Materials and methods

3.1 Hydrogel structures and materials

This thesis evaluates seven different hydrogels structures illustrated in Fig. 3.1. Each structure was assigned to a specific color for facilitating the reading of the results. Table 3.1 describes the raw materials, while Fig. 3.4 - 3.9 show the synthesis of each structure. Additionally, Table 10.3 in the *Chapter 10, Annexes* presents the equipment used for the synthesis.

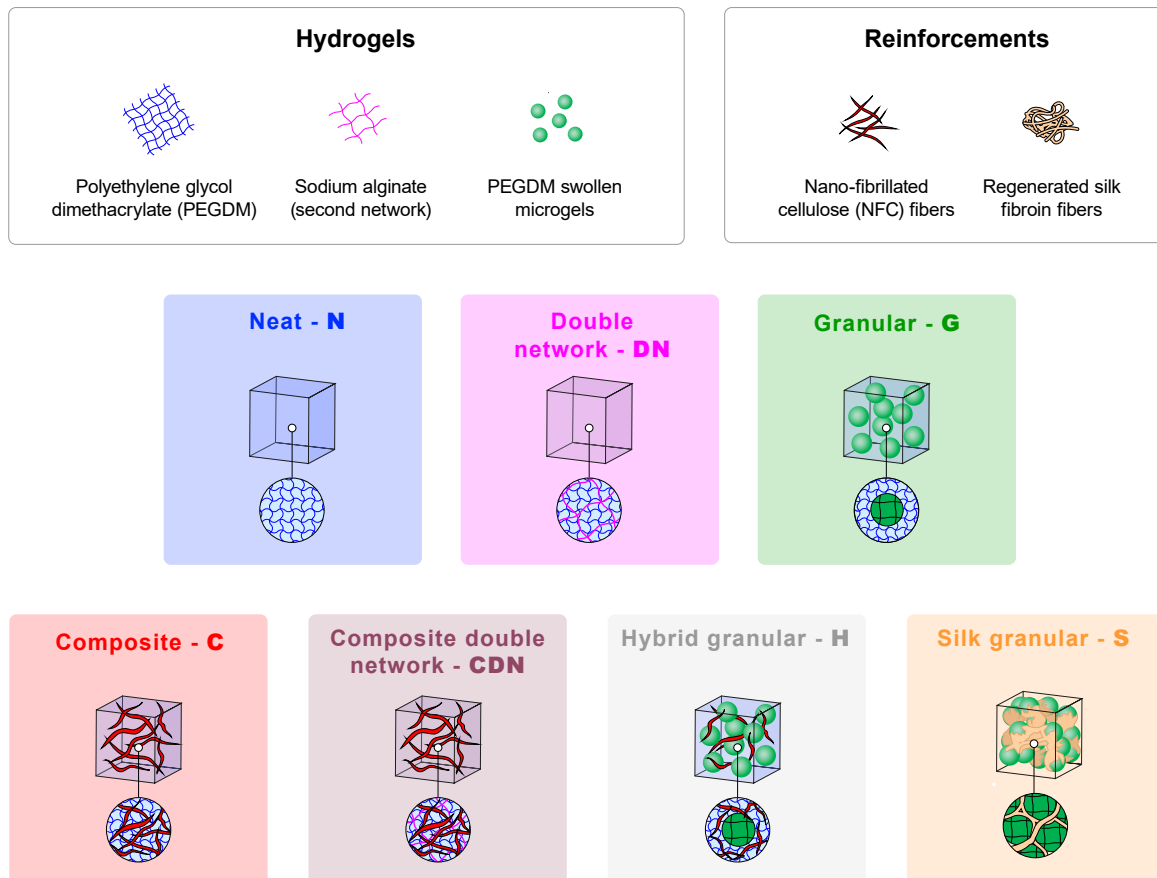


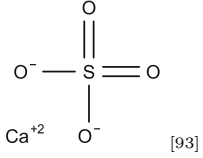
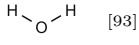
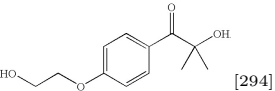
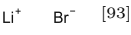
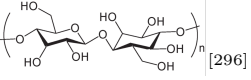
Figure 3.1: Hydrogel structures developed and evaluated in this Thesis. Each structure was assigned to a specific color for facilitating the reading of the results.

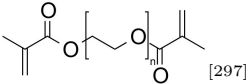
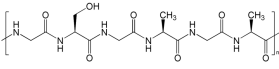
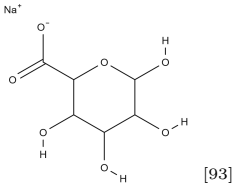
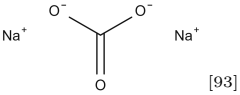
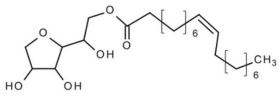
3.2 Synthesis and processing

3.2.1 Raw materials

All components used for the synthesis of different hydrogels are listed in Table 3.1.

Table 3.1: Raw materials for hydrogel synthesis.

Name (abbreviation)	Chemical structure	Function	Provider	Comments
Calcium Sulfate (CaS)	 [93]	Crosslinker for Sodium alginate.	Merck (CAS 7778-18-9)	Biocompatible, pH sensitive.
Demineralized water (DI)	 [93]	Aqueous phase of hydrogels.	Ministil P-6 (BWT, CH)	n/a
Irgacure 2959	 [294]	Photo-initiator for covalent crosslinking of PEGDM.	BASF (Basel, CH)	Water-soluble, FDA approved.
Lithium bromide	 [93]	Dissolve silk.	Merck (CAS 7550-35-8)	Commonly used to dissolve silk.
Mineral oil	Incorporate several molecules [295]	Oil used for oil-water emulsion.	Merck (CAS 8042-47-5)	Non-toxic, insoluble in water.
Nano-Fibrillated Cellulose (NFC) based on bleached softwood pulp	 [296]	Fiber reinforcement.	WMFC-Q-Advanced (Weidmann, CH)	Biocompatible, large surface-to-volume ratio, high stiffness and strength.
Phosphate Buffered Saline (PBS)	n/a	Storage solution.	Gibco (Basel, CH)	Physiological solution with a similar salt concentration of the human body.

Poly(Ethylene Glycol) Dimethylacrylate (PEGDM), $m_w=20$ kDa	 [297]	Neat hydrogel or, hydrogel matrix.	Polysciences (ref. 25406-25, Germany)	Biocompatible, widely used in biomedical application, fast and controlled photo-curing.
Silk fibroin	 [298]	Hydrogel reinforcement.	Swiss silk (Hinterkappelen, CH) base material: Bombyx mori)	Biocompatible, self-assembling, physical crosslinking Bombyx mori silk fibers were provided by Swiss silk.
Sodium alginate, medium viscosity	 [93]	Hydrogel matrix (sacrificial network).	Merck (CAS 9005-38-3)	Biocompatible, widely used in biomedical application, ionic crosslinking.
Sodium carbonate	 [93]	For degumming of silk fibers.	Merck (CAS 497-19-8)	Commonly used to remove sericin from silk fibers.
SPAN 80	 [299]	Non-ionic surfactant to stabilize oil-water emulsion.	Merck (CAS 1338-43-8)	Non-toxic, insoluble in water and soluble in organic solvent ^[300] .

Note that the PEGDM used in *Chapter 4. Single and double network hydrogels and their composites*. was synthesized in the laboratory of macromolecular and organic materials (LMOM) of Professor Holger Frauenrath, and NFC fibers were provided by EMPA (Dübendorf, Switzerland), where the base material was Zellstoff Stendal (Arneburg DE). For all other chapters, PEGDM was purchased by Polysciences (ref. 25406-25, Germany) and NFC fibers by Weidmann.

3.2.2 Sub-component synthesis

The synthesis of microgels and silk fibroin are shown in Fig. 3.2 and Fig. 3.3.

Microgels synthesis - MR

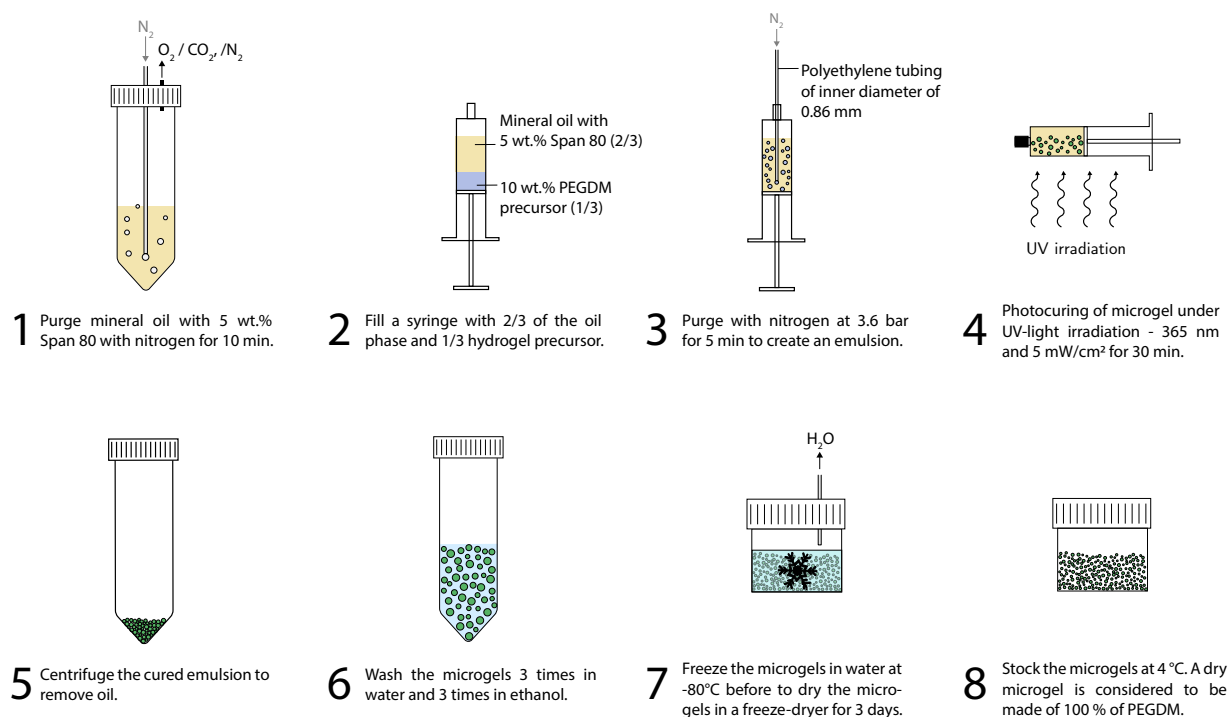


Figure 3.2: Synthesis steps of microgels - MR based on PEGDM hydrogels.

Silk fibroin solution preparation

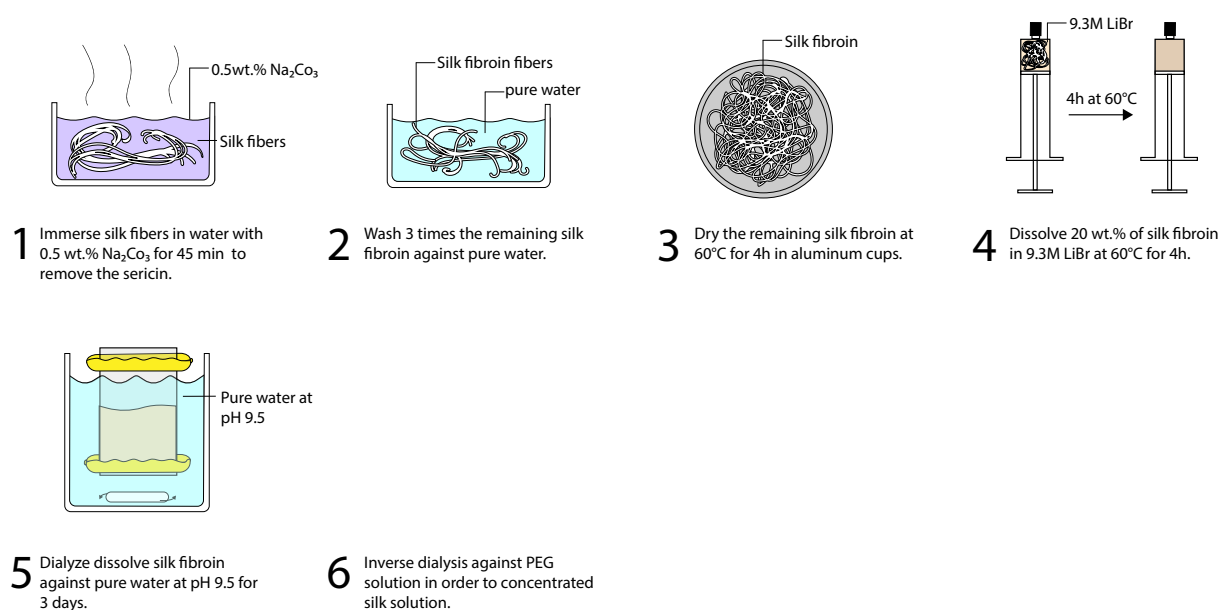


Figure 3.3: Synthesis steps of silk fibroin solution based on lithium bromide (LiBr).

3.2.3 Hydrogel synthesis

The synthesis of each structure is shown in Fig. 3.4 - 3.9.

Neat hydrogels synthesis - N

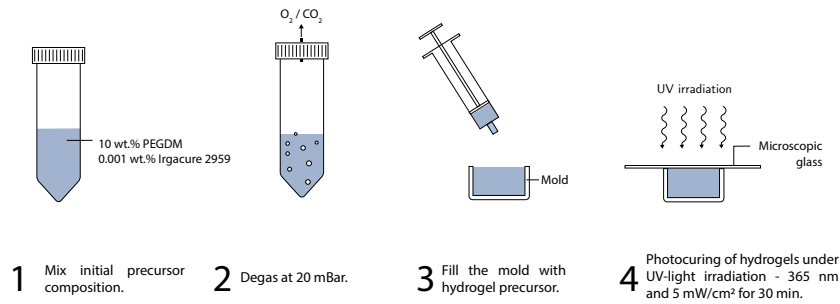


Figure 3.4: Synthesis steps of neat hydrogels - N.

Hydrogel composite synthesis - C

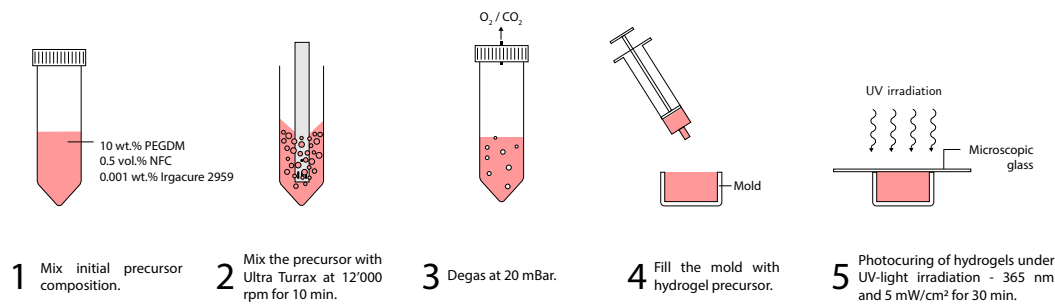


Figure 3.5: Synthesis steps of hydrogels composite - C.

Double network hydrogel synthesis - DN

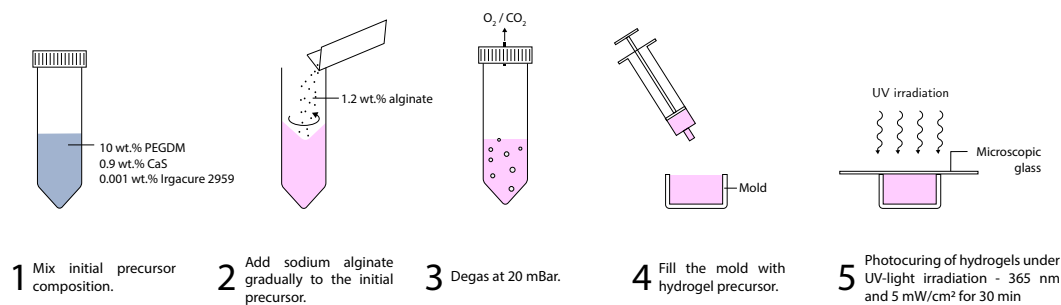


Figure 3.6: Synthesis steps of double network hydrogels - DN.

Composite double network hydrogel synthesis - CDN

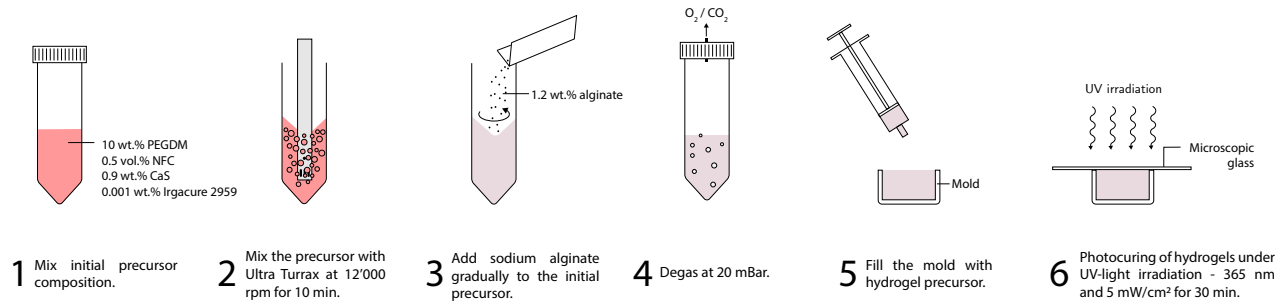


Figure 3.7: Synthesis steps of composite double network hydrogels - CDN.

Hybrid granular / granular hydrogel synthesis - H/G

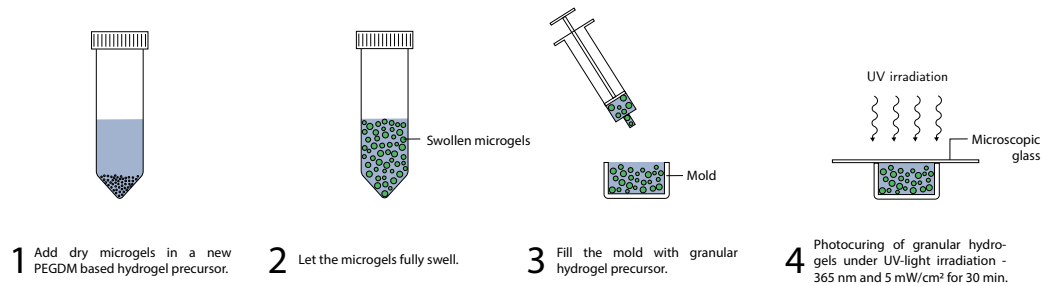


Figure 3.8: Synthesis steps of granular hydrogel - G based on PEGDM. These steps are applicable for hybrid granular hydrogel - H, where dry microgels are added to the precursor of hydrogel composites instead of neat hydrogels at step 1.

Self-assembled silk granular hydrogel synthesis - S

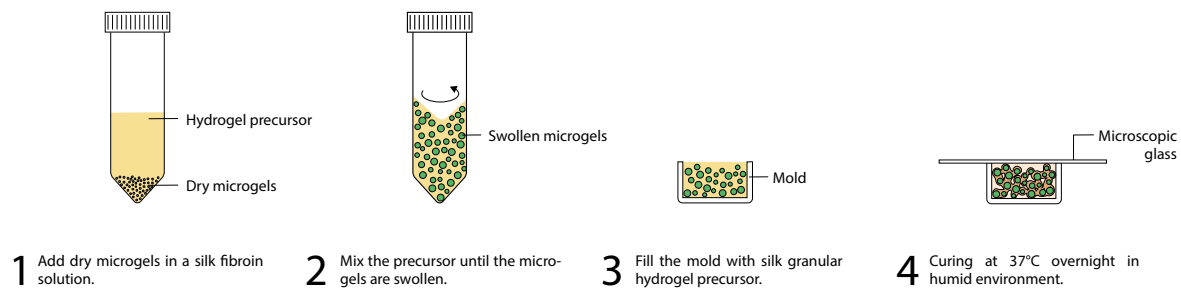


Figure 3.9: Synthesis steps of self-assembled silk granular hydrogel - S.

3.2.4 Casting

Casting molds for compression loading

The casting molds for the compression test were Eppendorf cap and measured either $\text{Ø}8\text{mm} \times 4.5\text{mm}$ or $\text{Ø}5.6\text{mm} \times 3\text{mm}$. They were filled with hydrogel precursors and covered with a microscope slide to avoid contact with oxygen. Fig. 3.10 shows representative samples.

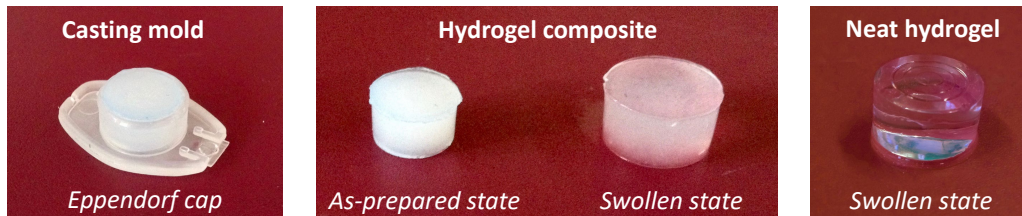
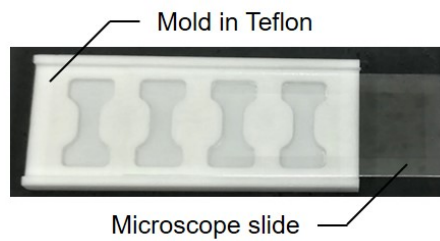
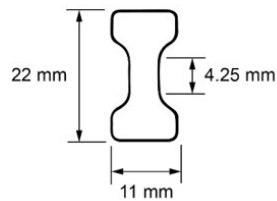


Figure 3.10: Representative composite hydrogels samples at as-prepared ($\text{Ø}8\text{mm} \cdot 4.5\text{mm}$) and swollen state and neat hydrogel at swollen state for compression test.

Casting molds for tensile and single notch edge tests

The molds for tensile and single notch edge tests were made in Teflon. Fig. 3.11 shows representative molds.

Dog bone sample for tensile test



Rectangular sample for single edge notch test

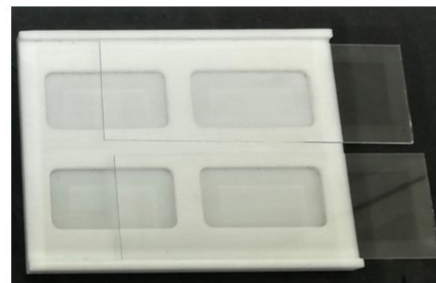
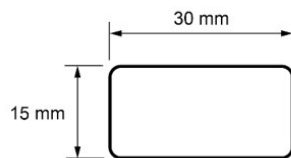


Figure 3.11: Casting molds of tensile and single notch edge tests.

Tissue - sample preparation

For preparing the sample for adhesion test, different bovine cartilages were prepared in a cylindrical shape Ø6,6 mm x 10 mm. The cartilage pieces were prepared from the superficial, middle, and deep zones of bovine articular cartilage obtained from the femoro-patellar groove.

The hydrogel, which is attached to the cartilage, was a larger cylinder with the dimension Ø15 mm x 4,5 mm.

Note that the tissue samples were first fixed into the mold before adding the hydrogel precursors on top of it. After polymerization, the hydrogel attached to the tissue was rapidly gripped for the adhesion test.

3.3 Sampling plan

If not specified otherwise, each test was performed with a minimum of three samples. The hydrogels are distinguished between different states:

- **As-prepared state:** untested sample in the *after synthesis state*.
- **Dry state:** dried untested sample.
- **Swollen state:** untested sample immersed in PBS or water for at least 24 hours for reaching the equilibrium water content.

3.4 Material characterization methods

The different properties of obtained hydrogels were quantified, and their microstructures were analyzed with the methods and equipment presented in Table 2.11 and 3.2.

Table 3.2: Test equipment used for the characterization of hydrogels.

Description	Function	Comments
Instron E3000 (Norwood) equipped with 250N load cell	Linear mechanical testing machine.	Adhesion test.
5kN Zwick (Zwick Roell) equipped with 10N and 100N load cell	Linear mechanical testing machine.	Unconfined compression, tensile and fracture testing.
VideoXtens (Zwick/Roell)	Integrated camera in the Zwick and virtual extensometer.	Record images at 25 fps for digital image correlation at the macroscopic scale.
Rheometer (TA Instruments AR2000ex) with parallel plates	Measure complex viscosity.	An oscillating strain sweep from 0.1 % to 1000% at 0.5 Hz.
Digital Image Correlation setup (Correlated solutions)	Measure the displacement field on the surface of samples.	Set-up includes: two cameras Grasshopper USB3 (monochrom, 5.0 Mpix, 75 fps), 70 mm lens Vicsnap V.9, VIC3D V.8.
Linkam TST350	Miniature tensile stage.	Tensile testing under an optical microscope (Olympus BX60) for digital image correlation at the microscopic scale.
Olympus BX60	Optical microscope.	Record imaged with a resolution of 0.67 $\mu\text{m}/\text{pixel}$ for digital image correlation at the microscopic scale.
Zeiss LSM 700 Invert	Fluorescence invert confocal microscope.	Imaging with the laser of 405 nm and the 20x lens.
Zeiss LSM 710	Invert confocal fluorescence microscope.	Imaging with the laser of 488 nm and the 20x lens in reflection mode.
Nikon Eclipse Ti2	Invert fluorescence microscope.	Observe cells and microgels.
3D laser scanning microscope (VK-X200 Keyence) with a 20x lens	Profilometer.	Observe the surface of hydrogels.
Keyence VHX-5000 with a 10x lens	Digital microscope.	Imaging hydrogels.
Fourier-transform infrared spectroscopy (FTIR) FT/IR-6300typeA	Measure crystallinity.	IR analysis covered the range between 800-3500 cm^{-1} with a resolution of 2 cm^{-1} .
Mettler Toledo (readability: 0.1 mg - 1 mg)	Digital scale.	Weight analysis.
Archimed setup (Figure 3.13)	Hydrogel's volume measurement.	Determination of the swelling ratio.

3.4.1 Imaging the morphology of fibers

The morphology of the NFC fibers in their native environment was observed via invert fluorescent confocal microscopy with the 20x lens. In order to distinguish NFC fibers from the matrix, hydrogel composites were dyed with calcofluor white stain (Sigma-Aldrich, Buchs, CH) that attaches to the cellulose only as shown in Fig. 3.12. The samples were then observed with a laser of 405 nm.

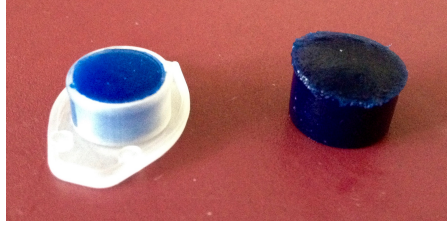


Figure 3.12: Representative hydrogel composite dyed with Calcofluor White stain for fluorescence confocal microscopy.

Similarly, the morphology and distribution of regenerated silk fibroin were observed in swollen hydrogels with an invert fluorescent confocal microscope (Zeiss LSM 700) equipped with a 20x lens and a laser of 555 nm. In order to enhance the fluorescence of silk fibroin fibers, the self-reinforced granular hydrogels were placed for at least 3 hours in 0.02 g/l Rhodamine B stain (Merck, CAS 81-88-9) before being placed in pure water for at least 2 hours.

3.4.2 Swelling ratio

The swelling ratio was assessed either by weight or by volume.

Weight

The swelling ratio of hydrogels based on weight only was determined with the following equation (3.1):

$$SR = \frac{(m_t - m_0)}{m_0} \quad (3.1)$$

where m_0 is the initial weight of hydrogel just after synthesis and m_t is the weight of hydrogel immersed in PBS or demineralized water for time t .

The main advantage of measuring swelling by weight is its simplicity. However, it lacks accuracy for assessing the variation in the volume of different hydrogels with various compositions because the apparent density differs from sample to sample.

Volume

The volume was obtained by using the *Archimedes'* principle with the setup shown in Fig. 3.13. The Archimedes principle allows to (i) assess with accuracy the variation in the volume of different hydrogels with various compositions, (ii) measure the real and apparent density, indicating, therefore, the presence of open porosity.

The measurements were divided into two steps. First, the hydrogel was patted dry with tissue and weighed at position 1 (see Figure 3.13). As the support is directly related to the scale platform, the recorded weight at position 1 corresponds to the sample's real weight. In the second step, the hydrogel was immersed in ultra-pure hexane placed at position 2. At this position, the recorded weight represents the weight of the hydrogel immersed in hexane. The difference of weight (Δm) between position 1 and position 2 corresponds to the weight of the displaced volume of the ultra-pure hexane, which is equivalent to the one of the hydrogel sample. Knowing the volumetric mass of hexane, *e.g.* $\rho_{hexane} = 0,659$ g/mL, the volume (V) of the hydrogel can be calculated with the following equation (3.3):

$$V = \Delta m \cdot \rho_{hexane} \quad (3.2)$$

The swelling ratio based on volume was then determined with the following equation (3.1):

$$SR = \frac{(V_t - V_0)}{V_0} \quad (3.3)$$

where V_0 is the initial volume of hydrogel just after synthesis and V_t is the volume of hydrogel immersed in PBS or demineralized water for time t .

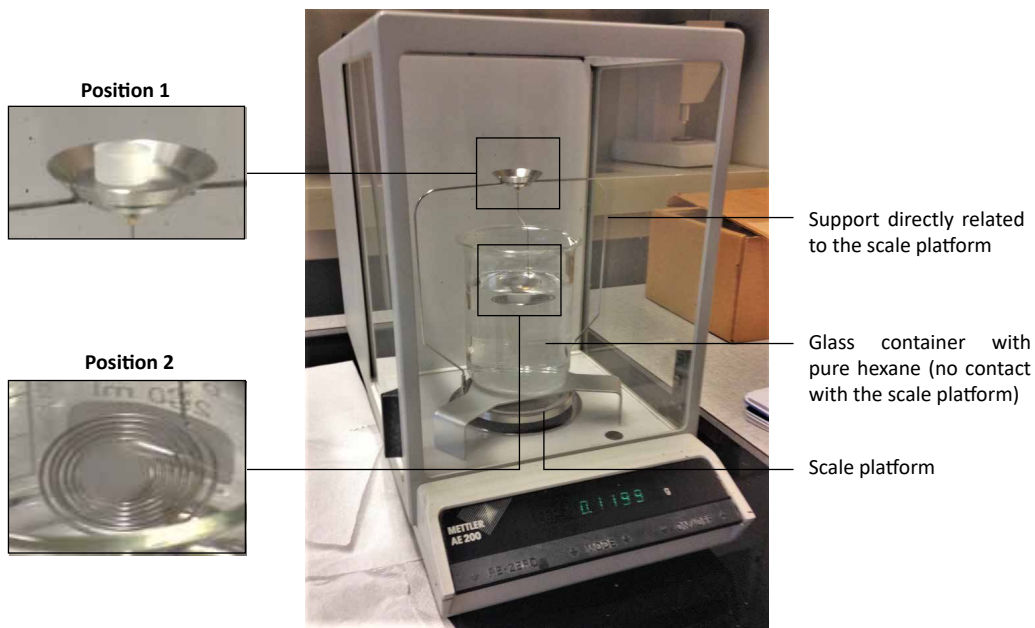


Figure 3.13: *Archimedes'* setup for the determination of the swelling ratio.

3.4.3 Rheology

The precursors' viscosity was evaluated at room temperature with a parallel plate rheometer (TA Instruments AR2000ex). An oscillating strain sweep at 0.5 Hz was then applied to the precursors, where the strain starts from 0.1% to 1000%.

In order to evaluate the curing time of neat and hydrogel composites under UV-light irradiation at a wavelength of 365 nm and an intensity of 5 mW.cm⁻², photorheology with a parallel plate rheometer under 6% of oscillating strain at 10 Hz were performed on their precursors.

3.4.4 Compression test

The default testing parameters for compression, tensile, single notch edge, and adhesion test are summarized in Table 3.3.

Table 3.3: Mechanical test parameters.

Description	Adhesion	Monotonic compression and tensile loading	Cyclic compression and tensile loading	Fracture
Load cell	250 N	100 N	100 N	100 N
Applied strain	Until rupture	Until rupture (or 90% in compression)	Incremental	Until rupture
Loading rate	0.1 mm/s	1 mm/s	0.5-1 mm/s	0.1-0.5 mm/s
Pre-load	0.05 N	0.02 N	0.02 N	0.02 N
Cycles number	1	1	3/5 per increment	1
Outputs	Engineering stress	<ul style="list-style-type: none"> Area recorded at pre-load Engineering stress and strain 	<ul style="list-style-type: none"> Area recorded at pre-load Engineering stress and strain 	Engineering stress

Compression tests were performed with the test machine Zwicky shown in Fig. 3.14 on swollen and unswollen samples. The compression and tensile setup were specially developed to test hydrogels. The compression samples were placed on a transparent glass plate. A mirror is put at 45° below the plate in order to reflect the bottom of the sample to the camera and measure the instantaneous area. The tensile sample was placed between two grips. Only the screw holes of the fixed part have internal (female) threads. Since the screws can freely move in the moveable part, the springs (0.4 mm of wire diameter) hold the hydrogel samples at constant pressure.

As a soft and flexible material, the real area was considered in the calculations. The true stress (σ_t) was derived from the engineering stress (σ_e) as described in the following equation (3.5). It is assumed that the volume was constant between each cycle as explained in equations (3.4).

$$A \cdot h = A_0 \cdot h_0 \quad (3.4)$$

where A and A_0 are the area and the initial area of the sample respectively, h and h_0 are the height and the initial height of the sample respectively.

$$\sigma_t = \frac{F}{A} = \frac{F}{A_0} \cdot \frac{h}{h_0} = \sigma_e(1 + \epsilon_e) \quad (3.5)$$

where F is the recorded load, $\sigma_e = \frac{F}{A_0}$ is the true stress, and $\epsilon_e = \frac{h-h_0}{h_0}$ is the true strain.

As shown in Fig. 3.15, the elastic modulus was determined between 10% and 15% applied strain, and the dissipated energy was defined as the area below the stress-strain curve (hysteresis).

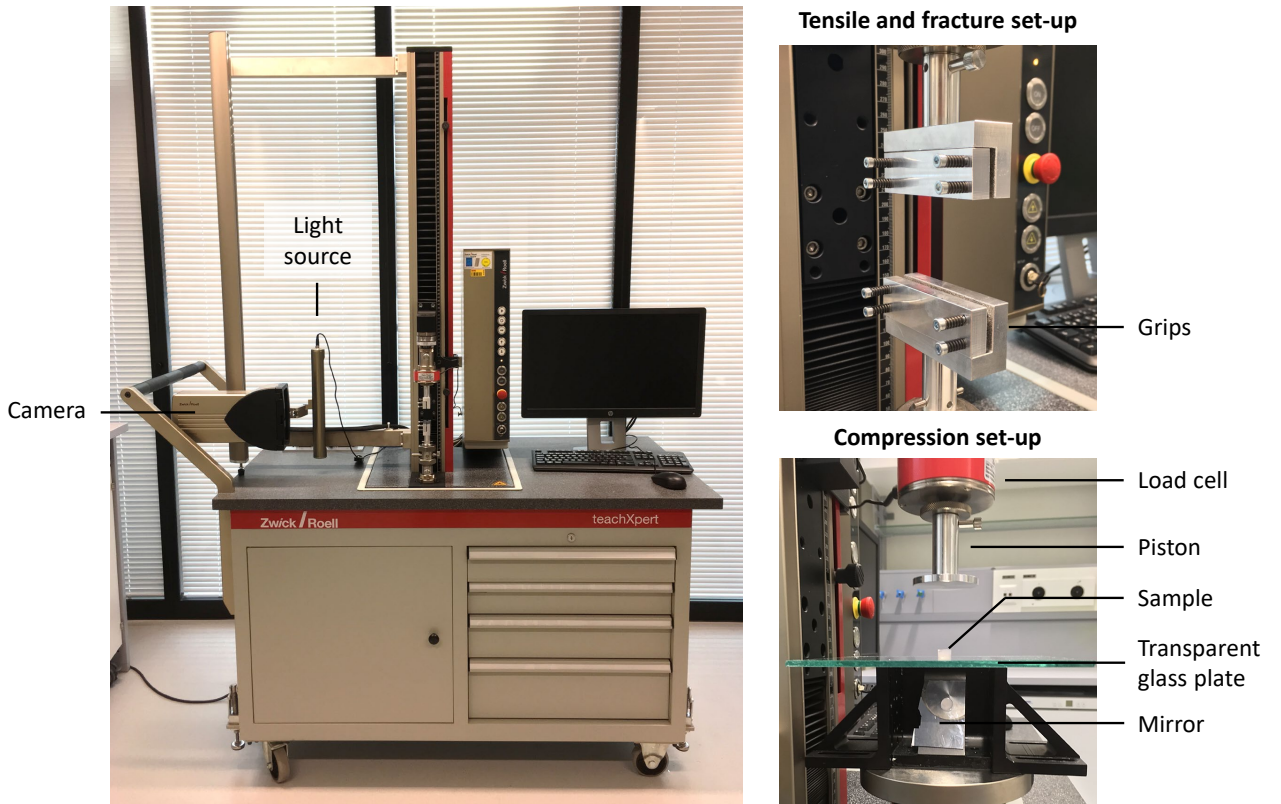


Figure 3.14: Tensile machine *Zwick* used for tensile, fracture, and compression tests.

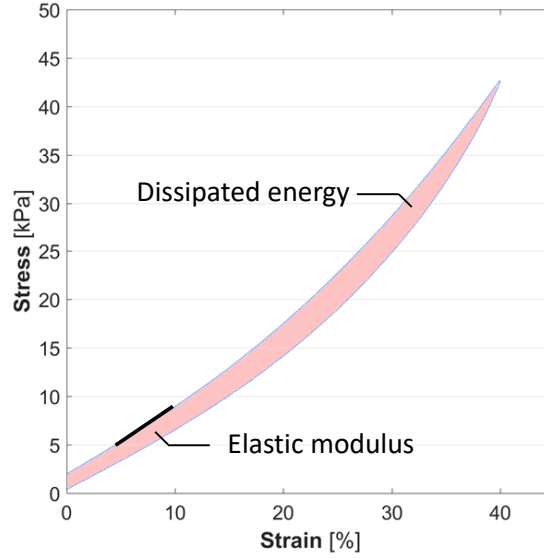


Figure 3.15: Definition of elastic modulus and dissipation of energy.

3.4.5 Tensile test

The tensile and single notch edge tests were performed with the test machine Zwicky, shown in Fig. 3.14, on swollen and unswollen samples. The samples were placed between self-customized grips. The tensile elastic modulus was determined by linear regression between 10% and 15% true strain measure with a virtual extensometer, while the dissipated energy was defined as the area below the stress-strain curve (hysteresis).

In *Chapter 5. Fracture properties of preloaded hydrogel composites*, the calibration for tensile samples was done via digital image correlation (Fig. 3.16a), which is described in section 3.4.7. The strain calculated by the displacement ratio of the grip-to-grip distance was compared with the strain measure on the straight part of the dog-bone sample. Since the two strains evolve linearly (Fig. 3.16b), a correction ratio (R_{corr}) was determined with the following equation (3.6) :

$$R_{corr} = \frac{\epsilon_{straight}}{\epsilon_{grip - to - grip}} \quad (3.6)$$

In the following chapters, the true strain was directly measured with the virtual extensometer VideoX-tens (Zwick/Roell).

3.4.6 Single notch edge test

Fig. 3.17 presents a representative stress-strain curve of a single notch edge test. The maximum stress of the true stress-strain curve defines the fracture strength of notched samples. The highlighted area in Fig. 3.17 represents the crack initiation energy density under the stress-strain curve until the first peak. Finally, the fracture energy γ was determined when the critical energy release rate G_c was

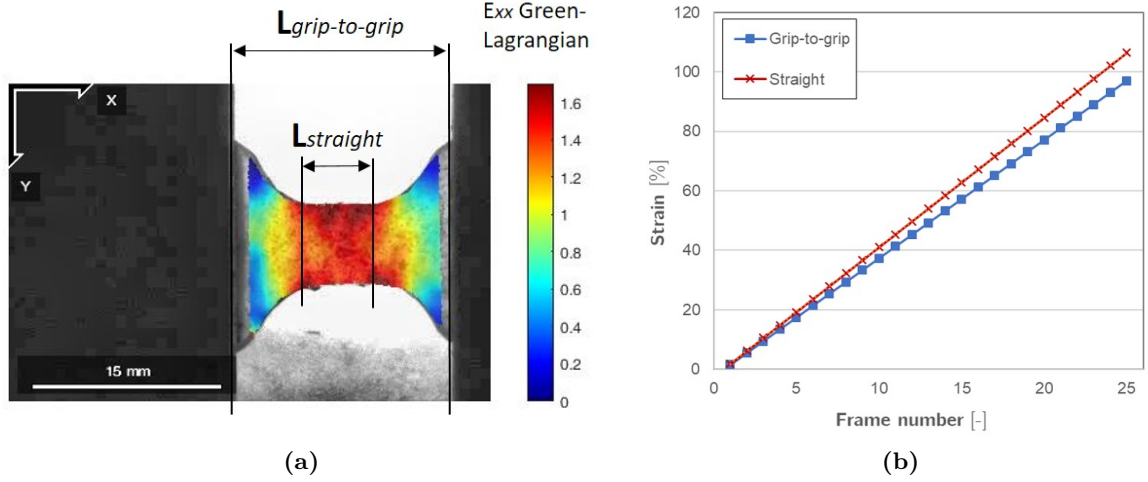


Figure 3.16: Calibration of dog-bone samples: (a) DIC of dog-bone samples to compare the Lagrangian strain along the x-axis calculated by the strain ratio of the grip-to-grip displacement with the strain of the straight part of the sample measured with a virtual extensometer, (b) linear evolution of the different strains.

reached. G_c was characterized by the equation (3.7)^[17].

$$G_c = 2 \frac{3}{\sqrt{\lambda_c}} c W_s(\lambda_c) \quad (3.7)$$

where c is the initial crack length and $W_s(\lambda_c)$ is the stored energy density of an un-notched sample under the critical stretch λ_c . The critical energy release rate G_c is calculated when the stretch λ_c reaches the first peak of a notched sample's stress-strain curve.

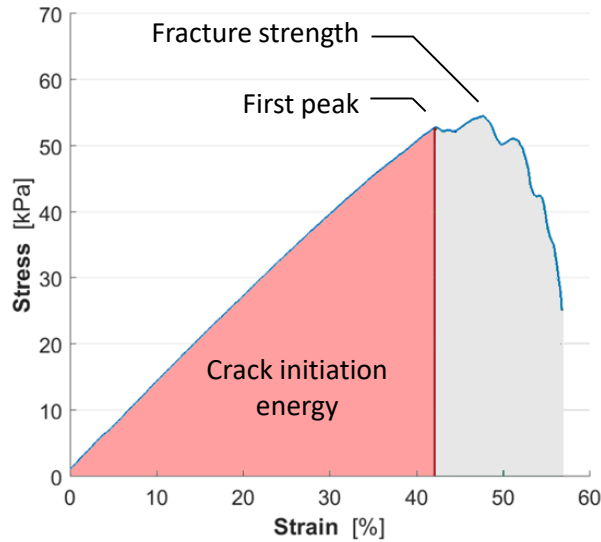


Figure 3.17: Definition of fracture strength and crack initiation energy of notched samples.

3.4.7 Digital image correlation analysis

Digital image correlation analysis permits to observe the strain field distribution on the surfaces of hydrogels samples in tracking specific points. In order to create a speckle pattern, Graphit 33 (Kontakt Chemie, Germany) was sprayed on the surface of notched samples to make a fine, randomly, and homogeneously distributed speckles pattern. For finer speckles pattern, used for DIC at the microscopic level, a drop of Graphit 33 dissolved in isopropanol was deposited on the surface of dog-bone samples and wipe a few seconds later with a lens cleaning tissue. Fig. 3.18 shows images of the resulting speckles pattern.

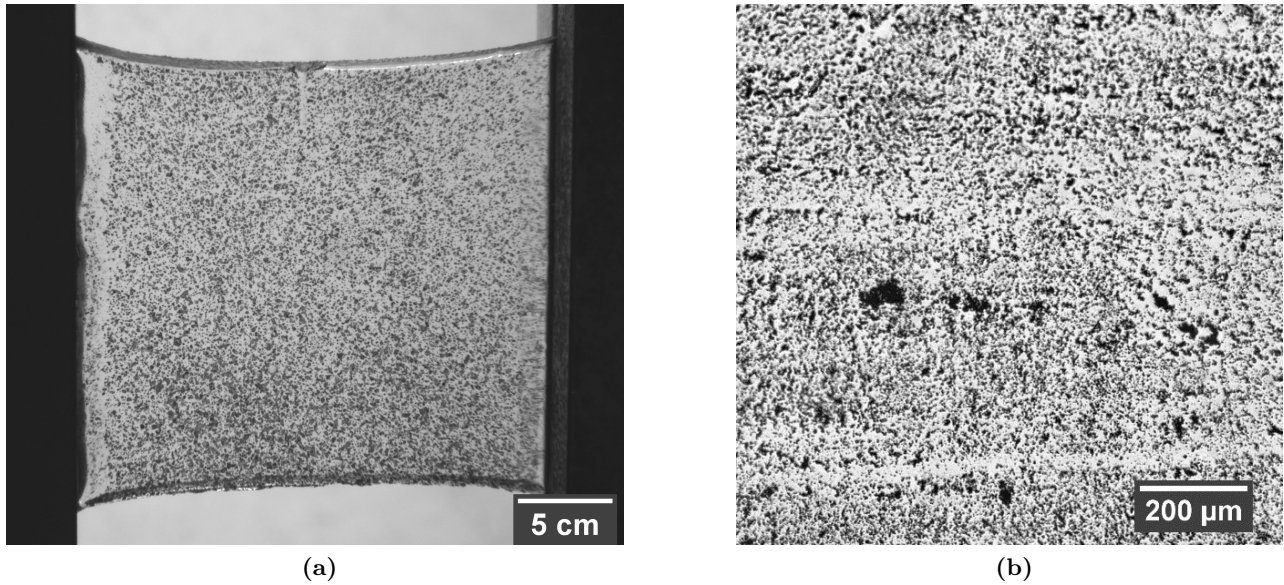


Figure 3.18: Speckle pattern on the surface of hydrogel for digital image correlation at (left) the macroscopic and (right) microscopic scale. Graphit 33 (Kontakt Chemie, Germany) was sprayed on the surface of notched samples to make a fine, randomly and homogeneously distributed speckles pattern. In order to obtain a finer speckles pattern for DIC at the microscopic level, a drop of Graphit 33 dissolved in isopropanol was deposited on the surface of dog-bone samples and wipe a few seconds later with a lens cleaning tissue.

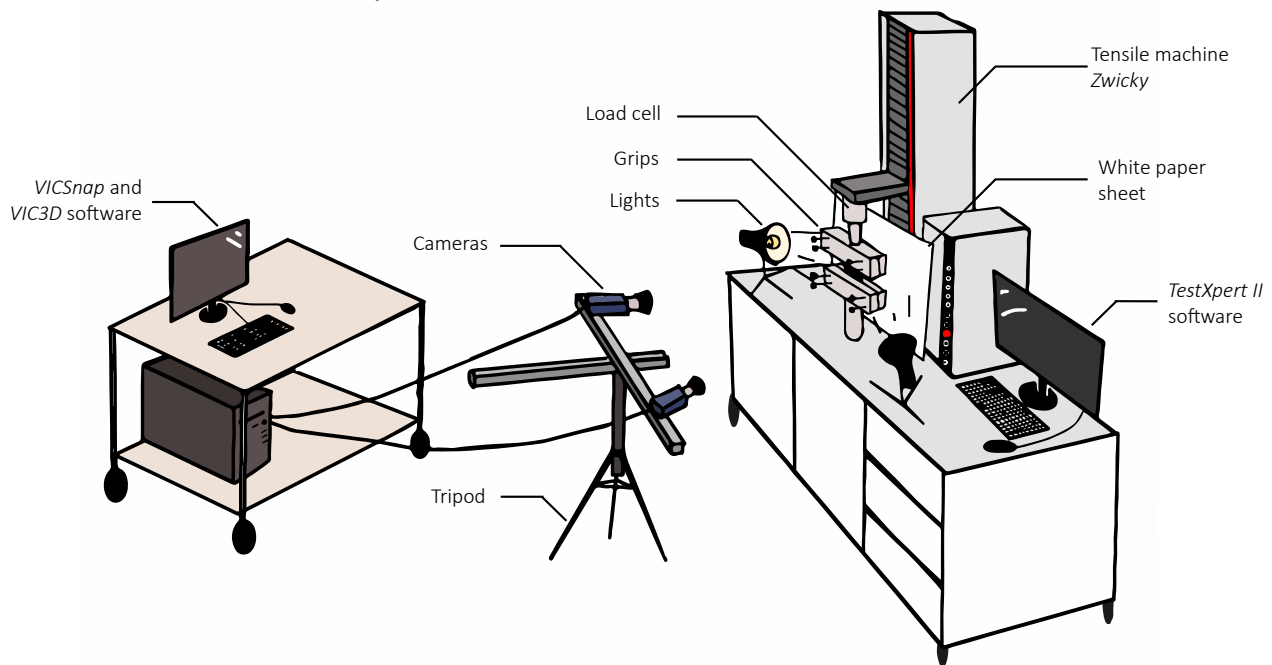
2D DIC analysis was performed with the open-source software ncorr V1.2 on Matlab R2016b. An integrated camera VideoXtens (Zwick/Roell) in Zwicky recorded the images. The reference image was defined when the applied load reached 0.04 N.

3D DIC analysis was done with the test equipment illustrated in Fig. 3.19 provided by correlated solutions according to the test parameters presented in Table 3.4. The test equipment incorporates two cameras Grasshoper USB3 (monochrom, 5.0 Mpix, 75 fps), 70 mm lens, the software Vicsnap V.9 for the recording of images, and VIC3D V.8 for the analysis.

All reference image was determined when the applied load reached 0.04 N.

Table 3.4: 3D digital image correlation parameters.

Description	Values
Angle	25°
Distance to sample	~ 470 mm
Lens	70 mm (Table 2 pos.5)
Camera resolution	~ 3.45 $\mu\text{m}/\text{pixel}$
Shutter opening	> 6
Exposition time	> 2.4 ms
Frame per second	100 – 500 ms/image (2-10 fps)
Ideal dot size	20 μm
Ideal subset	36 pixels
Ideal step	12 pixels

**Figure 3.19:** Setup for digital image correlation in 3D.

3.4.8 Adhesion test

The adhesion test setup, presented in Fig. 3.20, was developed by Peyman Karami. Unswollen samples were tested on bovine cartilage according to the test parameters describes in Table 3.3.

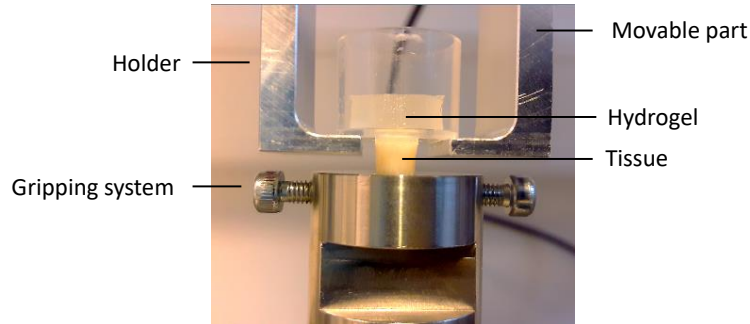


Figure 3.20: Adhesion setup.

3.4.9 Interfacial fracture test

The hydrogel-tissue fracture test was performed with the test machine Zwicky shown in Fig. 3.14 and 3.21 on unswollen samples. Rectangular tissue samples with a dimension of 20 mm \times 15 mm \times 2 mm (length \times width \times thickness) were placed in the molds used for fracture shown in Fig. 3.11. The hydrogel precursor was added to the remaining free placed (20 mm \times 15 mm \times 2 mm). Once polymerized, a sharp interfacial notch 3 mm length was created. The total dimension was, therefore, 40 mm \times 15 mm \times 2 mm.

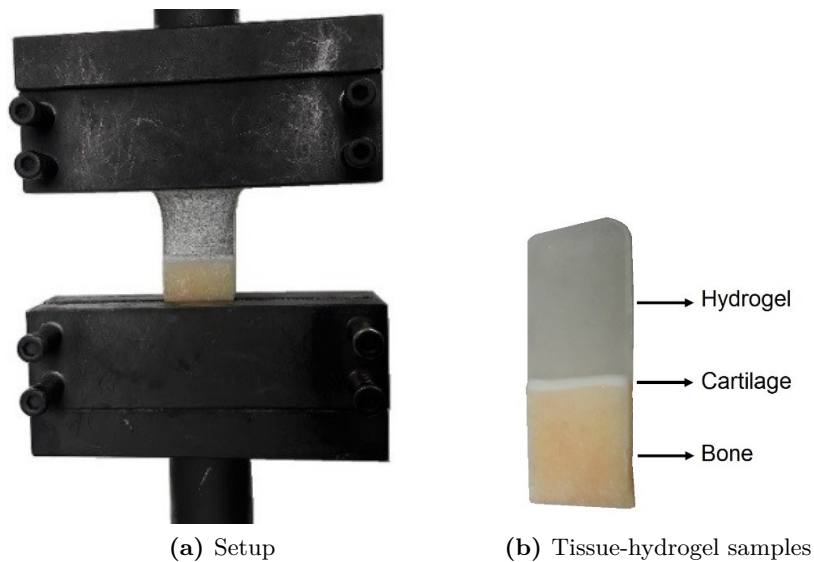


Figure 3.21: (a) Setup for interfacial fracture test (b) examples of the tissue-hydrogel sample, where the tissue is bovine articular cartilage.

3.4.10 Fourier-transform infrared spectroscopy

The crystalline structure of dry self-reinforced granular hydrogels was analyzed with Fourier transform infrared spectroscopy (FTIR) FT/IR-6300typeA. The IR analysis covered the range between 800-3500 cm^{-1} with a resolution of 4 cm^{-1} . The background was collected before testing the samples.

The FTIR spectras were analyzed with R using the package of *ChemoSpec*. The baseline drift was adjusted with the function *baselineSpectra*, where *modpolyfit* was set for the method, while the normalization was done with the function *normSpectra*, where *PQN* (*i.e.* Probabalistic Quotient Normalizatio) was set for the method^[301].

3.4.11 Cytocompatibility test

Cytocompatibility was evaluated via a direct contact test and proliferation study.

Direct contact test

Cylindrical hydrogels were first sterilized in an autoclave before being placed and fixed separately in the middle of cell culture vessels with a diameter of 35 mm. Bovine chondrocyte cells were then seeded around the samples (10000 cell/ cm^2). The following quantities were added to each vessel: 2.5 mL of cell culture medium, 10 vol% Fetal Bovine Serum (FBS), 1 vol% Penicillin Streptomycin (PS), and 1 vol% L-Glutamine. Finally, the samples were incubated at 37 °C in 5% CO_2 for one week. To observe the cells, they were stained with 1 mL methanol for 30 s followed by 1 mL diluted Giemsa solution.

Proliferation study

Bovine chondrocyte cells were cultured on a 6-well plate with 100'000 cells/well, where each well contains 6 ml of culture medium. Cell strainers with a mesh size of 70 μm were placed in the wells. Sterilized hydrogels, with 2.5 mm in thickness, were then deposited in the strainers. The culture medium was changed every two days. In order to study cell proliferation at different time points, the medium was aspirated and replaced with 1 ml of medium with 10 vol% PrestoBlue™ assay (A13261, Life Technologies) according to the manufacturer's instructions in each well. After incubation for 30 min, the solution was distributed in a black 96-well plate. The proliferation is evaluated with a microplate reader (Wallac 1420 Victor2, PerkinElmer) at a fluorescence wavelength of 595 nm. Each test is repeated three times, and at each time point, three wells without hydrogel were considered for the positive control.

Chapter 4

Single and double network hydrogels and their composites

Which hydrogel structure is suitable for load-bearing applications?

Load-bearing hydrogel implants must satisfy several criteria such as high toughness, good reliability, and stability. In the absence of standards, a testing protocol was established in this chapter to highlight the strengths and weaknesses of different hydrogel systems. It evaluates their biological, physical, mechanical, and adhesion properties, processing ease, as well as their long-term reliability. Four different hydrogel structures based on poly(ethylene glycol) dimethacrylate were tested: neat, composites, double network, and composite double network hydrogels. Composites were reinforced cellulose fibers, while the second network was alginate. Adding cellulose fibers and/or a second network significantly improved mechanical and adhesion properties in the *as-prepared state*. Nevertheless, the double network hydrogel lost all profits in the *swollen state*. Indeed, compared to neat hydrogels, double network hydrogels had at least 30% higher swelling ratios and 25% lower elastic moduli. In contrast, the addition of 0.5 wt.% cellulose fibers to neat hydrogels reduced swelling by more than 30% without seriously affecting the processability or the long-term reliability. Fatigue tests revealed that hydrogel composites successfully survive 10 million loading cycles at 20% applied strain. However, it became softer after the first loading cycles and behaved similarly to the *Mullins effect*. Nevertheless, its large swelling ratio, *i.e* 95 wt.%, and its compressive modulus, *i.e* 64 kPa, are still inappropriate for many applications in an unconfined environment, such as treating focal cartilage defect. Therefore, further research on controlling swelling and stiffness is necessary to extend their field of application

Keywords: neat, composite, double network, PEGDM, cellulose fibers, alginate, swelling ratio, mechanical test, adhesion to cartilage, fatigue.

Publications: "Composite double-network hydrogels to improve adhesion on biological surfaces", ACS applied materials & interfaces (2018)^[200], "Tailoring swelling to control softening mechanisms during cyclic loading of PEG/cellulose hydrogel composites", Composites Science and Technology (2018)^[31]

4.1 Introduction

Like living tissues, hydrogels are mainly composed of water, typically more than 80 wt.%. This attribute enables the transport of nutriment and supports new tissue growth. However, for using hydrogels in load-bearing applications, they have to satisfy important criteria illustrated in Fig. 1.2 on p.2. Load-bearing characteristics involve, for instance, high toughness, good reliability, and stability. These last decades, new structures such as interpenetrating polymer network, double network hydrogel, or composite were developed for significantly improving mechanical properties^[18–21]. However, their field of applications is often limited by their (i) toxic side reactions, (ii) low toughness, (iii) high swelling ratios, (iv) long-term reliability, (v) lack of adhesion to biological tissue, and/or (i) their processing ease.

Since no standardized protocol exists for evaluating load-bearing hydrogel implants nowadays, this chapter presents a testing protocol for comparing the strengths and weaknesses of single and double network structures and their composites. Those experiments evaluated their biological, physical, mechanical, and adhesion properties, processing ease, as well as their long-term reliability.

Fig. 4.1 presents four different hydrogel structures studied in this chapter: neat hydrogels, hydrogel composites, double network hydrogels, and double network hydrogel composites. The hydrogels were selected according to their characteristics detailed in Table 4.1, and their various potential for dissipating energy. Dissipative structures are believed to perform better in load-bearing situations, especially because they limit crack propagation in bulk and at the interface between tissue and implant. Here, the neat hydrogel made of a single polymer network is expected to be the softest structure with a low dissipative capability. On the contrary, the complex composite double network hydrogel should be the strongest and most dissipative.

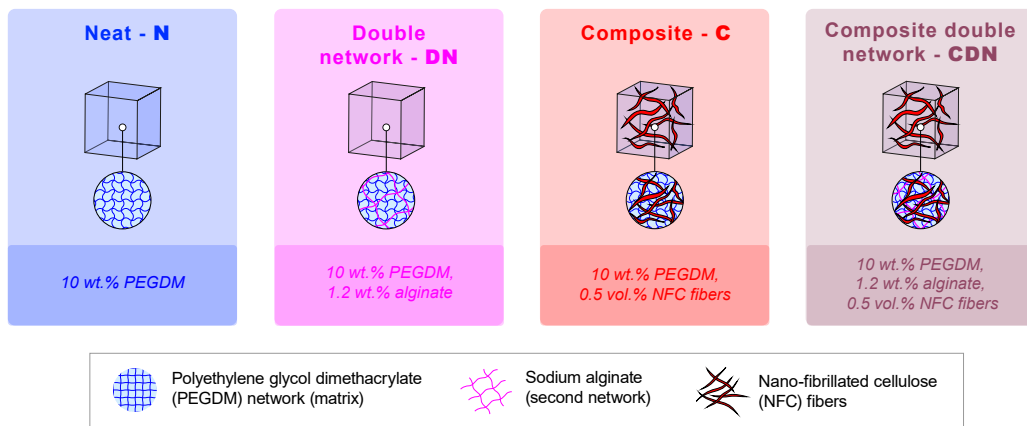


Figure 4.1: Structure and composition of neat, composite, double network, and double network hydrogels.

Table 4.1: Material approach.

Hydrogel components	Justifications	Goal
20 kDa poly(ethylene glycol)dimethacrylate (PEGDM) Matrix - network 1	20 kDa PEGDM <ul style="list-style-type: none"> • is commercially available. • have a low degradation rate. • have good stretchability. • is suitable for chemical modifications. 	A flexible polymer network is crucial for <ul style="list-style-type: none"> • toughness. • fatigue resistance. • manipulate hydrogels.
Sodium alginate (medium viscosity) Matrix - network 2	Sodium alginate <ul style="list-style-type: none"> • is commercially available. • have recoverable bonds. • has good biocompatibility. 	<ul style="list-style-type: none"> • The second network can significantly increase the toughness of hydrogels. • Recoverable bonds breaks can considerably improve fatigue resistance.
Nano-fibrillated cellulose (NFC) fibers Reinforcement	Cellulose fibers <ul style="list-style-type: none"> • is the most abundant biopolymer. • has a large surface-to-volume ratio. • has excellent mechanical properties. • is easy to incorporate in hydrogels. 	Reinforcement increases toughness in <ul style="list-style-type: none"> • sustaining high stress. • dissipating energy. • limiting crack propagation in inter-phase and bulk.

4.2 Materials and methods

4.2.1 Materials

20 kDa Poly(ethylene glycol) dimethacrylate (PEGDM) was synthesized in the laboratory of macromolecular and organic materials (LMOM) of Professor Holger Frauenrath. Sodium alginate (CAS 497-19-8) and calcium sulfate (CAS 7778-19-9) were supplied by Merck. Nano-fibrillated cellulose (NFC) were provided by EMPA (Dübendorf, Switzerland), where the base material was Zellstoff Stendal (Arneburg DE), Germany). SEM analysis shows that the NFC measure a few micrometers with diameters in the range of 2-100 nm^[141]. Irgacure 2959 from BASF was used as a photoinitiator.

4.2.2 Hydrogel synthesis

The full synthesis of the neat, hydrogel, double network, and composite double network hydrogels are described and illustrated in Fig. 3.4 - 3.7. The precursor of neat hydrogel was initially composed of 10 wt.% of PEGDM, 0.1 g · ml⁻¹% of Irgacure 2959, and distilled water (Fig. 3.4 on p. 43). The precursor of hydrogel composites had the same PEGDM concentration as the neat hydrogel, where 0.5 vol.% NFC were added and mixed with an Ultra Turrax (IKA T25 digital, SN 25 10G) at 12'000 RPS for 10 min (Fig. 3.5 on p. 43). For creating the double network and composite double network hydrogels, 0.9 wt.% of calcium sulfate was first mixed with the precursor of the neat and composite hydrogel, respectively, before progressively adding 1.2 wt.% of sodium alginate. The precursors, degassed at 20 mbar, were cast in Teflon molds and cover with a microscopic glass before being irradiated for 30 min

under UV-light irradiation at a wavelength of 365 nm and an intensity of 5 mW.cm⁻².

Table summarizes the dimension of casting molds 4.2.

Table 4.2: Sample geometries.

Sample type	Dimension	Tests
Cylinder Fig. 3.10	Ø8 mm x 4.5 mm	<ul style="list-style-type: none"> • Swelling ratio • Compression test • Long-term fatigue test • Cytotoxicity
Dog-bone Fig. 3.11	Cross-section of 5 x 2 mm	Tensile test
Rectangular Fig. 3.11	15 x 30 x 2 mm <i>Crack length of 3 mm</i>	Fracture test
Square attached to bovine cartilage Fig. 3.21	15 x 15 x 2 mm <i>Crack length of 3 mm</i>	Interfacial fracture strength
Cylinder attached to bovine cartilage Fig. 3.20	Ø15mm x 4.5mm	Adhesion test

4.2.3 Methods

The hydrogels were evaluated according to the major characteristics for load-bearing hydrogel implants illustrated in Fig. 1.2. In particular, the experiments assessed their biological, physical, mechanical, and adhesion properties, processing ease, as well as their long-term reliability.

Table 4.3 describes all methods used for the characterizations. More details on the tests can be found in *Chapter 3. Materials and methods*.

Table 4.3: Characterization methods.

Description	Property	Tests	Goal
Physical properties	Swelling ratio	Weight scale Variation of weight. <i>Section 3.4.2</i>	Assess dimensional stability once implemented in a human body.
	Complex viscosity	Oscillatory rheology Oscillating strain sweep from 0.1% to 1000% at 0.5 Hz. <i>Section 3.4.3</i>	Measure complex viscosity of hydrogel precursor for evaluating the injectability.
	Curing time	Oscillatory photo-rheology UV irradiation at 365 nm and $5 \text{ mW} \cdot \text{cm}^{-2}$ with an oscillating strain of 6% at 10 Hz. <i>Section 3.4.3</i>	Measure complex viscosity of hydrogel precursor for evaluating the injectability.
Mechanical properties	Compressive elastic modulus and dissipation of energy	Compression test Loading rate 0,1 mm/s and preloading 0,02N. <i>Section 3.4.4 and Fig. 3.14</i>	Evaluation of mechanical properties of as-prepared and swollen hydrogels in compression loading.
	Tensile elastic modulus and dissipation of energy	Tensile test Loading rate 0,1 mm/s and preloading 0,02N. <i>Section 3.4.5 and Fig. 3.14</i>	Evaluation of mechanical properties of as-prepared and swollen hydrogels in tensile loading.
	Fracture strength	Single notch edge test Loading rate 0,1 mm/s and preloading 0,02N. <i>Section 3.4.6 and Fig. 3.14</i>	Determination of fracture strength of as-prepared hydrogels.
Adhesion properties	Adhesion strength	Adhesion test Loading rate 0,1 mm/s and preloading 0,05N. <i>Section 3.4.8 and Fig. 3.20</i>	Measure adhesion of as-prepared hydrogel to bovine articular cartilage in tensile loading.
	Interfacial fracture strength	Tensile setup Loading rate 0,1 mm/s and preloading 0,02N. <i>Section 3.4.9 and Fig. 3.14</i>	Evaluation of interfacial fracture strength between cartilage and <i>as-prepared</i> hydrogels.
Biological properties	Cytotoxicity	Direct contact test and proliferation study 7 days at 37°C in 5% CO ₂ . <i>Section 3.4.11</i>	Control biocompatibility up to 7 days.
Reliability	Fatigue resistance	Cyclic compression loadings Loading rate 10 mm/s and preloading 0,02N. <i>Section 3.4.4 and Fig. 3.14</i>	Control of the long-term stability on swollen samples up to 10 millions loading cycles.
Fiber morphology	Microscopy	Fluorescence confocal microscopy At 405nm and 20x lens. <i>Section 3.4.1 on p.48</i>	Observed the morphology of cellulose fibers in hydrated hydrogels.

4.3 Results and discussion

The following results were partially published in *Composite science and technology*^[31] and *Applied material and interfaces*^[200].

4.3.1 Processability - rheology

Complex viscosity of the precursor

In order to evaluate the processing ease of neat hydrogels - *N*, hydrogel composites - *C*, double network hydrogels - *DN*, and composite double network hydrogels - *CDN*, the complex viscosity of their precursors was measured at room temperature with a parallel plate rheometer (TA Instruments AR2000ex) and presented in Fig. 4.2a. An oscillating strain sweep at 0.5 Hz was then applied to the precursors, where the strain starts from 0.1% to 1000%.

All precursors revealed apparent shear-thinning behavior and complex viscosities below 10 Pa · s, suitable for injecting the precursors through narrow needles^[7]. At quasi-static 0.1% oscillation strain, neat hydrogel had the lowest complex viscosity of about 0.1 Pa · s. Double network hydrogels were slightly more viscous, *i.e.* 1 Pa · s. Finally, adding 0.5 vol.% of cellulose fibers increased the complex viscosity by one order of magnitude, *i.e.* 10 Pa · s.

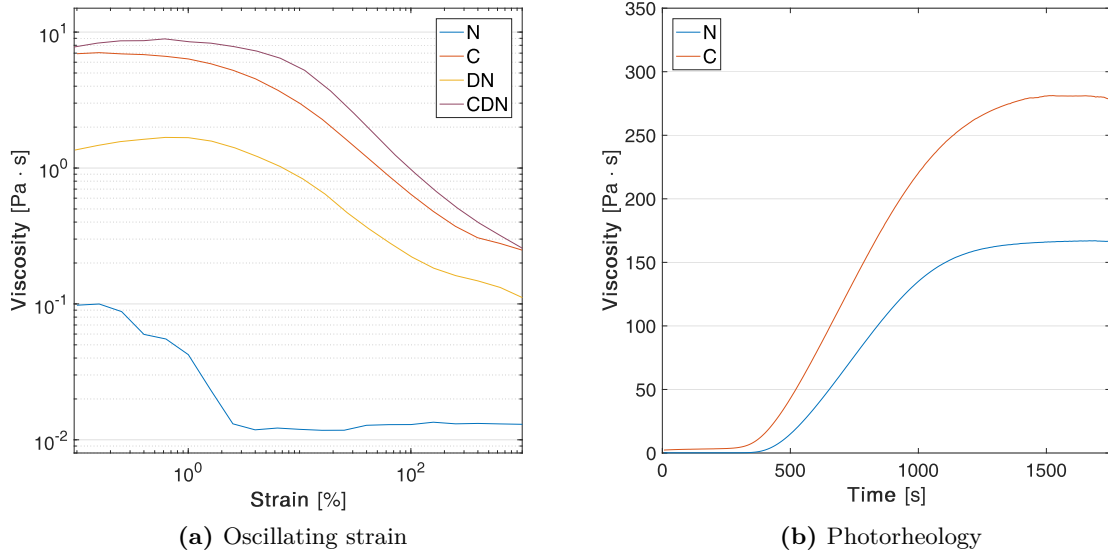


Figure 4.2: Rheology measurement of neat hydrogels - *N*, hydrogel composites - *C*, double network hydrogels - *DN*, and composite double network hydrogels - *CDN*. (a) Representative behavior of precursors' complex viscosity with a parallel plate rheometer under an oscillating strain sweep at 0.5 Hz at room temperatures. The measurements were rapidly taken after mixing the precursor, which was not degassed. (b) Representative photocuring behavior of precursors' complex viscosity with a parallel plate rheometer under 6% of oscillating strain at 10 Hz.

Curing time through photo-polymerization

In order to evaluate the curing time of neat and hydrogel composites, photo-rheology with a parallel plate rheometer was performed on their precursors under UV-light irradiation at a wavelength of 365 nm and an intensity of $5 \text{ mW} \cdot \text{cm}^{-2}$. The oscillating strain was fixed at 6% and 10 Hz. The resulting curing behaviors are presented in Fig. 4.2b.

The precursors were fully cured after 20 min, which represents quite a long time for biomedical applications. The photo-initiator used during synthesis, Irgacure 2959, is water-soluble and FDA approved^[89]. However, it is only poorly effective at a wavelength higher than 365 nm because its maximal absorption peak is located at around 295 nm, as shown in Fig. 2.1 in *Chapter 2. State of the art*^[88].

Nevertheless, the precursors containing cellulose fibers started curing about 1 minute before the neat precursor. It was previously reported^[23] that the fibers scattered light, promoting a homogenous polymerization and accelerating the gelation time.

4.3.2 Physical properties - swelling

Hydrogels enable minimally invasive treatment because the precursor can be injected through a small needle and cured *in situ* with UV-irradiation, for example. However, once implemented in the human body, the hydrogel is not necessary in its equilibrium *swollen state*. Swelling may be critical for some applications, such as for cartilage repair, where a continuous surface between hydrogel and tissue is required. The change in volume due to swelling or shrinking might create internal stresses in the bulk hydrogels or break the interface with the tissue. Therefore, knowing the swelling ratios of hydrogels are prerequisite for unconfined and semi-confined applications.

The swelling ratios of neat hydrogels - *N*, hydrogel composites - *C*, double network hydrogels - *DN*, and composite double network hydrogels - *CDN* were determined with equation (3.1) described in section 3.4.2 on p.48. The hydrogels were swollen in PBS, and demineralized water for at least 24h and their corresponding swelling ratios are reported in Fig. 4.3.

The reference neat hydrogel swelled $139 \pm 6 \text{ wt.}\%$ in PBS and $138 \pm 8 \text{ wt.}\%$ in demineralized water. The presence of cellulose fibers reduced swelling down to $95 \pm 7 \text{ wt.}\%$ in PBS and $94 \pm 5 \text{ wt.}\%$ in demineralized water. This effect was already reported previously^[23,125]. In contrast, adding a secondary alginate network to the neat hydrogel significantly increased swelling up to $185 \pm 5 \text{ wt.}\%$ in PBS and even more in demineralized water. Indeed, the swelling ratio was measured at $295 \pm 26 \text{ wt.}\%$, which is an increase of 37%. It was related to the ionic crosslinking constituting the secondary alginate network, which is very sensitive to the surrounding salt concentration. Nevertheless, the cellulose fibers in the composite double network hydrogels could decrease swelling again.

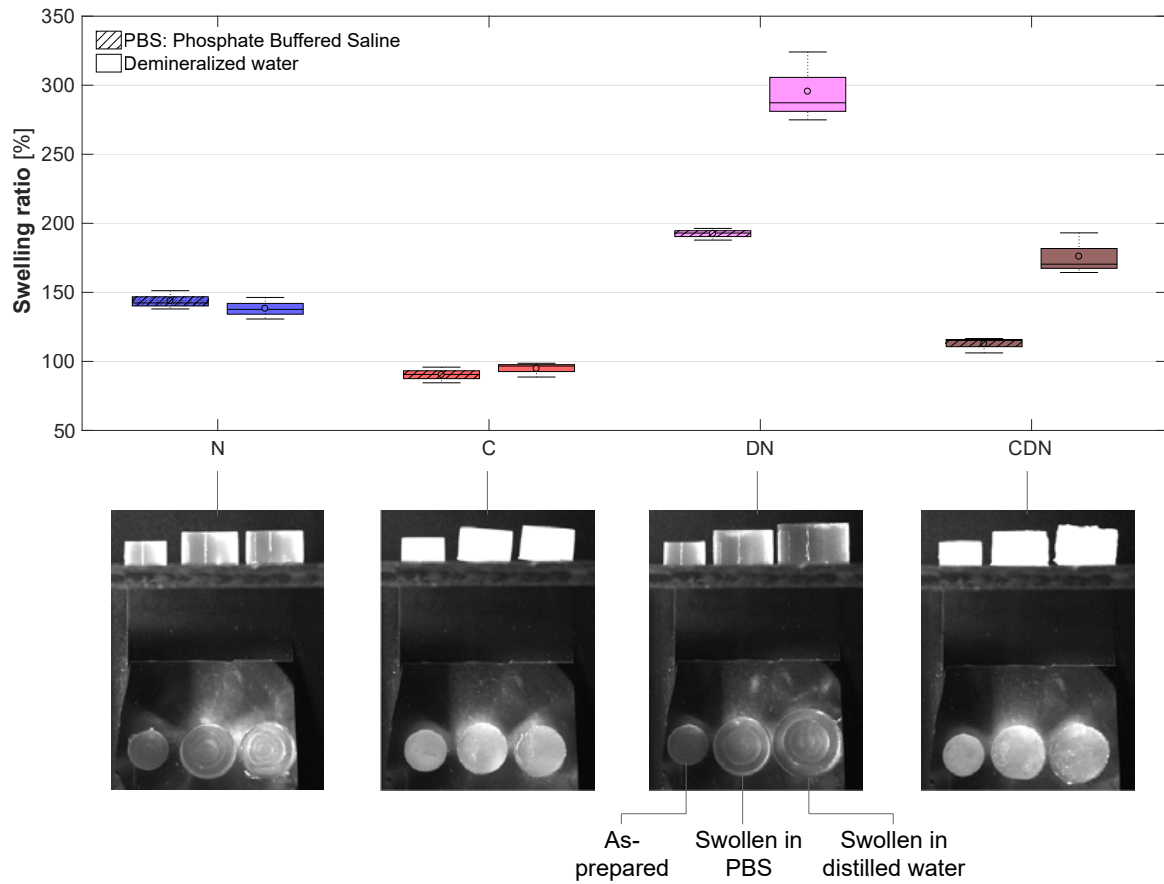


Figure 4.3: Swelling ratios of neat hydrogels - *N*, hydrogel composites - *C*, double network hydrogels - *DN*, and composite double network hydrogels - *CDN*, the samples in the *as-prepared* state and the *swollen* state.

4.3.3 Mechanical properties

Compression and tensile tests were performed on neat hydrogels - *N*, hydrogel composites - *C*, double network hydrogels - *DN*, and composite double network hydrogels - *CDN* in the *as-prepared* state according to the test parameters described in Table 3.3 on p. 50.

Fig. 4.4 presents the compressive and tensile elastic moduli obtained by linear regression between 5% and 10% applied strain and their dissipated energies were measured with the area of the stress-strain curve as shown in Fig. 3.15 on p. 52.

Although some variations between tensile and compressive loadings, the elastic moduli were measured between 30 kPa and 80 kPa.

The presence of fibers increased both elastic moduli and dissipated energies. Moreover, the elastic moduli were higher in tensile loading without alginate, probably because the fibers are more elastically active in the homogeneous tensile loading. The main sources for the dissipated energy were related to the disintegration of hydrogen bonds of the NFC network bonds between cellulose-cellulose or between PEGDM-cellulose^[23], to interfacial friction as well as the deformation of NFC fibers.

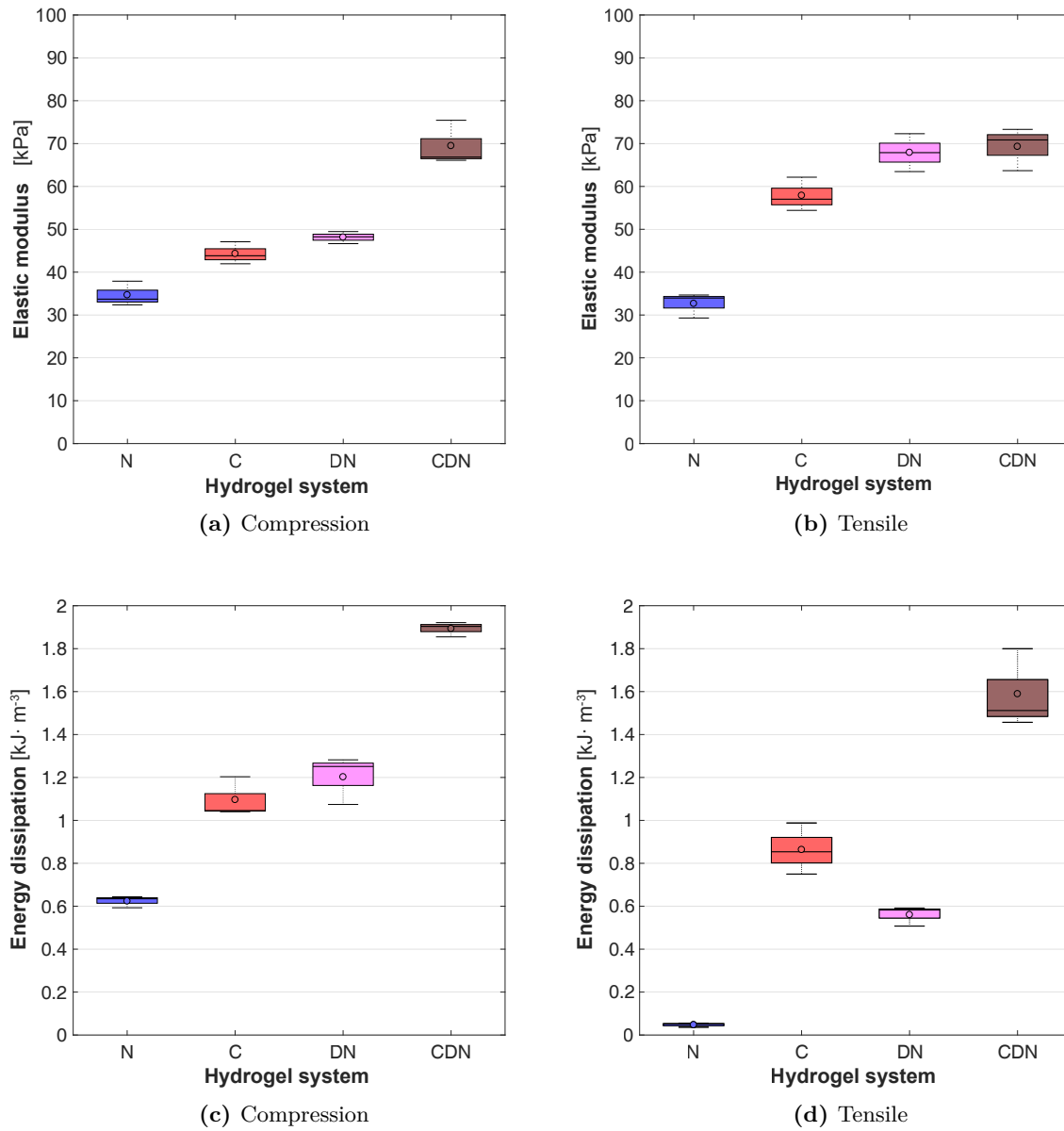


Figure 4.4: (a) Elastic moduli and (b) dissipated energies at 40% applied strains in compression and tensile of neat hydrogels - *N*, hydrogel composites - *C*, double network hydrogels - *DN*, and composite double network hydrogels - *CDN* in the *as-prepared state*.

Similarly, adding a secondary alginate network increased the elastic modulus probably because of stronger intermolecular friction and higher crosslinking density. In contrast, the breaking of ionic bonds explains that more energy was dissipated.

Effect of swelling on the compressive modulus

The effect of swelling on the compressive moduli was investigated on neat hydrogels - *N*, hydrogel composites - *C*, double network hydrogels - *DN*, and composite double network hydrogels - *CDN* according to the test parameters described in Table 3.3 on p. 50. Fig. 4.5 shows the resulting properties.

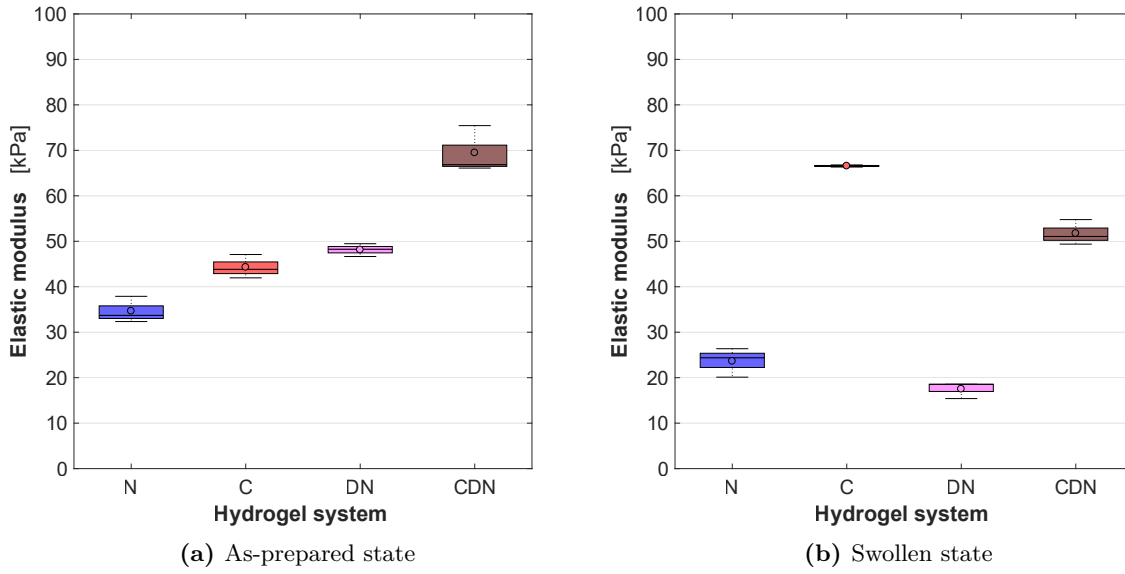


Figure 4.5: Effect of swelling on the compressive elastic modulus of neat hydrogels - N, hydrogel composites - C, double network hydrogels - DN, and composite double network hydrogels - CDN.

Neat, double network and composite double network hydrogels had lower elastic modulus in the *swollen state* compared to the *as-prepared state*. While neat and composite double network hydrogels showed a reduction of around 28%, the compressive modulus of double network hydrogel decreased by almost 62%. Surprisingly, the compressive modulus of hydrogel composite was enhanced by 45%.

Most hydrogels become softer when they swell^[28,206,302]. According to the statistical thermodynamics of rubber elasticity, the elastic modulus decreases by a factor of $(V_0/V)^{\frac{1}{3}}$ when the rubber swells, where V_0 is the volume of the network in the dry state and the V the volume of the sample at a specific swelling state^[201]. From a phenomenological perspective, water absorption disentangles the polymer chain and reduces the friction between them. Consequently, the hydrogel benefits of the enhanced mobility of the polymer chain^[206].

Nevertheless, in some cases, the stiffness of hydrogels increases when the hydrogel evolves from the *as-prepared state* to the equilibrium *swollen state*^[303,304]. For example, when polyampholyte hydrogels are immersed in an aqueous solution just after synthesis, co-ions and counter-ions are removed from its matrix^[303]. The volume of the hydrogel shrinks through this process and enhances the formation of ionic bonds. The latter positively influences the stiffness and the toughness of the hydrogel. The stiffening behavior was reported in thin-film hydrogel also^[304]. The increase in elastic modulus was associated with a decrease in entropy. The polymer side groups became charged when the hydrogel swelled and repelled one another, reducing possible polymer segments' configurations.

Since the neat hydrogel was softer in the *swollen state*, the stiffening induced by swelling observed in hydrogel composite was related to the NFC fibers only. To a certain extent, swelling reduces the

entropy of the NFC fibers. As suggested in Fig. 4.3, cellulose fibers prevent the hydrogel matrix from achieving its steady *swollen state*. In neat hydrogels, the steady *swollen state* is reached when the osmotic drive to dilute the polymer is balanced with the entropic resistance to strand extension of the polymer chain^[201]. In the case of hydrogel composites, the mechanical strand extension of the NFC network could limit the swelling. Similarly to the strain-stiffening mechanism observed in many elastomers and hydrogels, swelling pre-stretched the fiber network and reduces its configurational entropy. Consequently, the apparent elastic modulus increases. The origin might also be issued from the additional physical crosslinks between two entangled NFC fibers forming a more elastically active network due to swelling.

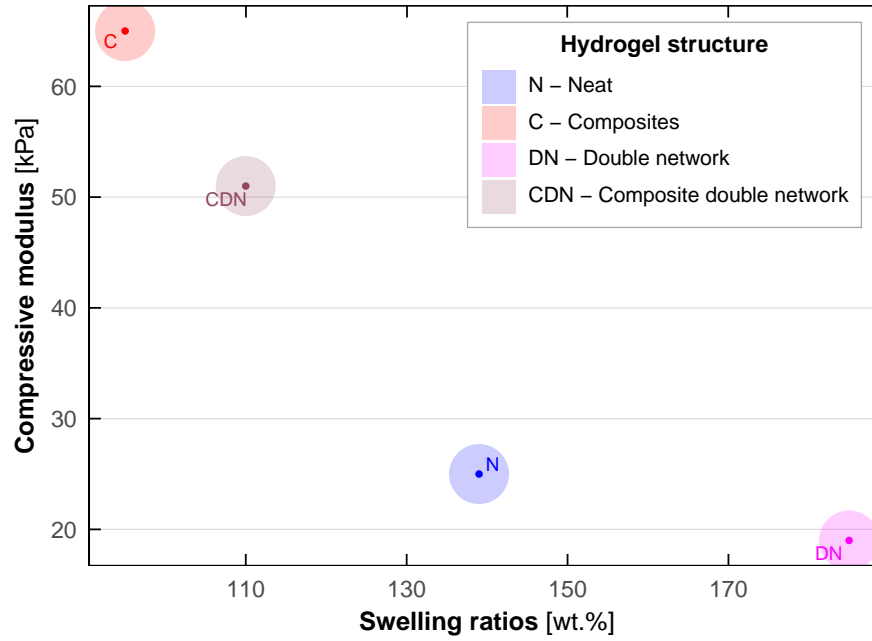


Figure 4.6: Property chart showing the compressive modulus of neat hydrogels - *N*, hydrogel composites - *C*, double network hydrogels - *DN*, and composite double network hydrogels - *CDN* in the *swollen state* in function of the swelling ratio.

Fig. 4.6 presents a property chart showing the compressive modulus in the *swollen state* according to the swelling ratio. The compressive moduli are larger for structures that swelled less. As mentioned in section 4.3.2, large swelling ratios may alter hydrogel's stability in an unconfined or semi-confined environment. Therefore, hydrogel composite shows better potential, among the studied structures, for being used as a load-bearing implant regarding the swelling and compressive modulus. Nevertheless, knowing that the elastic modulus of articular knee cartilage varied from 20 kPa to 6.5 Mpa^[165], its large swelling ratio of about 95 wt.% and its compressive modulus of 64 kPa are still inappropriate for many applications in an unconfined environment such as replacing the entire articular cartilage.

Distribution and morphology of fiber

To better understand the physical and mechanical properties of hydrogel composites, the morphology of the fibers in hydrated hydrogels was observed with fluorescence confocal microscopy. The hydrogel composite was swollen in 0.2 g/l Calcofluor White stain to dye the cellulose fibers only (see section 3.4.1 on p. 48).

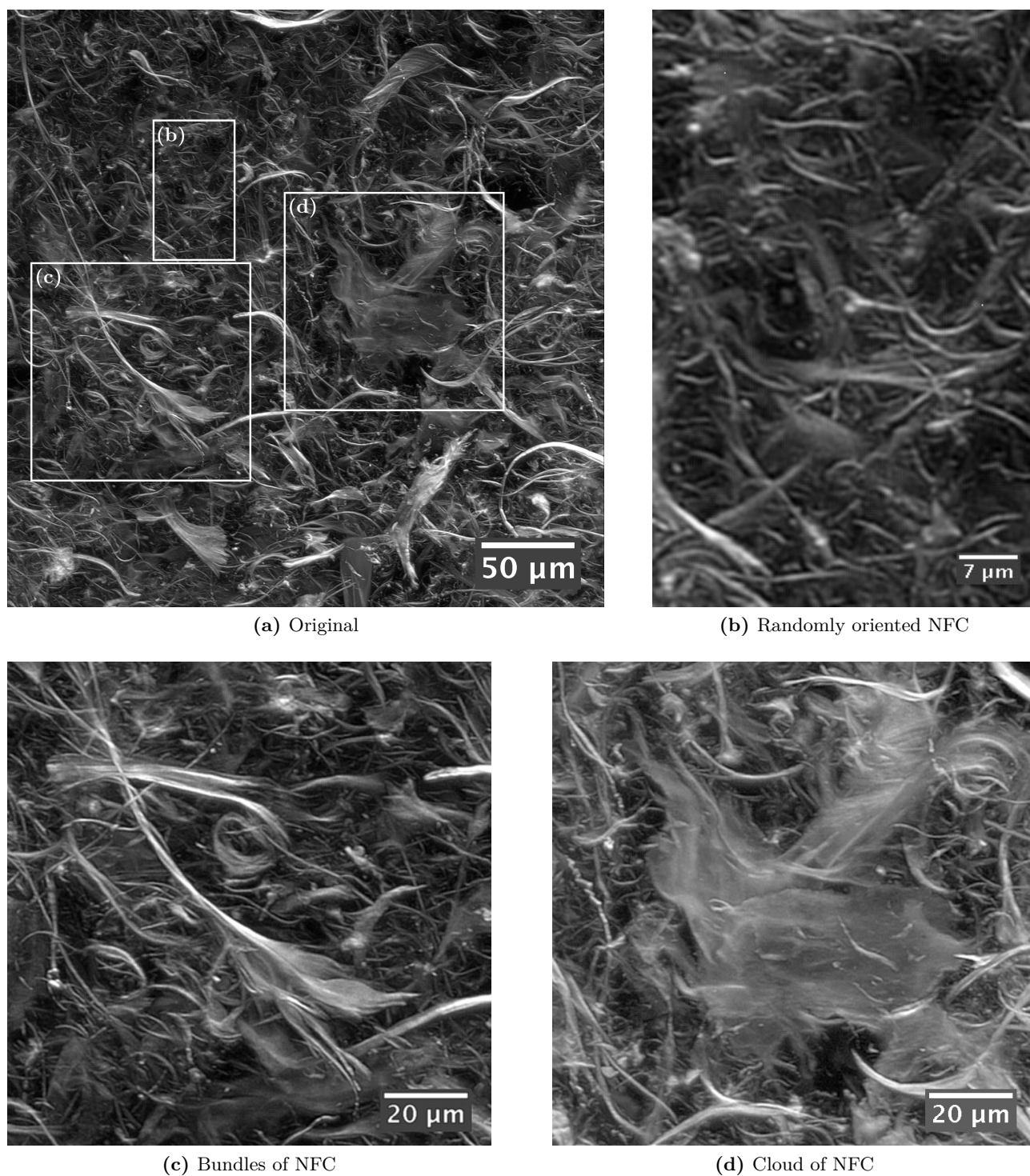


Figure 4.7: Z-stack projection of NFC fibers in a swollen composite hydrogel.

Fig. 4.7 presents a z-stack projection of NFC fibers in hydrated PEGDM hydrogels. The NFC fibers formed a network-like structure supporting, previously reported observation^[23]. Nevertheless, a broad diversity in size and morphology reflects the history of preparation. Fig. 4.7b presents a region of the hydrogel composite where the fibrils were well dispersed and randomly oriented. In contrast, Fig. 4.7c highlights a fiber that was not perfectly defibrillated. A bundle of aligned fibrils constituted the fiber, where some NFC were spreading out in the extremities. Those larger fibers may sustain the higher stresses in the system. Moreover, some clouds of NFC, observed in Fig. 4.7c, seems to be composed of tightly entangled and randomly oriented NFC. In such a complex and compact network, the physical hydrogen interactions and the potentially dissipated energy are expected to be high.

Fracture strength

The single notch edge tests were performed on neat hydrogels - *N*, hydrogel composites - *C*, double network hydrogels - *DN*, and composite double network hydrogels - *CDN* in the *as-prepared state* according to the test parameters in Table 3.3 on p.50. Fig. 4.8 presents the measured fracture strengths.

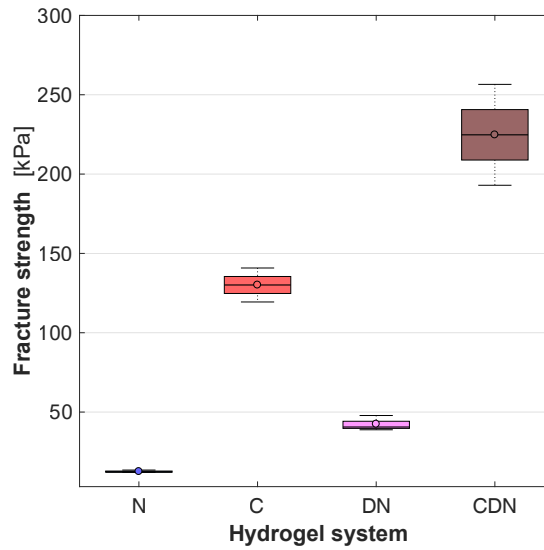


Figure 4.8: Fracture strength of neat hydrogels - *N*, hydrogel composites - *C*, double network hydrogels - *DN*, and composite double network hydrogels - *CDN* in the *as-prepared state*.

The fracture strength of double network hydrogels is about 3.5 times larger than that of neat hydrogel. Since the breaking of ionic bonds in the alginate network is easier than covalent crosslinking of the PEGDM network, ionic bonds broke most probably before the covalent bonds around the crack tips. Subsequently, double network hydrogel was able to release more energy by breaking bonds before crack propagation.

Nevertheless, when NFC fibers are added to the system, the fracture strength was almost 19 times higher than the neat hydrogels. This huge augmentation was mainly associated with fiber-bridging. Moreover, composite double network hydrogel fracture strength was significantly higher than that of

the hydrogel composite. Adding alginate might have a synergistic effect, which improves the interface/interphase quality between matrix and fibers. Besides, the trend of fracture strengths observed in Fig. 4.8 was similar to the trend of dissipated energy during tensile loadings shown in Fig. 4.4d, which suggests that both behaviors are tightly related.

The fracture behavior of hydrogel composites was further investigated in their *swollen* state in the following Chapter 5. *Fracture properties of preloaded hydrogel composites.*

4.3.4 Adhesion and interfacial fracture strength

The adhesion and interfacial fracture tests were performed according to the test parameters in Table 3.3 on p. 50 on biphasic samples: hydrogel samples in the *as-prepared state* shearing an interface with bovine cartilage (see Fig. 3.20 and Fig. 3.21 on p. 56). Note that the tissue samples were first fixed into the mold before adding the hydrogel precursors on top of it. After polymerization, the hydrogel attached to the tissue was rapidly gripped for the adhesion test.

The adhesion and interfacial fracture strengths of neat hydrogels - *N*, hydrogel composites - *C*, double network hydrogels - *DN*, and composite double network hydrogels - *CDN* are presented in Fig. 4.9.

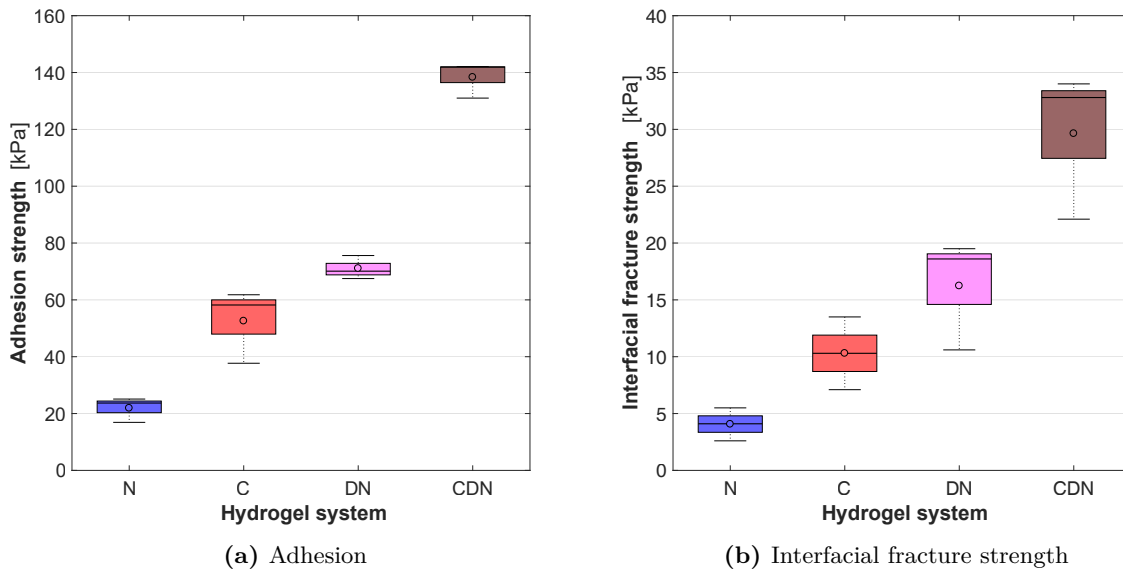


Figure 4.9: Adhesion and interfacial fracture strength of neat hydrogels - *N*, hydrogel composites - *C*, double network hydrogels - *DN*, and composite double network hydrogels - *CDN* in the *as-prepared state*. (a) Adhesion test on bovine cartilage - results of Peyman Karami (b) Interfacial fracture test between bovine cartilage and hydrogels.

Adhesion and interfacial fracture strengths showed similar trends. Indeed, except for double network hydrogels, the hydrogels failed at the interface during the adhesion test. Similar to the results obtained for the elastic moduli and fracture strengths, the presence of fibers increased the adhesion strengths from 21 kPa to 53 kPa for neat hydrogels and hydrogel composites respectively, and from 71 kPa to 138 kPa for the double network and composite double network hydrogels.

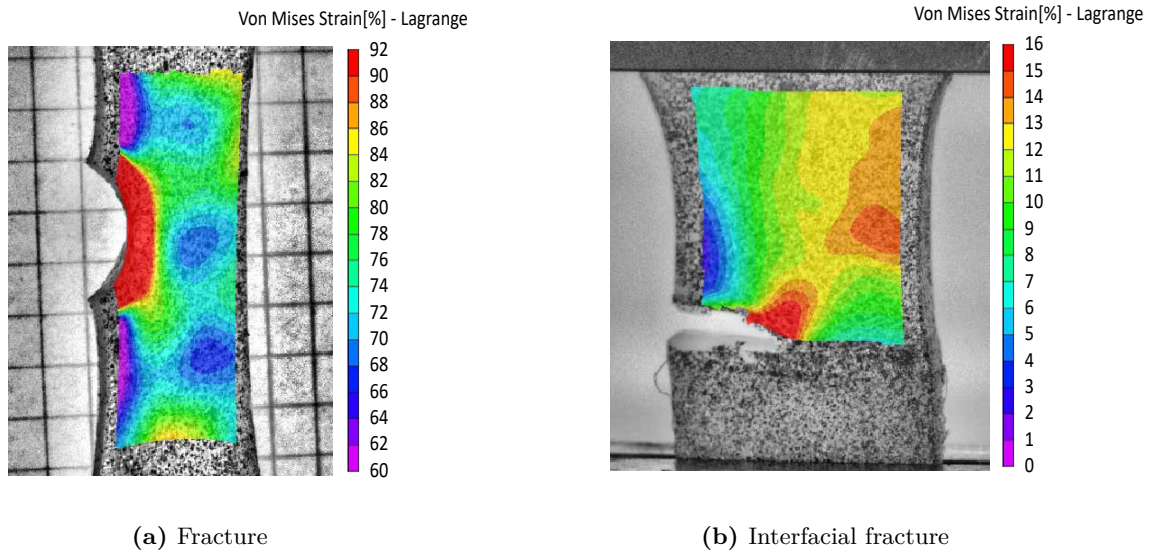


Figure 4.10: Digital image correlation images showing the strain distribution on the surface of hydrogel composites in the *as-prepared state* during (a) a single notch edge and (b) interfacial fracture tests.

It is generally accepted that the tougher the hydrogel is, the more energy is needed to propagate a crack and break the interface with the living tissue^[113]. Therefore, the huge difference of bulk fracture strengths observed in Fig. 4.8 could explain why the adhesion strength was the highest for composite double network hydrogels: since the hydrogel can absorb more energy before the propagation of a crack, the interface with the tissue is better protected.

The strain field around the crack type was observed with digital image correlation (DIC) in 3D and analyzed with the software VIC3D. As shown in Fig. 4.10, the largest deformations were located around crack tips. The strain concentration of interfacial fracture samples was shifted at 45° from the crack tip to the hydrogel highlighting how stress is transferred from the interface to hydrogel.

A direct relation between adhesion and bulk fracture strength could not be achieved. Indeed, double network hydrogels showed higher adhesion strength than hydrogel composites, while their bulk fracture strength and energy were significantly lower. Alginate has a higher affinity with the cartilage surface, probably through weak hydrogen bonds, which allows a better stress transfer to the bulk material.

4.3.5 Biological properties - cytocompatibility

In order to simplify the assessment of biological properties, only composite double network *CDN* hydrogels were evaluated because it contains all components of the four systems. Direct contact test and proliferation study described in section 3.4.11 on p. 57 were performed. The results are shown in Fig. 4.11.

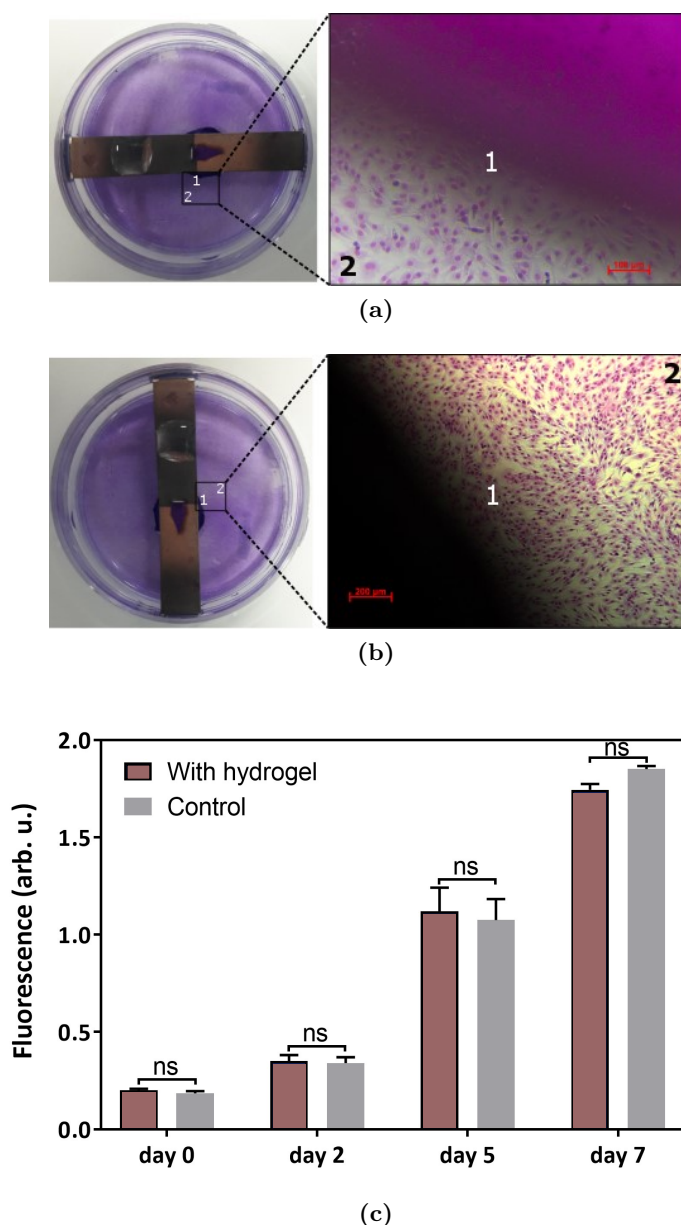


Figure 4.11: Cytocompatibility of composite double network hydrogels in the *swollen state* (a,b) Direct contact test showing the distribution of cells, died with Giemsa, around the hydrogel. The cells' morphology in contact with the hydrogel samples demonstrates was similar to areas far from the hydrogel. (c) Cells proliferation study with/without the presence of the *CDN* hydrogel showing no significant difference between the samples with hydrogel and control group over seven days. The maximum fluorescence on day 7, corresponding to the maximum proliferation possible in the used wells.

After being stained with Giemsa, the cells' distribution around the hydrogel was observed with the direct contact test. The cells' morphology in contact with the hydrogel samples was similar to cells far from the hydrogel, which suggests that the hydrogel doesn't significantly alter the cells' viability. Indeed, the study of cell proliferation showed that there were no significant differences between the hydrogel and the control group over seven days. It confirmed that the hydrogel does not significantly affect cell proliferation.

4.3.6 Long-term reliability

Degradation

Since degradation assessments are time-consuming experiments, the degradation behavior was rapidly evaluated according to brief literature research.

20 kDa PEGDM and cellulose fibers are biodurable materials over a long period^[1,254,305], while the ionic bonds between alginate polymer chains degrade in short-term. Nevertheless, the covalent bonds inside the alginate polymer chain take much more time^[56].

High-cycle fatigue tests

Due to the rapid degradation of the alginate-based hydrogel, the long-term fatigue assessment was only performed on neat hydrogels - *N* and hydrogel composites - *C* in their *swollen state*. The maximum applied strain was 20% following the physiological loading conditions of intervertebral discs. Fig. 4.12 presents the cyclic evolution of the elastic modulus. Note that the batch of 20 kDa PEGDM differs from previous experiments, explaining the variations observed in elastic moduli in the *swollen state*.

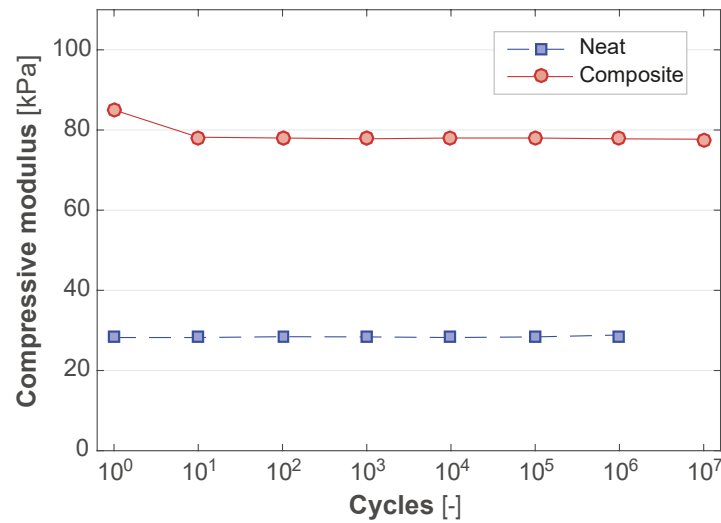


Figure 4.12: Cyclic evolution of the elastic modulus of swollen neat hydrogel and hydrogel composite in high-cycle fatigue.

Hydrogel composites successfully survive 10 million loading cycles. However, during the 10 first cycles, the stiffness of hydrogel composite reduced by almost 10%. In comparison, the representative neat hydrogel was not affected by 1 million loading cycles. Since the softening observed in the first 10 cycles occurred in the hydrogel composite only, it was related to the cellulose fibers. Therefore, a re-arrangement or damage to cellulose fibers may explain this behaviour.

In order to better characterize the softening behavior, low-cycle fatigue was carried out on the same hydrogels.

Low-cycle fatigue

A low-cycle fatigue test was performed on neat hydrogels, and hydrogel composites in their equilibrium *swollen state* at a maximum applied strain of 70%. Fig. 4.13 presents the cyclic evolution of the loading-unloading curve, the elastic modulus, and the dissipation of the energy .

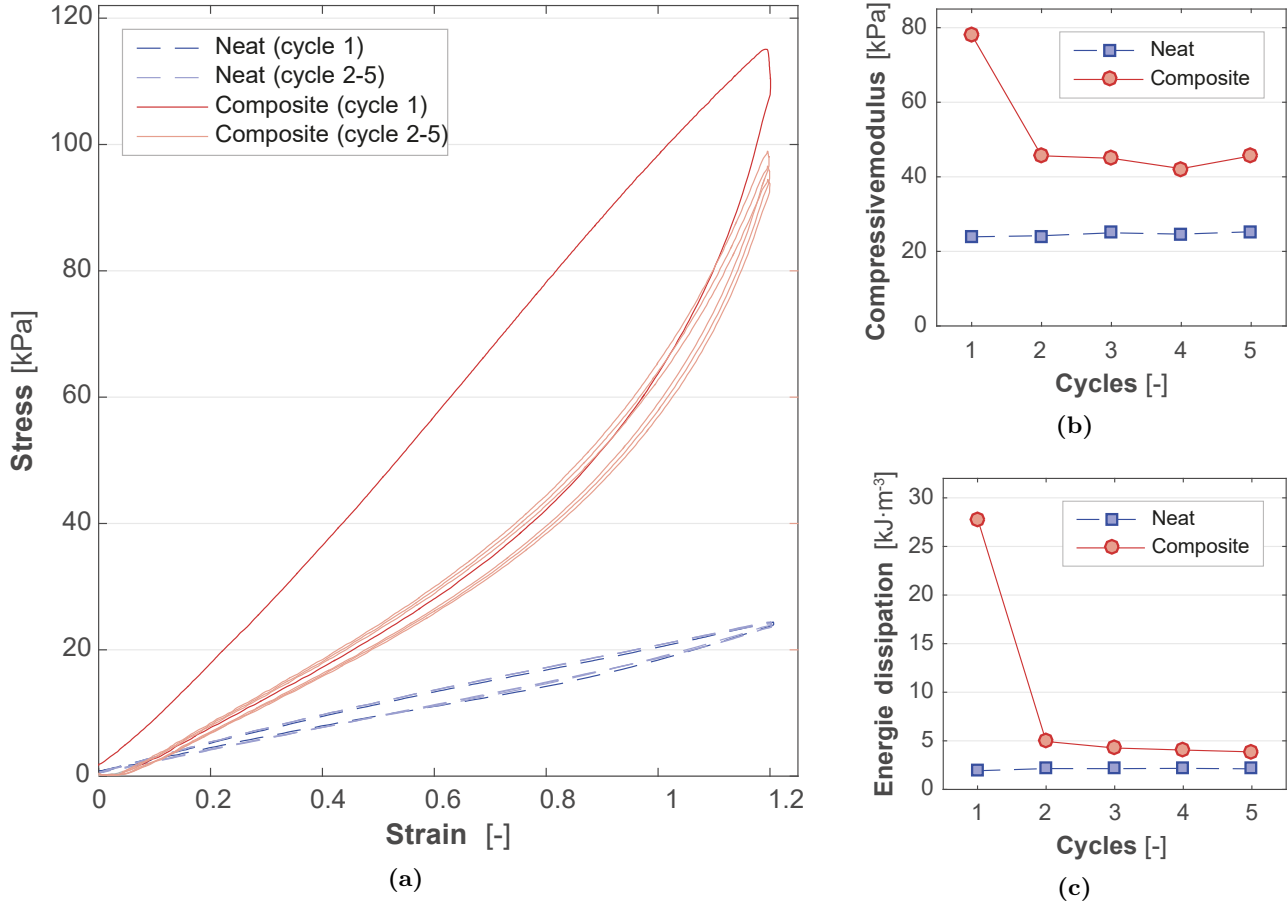


Figure 4.13: (a) Representative loading/unloading stress-strain curves at 70% maximum applied strain for 5 cycles, (b) cyclic evolution of the elastic modulus, and (c) the energy dissipation of swollen neat hydrogel and hydrogel composite.

The neat hydrogel's low-cycle fatigue behavior remained constant, which indicates that no significant structural change occurred inside the material. However, the hydrogel composite's fatigue behavior exhibited a large hysteresis during the first cycle (Fig. 4.13a). The elastic modulus decreased from 80 kPa in the first cycle to 45 kPa for the following cycle, while the dissipated energy was significantly reduced from 28 kJ/m³ to 5 kJ/m³. Nevertheless, both, the elastic modulus and the dissipated energy remained higher than in the neat hydrogel (Fig. 4.13b and 4.13c).

The effect of applied strain on the hydrogels' mechanical response was evaluated by applying successive cycles where the strain was progressively increased from 10% to 70%. Fig. 4.14 shows representative loading-unloading curve.

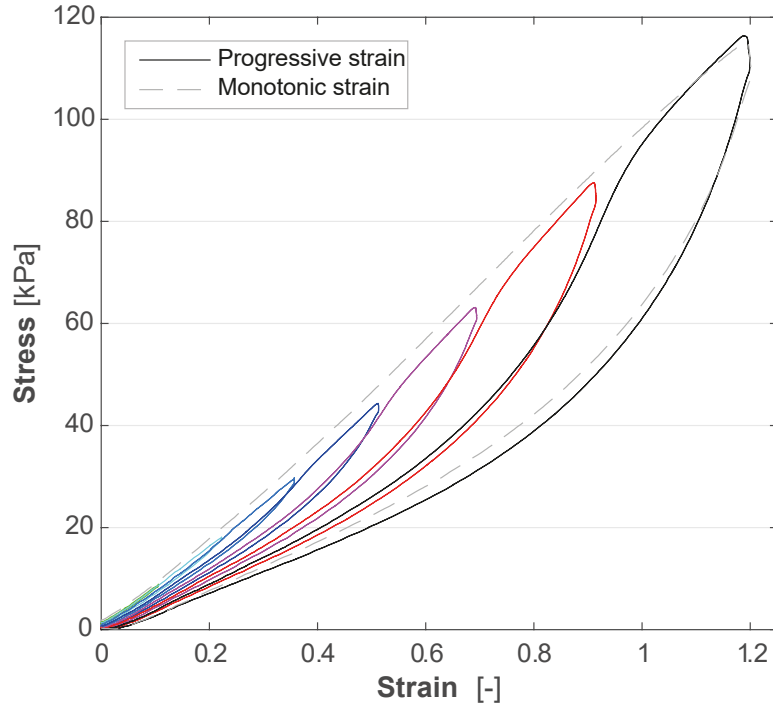


Figure 4.14: Representative loading/unloading stress-strain curves of swollen composite hydrogels at different applied strains.

The material response was affected by the loading history. As shown in Fig. 4.14, after the first cycle, the loading curve followed the same path as the previous unloading curve. When the maximum extension previously applied was exceeded, the material response returned on the same path as the monotonic loading curve. The softening appeared, therefore, only for strain lower or equal to the maximum strain ever applied. Similar behavior was previously seen in elastomers, like in filled rubber^[246] but also in some hydrogels, mostly composite or double network hydrogels (see Table 2.10 on p. 35). This phenomenon is usually referred to as the *Mullins effect*, which is not well understood yet. Several phenomena can provoke such behavior as described in section 2.8 in *Chapter 2. State of the art*. Nevertheless, regarding the hydrogels, it is essentially associated with the breaking of bonds^[26]. In the studied hydrogel composite, the behavior similar to the *Mullins effect* might be issued from the gradual disintegration of the NFC network, especially the breaking of the hydrogen bonds between the NFC.

The softening behavior was further investigated in the following *Chapter 5. Fracture properties of preloaded hydrogel composites*, in order to understand better and predict how it affects the long-term reliability of hydrogel composites.

4.4 Conclusions

This chapter highlighted the strengths and weaknesses of single and double network structures and their composites. Those experiments included the evaluation of the material's processing ease, biological, physical, mechanical, and adhesion properties as well as of long-term reliability.

Four different hydrogel structures based on poly(ethylene glycol) dimethacrylate were tested: neat, composites, double network, and composite double network hydrogels. Composites were reinforced with nano-fibrillated cellulose fibers, while the second network was alginate. Adding cellulose fibers and/or a second network significantly improved mechanical and adhesion properties in the *as-prepared state*. Nevertheless, the secondary alginate network lost all profits in the *swollen state*. Compared to neat hydrogels, double network hydrogels had at least 30% higher swelling ratios and 25% lower elastic moduli. In contrast, adding 0.5 wt.% cellulose fibers to neat hydrogels could reduce swelling by more than 30% without seriously affecting the processability and long-term reliability.

High-cycles fatigue tests revealed that hydrogel composites successfully survive 10 million loading cycles at 20% applied strain. However, after the first loading cycle, its stiffness was reduced by almost 10%. The behavior is similar to the *Mullins effect*. To better understand and predict how cyclic loading affects energy dissipation and long-term resistance in hydrogel composites, the softening behavior is further studied in *Chapter 5. Fracture properties of preloaded hydrogel composites*.

Moreover, hydrogel composites still have large swelling ratios and quite low compressive modulus, which are inappropriate for applications in an unconfined environment. An extensive parametric study on the composition and structure of hydrogels will be performed in *Chapter 6. Hybrid granular hydrogels* for elaborating complete property charts summarizing mechanical, swelling, and rheological properties.

Chapter 5

Fracture properties of preloaded hydrogel composites

How cyclic loading affects mechanical properties and microstructures?

The fracture properties of hydrogels, which present similar characteristics to the *Mullins effect*, are expected to decrease under repeated cyclic loading. Therefore, we assessed how cyclic loading affects the fracture behavior, the distribution of strain fields, and the microstructure of hydrogel composites reinforced with nano-fibrillated cellulose fibers. Surprisingly, we observed that preloading before creating a notch in the hydrogel composite increased the fracture strength of pre-notched samples, while the corresponding fracture energy decreased. A digital image correlation analysis was performed at the macro- and microscopic scale to understand this behavior and obtain local information on the strain field. Additionally, the morphology of cellulose fibers was directly observed through fluorescence confocal microscopy before and after cyclic loading at different maximal applied strains. Microscopy results showed that cyclic loadings re-arranged the fiber network and relaxed local residual stresses in the hydrogel composite. The re-arrangement of the fiber network decreased the overall elastic modulus and correspondingly the fracture energy. However, it helped the hydrogel composite to accommodate larger strains before the crack started to propagate, which subsequently improved the pre-notched sample's fracture strength.

Keywords: hydrogel composite, nano-fibrillated cellulose fibers, Mullins effect, fracture mechanics, digital image correlation, confocal microscopy.

Publication: "Cyclic loading of a cellulose/hydrogel composite increases its fracture strength", Extreme Mechanics Letters (2018)^[306]

5.1 Introduction

In previous *Chapter 4. Single and double network hydrogels and their composites*, poly(ethylene glycol) dimethacrylate (PEGDM) hydrogel reinforced with nano-fibrillated cellulose (NFC) fibers showed promising properties to be used as a permanent load-bearing implants^[1]. In particular, the long-term reliability of the hydrogel composite was evaluated under high-cyclic fatigue loading. Specifically, 10 million compression cycles at 20% strain were applied^[31]. As for other tough hydrogels based on double network structures^[27,199], a softening behavior appeared after the first loading cycle^[31,76], highlighted by an initial decrease of 10% of the elastic modulus. Furthermore, low-cycle fatigue tests showed that the softening appeared for strain lower or equal to the maximum strain ever applied (see section 4.3.6). This phenomenon is usually referred to as the *Mullins effect*. The softening behavior is mostly related to the breaking of bonds or the re-arrangement of the material microstructure^[27,246,307]. Those changes in the material may also affect other properties, such as the swelling ratio^[31] or the toughness^[308]. However, only a few studies evaluated the evolution of different mechanical or physical properties of hydrogels under cyclic loading^[309]. Recently, fatigue fracture were performed on simple^[310], double network^[310,311] and self-recovery hydrogels^[312]. The test concluded that the fracture behavior of the tested hydrogels is sensitive to fatigue loading. In particular, the fracture energy of double network hydrogel had progressively reduced after each loading cycle.

Since PEGDM-cellulose hydrogel composite shows similar softening behavior to double network hydrogels, we expected that its fracture properties would diminish as well after being cyclically loaded. To clarify this and understand the governing phenomena behind the observed Mullins effect, we evaluated the fracture properties of PEGDM-cellulose hydrogel composite in this work. In particular, we investigated how cyclic loading affects the fracture strength and energy of pre-notched samples, the distribution of the strain fields, and the hydrogel's microstructure. Fig. 5.1 illustrated the structure of neat hydrogels and hydrogel composites.

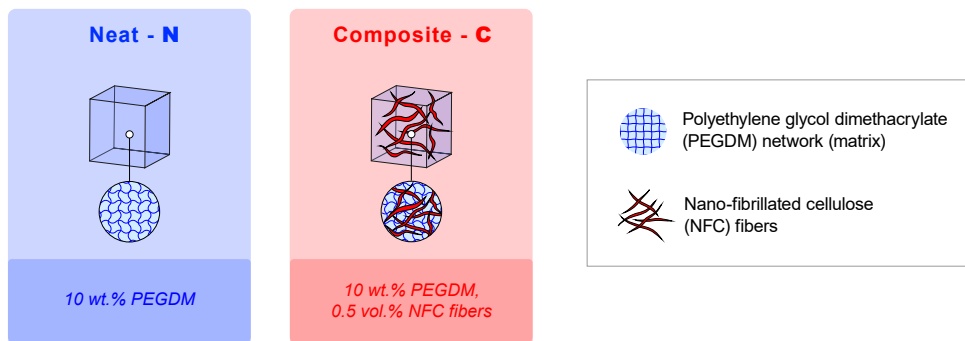


Figure 5.1: Structures and compositions of neat hydrogel and hydrogel composite.

Fig. 5.2 presents the multi-scale analysis adopted for the study. The swollen hydrogel composites were either virgin or cyclically preloaded before performing a fracture test (Fig. 5.2a). The hydrogels' overall fracture properties were then measured with a single edge notch test (Fig. 5.2e). In paral-

lateral, digital image correlation (DIC) analysis was performed at the macro- and microscopic level (Fig. 5.2d) for obtaining local information about the distribution of strain fields. Finally, the morphology of the NFC network in the hydrogel composites was observed after different preloading conditions with fluorescence confocal microscopy (Fig. 5.2b).

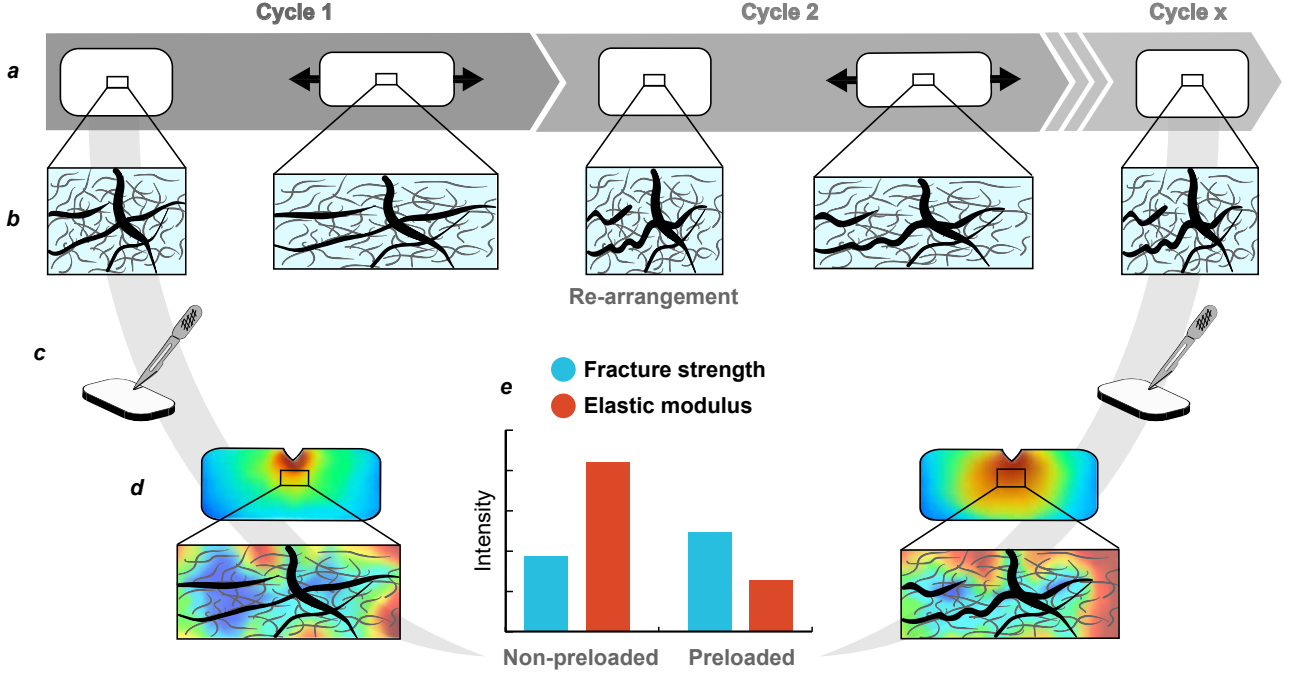


Figure 5.2: Effect of cyclic preloading on the distribution of strain fields, the fracture strength of pre-notched samples, the microstructure and the elastic modulus of hydrogel composite: (a) cyclic tensile preloading on unnotched hydrogel composite, (b) evolution of the microstructure after cyclic loading obtained with fluorescence confocal microscopy, (c) initiating a crack with a scalpel on non-preloaded or preloaded samples, (d) distribution of strain fields around the crack tips measured at the macroscopic and microscopic level, and (e) comparison of representative overall fracture strengths and elastic moduli of the non-preloaded and the preloaded hydrogel composite.

5.2 Materials and methods

5.2.1 Materials

20 kDa Poly(ethylene glycol) dimethacrylate (PEGDM) was purchased by Polysciences (ref. 25406-25, Germany). Nano-fibrillated cellulose (NFC) from bleached softwood pulp (Elemental Chlorine Free (ECF), Zellstoff Stendal, Germany) were prepared as reported in^[23]. SEM analysis shows that the NFC measure a few micrometers with diameters in the range of 2-100 nm^[141].

5.2.2 Hydrogel synthesis

Hydrogels were synthesized according to an established protocol^[23], which is illustrated in Fig. 3.4 and 3.5 on p. 43. The neat hydrogel corresponds to 10 wt.% PEGDM hydrogel without NFC, while hydrogel composites are composed of 10 wt.% PEGDM with 0.5 vol.% NFC. All samples were tested

in *swollen state*. The geometries of the molds are shown in Fig. 3.11 on p.45. The molds for single edge notch tests are rectangular with the size of 30 mm x 15 mm x 2 mm (length x width x depth), while the dog-bone molds used for simple tensile test measures 11 mm x 5 mm x 2 mm.

5.2.3 Cyclic tensile loading

Cyclic tensile loading was performed on swollen neat hydrogel and hydrogel composite with the tensile machine (5 kN Zwicky equipped with a 100 N load cell, Zwick Roell, Germany) shown in Fig. 3.14 on p. 51 at a constant strain rate of 0.023 1/s. The strain applied on dog-bone samples, started at 30% and was progressively increased by 20% up to 110%.

The calibration for tensile samples was calibrated via digital image correlation (Fig. 3.16a). The strain calculated by the displacement ratio of the grip-to-grip distance was compared with the strain measure on the straight part of the dog-bone sample. Since the two strains evolve linearly (Fig. 3.16b), a correction ratio (R_{corr}) was determined with the equation (3.6).

5.2.4 Preloading of hydrogels

Cyclic tensile loading was performed on swollen neat hydrogel and hydrogel composite with the tensile machine Zwicky at a constant strain rate of 0.023 1/s. Rectangular samples underwent five cycles at different maximal applied strains: 30%, 50%, or 70%.

5.2.5 Tensile loading under optical microscope

Dog-bone samples were mounted on a miniature tensile stage (Linkam TST350) and placed under an optical microscope (Olympus BX60). Five cycles were performed on hydrogels at 0.5 mm/s up to 50% applied strain. At each increase of 2% of applied strain, individual images of the deformed hydrogel surfaces were taken with a resolution of 0.67 $\mu\text{m}/\text{pixel}$.

5.2.6 Single edge notch test

A single edge notch test was performed on rectangular swollen preloaded and non-preloaded neat hydrogel and hydrogel composite with the tensile machine Zwicky. Preloaded samples underwent five tensile cycles at a constant strain rate of 0.023 1/s, which corresponds to a displacement rate of 0.5 mm/s, up to different applied strains (30%, 50%, and 70%) before a 3 mm crack was cut with a scalpel in the hydrogels (Fig. 5.2c). The samples were then loaded at 0.5 mm/s until rupture. In parallel, the test was recorded with a camera videoXtens (Zwick/Roell) at 25 fps with a resolution of 0.1 mm/pixel. The images were used to determine and calculate the variation of the cross-sectional area during the test, providing true stress.

The maximum stress of the true stress-strain curve defines the fracture strength of notched samples. The highlighted area in Fig. 3.17 represents the crack initiation energy density under the stress-strain

curve until the first peak. Finally, the fracture energy was determined when the critical energy release rate G_c was reached. G_c was characterized by the equation (3.7)^[17].

5.2.7 Digital image correlation analysis

Graphit 33 (Kontakt Chemie, Germany) was sprayed on the surface of notched samples to make a fine, randomly, and homogenously distributed speckles pattern. In order to obtain a finer speckles pattern for DIC at the microscopic level, a drop of Graphit 33 dissolved in isopropanol was deposited on the surface of dog-bone samples and wipe a few seconds later with a lens cleaning tissue. Images of the resulting speckles pattern are shown in Fig. 3.18a on p. 54. DIC analysis was then performed with the open-source software ncorr V1.2 on Matlab R2016b. The reference images were taken when the applied load reached 0.04 N.

5.2.8 Fluorescence confocal microscopy

The morphology of the NFC fibers was observed in their native environment with an inverted fluorescent confocal microscope (Zeiss LSM 700) equipped with a 20x lens and a laser of 405 nm. The hydrogel composite was placed for at least 6 hours in 0.2 g/l Calcofluor White stain (Sigma-Aldrich, Buchs, CH) and 4 vol.% of 10 wt.% potassium hydroxide to dye the NFC fibers.

5.3 Results and discussion

5.3.1 Cyclic tensile loading and Mullins effect

Fig. 5.3a and Fig. 5.3b show representative cyclic tensile loadings on dog-bone samples of neat hydrogel and hydrogel composites. The applied strain started at 30% and was progressively increased by 20% after each 5th cycle until rupture of the hydrogel.

The elastic tensile modulus was determined by linear regression between 10% and 15% applied strains. Adding 0.5 wt.% of NFC fibers to the PEGDM matrix significantly increases the elastic modulus from 19 ± 0.6 kPa to 118 ± 3.6 kPa. However, as shown in previous *Chapter 4. Single and double network hydrogels and their composites*, the hydrogel composite becomes softer after the first loading cycle before to remain constant until the maximum strain previously applied is exceeded. In contrast, the behavior of neat hydrogel did not change under cyclic loading. This behavior was related to the *Mullins effect*. Nevertheless, we observed that at a constant applied strain of 20 %, the hydrogel composites had stabilized its elastic modulus after the first cycle and withstand 10 million loading cycles. Since neat hydrogel shows no difference, the softening and dissipation of energy is probably originated from the disintegration of hydrogen bonds of the NFC network (bonds between cellulose-cellulose or between PEGDM-cellulose)^[23], from interfacial friction, and the deformation of NFC fibers.

To better understand the fracture behavior, single notch edge tests were performed on neat hydrogels and hydrogel composites, which were either preloaded or not.

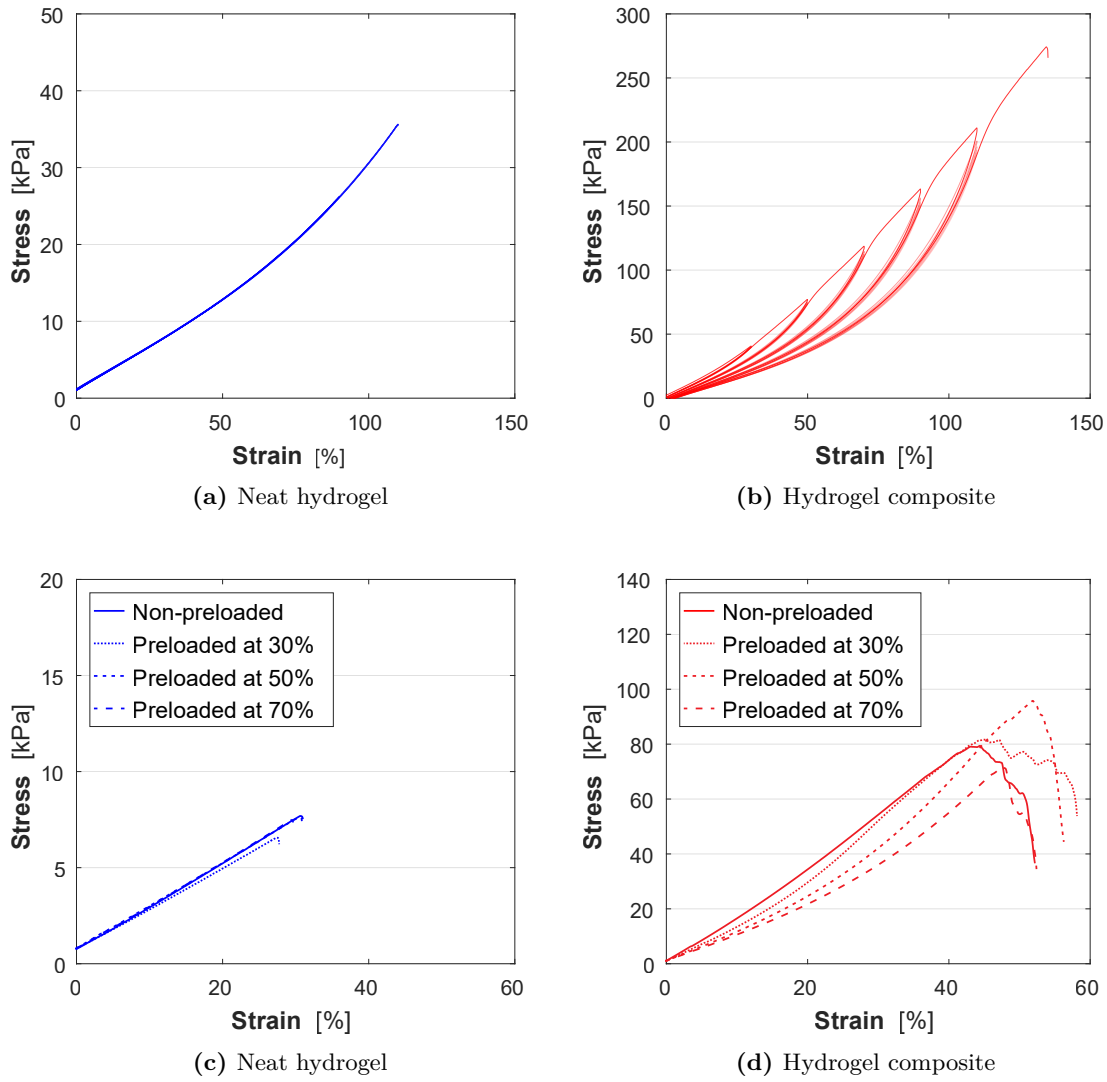


Figure 5.3: Representative cyclic tensile loadings of swollen (a) neat hydrogels and (b) hydrogel composites: the hydrogel composite shows similar softening behavior to the Mullins effect. Single edge notch test of non-preloaded and preloaded (c) neat hydrogels and (d) hydrogel composites: cyclic loading affected hydrogel composite fracture properties, whereas the neat hydrogel showed no difference.

5.3.2 Single edge notch test on hydrogels with and without preloading

Since most softening happens at the first cycle, rectangular hydrogel samples were preloaded five times before creating a notch in the material and performing the single edge notch test. Fig. 5.3c and Fig. 5.3d show the corresponding fracture behavior of non-preloaded or preloaded neat hydrogel and hydrogel composites.

With or without preloading, the fracture strength of notched samples increases more than ten times with the presence of NFC fibers. The significant improvement is due to (i) the five times larger elastic modulus of the hydrogel composites and most probably to (ii) some fiber bridging. Moreover, the preloading of hydrogel composites clearly affected their fracture behavior, whereas neat hydrogel exposed no difference.

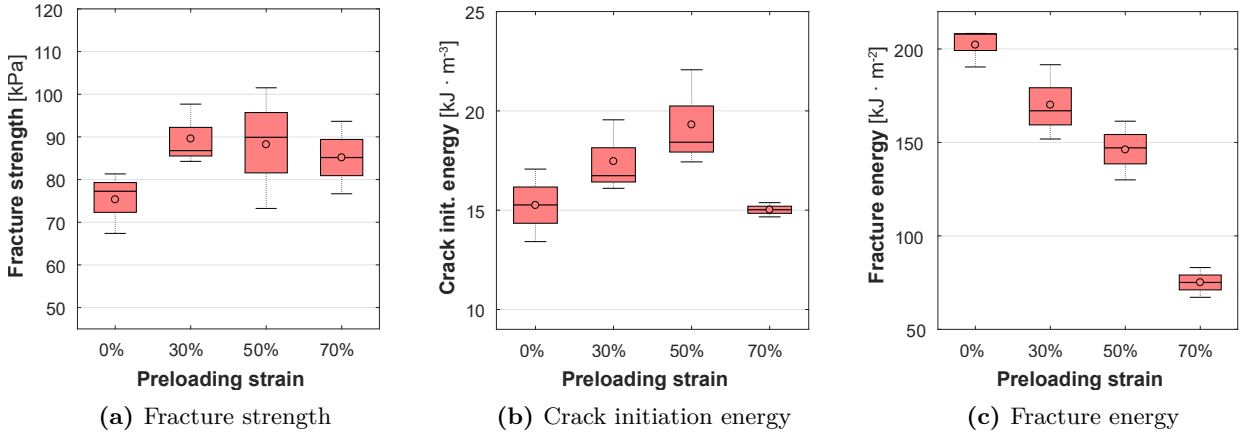


Figure 5.4: (a) Fracture strength, (b) crack initiation energy, and (c) fracture energy of hydrogel composites preloaded at different strains. Up to 50% applied strain, the fracture strengths and crack initiation energies were increasing while the fracture energy was decreasing.

Fig. 5.4 shows the fracture strength of notched samples, the crack initiation energy, and the fracture energy of several non-preloaded and preloaded hydrogel composites at 30%, 50%, and 70% applied strain. Note that the fracture strength is conventionally designed for un-notched samples, while the fracture strength reported in Fig. 5.4a is measured on notched samples. The creation of a crack reduces, therefore, significantly their strength and stretchability^[313,314].

The fracture energy is commonly used to describe the fracture properties of any materials. It represents the amount of strain energy required to propagate a crack in a pre-notched sample. The fracture energy of non-preloaded hydrogels, $223 \pm 10 \text{ J/m}^2$ (Fig. 5.4c), is in the range of conventional hydrogel composites^[315]. Similar to the results obtained on fatigue fracture for double network hydrogels^[310,311], the fracture energy decreased progressively with the applied strain during preloading. The *Mullins effect* anticipated this behavior. Indeed, an increasing softening will reduce the stored energy in an un-notched sample and, consequently, the available fracture energy (see equation (2)). Note that the residual strain after five cycles was consequent. Therefore, the stress-strain curves were recalibrated for the calculation of the fracture energy. However, the fracture strength of non-preloaded samples is around $75 \pm 7 \text{ kPa}$ and surprisingly increases to $90 \pm 7 \text{ kPa}$ when 30% strain is applied as preloading. Similarly, the crack initiation energy, based on notched samples only, increases by 27% when 50% strain is applied as preloading. However, after 50% applied strain, the overall fracture properties start to deteriorate, indicating that the hydrogel composite has undergone some irreversible damage. Several damage phenomena such as fiber bridging, fiber network re-arrangement, and decohesion at interfaces may explain the observed variations of fracture strengths, crack initiation, and fracture energies. In order to investigate these phenomena, a multi-scale approach was adopted. As a first step, digital image correlation (DIC) analysis was performed in parallel to the single notch edge test to obtain local information on the strain field, particularly around the crack tip^[308,316,317].

5.3.3 Distribution of strain fields at macroscopic scale

About 150 images were extracted from the video recorded during the single notch edge test and analyzed with DIC. Fig. 5.5 shows the Eulerian strain field in the loading direction around the crack tip of hydrogel composites when the crack starts to propagate.

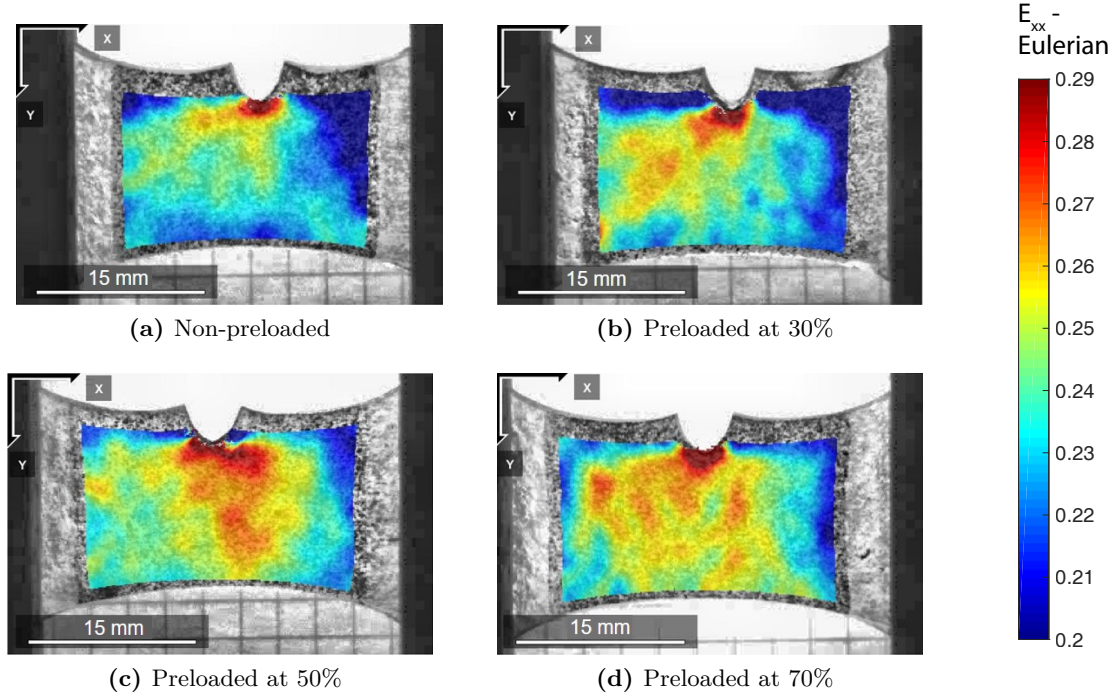


Figure 5.5: Digital image correlation analysis showing the Eulerian strain along the x-axis around the crack tip, which starts to propagate in hydrogel composites preloaded at different strain conditions. The distribution of strain fields became larger after preloading.

5.3.4 Distribution of the strain fields at microscopic scale

Considering the size of the NFC fibers (a few micrometers in length^[141]), the strain field at the microscopic scale may significantly be influenced in every direction. Therefore, the Lagrangian hydrostatic strain field of un-notched composite and neat hydrogels was observed at the microscopic level (Fig. 5.6). Dog-bone samples were fixed on a miniature tensile machine, placed under an optical microscope, and cyclically loaded at 50% strain along the x-axis. In parallel, about 30 pictures were extracted at cycle 1 and 5.

Fig. 5.6a and Fig. 5.6b present the local distribution of strain fields observed in the center of dog-bone hydrogel composites at 25% applied strain in cycle 1 and 5. The strain field of the hydrogel composite is inhomogeneous in comparison to the one of the neat hydrogel. Indeed, the local hydrostatic strain varied from 0.1 to 0.7. The inhomogeneity is probably related to the distribution of NFC fibers. Since NFC fibers are 100'000 time stiffer ($E = 1.7 \text{ GPa}$ ^[141]) than the PEGDM matrix ($E = 20 \pm 0.6 \text{ kPa}$), the fibers, in particular the larger ones, that are oriented in the loading direction (x-axis) limit signif-

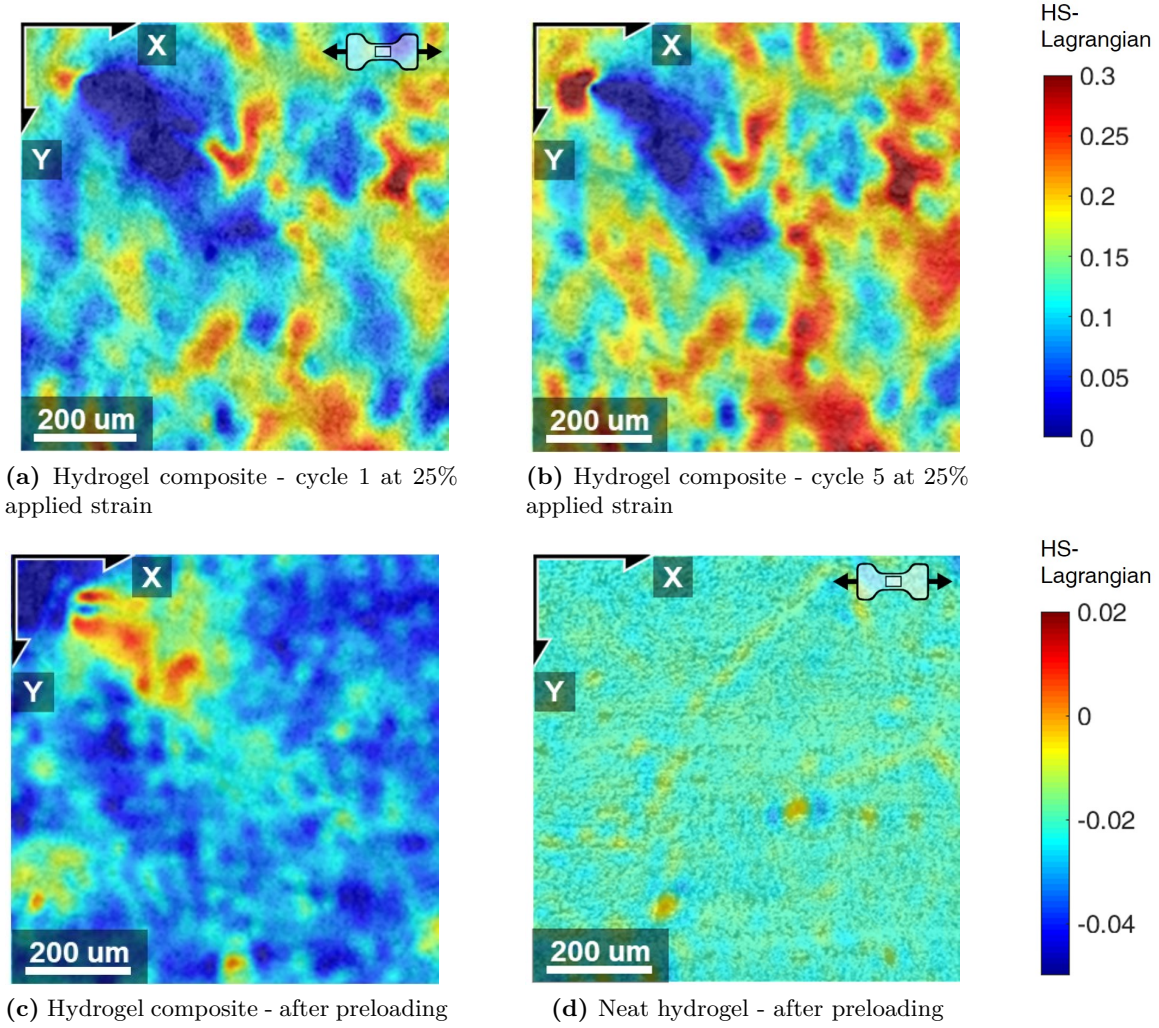


Figure 5.6: Lagrangian hydrostatic strain (HS) field at the hydrogels' microscopic scale under cyclic tensile loading in the x-direction. The strain field of hydrogel composite was inhomogeneous. Compression and tensile regions appeared after preloading, meaning that the hydrogel composite underwent some re-arrangement. After preloading, more regions deform at a larger strain.

icantly local deformations (blue regions) as suggested in Fig. 5.2b and mentioned as well by another study^[318]. The stress around those large fibers is therefore expected to be high.

Moreover, similar to the above macroscopic results, more regions deform at higher strains in preloaded composites. After loading, compression and tensile regions appear in the hydrogel composite, as shown in Fig. 5.6c. Since no difference was observed in the neat hydrogel (Fig. 5.6d), the NFC fiber network probably underwent some re-arrangement after the first loading cycle. Furthermore, a previous study showed that the fiber network is probably pre-strained after swelling because (i) the hydrogel composite swells less than the neat hydrogel and (ii) the swelling ratio of the hydrogel composite increases after mechanical tests^[31]. Therefore, mechanical loading may also relax some internal stresses in the composite. In order to support the obtained results, the morphology of the studied material was observed with fluorescence confocal microscopy.

5.3.5 Direct observation of the NFC morphology

Fig. 5.7a and Fig. 5.7b represent Z-projection and color coded hyperstack images presenting the evolution of the NFC network inside the same hydrogel composite after different preloading conditions: 0%, 30%, 50% and 70% applied strains. The images are taken in the center area of the dog-bone sample. The distance between each frame is 0.75 mm. Each color corresponds to a specific depth and give thus information on the space distribution of the fiber network.

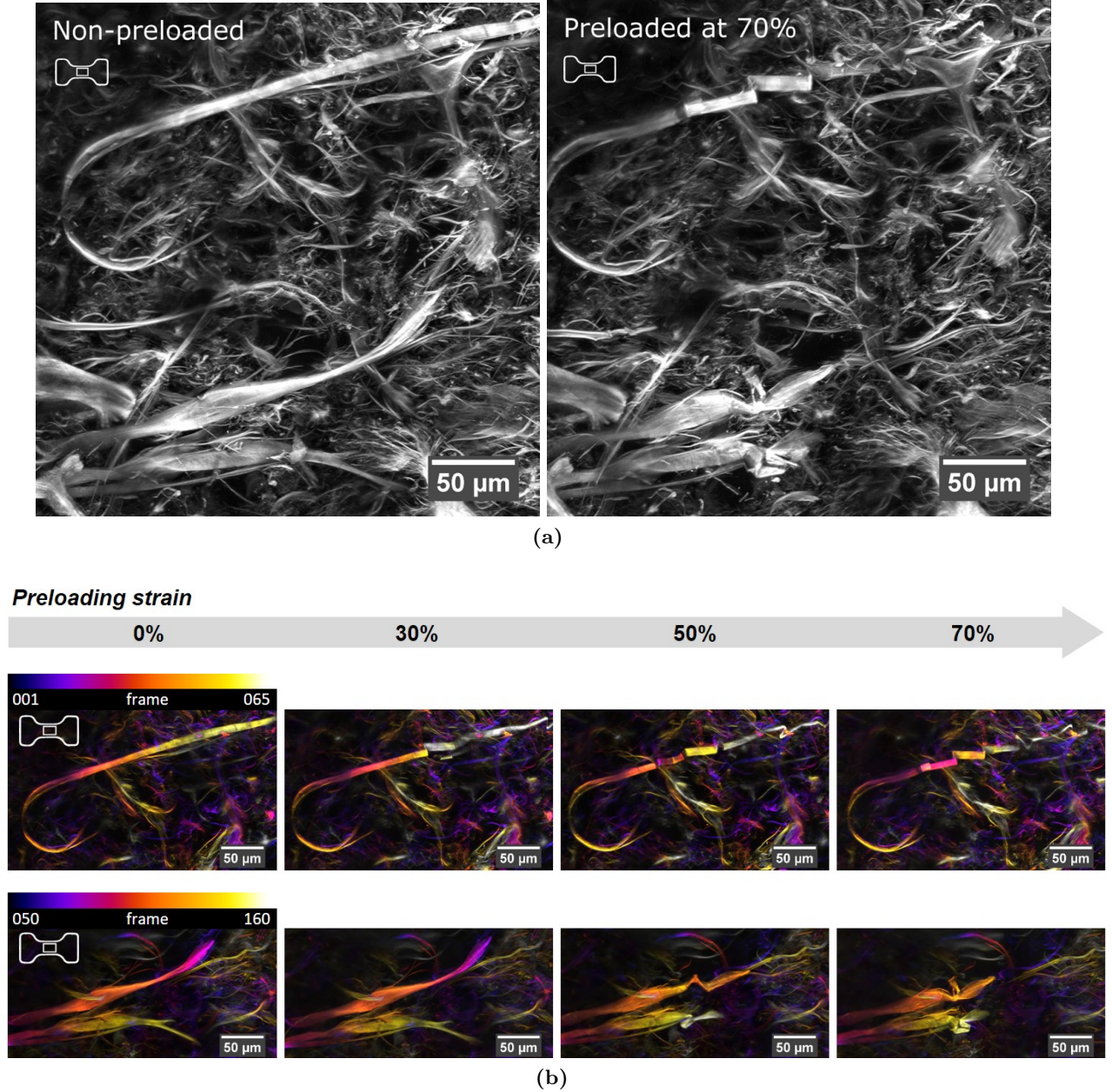


Figure 5.7: (a) Z-projections and (b) color-coded hyperstack images taken with fluorescence confocal microscopy showing the evolution of the NFC microstructure of a swollen hydrogel composite after being preloaded at different applied strains. The loading direction was parallel to the scale bar. Each color corresponds to a specific depth (distance between each frame is 0.75 mm). Local modifications such as displacement and deformation of the fibers network appeared progressively when the preloaded strain was increased.

As shown in Fig. 5.7a and Fig. 4.7, the natural fibers vary in size, morphology, and local space distribution. Consequently, their behavior under deformation is expected to differ, which would explain the observed heterogeneity of the strain fields' distribution at the microscopic level in Fig. 5.6a and Fig. 5.6b. As shown in Fig. 5.7a, the hydrogel composite keeps the global three-dimensional microstructure of the NFC fibers after being cyclically preloaded. However, small expansion and local modifications of the fiber network appear after preloading. The primary damage mechanism is related to the larger fibers in the loading direction that underwent permanent deformations after cyclic loading. Fig. 5.7b shows their gradual changes in morphology. They probably reached either their failure strength or their elastic limit, expressed by the buckling of some NFC fibers. Indeed, after removal of the load, the hydrogel composite returns to its initial position and compress the freshly elongated fibers that consequently deformed out of their initial planes. The observed damage is favored with the applied strain, reducing the elastic modulus and fracture energy. The overall fracture properties start to deteriorate, particularly after 50% preloading strain because of the too high level of damage.

The NFC fibers were subjected to similar deformations around the crack tip. For observing this, a notch was created in a non-preloaded hydrogel. After being dyed with Calcofluor white stain, the notched hydrogel was stretched to propagate the crack a few millimeters. A piece of paper was placed in the crack to keep it slightly open before placing the hydrogel under the confocal microscope. Fig. 5.8 shows the resulting Z-projections.

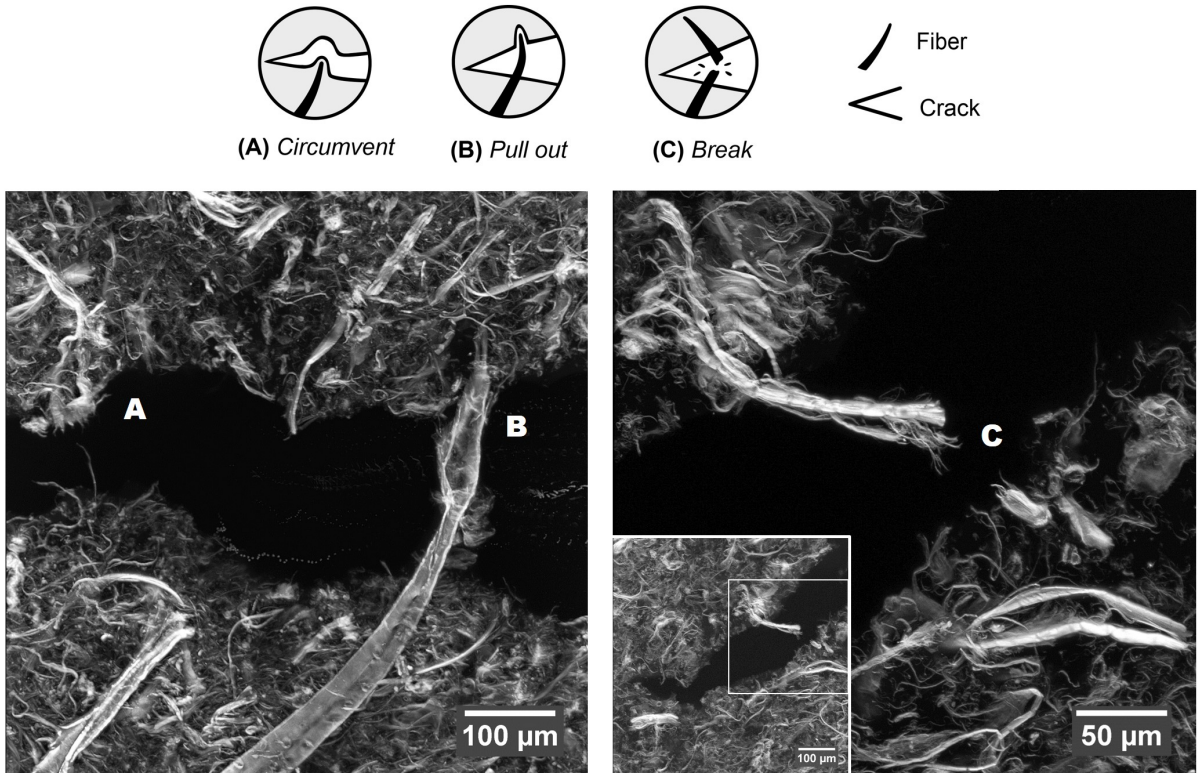


Figure 5.8: Z-projections taken with fluorescence confocal microscopy showing NFC fibers in a hydrogel composite close to a crack surface. The crack circumvented the large NFC fibers (A), pulled out (B), or broke (C) some NFC fibers, which demonstrates the existence of fiber bridging phenomena in the hydrogel composite.

The morphology of fibers close to the crack's surface suggests that the fibers underwent permanent deformation as well when the crack propagated. Moreover, Fig. 5.8 demonstrates that the cracks circumvented large NFC fibers (A), pulled out (B), or broke (C) some NFC fibers. These observations confirm the importance of fibers morphology and bridging phenomena on the toughness of hydrogel composites. Indeed, as seen in Fig. 5.8, fibers larger than 20 μm in diameters certainly provide a strong bridging effect and thus contribute to the composite toughness.

This study shows that cyclic loading re-arranges locally the fiber network (Fig. 5.2a and 5.2b, Fig. 6). During the first loading cycle, some NFC fibers deform plastically or break, which dissipate energy, as shown with the large hysteresis of the stress-strain curve in Fig. 5.3b. In the second loading cycle, the hydrogel dissipates much less energy because the re-arranged and/or broken fibers are relaxed. The altered NFC network reduces, therefore, the available energy for fracture in the hydrogel composite and its overall elastic modulus (Fig. 5.2e, Fig. 5.3b, Fig. 5.4c) but also relaxes some internal stresses. Consequently, the stress concentration around those fibers is diminished and somehow homogenized (Fig. 5.6). As DIC results suggest, the material can deform more easily around these affected regions. During the single edge notch test, the strain is concentrated around the crack tip. In such inhomogeneous strain field conditions, the local energy is related to the strain level. Thus, the energy around the crack tip is higher than elsewhere in the material. DIC results showed that the strain distribution around the crack tip becomes larger after cyclic loading. Since more regions in the preloaded material are deformed at higher strains, more energy can be absorbed and distributed in the material strain before the crack starts to propagate (Fig. 5.2d, Fig. 5.5, Fig. 5.6). Therefore, up to the preloading strain level where damage starts to dominate (*i.e.* above 50% applied strain), preloading increases the total crack initiation energy (Fig. 5.4b) and the fracture strength (Fig. 5.2e, Fig. 5.4a) of notched samples in contrast to the fracture energy.

5.4 Conclusions

The presence of NFC fibers in the PEGDM matrix significantly increased the stiffness and the toughness of the hydrogels. However, similar to the *Mullins effect*, the hydrogel composite became softer after the first loading cycle before reaching a constant mechanical behavior. Preloading the hydrogel composite up to 50% applied strain surprisingly increased the fracture strength of notched samples and the crack initiation energy by more than 20%, while the corresponding fracture energy decreased.

The results on fibers' visualization showed that cyclic preloading re-arranged the fiber network, relaxing and reducing residual stresses in the hydrogel composite. The re-arrangement and deformation of the nano-fibrillated cellulose fibers decreased somehow the macroscopic elastic modulus and correspondingly the fracture energy. However, it helped the hydrogel composite accommodate larger strains before the crack started to propagate, which subsequently improved the fracture strength and the total crack initiation energy of the pre-notched sample. Above 50% applied preloading strain, relaxation, and re-arrangement of the fibers network started to be dominated by damage and failure.

In summary, the study showed that cyclic loading on hydrogel composites did not deteriorate the mechanical properties. Small preloading strain might even be beneficial for reducing residual stresses. Hydrogel composite remains a suitable candidate for load-bearing implants, despite their relatively large swelling ratios and low stiffnesses. Therefore, the next step is to understand better the relationships between mechanical, swelling, and rheological properties.

Chapter 6

Hybrid granular hydrogels

How to decouple hydrogel properties with microgels and cellulose fibers?

Developing hydrogels with optimal properties for specific applications is challenging as most of these properties, such as toughness, stiffness, swelling, or deformability, are interrelated. The improvement of one property usually comes at the cost of another. To decouple the interdependence between these properties and extend the range of material properties for hydrogels, we propose a strategy that combines composite and microgels approaches. The study focused first on tailoring the swelling performance of hydrogels while minimally affecting other properties. The underlying principle was to partially substitute some hydrogels with pre-swollen microgels composed of the same materials. Swelling reductions up to 45% were obtained. Those granular hydrogels were then reinforced with nano-fibrillated cellulose fibers obtaining hybrid granular materials to improve their toughness and further reduce their initial swelling. Four different structures of neat, granular, and composite hydrogels, including 63 different hydrogel compositions based on 20 kDa poly(ethylene glycol) dimethacrylate showed that the swelling ratio could be tailored without significantly affecting elastic modulus and deformation performance. The results explain the role of the PEGDM precursors on the swelling of the microgels as well as the influence of the microgel and fiber contents on the final properties. Moreover, the precursors of hydrogels with similar mechanical or swelling performance were injectable with a wide range of complex viscosities from 0.1 Pa · s to over 1000 Pa · s offering new opportunities for applications in confined as well as in unconfined environments.

Keywords: hybrid granular hydrogel, microgels, nano-fibrillated cellulose fibers, swelling, elastic modulus, processability.

Publication: "Hybrid granular hydrogels: combining composites and microgels for extended ranges of material properties", Soft Matter (2020) ^[319]

6.1 Introduction

The development of hydrogels with optimal properties is challenging as most of these properties, such as toughness, stiffness, fatigue resistance, swelling, or processing ease, are interrelated. The improvement of one property usually comes at the cost of another as observed in many hydrogel structures including neat, double network, or composite hydrogels^[18,19,27,31,199,200]. In particular, controlling the swelling performance while minimally affecting other properties, such as stiffness or deformation performance, is challenging. Different strategies have been investigated to tailor swelling. Changing the crosslinking type, crosslinking density, the polymer content, the polymer chain length, or the polymer's hydrophilicity are commonly used methods. These approaches are efficient but often at the expense of other properties such as biocompatibility, stiffness, toughness, or processability^[23–25]. Recent methods employ crosslinking centers in the hydrogel, such as functionalized core-shell microgels or self-assembled micelles, to bridge the polymer chains^[197,209,210]. For example, Zhang et al. reported that their micelle-crosslinked hyaluronate hydrogel could be compressed up to 75% applied strain with an elastic modulus of 310 kPa and a swelling ratio of 9% only^[210]. Alternatively, influencing the polymer chain's maximum strand extension, such as incorporating rigid particles or fibers, may control swelling^[28]. Moreover, apart from improved mechanical properties, the addition of reinforcement increases the dissipation mechanisms such as friction with the matrix or chemical interactions^[7,28,115,116].

In parallel, the viscosity of hydrogel precursors must be tailored according to the application. For example, low precursors' viscosity would be suitable for confined applications, such as replacing nucleus pulposus^[1], while precursors of high viscosity would be ideal for unconfined applications like the replacement of focal cartilage defects without the use of a membrane^[320] or to 3D printed complex unconfined structures^[7].

Similar to swelling of a hydrogel, hydrogel precursor's viscosity can be controlled by changing the polymer content, chain length, or adding fillers or reinforcements^[321]. Recently, granular hydrogels have gained a lot of attention because of their particular microstructure of contacting microgels^[32–39]. Indeed, the precursor composed of jammed microgels is highly shear-thinning, which is ideal for creating structures with inherent stability in unconfined applications or 3D printing^[37–39]. Additionally, open microporosity emerges between the microgels, which promotes the transport of nutriment or cells. To our knowledge, other hydrogel structures could not achieve this unique combination of properties.

Here we explore a new strategy by combining granular and composite hydrogels to control mechanical and swelling properties as well as the precursor viscosity. Incorporating microgels would significantly increase the viscosity of the precursor and form granular hydrogels (Fig. 6.1)^[37–39]. Moreover, we believe that substituting a part of the neat hydrogel (Fig. 6.1c) with pre-swollen microgels composed of the same material is a simple way to control the swelling of hydrogels. Indeed, once the granular hydrogels (Fig. 6.1d) are immersed in water, mainly the surrounding matrix would swell. The second approach is to add nano-fibrillated cellulose (NFC) fibers in the hydrogels to obtain hydrogel com-

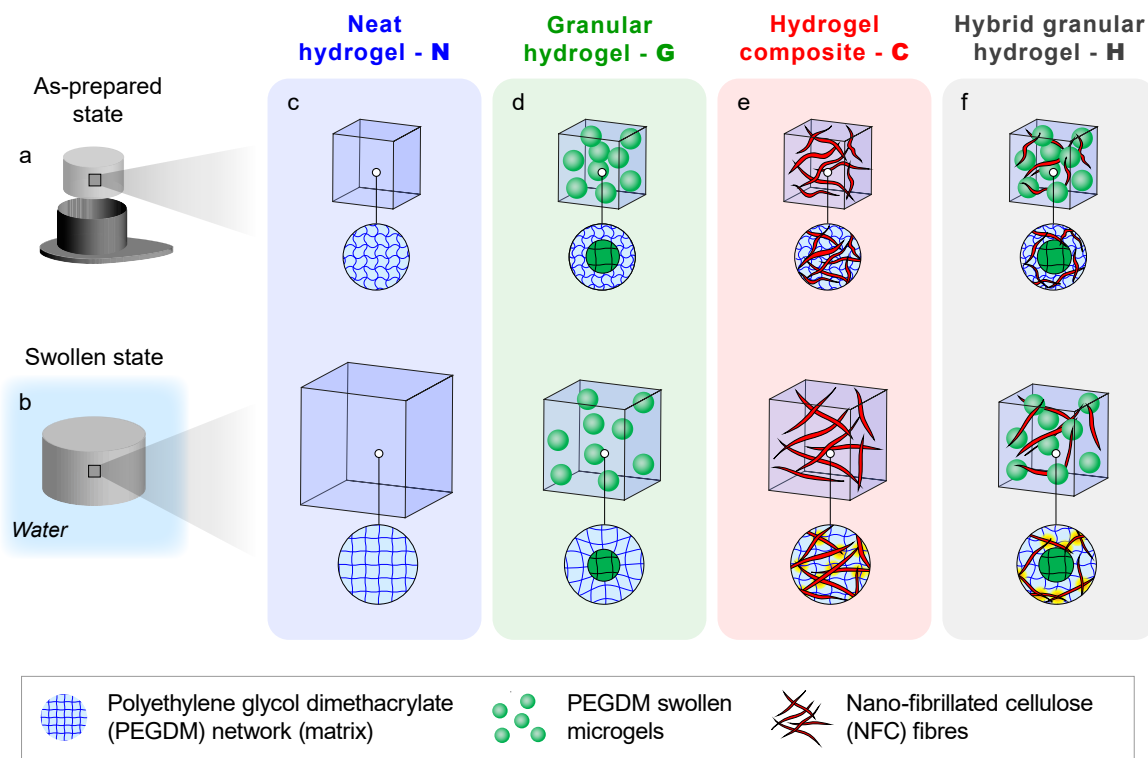


Figure 6.1: Swelling behavior from (a) the as-prepared state to (b) the fully swollen state of four different hydrogel structures: (c) neat hydrogel, (d) granular hydrogel, (e) hydrogel composite and (f) hybrid granular hydrogel.

posites (Fig. 6.1e) with improved toughness and reduced swelling^[23,31,306]. Finally, hybrid granular hydrogels (Fig. 6.1f) combines granular and composite hydrogels. To understand the effect of the microgel and fiber contents on the processing ease, swelling, and mechanical behavior of the four different structures, 63 different hydrogel compositions based on 20 kDa poly(ethylene glycol) dimethacrylate (PEGDM) were studied.

6.2 Materials and methods

6.2.1 Materials

20 kDa poly(ethylene glycol) dimethacrylate (PEGDM) was purchased from Polysciences (ref. 25406-25, Germany). Nano-fibrillated cellulose (NFC) fibers from bleached softwood pulp were provided by Weidmann (WMFC-Standard). The length of most fibers varies between 50-500 μm , while their diameters between 0.1-10 μm . 20 kDa poly(ethylene glycol) (CAS 25322-68-3), mineral oil (CAS 8042-47-5), and span 80 (CAS 1338-43-8) were supplied by Merck. Irgacure 2959 from BASF was used as a photoinitiator.

6.2.2 Synthesis of hydrogels

The synthesis of microgels, initially composed of 10 wt.% PEGDM, is described in Fig. 3.2 on p. 42 in *Chapter 3. Materials and methods*. The particle size distribution of microgels was measured with a digital particle size analyzer (Saturn DigiSizer II, micromeritics). The refractive index was estimated at 1.334 with a tomographic microscope (3D Nanolive Cell Explorer) and the density at 1.01 g/c³. As shown on Fig. 6.2 the size of particles varied from 20-160 μm .

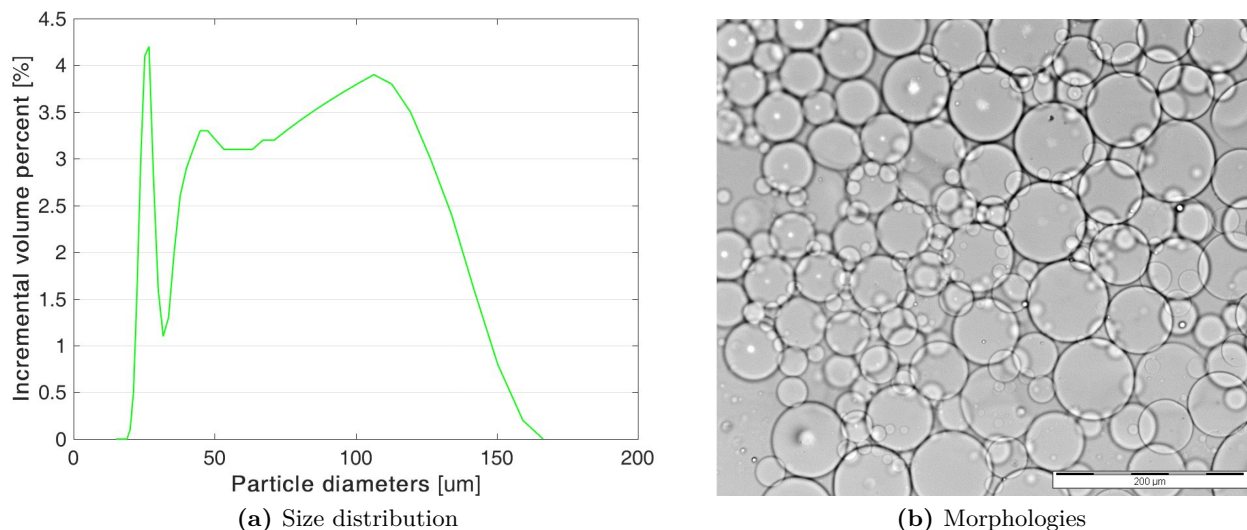


Figure 6.2: (a) The size distribution of microgels measured with a digital particle size analyzer (Saturn DigiSizer II, Micromeritics) and (b) the morphology of microgels observed with an inverted optical microscope (Eclipse Ti2, Nikon).

The full synthesis of the neat hydrogel, hydrogel composite, granular hydrogel, and hybrid granular hydrogels are described and illustrated in Fig. 3.4-3.8. The precursor of neat hydrogels was composed of 7 - 11 wt.% of PEGDM, 0.1 g · ml⁻¹% of Irgacure 2959 and distilled water (Fig. 3.4 on p. 43). The precursor of hydrogel composites had the same PEGDM concentration as the neat hydrogel, where 0.1-0.5 vol.% NFC were added and mixed with an Ultra Turrax (IKA T25 digital, SN 25 10G) at 12'000 RPS for 10 min (Fig. 3.5 on p. 43). Granular hydrogels had a similar composition as neat hydrogels, but their precursors contained pre-swollen microgels composed of the same materials. Therefore, 3-6 wt.% of dried microgels were pre-swollen in PEGDM precursor of different concentration, 2-7 wt.%, in order to get a total PEGDM amount between 7-11 wt.% (Fig. 3.8 on p. 44). Note that the total PEGDM amount adds the weight of dried PEGDM microgels with the PEGDM contained in the precursor. Finally, the precursor of hybrid granular hydrogels had a similar composition than granular hydrogels where 0.1-0.5 vol.% of NFC fibers were added (Fig. 3.8). The precursors, degassed at 20 mbar, were cast in Teflon molds and cover with a microscopic glass before being irradiated for 30 min under UV-light irradiation at a wavelength of 365 nm and an intensity of 5 mW.cm⁻². The gel fraction value of neat hydrogels - 10 wt.% PEGDM was previously measured to be around 94%^[23].

Table summarizes the dimension of casting molds 6.1.

Table 6.1: Sample geometries.

Sample type	Dimension	Tests
Cylinder Fig. 3.10	Ø8mm x 4.5mm	<ul style="list-style-type: none"> • Swelling ratio • Compression test
Dog-bone Fig. 3.11	Cross-section of 5 x 2 mm	Tensile test
Rectangular Fig. 3.11	15 x 30 x 2 mm <i>Crack length of 3 mm</i>	<ul style="list-style-type: none"> • Fracture test • Gradients • Direct contact test

6.2.3 Swelling ratios

The volume of the samples was determined with Archimedes' principle. The samples were immersed in extra pure hexane (99+%, Fisher Chemical) with a density of $\rho = 0.659$ g/l. For reaching the equilibrium swelling state, the hydrogels were immersed in distilled water for at least 24h before measuring the swelling ratio (SR) with equation (3.3) on p. 49. The average swelling ratios and their corresponding standard deviation errors were based on three different samples.

6.2.4 Mechanical properties

Compression and tensile test

Cyclic compression and tensile loadings were performed as previously described in section 3.4.4 on p. 50 on swollen hydrogels with a tensile machine (5 kN Zwicky equipped with a 100 N load cell, Zwick Roell, Germany) presented in Fig. 3.14 on p. 51 at a constant displacement rate of 1 mm/s. For evaluating the real stress, it was considered that no change of volume occurs during loading time. Three samples were tested in *swollen state* under cyclic loading-unloading compression loading. They were five different stages during the tests:

- Stage 1: 3 cycles between 0% and 30% applied strain
- Stage 2: 3 cycles between 0% and 50% applied strain
- Stage 3: 3 cycles between 0% and 70% applied strain
- Stage 4: 3 cycles between 0% and 90% applied strain
- Stage 5: loading up to rupture if the samples could sustain deformation up to 90%

The pre-loading was 0.05 N and 0.02 N for compression and tensile test respectively, The elastic moduli were then determined by linear regression between 10% and 15% applied strain during the first loading cycles. Note that for the tensile test, a virtual extensometer recorded the true strain (VideoXtens, Zwick / Roell).

Single edge notch test

A single edge notch test was performed on rectangular swollen hydrogels with the tensile machine Zwicky. A crack of 3 mm was cut with a scalpel in the hydrogels before testing the sample at a loading rate of 0.5 mm/s until rupture. The fracture energy is defined when a critical energy release rate G_c is reached. G_c was characterized with the equation (3.7) on p. 53^[17].

6.2.5 Digital image correlation analysis

Graphit 33 (Kontakt Chemie, Germany) was sprayed on samples' surface to make a fine, randomly, and homogenously distributed speckles pattern. 3D DIC analysis was then performed with the test equipment illustrated in Fig. 3.19 provided by correlated solutions according to the test parameters presented in Table 3.4. The test equipment incorporates two cameras Grasshopper USB3 (monochrom, 5.0 Mpix, 75 fps), 70 mm lens, the software Vicsnap V.9 for the recording of images, and VIC3D V.8 for the analysis. The reference image was taken when the applied load reached 0.04 N.

6.2.6 Microstructures

The morphology and distribution of the NFC fibers were observed in swollen hydrogels with an inverted fluorescent confocal microscope (Zeiss LSM 700) equipped with a 20x lens and a laser of 405 nm. For enhancing the fluorescence of NFC fibers, hydrogel composites and hybrid granular hydrogels were placed for at least 3 hours in 0.2 g/l Calcofluor White stain (Sigma-Aldrich, Buchs, CH) and 4 vol.% of 10 wt.% potassium hydroxide.

The surface of rupture and the microgels in freeze-dried hydrogels were observed with scanning electron microscopy (Zeiss Gemini) at 3.00 kV.

The surface profile of swollen broken hybrid granular hydrogels was imaged with a 3D laser scanning microscope (VK-X200 Keyence) with a 20x lens.

6.2.7 Rheology

The complex viscosity of hydrogel precursors was evaluated at room temperature with a parallel plate rheometer (TA Instruments AR2000ex). An oscillating strain sweep at 0.5Hz was then applied to the precursors, where the strain starts from 0.1 % to 1000%.

6.2.8 Direct contact test

Hybrid granular hydrogels were sterilized in an incubator at 121°C and 15 lbs before being placed and fixed separately in the middle of cell culture vessels with a diameter of 35 mm. Fibroblasts from the embryo of albino mice were then seeded around the samples (400'000 cells). The following quantities were added to each vessel: 2.5 mL of cell culture medium, 10 vol% Fetal Bovine Serum (FBS), 1 vol% Penicillin Streptomycin (PS), and 1 vol% L-Glutamine. Finally, the samples were incubated at 37 °C in 5% CO₂ for four days. To observe the cells, they were stained with 1 mL methanol for 30 seconds followed by 1 mL diluted Giemsa solution.

6.3 Results and discussions

6.3.1 Swelling and mechanical properties

The swelling behavior and mechanical performance in compression of neat hydrogels, hydrogel composites, granular, and hybrid granular hydrogels are reported in a property chart in Fig. 6.3. Fig. 6.3 also presents the nomenclature, which was adopted to describe all 63 compositions. Note that the fibers were not incorporated in the microgels because the length of a few hundred micrometers of most fibers exceeded the microgels' size, between 20-160 μm . Thus, the microgels' composition was kept the same for all granular compositions at 10 wt.% PEGDM in the *as-prepared state*. Since the initial composition of microgels was the same as the one of the neat hydrogel N₁₀, their mechanical properties are expected to be similar.

Despite 20 kDa PEGDM formed the bulk hydrogels of all structures, each structure covered a distinguishable zone in Fig. 6.3. Neat hydrogels had the largest swelling ratio for similar elastic modulus. Both swelling ratio and compressive modulus increased with the PEGDM content. For a given compressive modulus, granular hydrogels had a lower swelling ratio than neat hydrogels, mostly below 15 kPa. As previously mentioned in *Chapter 4. Single and double network hydrogels and their composites*^[23,306], adding fibers to neat hydrogels reduced swelling and increased the compressive modulus. This effect was promoted by increasing the fiber content from 0.1 to 0.5 of vol.% NFC. The hybrid granular hydrogels revealed similar behavior.

The loading curves in compression of all hydrogels reinforced with NFC fibers, being the hydrogel composites and the hybrid granular hydrogels, had similar characteristics to the *Mullins effect*. As shown in Fig. 6.4, the hydrogel became softer after the first loading cycle. This behavior was previously related to a local rearrangement of the fiber network^[306]. Most samples could resist more than 85% applied strain. Some granular hydrogels' compositions denoted with "***" in Fig. 6.3 broke at lower strain, especially structures with low PEGDM concentrations in the surrounding matrix. Surprisingly, some hybrid granular hydrogels also showed some weakening at a higher cellulose concentration, 0.5 vol.%, probably because of lower fiber dispersion and aggregates. Fig. 6.5 presents such a broken hybrid granular hydrogel and its surface of rupture. Interestingly, broken granular and

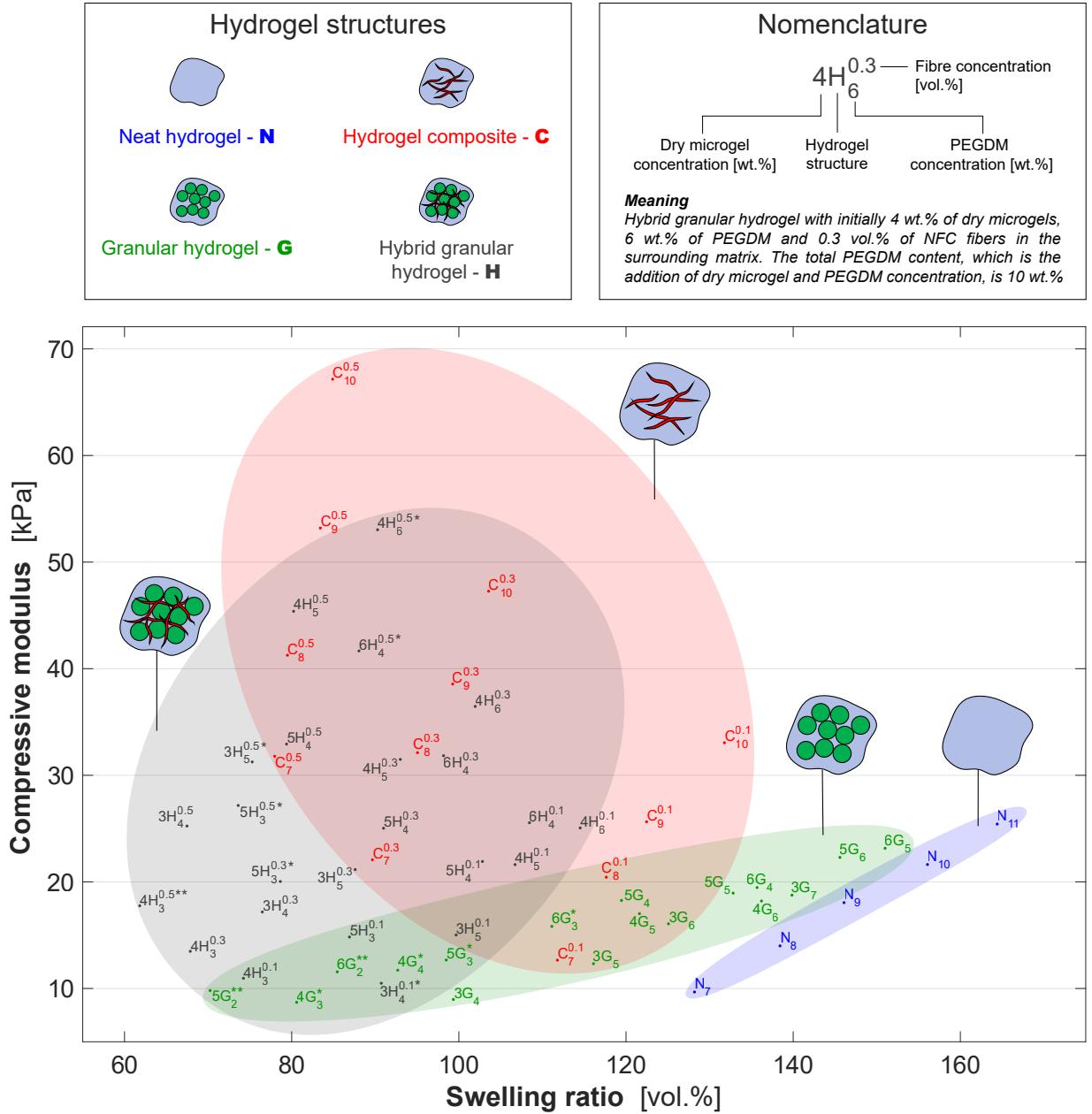


Figure 6.3: Property chart of four different hydrogel structures with various compositions showing the compressive modulus determined between 10% and 15% applied strain in compression as a function of the swelling ratio measured with Archimedes' principle with equation (3.3). Most of the samples could resist more than 85% applied strain. Those denoted with "*" broke between 80-85% applied strain and with "**" between 60-80% applied strain.

composite structures could almost recover their original shape, as shown in Fig. 6.5a, and still sustain compression loading up to 98% applied strain. The rupture surface profile of a swollen hybrid granular hydrogel presented in Fig. 6.5b and 6.5c indicates that the crack surrounded and pulled-out microgels during its propagation. Meaning that the tough microgels did not break and that the interface between the microgels and the matrix was weaker than the bulk hydrogels. The occurrence of such interfacial decohesion is known to increase the toughness in composite materials^[322].

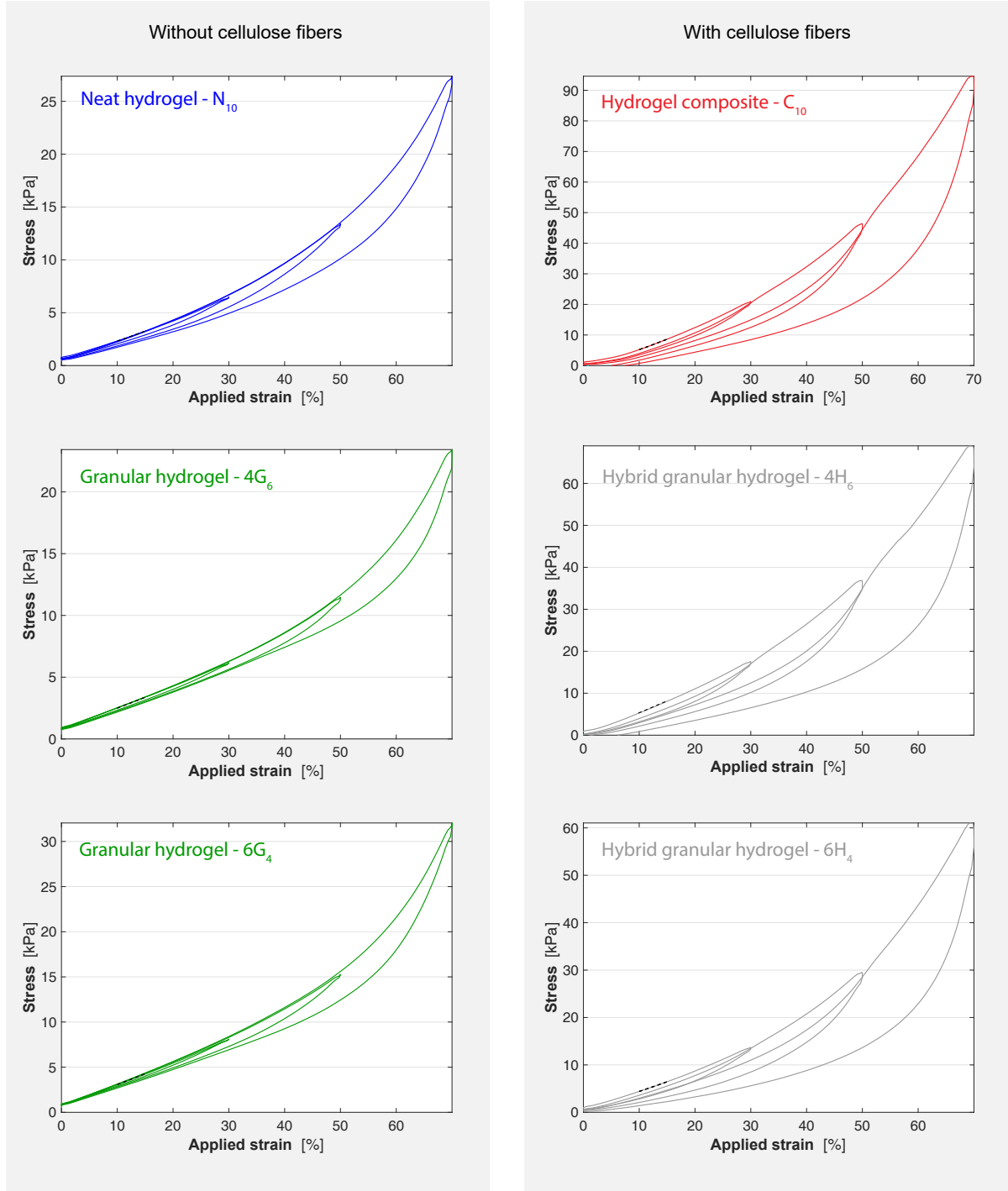


Figure 6.4: Representative cyclic compression loadings of neat, composite, granular, and hybrid granular hydrogels. Neat and granular hydrogels fully recovered, while composite structures showed characteristics similar to the *Mullins effect*: they became softer after the first loading cycles. The dashed line highlights where the elastic modulus was measured.

To complete the mechanical characterization, tensile properties and fracture energy of some compositions were evaluated and presented in Fig. 6.6 and Fig. 6.7. Fig. 6.6 is a property chart that shows the tensile modulus determined between 10% and 15% applied strain as a function of the maximum deformation. Neat hydrogels exhibit the lowest tensile modulus, while hydrogel composites the highest. However, contrary to compressive modulus, granular hydrogels performed better than neat hydrogels

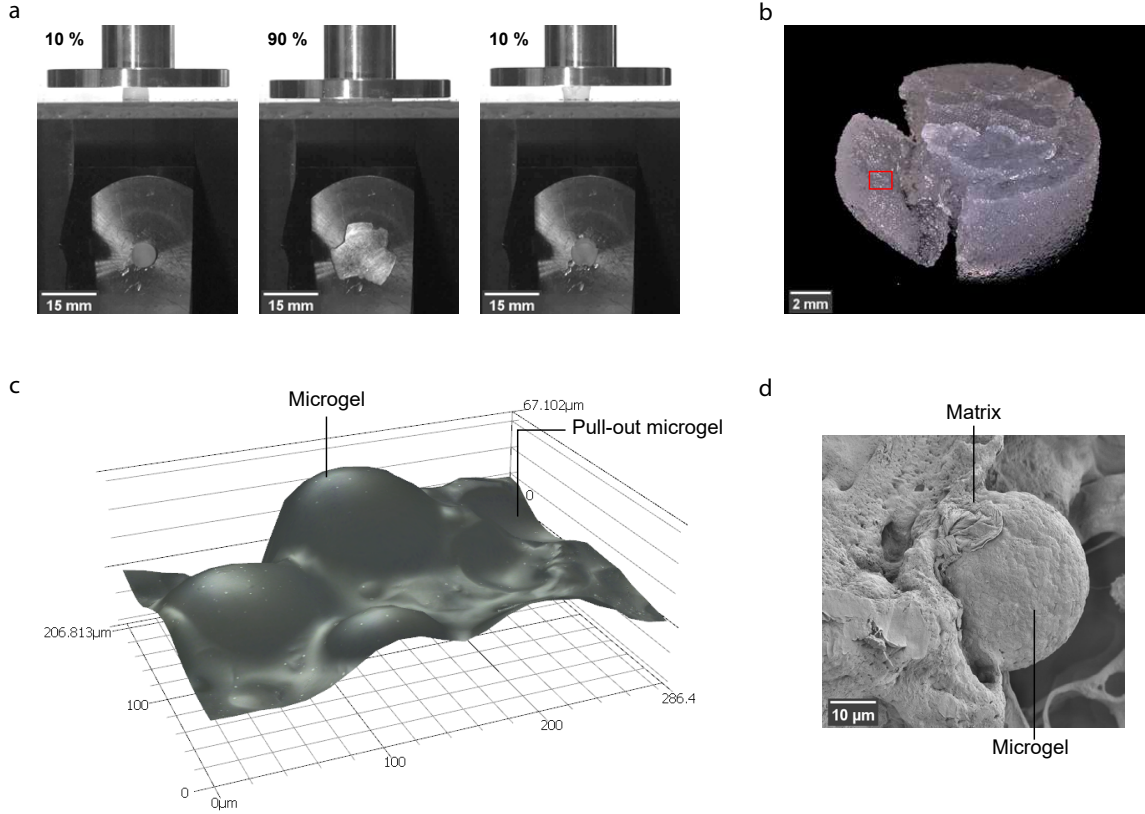


Figure 6.5: Deformation to rupture of a representative broken hybrid granular hydrogel and the failure mechanisms at the surface of rupture. (a) Cyclic compression before, during, and after 90% applied strain. The cross-section was visualized with a mirror at 45° under transparent support. (b) The image was taken with a digital microscope showing the sample $5H_3^{0.5}$ that broke around 83% applied strain in compression. (c) The representative surface profile of a swollen sample was highlighted with a red square in (b), showing how a crack had surrounded microgels during its propagation. (d) SEM images showing the interfacial decohesion between a microgel and the surrounding matrix.

in tensile loading. The reason for this different behavior is not clear at this stage. It might be due to (i) the interpenetration of the matrix's polymer network in the microgels' polymer network, (ii) the microgels' confinement degree, or (iii) the more solicited interfaces between matrix and microgels.

On average, all tested samples could sustain more than 90% true strain regarding the maximal deformation. The large error bars of neat hydrogels suggest a more brittle behavior than other structures. Moreover, similar to the maximum strain observed in compression, hybrid granular hydrogels $6H_4^{0.5}$ showed lower stretchability than $6G_4$ despite its higher fiber concentration, which is not the case for $C_{10}^{0.5}$ or $4H_6^{0.5}$. However, more samples would be required for better evaluating the maximal deformation because of wide error bars.

In parallel, a single notch edge test was performed for characterizing fracture energy of 6 representative compositions: neat hydrogel - N_{10} , hydrogel composite - $C_{10}^{0.5}$, granular hydrogels - $4G_6$ and $6G_4$, and hybrid granular hydrogels - $4H_6^{0.5}$ and $6H_4^{0.5}$. Fig. 6.7 shows the resulting fracture energies. Similar to tensile modulus, the fracture energy of granular hydrogels is higher than neat hydrogels. As shown in Fig. 6.5b and 6.5c, the crack surrounded and pulled-out microgels during its propagation. Therefore,

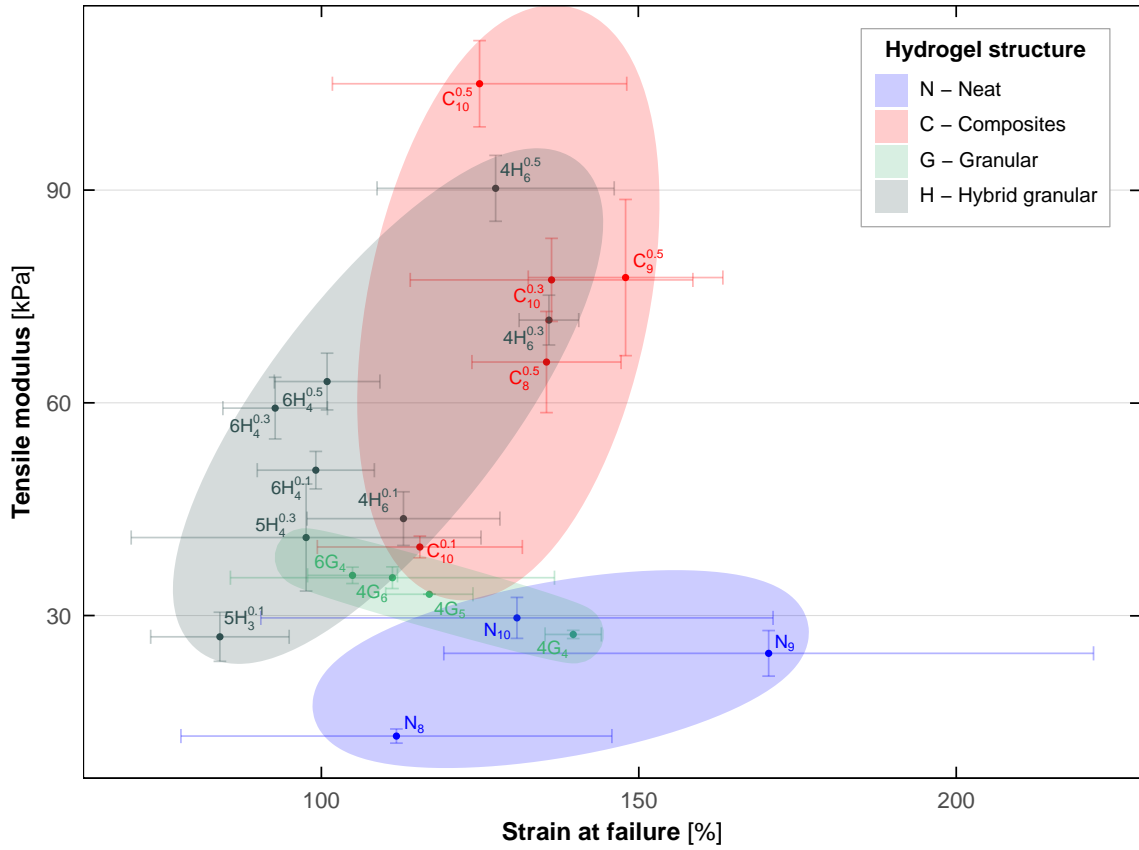


Figure 6.6: Property chart showing the tensile modulus determined between 10% and 15% applied strain as a function of the maximum deformation of four different hydrogel structures.

the surface of rupture is larger and more energy costly than the one of neat hydrogels. As mentioned in *Chapter 5. Fracture properties of preloaded hydrogel composites*, the addition of cellulose fibers to neat hydrogels significantly improved the fracture properties. However, the effect is consistent with granular structures. Indeed, similar to the maximal elongation observed in tensile loading, $6H_4^{0.5}$ has nearly the same fracture energy as $6G_4$, while $4H_6^{0.5}$ could reach almost the same range as $C_{10}^{0.5}$. Moreover, while $4G_6$ and $6G_4$ have very similar fracture energies, $4H_6^{0.5}$ and $6H_4^{0.5}$ exhibits a huge difference although their very close compositions. As mentioned, the difference is probably due to lower fiber dispersion and aggregates between microgels. Fig. 6.7c presents digital image correlation images showing the *von Mises Strain* around the crack tip. Interestingly, compared to $4H_6^{0.5}$ or $C_{10}^{0.5}$, $6H_4^{0.5}$ have a much more localized strain concentration around the crack. It seems that it accommodates fewer strains before crack starts to propagate. This observation highlights that the mechanical properties might be influenced more by the microstructure than the compositions.

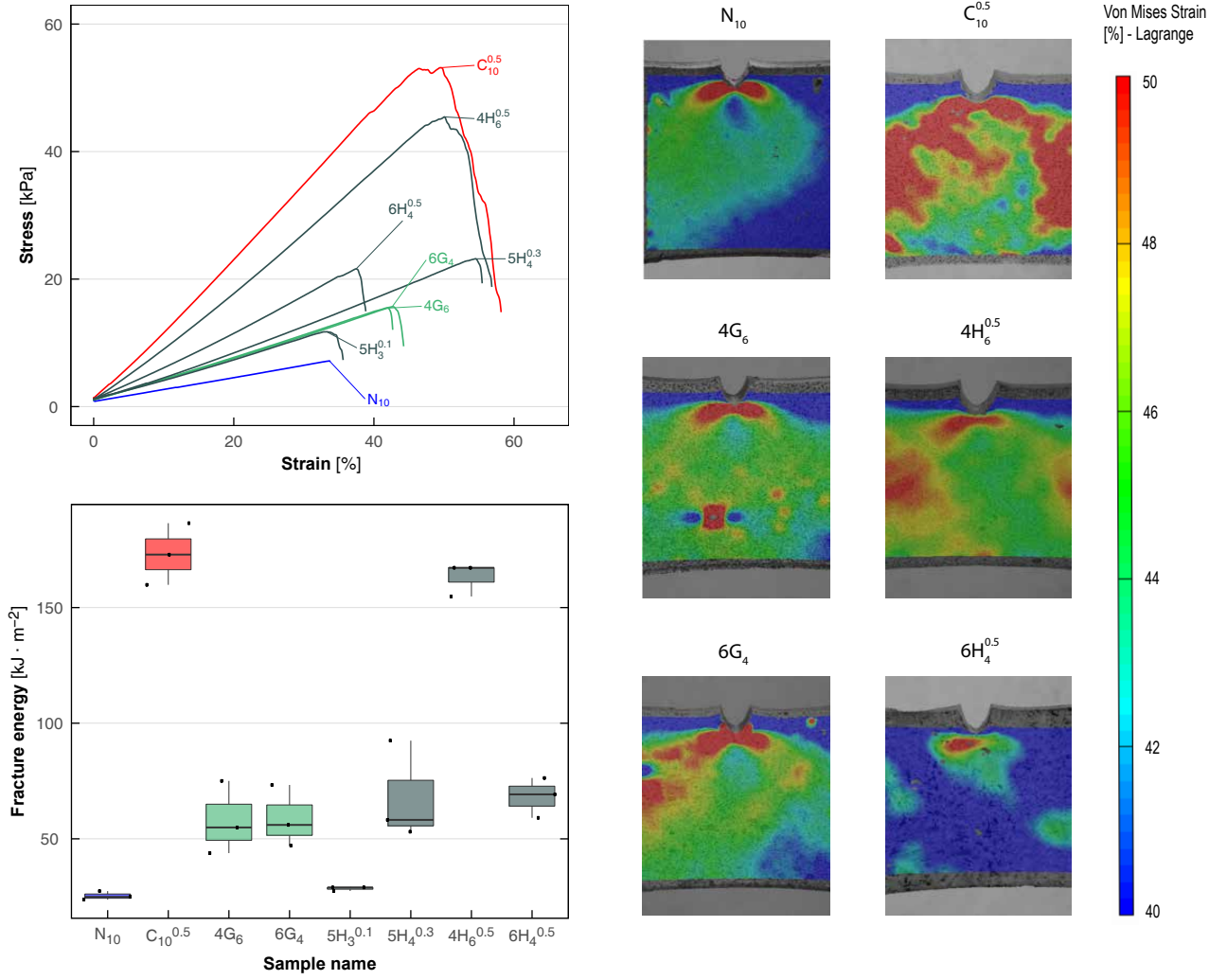


Figure 6.7: Fracture properties of neat hydrogel, hydrogel composites, granular hydrogel and of hybrid granular hydrogels: (a) representative curve of single notch edge tests, (b) fracture energy evaluated with equation (3.7) on p. 53 and (c) digital image correlation images showing the *von Mises strain* around the crack tip, which starts to propagate.

6.3.2 Effect of pre-swollen PEGDM microgels

Fig. 6.8 presents the swelling behavior of neat and granular hydrogels. As previously observed, granular hydrogels had lower swelling ratios as neat hydrogels. In order to better analyze the difference, the reduction of swelling was defined as following:

$$\text{Reduction of swelling (vol.\%)} = 100 * \frac{(SR_{N_x} - SR_{yG_z})}{SR_{N_x}} \quad (6.1)$$

where "G" and "N" stand for granular and neat hydrogels respectively. The sum of the dry microgel content "y" and PEGDM contained in the surrounding matrix "z" is equal to the PEGDM content "x" of the neat hydrogel. For example, the swelling ratio of granular hydrogel - 3G₄ is compared with the one of neat hydrogel - N₇. The error bars were calculated based on error propagation rules from the swelling ratios' standard errors.

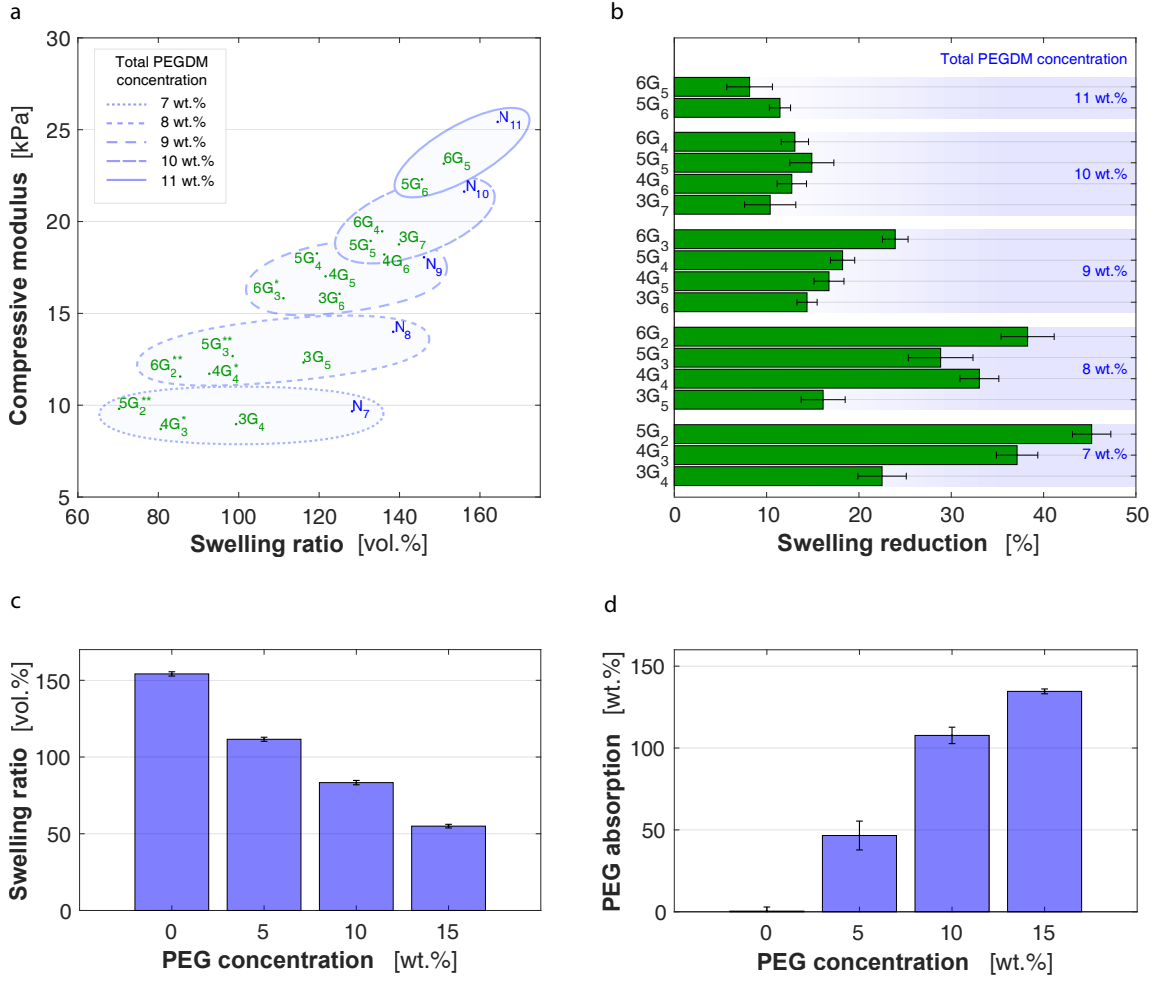


Figure 6.8: Swelling behavior of granular hydrogels: (a) property chart presenting the compressive elastic modulus vs. the swelling ratio obtained with equation (3.1), (b) swelling reduction evaluated with equation (6.1), where the total PEGDM content is the addition of dry microgel and PEGDM concentration. Influence of the PEG concentration of the immersion solutions on (c) the swelling ratio of the neat hydrogel N₁₀ and (d) on the PEG absorption in the neat hydrogel N₁₀ determined with equation (6.2).

Fig. 6.8b shows that substituting neat hydrogels with pre-swollen microgels could reduce swelling by up to 45 ± 2 %. Furthermore, the reduction of swelling was more efficient at lower total PEGDM concentrations, higher microgel content, and lower PEGDM concentrations in the matrix. The smallest reduction of about 10% was measured for 11 wt.% of total PEGDM content, where granular hydrogels and neat hydrogels presented similar swelling ratios of 160%. The elastic moduli increased proportionately with the total PEGDM amount. Unlike the swelling reduction, the elastic modulus depended on the material composition rather than on the hydrogel's microscopic structure.

To better understand granular hydrogels' swelling behavior, the pre-swelling of microgels in the matrix precursor was investigated. Hydrogels of the same initial composition of microgels, 10 wt.% PEGDM, were first dried before being swollen in different water/20kDa polyethylene glycol (PEG) solutions. As shown in Fig. 6.8c, the swelling ratio, obtained with equation (1), significantly decreased with increasing PEG concentration, probably due to the osmotic pressure induced by PEG^[156]. It suggests that microgels pre-swell less in precursors of higher PEGDM concentrations. Thus, once

polymerized and immersed in water, those granular hydrogels would swell more because the microgels were not fully swollen. In other words, higher pre-swelling levels of microgels induced by lower PEGDM concentrations in the matrix will better reduce swelling. For the hydrogels evaluated in this study, it is expected that above 11 wt.% of total PEGDM, the reduction of swelling becomes negligible.

To estimate if PEGDM diffuses from the precursors into the microgels, three neat hydrogels N₁₀ with the same initial composition as the microgels were first dried and weighed (m_{dry}) before being swollen in different PEG solutions. Then the hydrogels were retrieved from the solutions, dried, and weighed (m_{PEGdry}) again. The PEG absorption (PEG_{abs}) was estimated as following:

$$PEG \text{ absorption}(wt. \%) = 100 \frac{(m_{dry} - m_{PEGdry})}{m_{dry}} \quad (6.2)$$

As shown in Fig.6.8d, the PEG absorption increased with the PEG concentration in the hydrating solution, probably due to convective effects when the hydrogel swells from the dry state. Similarly, PEGDM from the precursor is expected to diffuse into the microgels, strengthening the interface between microgels and the matrix and homogenizing the PEGDM concentration in the granular hydrogels. Nevertheless, the variations in swelling and local PEGDM concentrations make it difficult to estimate the precise volume occupied by microgels in granular hydrogels. Moreover, for better assessing the swelling behavior of microgels, the monodisperse distribution would be required to consider the effective role of their surface to volume ratio^[323]. Indeed, measuring swelling by statistical methods would be easier than tracking individual microgels.

Furthermore, recent studies showed that the microgels might have different crosslinking densities and distributions than the neat hydrogel at the microscale, which would affect their swelling and mechanical properties^[323–325]. Therefore, further analysis, such as assessing the density of consumed crosslinking by Fourier-transform infrared (FTIR) or by nuclear magnetic resonance (NMR) spectroscopy, would help understand the different mechanisms occurring during granular hydrogels synthesis. For example, it might clarify if the PEGDM from the matrix diffuses in the microgels and forms local interpenetrated polymer networks.

6.3.3 Effect of cellulose fibers

Fig. 6.9 presents the effect of incorporating NFC fibers in neat hydrogels, *i.e.* hydrogel composites, and the matrix of the granular hydrogels, *i.e.* hybrid granular hydrogels. As observed in Fig. 6.3 and Fig. 6.6a, adding fibers increased the elastic moduli and reduced the swelling ratios of both structures. Highlighted with a steeper linear regression in Fig. 6.9a, the effect of fibers was getting stronger with increasing the fiber concentration from 0.1 to 0.5 vol.% NFC and started to dominate the effect of the total PEGDM content.

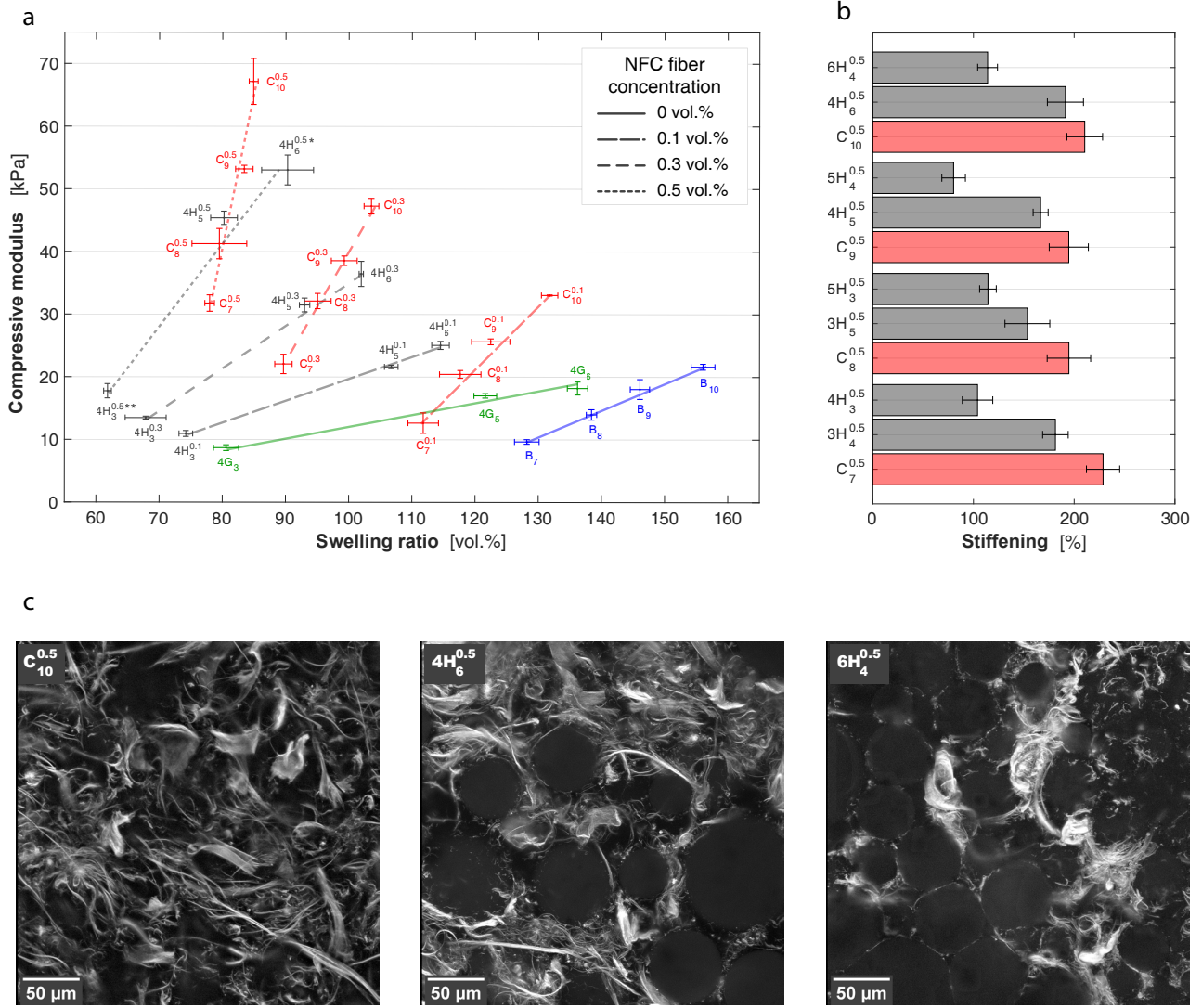


Figure 6.9: Effect of NFC fiber concentration. (a) Property chart presenting the compressive elastic modulus vs. the swelling ratio. The effect of the fiber concentration is highlighted with linear fits. (b) Stiffening achieved when 0.5 vol.% of NFC fibers are added to the analogous hydrogel, calculated with equations (6.3) and (6.4) (c) Z-stack projection of 7.5 μm in depth taken with a fluorescent confocal microscope showing the NFC fibers and microgels incorporated in swollen hydrogels.

Fig. 6.9b reports the different stiffening achieved when 0.5 vol.% of NFC fibers were added to the analogous neat hydrogel, in red, and granular hydrogel, in grey. The stiffening was calculated as described in equation (6.3) for conventional structure and equation (6.4) for granular structures.

$$\text{Stiffening}(\%) = 100 * \frac{(E_{C_x^{0.5}} - E_{N_x})}{E_{N_x}} \quad (6.3)$$

where “N” and “C” are the abbreviations of neat hydrogel and hydrogel composite respectively and “x” for the PEGDM concentration.

$$\text{Stiffening}(\%) = 100 * \frac{(E_{yH_x^{0.5}} - E_{yG_x})}{E_{yG_x}} \quad (6.4)$$

where "H" and "G" stand for granular and hybrid granular hydrogels, "y" for the dry microgel content, and "x" for the PEGDM contained in the surrounding matrix. For example, the elastic modulus of the hydrogel composite C₁₀ was compared with that of the neat hydrogel N₁₀ and reached a 200% stiffening. Note that the error bars were calculated based on the error propagation rules from the standard errors of the elastic moduli.

While this stiffening of 200% achieved by the hydrogel composites seemed not affected by the total PEGDM amount, the granular structures showed more variations. In particular, the stiffening was reduced from around 200% to 80% at higher microgel concentrations and lower PEGDM contents in the surrounding matrix.

The fiber distribution in swollen hydrogel composites and hybrid hydrogels was observed under a fluorescent confocal microscope to understand the stiffening behavior. Fig. 6.9c shows z-stack projections of swollen hydrogels containing initially a total PEGDM concentration of 10 wt.% and 0.5 vol.% of NFC fibers. The fibers in the hydrogel composite (C₁₀^{0.5}) were better dispersed compared to hybrid granular hydrogels (4H₆^{0.5}, 6H₄^{0.5}). Indeed, the presence of local fiber concentration and the formation of aggregates increased with the microgel concentration. Both affected the stiffening efficiency and the deformability of hybrid granular hydrogels. The use of shorter cellulose fibers may improve their dispersion, while finer fibers might better surround microgels due to higher flexibility.

6.3.4 Processing

The processing ease of the developed hydrogel structures for different applications depends on the hydrogel precursors' processability. Therefore, their rheological behavior was studied with a parallel plate rheometer at 0.5 Hz and oscillating strains going from 0.1% to 1000%. Fig. 6.10 presents the range of complex viscosities observed at quasi-static 0.1% strain of different hydrogel precursors

Neat hydrogel precursors had a very low complex viscosity, less than 0.1 Pa · s. At 0.1% strain, the complex viscosity of hydrogel composite precursors increased from 0.1 to 10 Pa · s with the fibers concentrations. Both precursors would still be convenient to be injected through narrow needles. The complex viscosities of the precursors of granular and hybrid granular hydrogels varied from 2 to 1000 Pa · s and could thus be up to 10'000 times more viscous than that of neat hydrogel precursors. Moreover, above 500 Pa · s, the precursors started to behave similarly to jammed microgels, as shown in Fig. 6.10. Additionally, the complex viscosity decreased with increasing PEGDM concentration in the matrix precursor since PEGDM act as a lubricant for the microgels. As already mentioned in the study on the swelling, at higher PEGDM concentrations in the precursor, the microgels occupy less volume, and PEGDM reduces friction between them. Moreover, all precursors of the hydrogel

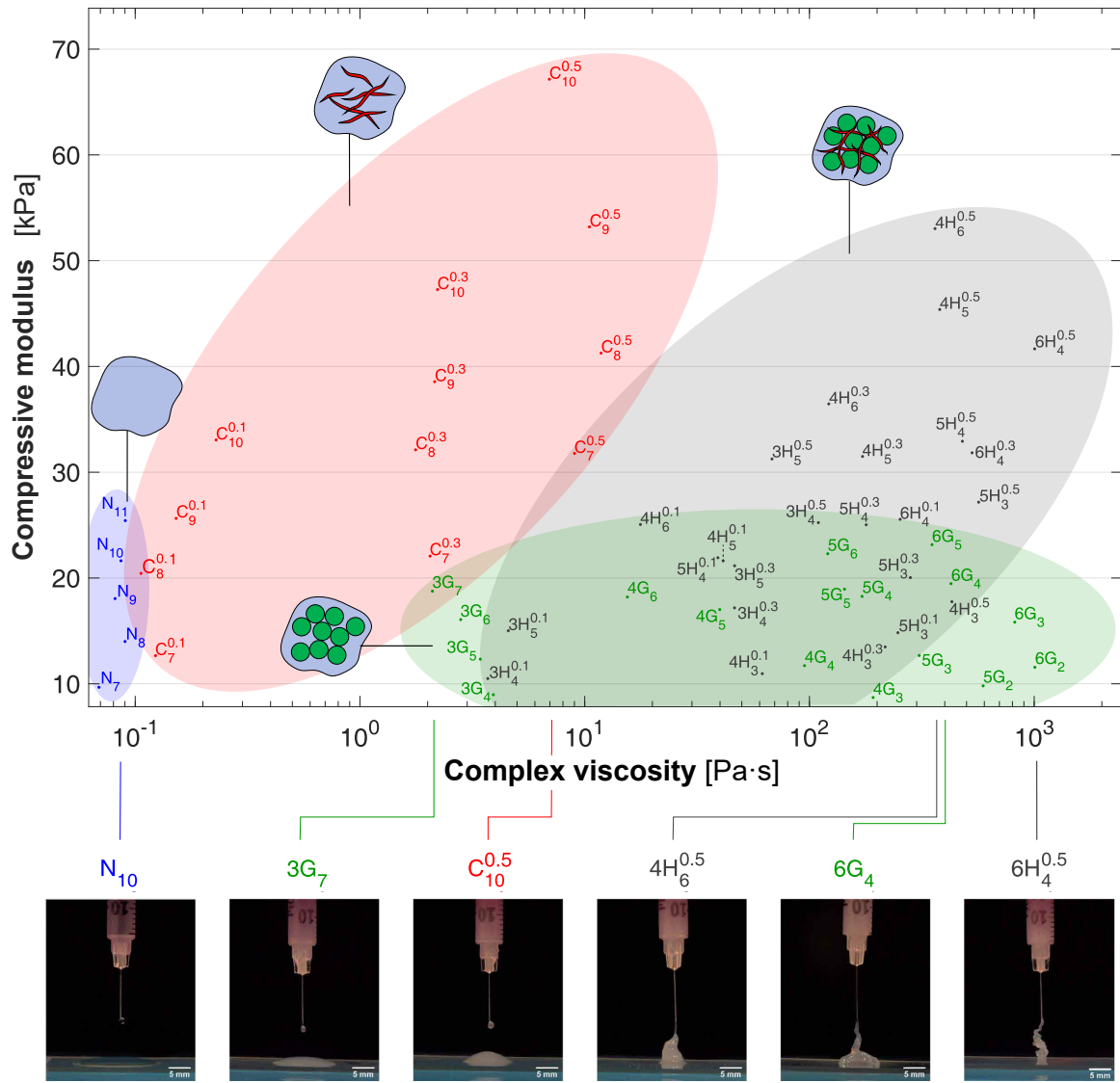


Figure 6.10: Property chart of four different hydrogel structures with various compositions showing the elastic modulus in compression as a function of the complex viscosity of the precursors at 0.1% oscillation strain and 0.5 Hz. Although a wide range of viscosity was achieved, all precursors were injectable through a needle with an inner diameter of 0.133 mm.

composites and hybrid granular hydrogels showed obvious shear-thinning behavior after 10% strain, as shown in Fig. 6.11. This behavior represents a key advantage for continuous placement of materials before or during the crosslinking via 3D printing manufacturing.

In summary, depending on the hydrogel structure, a broad range of precursor's complex viscosities could be obtained while keeping similar hydrogels' mechanical properties, which offers new application opportunities. For example, low precursors' complex viscosity would be suitable for confined applications, such as replacing the nucleus pulposus^[1], while precursors of high viscosity would be ideal for unconfined applications like the replacement of focal cartilage defects without the use of a membrane^[320] or to 3D printed complex unconfined structures^[7].

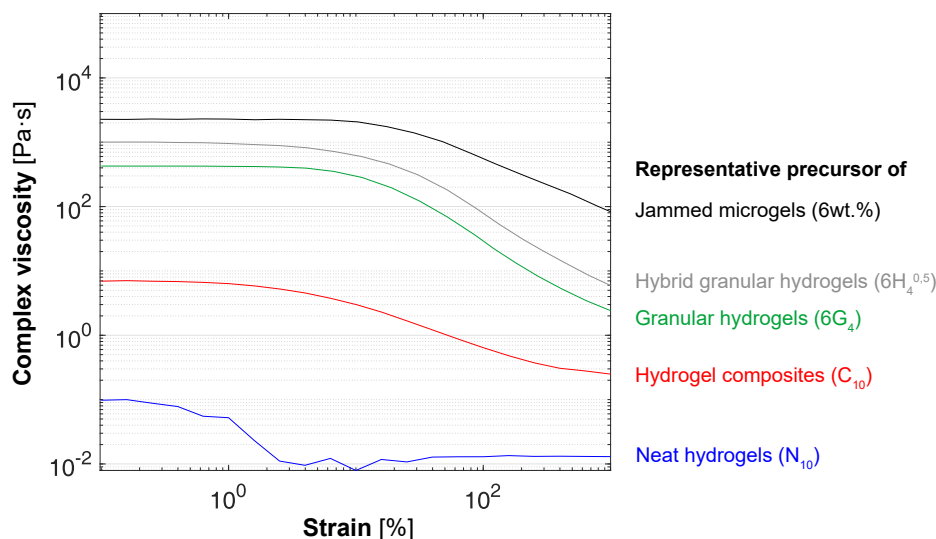


Figure 6.11: Representative behavior of precursors' complex viscosities measured with a parallel plate rheometer (TA Instruments AR2000ex) under an oscillating strain sweep at 0.5 Hz at room temperature. All precursors except that of neat hydrogels showed obvious shear-thinning behavior.

6.3.5 Direct contact test

The biocompatibility of hybrid granular hydrogels was rapidly assessed with a direct contact test for four days. Fig. 6.12 presents the resulting images taken with an inverted microscope (Nikon, Ti2). $4H_6^{0.5}$ was selected for being the representative sample because the hydrogels contained all elements and had the highest mechanical performance of hybrid granular hydrogels.

As shown in Fig. 6.12b, the hydrogel slightly retracted during the staining process with Giemsa. Nevertheless, the fibroblasts from the embryo of albino mice grew well around and under the hydrogels after four days. The morphology of the cellular network was similar to the one far from the sample (Fig. 6.12a). Subsequently, the direct contact test suggested that hybrid granular hydrogels show no significant toxic reactions.

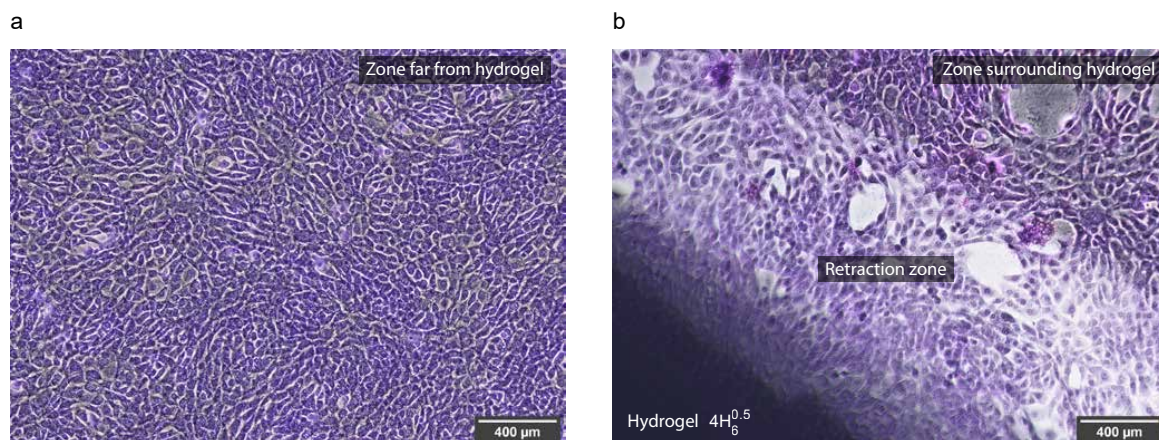


Figure 6.12: Direct contact test of hybrid granular hydrogel: $4H_6^{0.5}$. Fibroblasts from embryo of albino mice were fixed with methanol after four days and stained with Giemsa procedure.

6.4 Conclusions

A novel strategy was proposed for better controlling mechanical and swelling properties as well as the precursor viscosity by combining granular and composite hydrogels.

An extensive assessment of different structures, including 63 different hydrogel compositions based on PEGDM, showed that the swelling ratio could be tailored from 60 vol.% to 165 vol.% without significantly losing stiffness and deformation. Integrating pre-swollen microgel into neat hydrogels could reduce swelling up to 45%. The achievable swelling reduction is given by the microgels concentration and the total PEGDM content. The studied material system encountered a negligible swelling reduction at above 11 wt.% of total PEGDM content, where granular hydrogels and their representative neat hydrogels had similar swelling ratios. The reason was related to the swelling degree of microgels that would pre-swell less in precursors of higher PEGDM concentrations.

For a given elastic modulus, granular hydrogels had lower swelling ratios than neat hydrogels, especially below 15 kPa. Adding fibers reduced swelling and increased the elastic modulus of the hydrogel composites and the hybrid granular structures. The effect was getting stronger with increasing fiber content and became predominant above a fiber concentration of 0.3 vol.%. However, too high local concentrations of cellulose fibers confined between the microgels could lead to earlier failure.

All precursors were injectable and the one incorporating microgels and/or cellulose fibers showed obvious shear-thinning behavior required for advanced 3D printing. This opens a new horizon for processing in confined as well as in unconfined environments and using these material systems when precise control of stiffness and swelling is needed. Based on these first hybrid granular structures, the integration of other hydrogels, microgels, and fibers can be envisaged. Indeed, the overall swelling ratios reported in this study remains quite large. Further research needs to be carried out to better control and reduce this property. The next *Chapter 7. Self-reinforced granular hydrogel with silk fibroin fibers* focuses, therefore, on developing new granular structures reinforced with other bio-fibers.

Chapter 7

Self-reinforced granular hydrogel with silk fibroin fibers

How to process granular hydrogels with silk fibroin regenerated in situ?

Granular hydrogels with high stability, strength, and toughness are laborious to develop. Indeed, the precursor of granular hydrogel exhibits inherent stability due to friction and cohesive forces between microgels. Nevertheless, to enhance mechanical properties, often post-curing, such as post-photopolymerization, is required to bind microgels chemically. Here a new strategy was investigated to reinforce and maintain microgels together with a novel self-reinforced silk granular hydrogel composed of 20 kDa poly(ethylene glycol) dimethacrylate microgels and regenerated silk fibroin fibers. The principle is to locally concentrate and regenerate silk fibroin *in situ* using microgel swelling. We showed that silk fibroin in most compositions was homogeneously distributed and had successfully regenerated *in situ* around microgels, holding them together in a network-like structure. FTIR analysis revealed the presence of amorphous and crystalline silk fibroin, where 50% of the secondary structures could be assigned to strong β -sheets. Silk granular hydrogels exhibited swelling ratios between 5 vol.% and 60 vol.% and elastic moduli between 58 kPa and 296 kPa. Swelling increased proportionally with the microgel content, suggesting that mainly microgels governed swelling. In contrast, the elastic modulus increased almost linearly with silk fibroin content, and higher microgel content further pronounced the enhancement. Silk granular hydrogel initially composed of 5 wt.% of dry microgels presented the best compromise between mechanical and swelling properties. Subsequently, we proposed a synthesis method for obtaining optimal silk granular hydrogels by choosing the right initial concentration of microgels. Finally, we showed that the precursor silk granular hydrogel could be injected and cast it in shape into a given volume.

Keywords: self-reinforced granular hydrogel, microgels, silk fibroin, swelling, elastic modulus, processability, FTIR.

7.1 Introduction

Granular hydrogels have gained considerable attention recently. Their particular microstructure composed of contacting microgels offers an extended range of material properties for biomedical applications^[32–39] or 3D printing^[37–39]. Indeed, their precursor, only composed of microgels, is injectable and can be tailored in composition to explore additional biological, physical, and mechanical properties^[33]. The granular hydrogel exhibit inherent stability due to friction and cohesive forces between microgels. Nevertheless, since mechanical properties stay relatively low, often post-curing, such as post-photopolymerization, is required to bind microgels chemically^[32,39].

In the previous *Chapter 6. Hybrid granular hydrogels*, pre-swollen microgels were embedded in a neat or hydrogel composites in order to maintain the microgels together. By combining composites and microgels approaches, we showed that the elastic modulus could be tailored between 10 kPa and 70 kPa and swelling between 60 vol.% and 170 vol.%, while most hydrogel could sustain more than 85% applied strain in compression. Nevertheless, the level of swelling remains excessive for many unconfined or semi-confined applications. In particular, we observed that mainly the matrix surrounding the microgels swells and significant influence on the pre-swelling degree of microgels themselves.

Therefore, to further reinforce and reduce swelling of granular hydrogels using the same microgels, the effect of the surrounding matrix on swelling has to be minimized. Here we explore a new self-reinforced granular hydrogel composed of microgels and self-assembled silk fibroin fibers, as illustrated in Fig. 7.1.

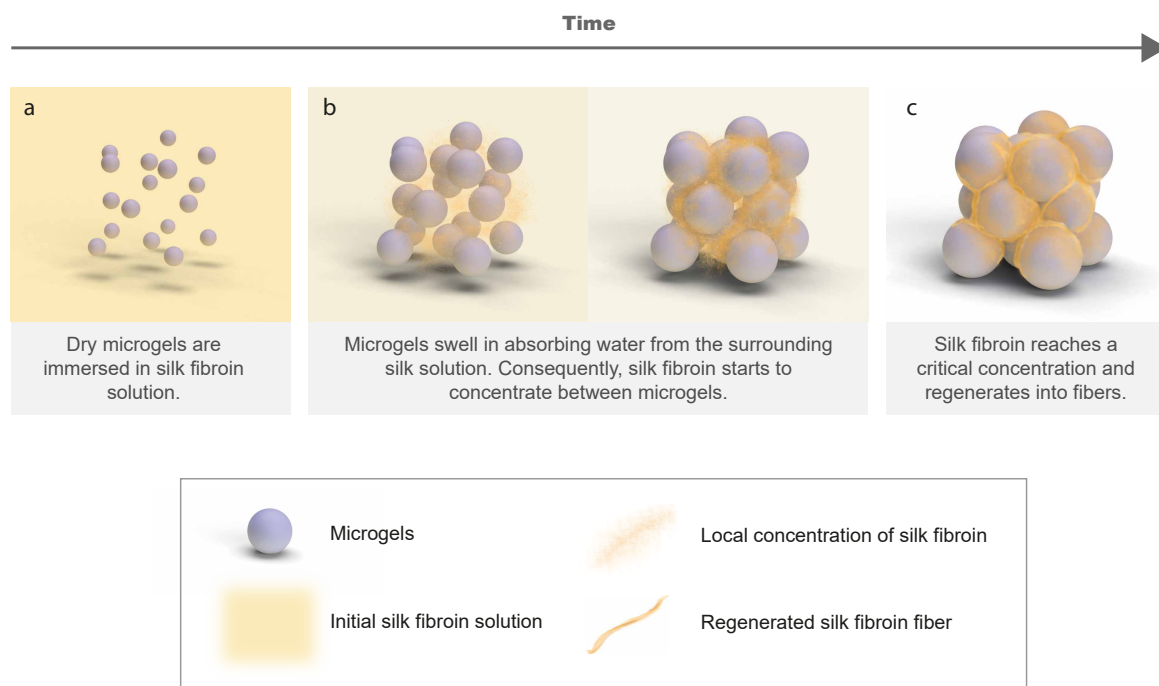


Figure 7.1: Illustration showing how to control the regeneration silk fibroin fibers *in situ* with microgels swelling.

Due to their remarkable biocompatibility and mechanical properties, silk fibroin fibers are already used in several biomedical applications such as surgical suture, mesh, or garment as well as in electronic and optics applications^[145,146,326]. Silk fibroin fibers can be used in their native form or being dissolved and regenerated in various morphologies such as hydrogels, foams, films, or microparticles^[145,152]. These versatile structures, illustrated in Fig. 2.3 on p. 18 raise new application opportunities for drug delivery, artificial skin, contact lenses, gene delivery system, cartilage repair, or bone graft^[145]. In particular, regenerated silk fibroin degrades slowly and is bioresorbable, essential characteristics for load-bearing applications.

Additionally, the gel transition of silk fibroin solution can be controlled with different methods such as (i) silk fibroin concentration, (ii) temperature, (iii) sonication/ultrasound, (iv) non-solvent inducing phase separation, (v) pH or (vi) osmotic stress^[71,146,149,153–156]. For example, when polyethylene is mixed with silk fibroin solution, it induces an osmotic pressure to silk fibroin and reduces therefore the gelation time^[155,156].

Here, to regenerate silk fibroin *in situ* in granular hydrogels, we use microgels' swelling to locally concentrate silk fibroin. Dry microgels were added in silk fibroin solution (Fig. 7.1a) and absorbed the water from the surrounding silk solution to swell. Subsequently, silk fibroin was more concentrated between the microgels (Fig. 7.1b). Once the silk fibroin reached a critical concentration, it started to crystallize and regenerated into fibers around microgels (Fig. 7.1c).

To understand how microgel and silk fibroin contents affect the swelling and mechanical behavior of silk granular hydrogels, 12 different hydrogel compositions based on 20 kDa poly(ethylene glycol) dimethacrylate (PEGDM) were studied.

7.2 Materials and methods

7.2.1 Materials

20 kDa poly(ethylene glycol) dimethacrylate (PEGDM) was purchased from Polysciences (ref. 25406-25, Germany). *Bombyx mori* silk fibers were provided by swiss silk. Mineral oil (CAS 8042-47-5) and span 80 (CAS 133-43-8) were supplied by Merck. Irgacure 2959 from BASF was used as a photoinitiator.

7.2.2 Synthesis of microgels

The synthesis of microgels, initially composed of 10 wt.% PEGDM, are described in Fig. 3.2 in *Chapter 3. Materials and methods*. The particle size distribution of microgels was measured with a digital particle size analyzer (Saturn DigiSizer II, micromeritics), where the refractive index was estimated at 1.334 with a tomographic microscope (3D Nanolive Cell Explorer) and the density at 1.01 g/cm³. As shown in Fig. 6.2 the size of particles varied from 20-160 μm .

7.2.3 Synthesis of silk fibroin

Silk fibroin was extracted from *Bombyx mori* silkworms. As illustrated in Fig. 3.3 in *Chapter 3. Materials and methods*, silk fibers were boiled in water containing 0.05 wt.% of sodium carbonate (Na_2CO_3) for 45 min and washed three times with pure water to remove sericin. After drying at 60°C for 4h, the remaining silk fibroin was dissolved in 80 wt.% 9.3M lithium bromide for 4h, before to be dialyzed for three days against pure water. The final concentration of silk fibroin was measured at 4.5 wt.%, while the pH was adjusted at 9.5 by adding ammonium at low concentration to avoid early crystallization^[327].

7.2.4 Synthesis of self-reinforced silk fibroin granular hydrogel

Self-reinforced granular hydrogels were synthesis as shown in Fig. 3.9 on p. 44. The concentration of microgels was progressively increased from 4 wt.% to 6 wt.%, while silk fibroin concentration from 2 wt.% to 5 wt.%. The precursors were cast in polylactic acid (PLA) molds and cover with a microscopic glass before being placed in an incubator at 37°C for 12h. Table 6.1 on p. 96 summarizes the dimension of casting molds.

The nomenclature is presented in Fig. 7.2. For example, $5S^5$ represents a silk granular hydrogel, which was initially composed of 5 wt.% of dry microgels and 5 wt.% of silk fibroin.



Figure 7.2: Nomenclature designing structures and compositions of silk granular hydrogels.

Note that the nomenclature follows the same rule than the one defined in previous previous *Chapter 6. Hybrid granular hydrogels*. As a reminder the global nomenclature is described in Fig. 7.3.

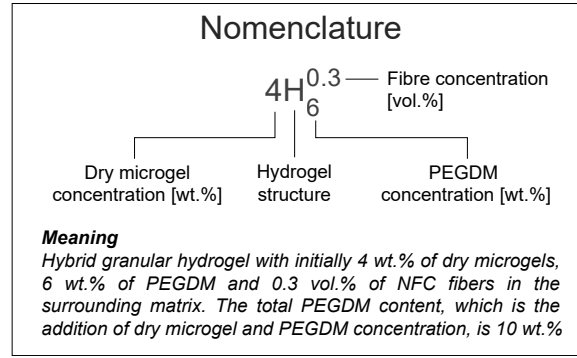


Figure 7.3: General nomenclature designing structures and compositions of studied hydrogels.

7.2.5 Swelling ratios

The volume of the samples was determined with Archimedes' principle. The samples were immersed in extra pure hexane (99+%, Fisher Chemical) with a density of $\rho = 0.659$ g/l. For reaching the equilibrium swelling state, the hydrogels were immersed in distilled water for at least 24h before measuring the swelling ratio (SR) with equation (3.3) on p. 49. The average swelling ratios and their corresponding standard deviation errors were based on three different samples.

7.2.6 Mechanical properties

Compression and tensile test

Cyclic compression and tensile loadings were performed as previously described in section 3.4.4 on p. 50 on swollen hydrogels with a tensile machine (5 kN Zwick equipped with a 100 N load cell, Zwick Roell, Germany) presented in Fig. 3.14 on p. 51 at a constant displacement rate of 1 mm/s. For evaluating the real stress, it was considered that no change of volume occurs during loading time. Three samples were tested in the *swollen state* under cyclic loading-unloading compression loading. They were five different stages during the tests:

- Stage 1: 3 cycles between 0% and 30% applied strain
- Stage 2: 3 cycles between 0% and 50% applied strain
- Stage 3: 3 cycles between 0% and 70% applied strain
- Stage 4: 3 cycles between 0% and 90% applied strain
- Stage 5: loading up to rupture if the samples could sustain deformation up to 90%

The pre-loading was 0.05 N and 0.02 N for compression and tensile test respectively, The elastic moduli were then determined by linear regression between 10% and 15% applied strain during the first loading cycles. Note that for the tensile test, a virtual extensometer recorded the true strain (VideoXtens, Zwick / Roell).

Single edge notch test

A single edge notch test was performed on rectangular swollen hydrogels with the tensile machine Zwick. A crack of 3 mm was cut with a scalpel in the hydrogels before testing the sample at a loading rate of 0.5 mm/s until rupture. The fracture energy is defined when a critical energy release rate G_c is reached. G_c was characterized with the equation (3.7) on p. 53^[17].

7.2.7 Digital image correlation analysis

Graphit 33 (Kontakt Chemie, Germany) was sprayed on samples' surface to make a fine, randomly, and homogeneously distributed speckles pattern. 3D DIC analysis was then performed with the test equipment illustrated in Fig. 3.19 provided by correlated solutions according to the test parameters presented in Table 3.4. The test equipment incorporates two cameras Grasshopper USB3 (monochrome, 5.0 Mpix, 75 fps), 70 mm lens, the software Vicsnap V.9 for the recording of images, and VIC3D V.8 for the analysis. The reference image were taken when the applied load reached 0.04 N.

7.2.8 Microstructures

The morphology and distribution of the regenerated silk fibroin were observed in swollen hydrogels with an inverted fluorescent confocal microscope (Zeiss LSM 700) equipped with a 20x lens and a laser of 555 nm. For enhancing the fluorescence of silk fibroin fibers, the self-reinforced granular hydrogels were placed for at least 3 hours in 0.02 g/l Rhodamine B stain (Merck, CAS 81-88-9) before being placed in pure water for at least 2 hours.

7.2.9 Crystallinity

The crystalline structure of dry self-reinforced granular hydrogels was analyzed with Fourier transform infrared spectroscopy (FTIR) FT/IR-6300typeA. The IR analysis covered the range between 800-3500 cm^{-1} with a resolution of 4 cm^{-1} . The background was collected before testing the samples.

The FTIR spectras were analyzed with R using the package of *ChemoSpec*. The baseline drift was adjusted with the function *baselineSpectra*, where *modpolyfit* was set for the method, while the normalization was done with the function *normSpectra*, where *PQN* (*i.e.* Probabalistic Quotient Normalizatio) was set for the method^[301].

The secondary structures were evaluated through the deconvolution of FTIR spectra near the amide I region (*i.e.* 1550-1750 cm^{-1}) using the Multiple Peak Fit package from the software OriginPro (Origin 2020b). The first step was to subtract a linear baseline in the amide I region from untreated absorption spectra. The curve was then smooth with a smoothing window size of 10 before using the second derivative of the spectra to determine the number and position of peaks. Then Gaussian curves were employed for deconvoluting the spectra, with fixed baseline and peak centers.

7.2.10 Direct contact test

Silk granular hydrogels were sterilized in an incubator at 121°C and 15 lbs before being placed and fixed separately in the middle of cell culture vessels with a diameter of 35 mm. Fibroblasts from the embryo of albino mice were then seeded around the samples (400'000 cells). The following quantities were added to each vessel: 2.5 mL of cell culture medium, 10 vol% Fetal Bovine Serum (FBS), 1 vol% Penicillin Streptomycin (PS), and 1 vol% L-Glutamine. Finally, the samples were incubated at 37 °C in 5% CO₂ for four days. To observe the cells, they were stained with 1 mL methanol for 30 seconds followed by 1 mL diluted Giemsa solution.

7.3 Results and discussion

7.3.1 Swelling and mechanical properties

The swelling behavior and mechanical performance in compression of silk granular hydrogels - *S* are shown in a property chart in Fig. 7.4 and were compared with neat hydrogels - *N*, hydrogel composites - *C*, granular hydrogels - *G* and hybrid granular hydrogels - *H*, which were studied in the previous Chapter 6. *Hybrid granular hydrogels*.

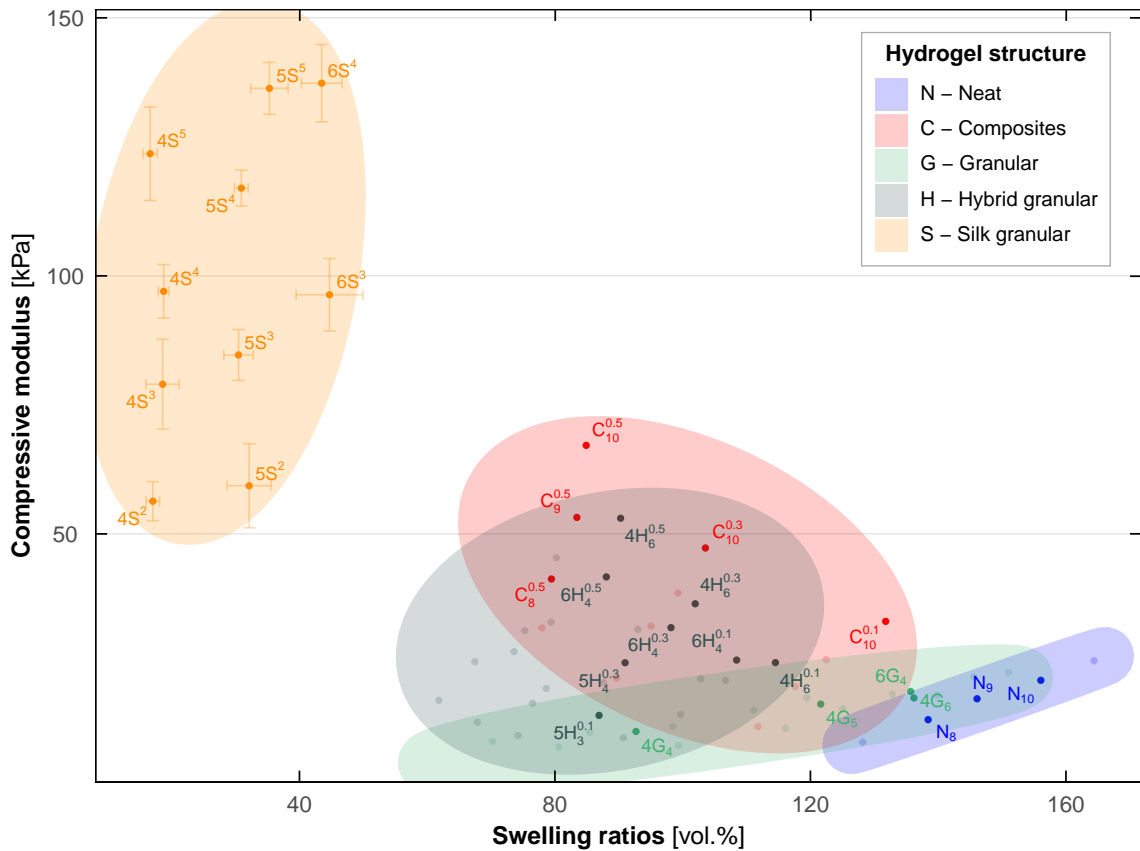


Figure 7.4: Property chart of five different hydrogel structures with various compositions showing the elastic modulus determined between 10% and 15% applied strain in compression as a function of the swelling ratio measured with Archimedes' principle.

Silk granular hydrogels exhibited swelling ratios between 5 vol.% and 60 vol.% and compressive moduli between 58 kPa and 136 kPa. At similar elastic modulus, around 55 kPa, self-reinforced granular hydrogels $4S^2$ and $5S^2$ presented significantly lower swelling ratios, 17.1 ± 1.1 vol.% and 32.1 ± 3.4 vol.% respectively, than hydrogel composites $C_9^{0.5}$ with 83.4 ± 1.4 vol.%. Moreover, the compressive modulus of $5S^5$ and $6S^4$ at around 135 kPa, were almost two times higher than that of $C_{10}^{0.5}$ with 67.1 ± 3.7 kPa. Note that the compositions $6S^2$ and $6S^5$ were not reported because the gelation of silk occurred during the mixing of the microgels with the silk fibroin before creating adequate samples.

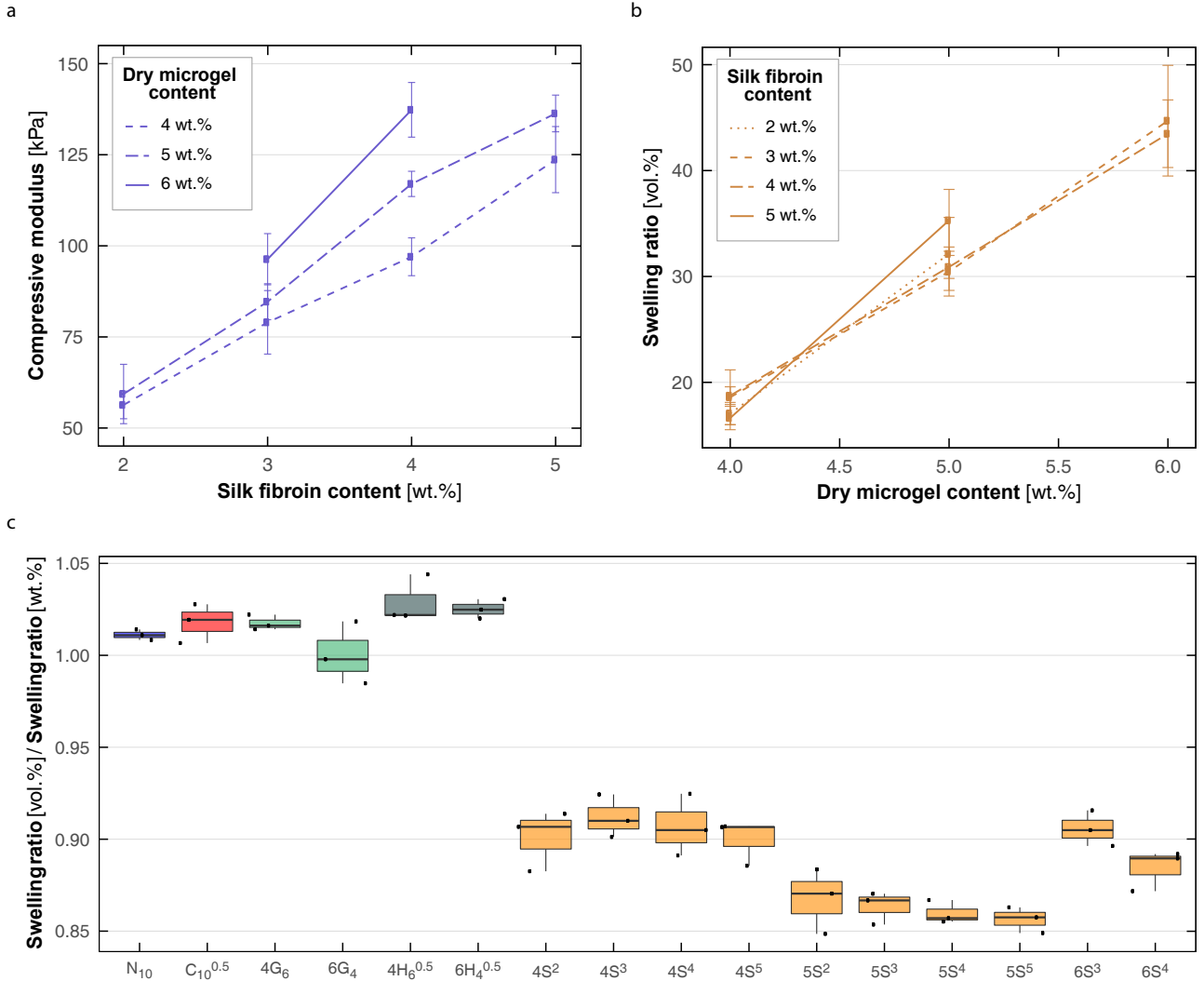


Figure 7.5: Influence of the microgel and silk fibroin content on swelling and mechanical performances. (a) The compressive modulus as a function of the silk fibroin content highlighting almost a linear behavior. (b) The swelling ratio as a function of the microgel content showing linear behaviors. (c) The swelling ratio measured by volume over the swelling ratio determined by weight showing a potential open porosity network.

As highlighted in Fig. 7.5, both silk fibroin content and microgel concentration are influencing the compressive modulus. In particular, since regenerated silk fibroin is significantly stiffer than PEGDM hydrogel and can reach a few hundreds of MPa^[328], the compressive moduli of silk granular hydrogel increased almost linearly with silk fibroin content (Fig. 7.5a). Nevertheless, increasing microgel con-

centration also contributed to augment the mechanical properties. The improvement might be due to higher polymer content or to the confinement degree of microgels. Indeed, the microgels are not fully free to deform because the stiffer silk fibroin matrix surrounds them. Subsequently, the water in the confined or semi-confined microgels is incompressible, which augments the apparent compressive modulus of the silk granular hydrogels.

Interestingly, as shown in Fig. 7.5b, the swelling of silk granular hydrogels increased proportionally with the microgel content, suggesting that only microgels govern swelling. This linear behavior allows to estimate the water content of the microgels. Fig. 7.6 presents the water content of microgels in each composition estimated with the equation (7.1). The final water content (WC) of microgels was determined to be around 97 wt.%. In comparison, the final water content of neat hydrogel - N₁₀ was estimated at around 96 wt.%.

$$WC[wt.\%] = 100 - \frac{MR[wt.\%]}{water[wt.\%] + MR[wt.\%] + \delta m} \quad \delta m = \frac{SR[wt.\%]}{1 - SR[wt.\%]/100} \quad (7.1)$$

where MR [wt.%] and water [wt.%] are the concentration of dry microgels and water respectively in the as-prepared state and SR [wt.%] is the swelling ratio based on weight.

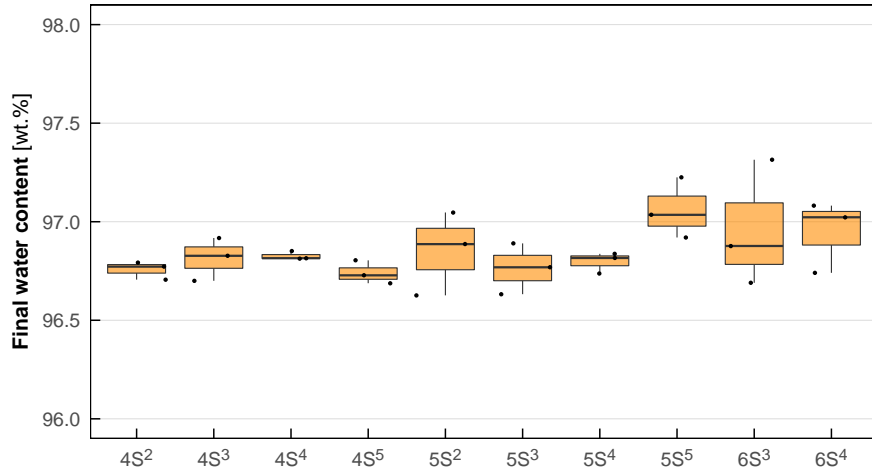


Figure 7.6: Estimation of the water content of microgels in the *swollen state* with equation (7.1).

Moreover, the swelling ratios of silk granular hydrogels based on volume differed from the ones measured by weight. Fig 7.5c revealed that the swelling ratios determined by volume were smaller. The volume before and after swelling was measured using the Archimedes principle. In contrast to weight measurements, the hydrogels were immersed in a fluid (*i.e.* hexane) for measuring their volume, which can fill open pores. Therefore, the smaller swelling ratios based on Archimedes measurement suggests a potential open porosity in the silk granular hydrogels.

For completing the mechanical characterization, tensile properties were evaluated and presented in Fig. 7.7, which is a property chart that presents the tensile modulus, determined between 10% and 15% applied strain, as a function of strain at failure. The tensile moduli of silk granular hydrogels (*i.e.*

86-296 kPa) were significantly larger than hydrogel composite - *C* (*i.e.* 39-105 kPa) or hybrid granular hydrogel - *H* (*i.e.* 27-90 kPa). However, as observed in many other materials, an increase in stiffness is mostly accompanied by a decrease in elongation. The average strains measured at failure (*i.e.* 29-62%) were dramatically smaller than the other structures. The lower elongations were probably driven by the maximal extension of regenerated silk fibroin itself. Indeed, it was reported that the elongation of regenerated silk fibroin hardly exceeds 65% [328].

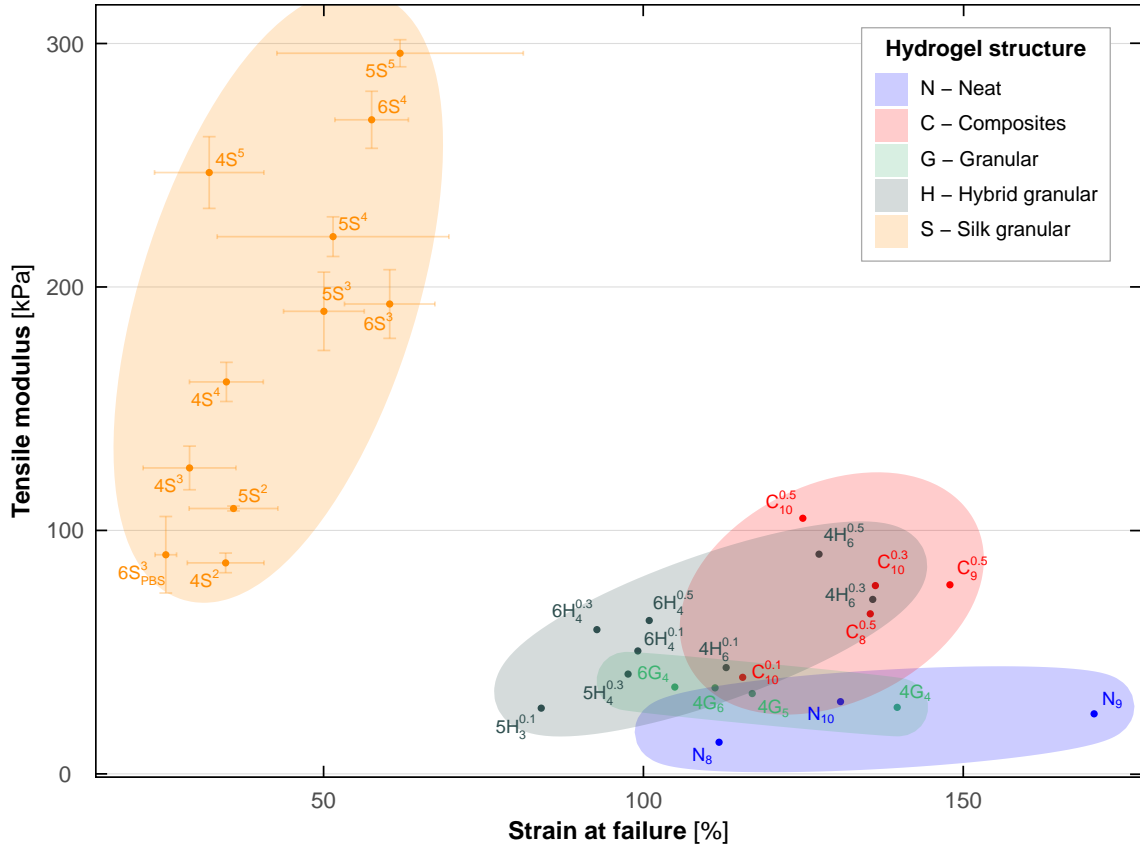


Figure 7.7: Property chart of five different hydrogel structures with various compositions showing the tensile modulus determined between 10 and 15% applied strain as a function of the strain at failure.

Compression and tensile test were performed under incremental cyclic loading. Fig. 7.8 shows, representative stress-strain curves in (a) compression and (b) tensile of silk granular hydrogel. All silk granular hydrogels became softer after the first loading cycle and exhibited large hysteresis, similar characteristics to the *Mullins effect*. For hydrogels reinforced with cellulose fibers, the behavior was previously related to a local rearrangement of the fiber network [306]. For silk granular hydrogels, the behavior may be due to the breaking of bonds in regenerated silk fibroin or around its interface with microgels. Moreover, the tensile moduli, *i.e.* 86-296 kPa, were significantly larger than compressive moduli, *i.e.* 58-136 kPa. We hypothesize that microgels principally contribute to compressive modulus, while silk fibroin fibers mainly participate in the tensile modulus.

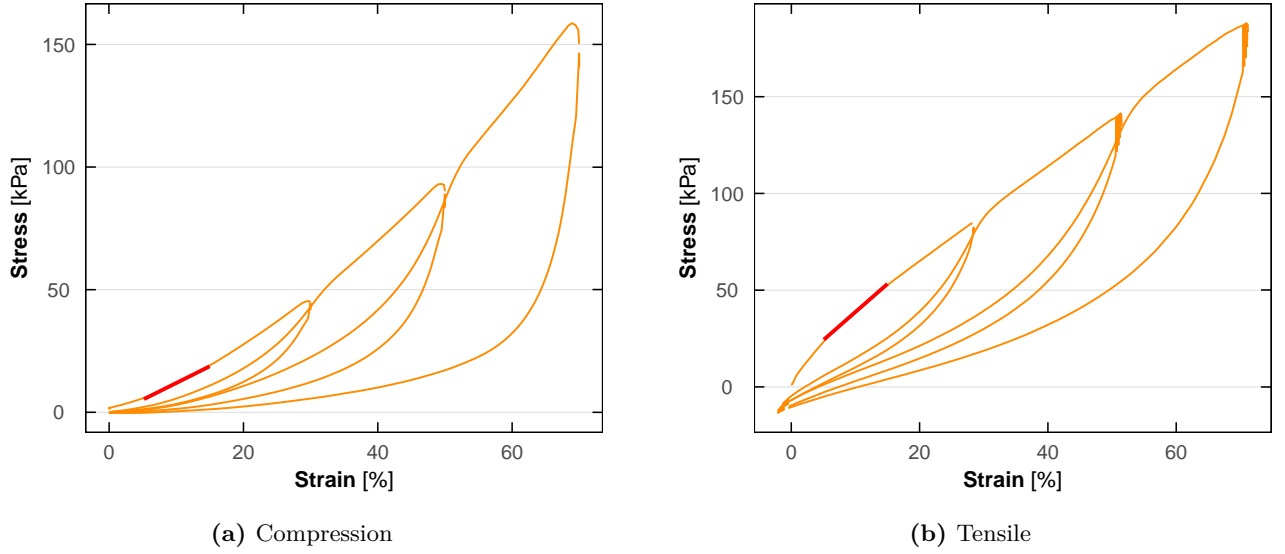


Figure 7.8: Representative cyclic loadings in (a) compression and (b) tensile of silk granular hydrogel - 5S⁵.

In parallel, single notch edge tests were performed for characterizing fracture energy of the composition 5S⁵. Fig. 7.9 shows the resulting fracture energies. The fracture energy reached an average of $400 \text{ kJ} \cdot \text{m}^{-2}$. The value was significantly higher than the hydrogel composites. However, the error is quite large due to some difficulties in processing larger samples.

Fig. 7.9c presents digital image correlation images showing the *von Mises strain* around the crack tip. Compared to hydrogel composites and hybrid granular hydrogels, the strains were very concentrated around the crack tip, suggesting that most of the energy was not well distributed in the hydrogel. It implies that the regenerated silk fibroin or/and the interface between microgels and silk fibroin are weak and break rapidly during crack propagation before transferring stress efficiently. Hence, enhancing the quality of the interfaces or/and the regenerated silk fibroin may significantly augment the fracture energy. Another possibility would be to incorporate cellulose fibers into the silk granular hydrogels. Indeed, several research groups have already developed cellulose and silk fibroin composites because it was observed that cellulose promotes structural changes by making electrostatic interactions, covalent, and hydrogen bonds with fibroin^[328].

In summary, silk granular hydrogels initially containing 4 wt.% of dry microgels swelled the less. However, those composed of 5 wt.% of dry microgels presented the best compromise between mechanical and swelling properties. In particular, the composition of 5S⁵ revealed promising results. Subsequently, a synthesis method for determining the recommended initial concentration of dry microgels in silk granular structures is proposed and explained in Fig. 7.10. For example, neat hydrogel N₁₀ has the same composition as the microgels. Both were initially composed of 10 wt.% of 20 kDa of PEGDM. Since the final polymer content of swollen neat hydrogels was measured at around 4 wt.%, the recommended initial concentration of dry microgels was estimated at 5 wt.%, which is 4 wt.% added to 1 wt.%. The addition of less or more than 1 wt.% will generate a too loosely or compact

granular structure inhibiting the adequate formation of silk fibers. Note the value of 1 wt.% was determined empirically. In order to generalize the rule, the method needs to be validated with other microgels.

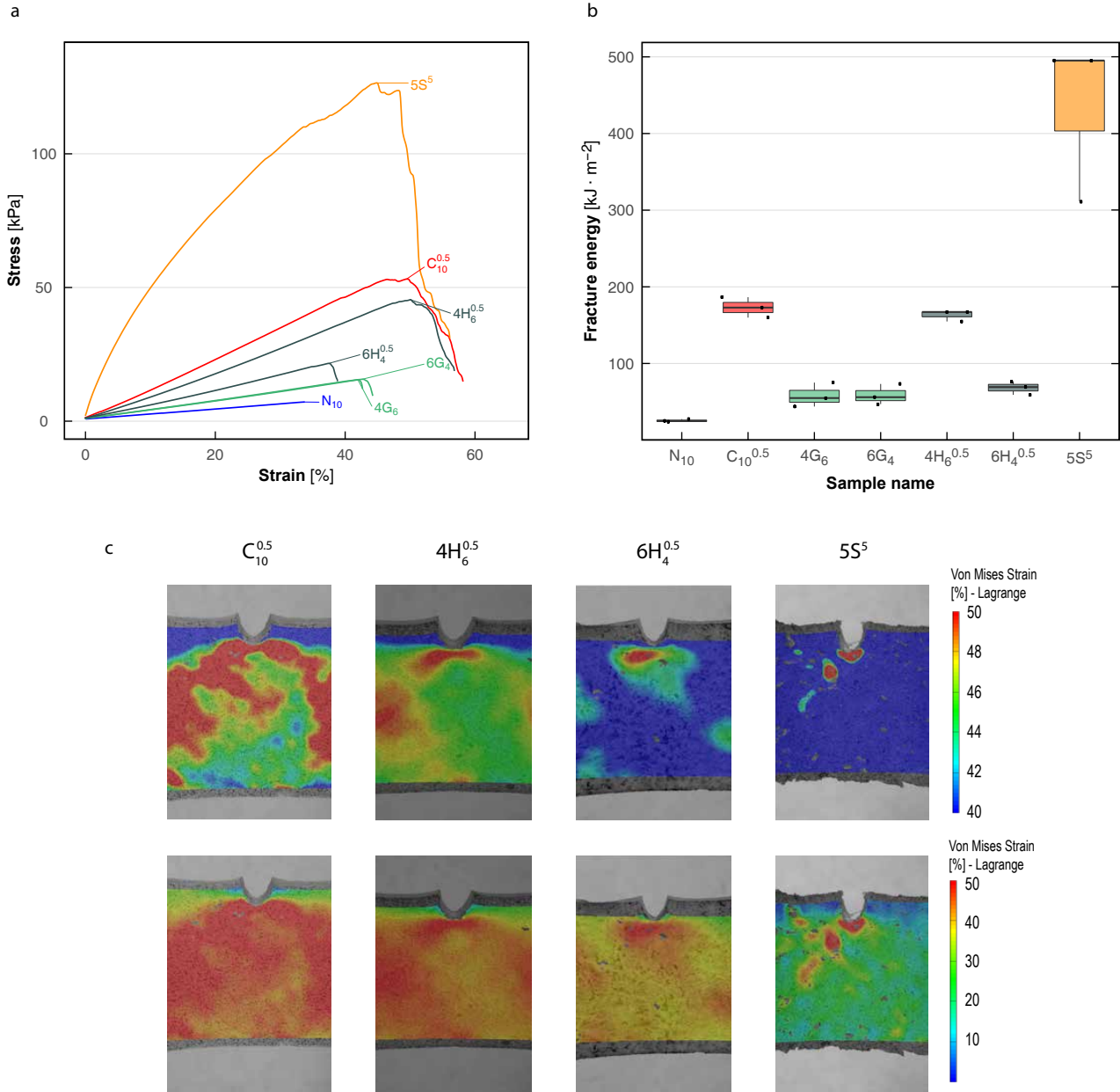
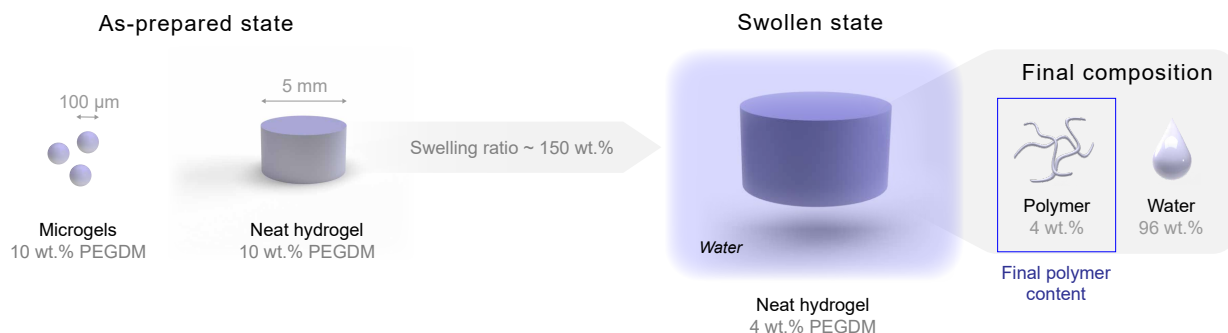


Figure 7.9: Fracture properties of neat hydrogel - N_{10} , hydrogel composites - $C_{10}^{0.5}$, granular hydrogel - $4G_6$ and $6G_4$ and of hybrid granular hydrogels - $4H_6^{0.5}$ and $6H_4^{0.5}$ and of silk granular hydrogel - $5S^5$: (a) representative curve of single notch edge tests, (b) fracture energy evaluated with equation (3.7) on p.53 and (c) digital image correlation images showing the *von Mises strain* around the crack tip, which starts to propagate.

STEP 1: determine final polymer content

Since measuring the composition of swollen microgels is challenging, the final polymer content is determined with swollen neat hydrogel, which has the same initial concentration as the microgels

**STEP 2: calculate the initial microgel content**

The initial microgel content is obtained by adding 1 wt.% of polymer to the obtained final composition of the swollen hydrogel. Note that the value of 1 wt.% was determined empirically for creating an optimal silk granular hydrogel.

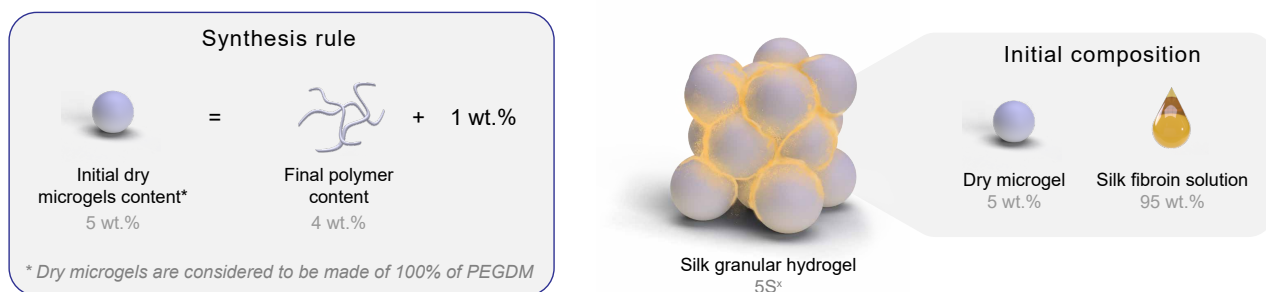


Figure 7.10: Synthesis method for creating an optimal silk granular hydrogel.

7.3.2 Microstructure and crystallinity of silk fibroin

The morphologies of silk granular hydrogels were observed under a fluorescent confocal microscope and shown in Fig. 7.11.

Silk fibroin was homogeneously distributed in most compositions and had successfully regenerated *in situ* around microgels, maintaining them together in a network-like structure. At higher microgel concentration, such as in the composition $6S^3$, the microgels were no more spherical, suggesting that silk fibroin started to crystallize before the microgels could freely pre-swell. Close to the surface, silk fibroin regenerated in a membrane-like structure. The difference in morphology might be initiated during the swelling of microgels in the silk fibroin solution. Indeed, silk fibroin was probably more concentrated between the microgels and regenerated faster than near the sample's extremities. Moreover, a broken sample's surface showed that the crack had surrounded the microgels during its propagation. It indicates that the interface silk fibroin - PEGDM microgels or silk fibroin fibers were weaker than the microgels.

Silk fibroin is polymorph and is usually distinguished between Silk I and II. Silk I represents the metastable silk fibroin, which contains mainly amorphous structures such as α -helices or random coil. Silk II is the solid silk fibroin and is mainly constituted of antiparallel β -sheets, which provide high

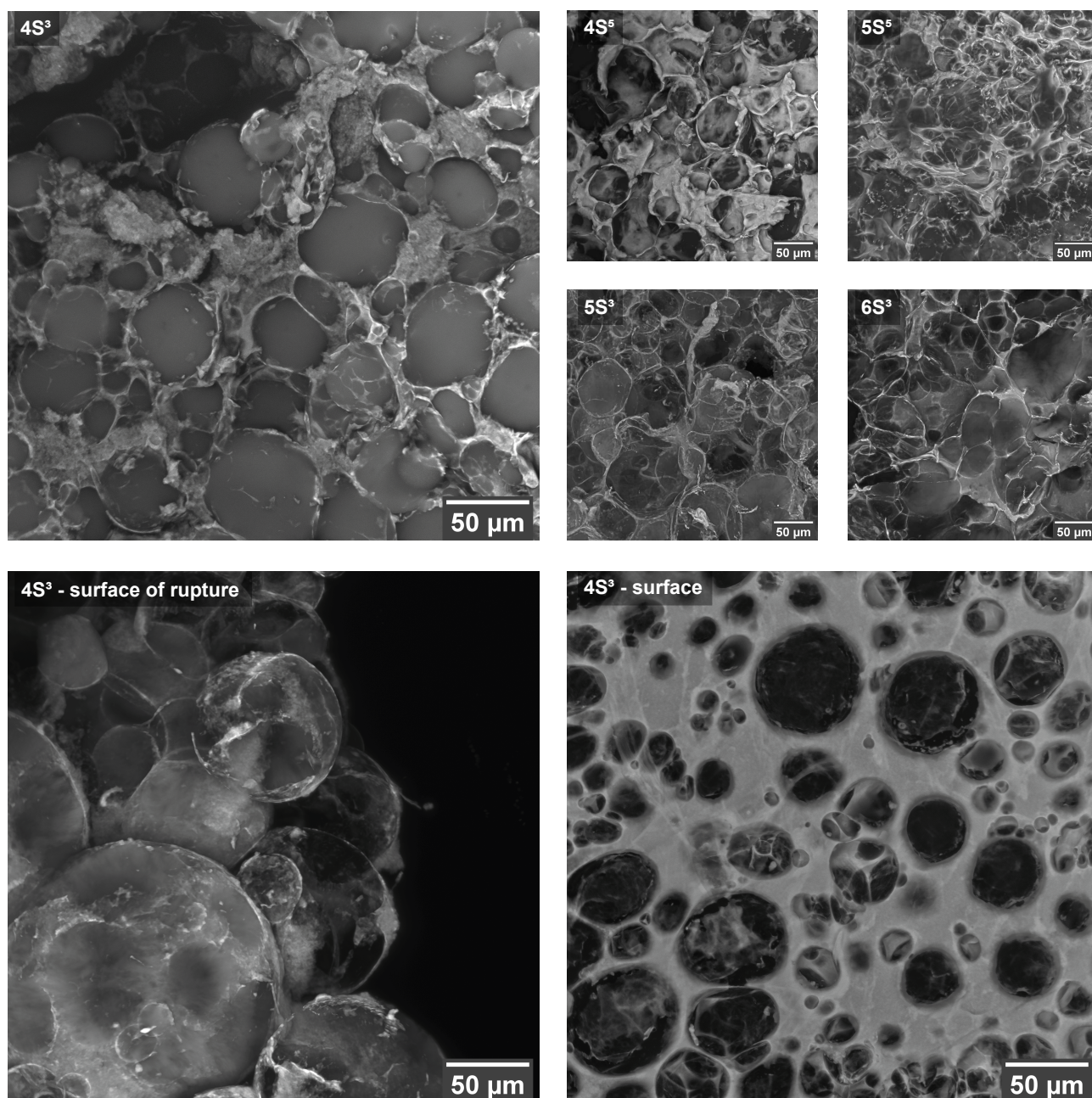


Figure 7.11: Z-projections taken with fluorescence confocal microscopy showing the internal microstructures of different silk granular hydrogels self-reinforced with regenerated silk fibroin fibers as well as the morphologies of regenerated silk fibroin close to the surface of the sample and the surface of rupture.

tensile strength. Note that Silk I can be converted in Silk II by external stimuli such as elongation, ultrasound, or temperatures^[145,146,329,330]. The crystallinity significantly influences the physical, mechanical, biological, and degradation properties. For example, the strong β -sheets have higher strength and are more hydrophobic, which slows down the degradation^[146].

The classical technique for determining the crystalline structures of regenerated silk fibroin is to inspect dry samples by Fourier-transform infrared spectroscopy (FTIR) and assign the secondary structures according to Table 7.1. Thus, silk granular samples, old of at least 48 hours, were slowly dried at

room temperature for 15 hours before being placed in a vacuum oven for 2 hours at 60°C. The infrared analysis covered then the range between 800-3500 cm^{-1} with a resolution of 4 cm^{-1} .

Table 7.1: Absorbance peaks of secondary structures of silk fibroin^[328,331–334]

Secondary structure	Wavelength [cm^{-1}]
Side chains	1605-1615
β -sheet (weak)/aggregate β -strand	1616-1621
Parallel β -sheet	1620
Anti-parallel β -sheet	1623
β -sheet (strong)	1618, 1621-1638
Random coil	1638-1654
α -helices	1655-1662
β -turns	1663-1696, 1715
β -sheet (weak)	1697-1703

The absorption spectra of the representative sample, 5S⁵, was first compared with that of dry microgels, mainly composed of PEGDM, for identifying the PEGDM phase in silk granular hydrogel. As shown in Fig. 7.12, contrary to microgels, the representative hydrogel 5S⁵ strongly adsorbed in the amide I (1600-1700 cm^{-1}) and II (1500-1600 cm^{-1}) regions^[332]. Thus, the absorption in these regions was associated with silk fibroin only. While the dried silk fibroin solution exhibited amorphous and crystalline structures, silk granular hydrogels had mainly absorption peaks belonging to silk II.

The peaks shown in Fig. 7.12 can be assigned to secondary structures according to the Table 7.1. The main peak around 1622 cm^{-1} corresponds to strong β -sheets, while the one close to 1697 cm^{-1} to weak β sheets.

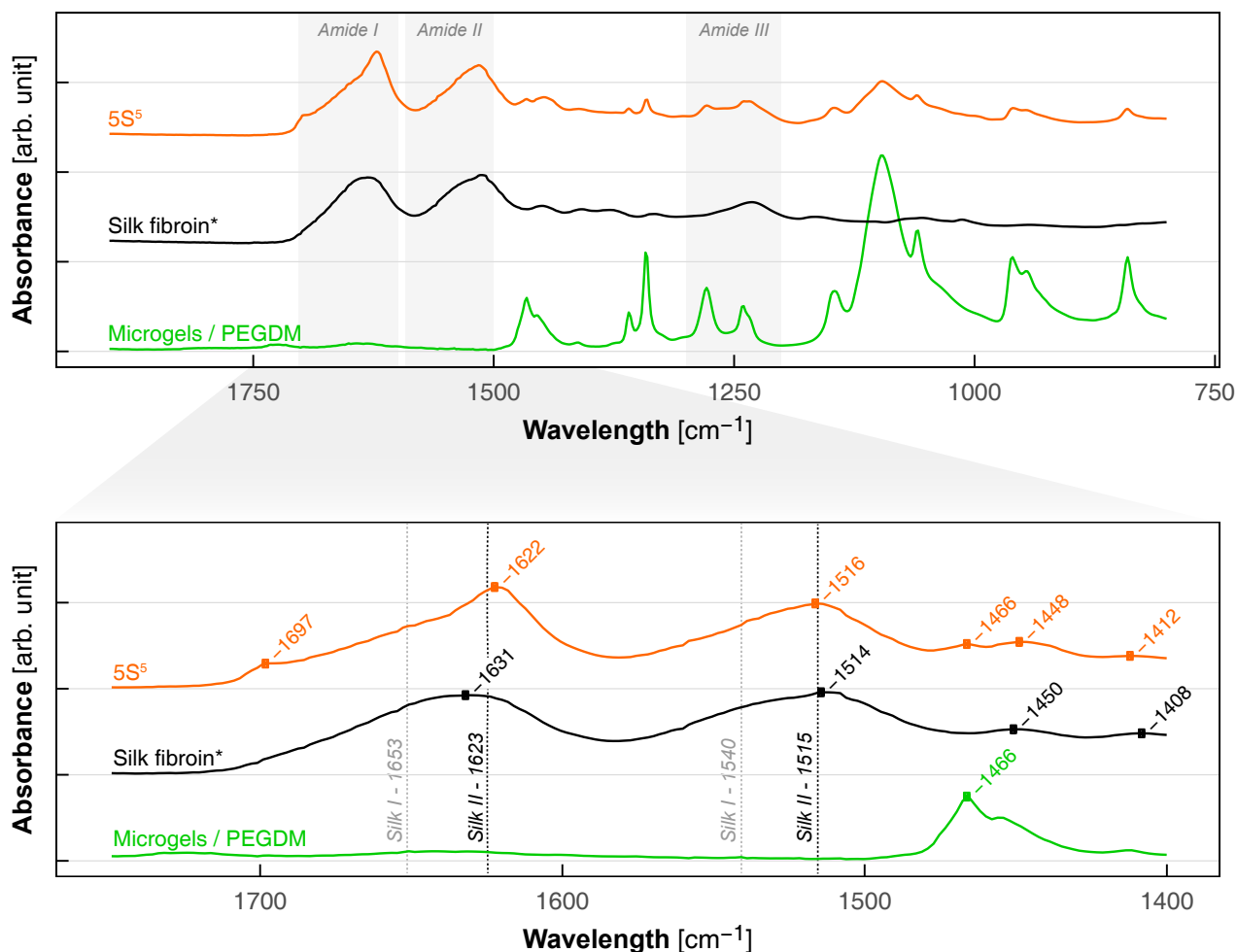


Figure 7.12: Fourier-transform infrared spectroscopy (FTIR) of dry silk granular hydrogel, regenerate silk fibroin, and microgels. PEGDM does not significantly adsorb in the amide I and II, which is ideal for comparing the structure of self-assembled silk fibroin in dry granular hydrogels. *Silk fibroin solution was dried for 2h at 60°C.

The secondary derivatives of convoluted IR Spectra revealed the hidden peaks, which are shown in Fig. 7.13. They highlighted the presence of α -helices or random coils in the structure as well as β -turns.

A more in-depth analysis was performed in deconvoluting the IR spectra with Gaussian curves and presented in Fig. 7.13. This process allowed us to estimate the percentage of each secondary structure. For silk granular hydrogels 5S⁵, a strong β -sheet represents almost 54% of the secondary structures, while the α -helices and random coils constitute around 10% respectively. Note that the signals highlighted with the secondary derivatives of convoluted IR Spectra are small. Therefore, a more accurate analysis would require a better resolution of the measurements.

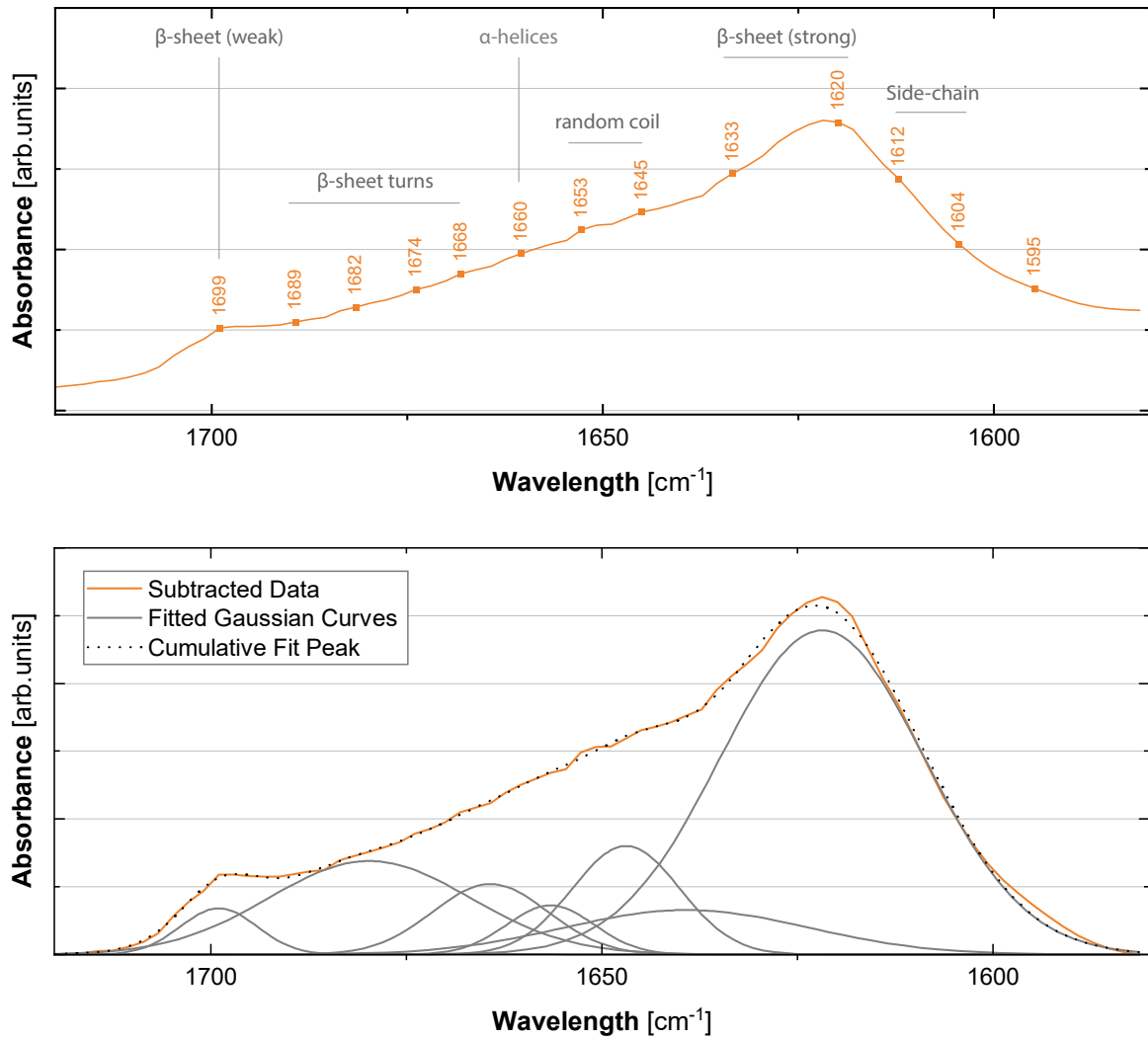
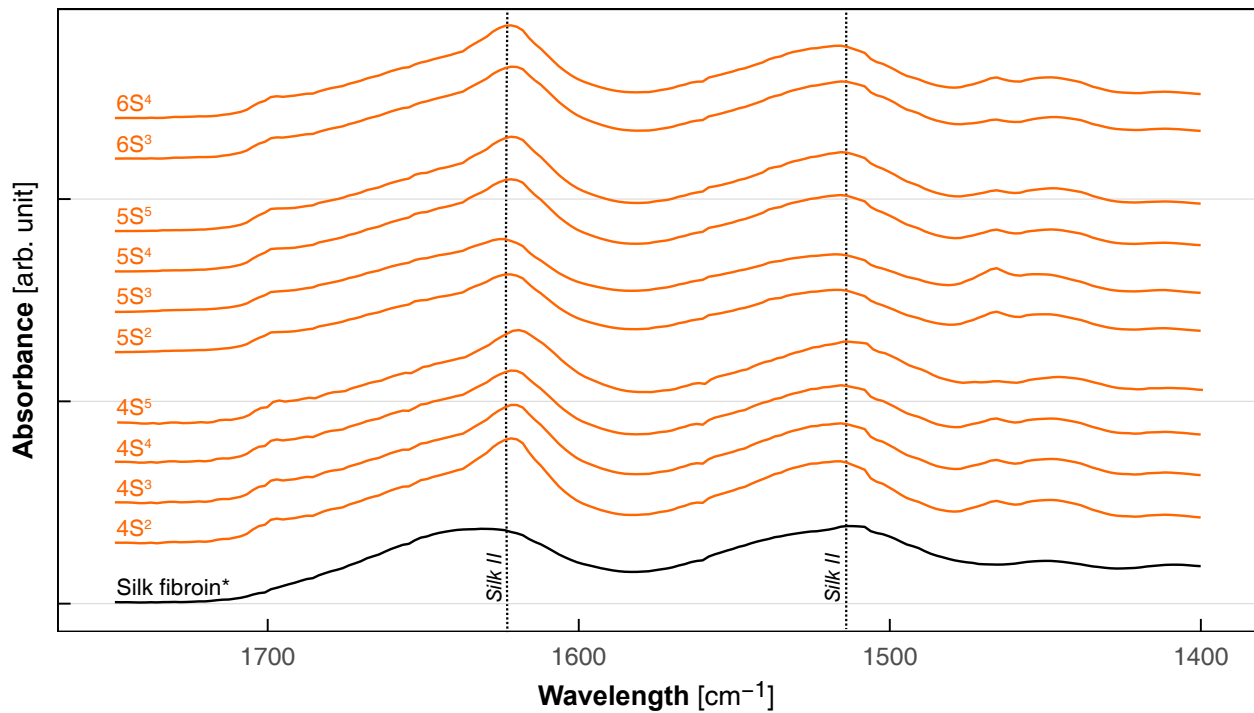


Figure 7.13: Secondary structures of silk fibroin regenerate in silk granular hydrogel. (a) Hidden peaks revealed by the second derivative of the convoluted IR spectra of silk granular hydrogel - 5S⁵. (b) Deconvolution of FTIR spectra using Gaussian curves of silk granular hydrogel - 5S⁵.

Fig. 7.14 presents the absorption spectra of silk granular hydrogels. All compositions showed similar behavior and have their main peak at 1622 cm⁻¹, which is assigned to strong β -sheet structure^[331–334]. The spectra of 5S² and 5S³ were slightly shifted to larger wavelength suggesting that the amorphous phase was slightly more abundant.

Table 7.2: Assigned secondary structures of silk granular hydrogel - 5S⁵ determined from deconvoluted Gaussian curves from FTIR Spectra.

Peak ID	Peak center [cm ⁻¹]	Peak area [cm ⁻¹]	Peak area [%]	Secondary structures
1	1622	15,6	53,5	β -sheet (strong)
2	1639	2,6	8,8	Random coil
3	1647	2,8	9,5	Random coil
4	1657	1	3,5	α -helices
5	1664	1,9	6,6	β -turn
6	1680	4,4	15,2	β -turn
7	1699	0,8	2,9	β -sheet (weak)

**Figure 7.14:** FTIR of silk fibroin fibers regenerated *in situ* in silk granular hydrogels.

7.3.3 Processing

Characterizing the processability of silk granular hydrogels is laborious because the gelation time of silk granular hydrogel varied from minutes to several hours. The regeneration time of silk fibroin is balanced between silk fibroin concentration and pH. Silk fibroin started to concentrate between microgels as soon as they started to swell and absorb the water from the silk fibroin solution. At higher microgel concentration, silk fibroin was more concentrated due to stronger swelling pressure from the micro-

gels and regenerated faster^[326,335]. In parallel, lower pH will promote crystallization^[326,327,336,337]. Nevertheless, the precursors did not have the same acidity. The pH of the initial silk fibroin solution was adjusted to 9.5 for avoiding early crystallization^[327], while demineralized water has a pH of 4.5. Since the pH of the precursors was not adjusted after mixing silk fibroin solution with water, the pH of precursor progressively increased with silk fibroin concentration, which slowed down the gelation.

Moreover, the regeneration speed of silk fibroin was most probably not homogeneous in the hydrogel self. Indeed, depending on their size, microgels adsorbed more or less water from silk solution, which created a local gradient in silk fibroin concentration. Additionally, dry microgels often formed agglomerates. Fig. 7.15 illustrates how agglomerates swell as a single massive particle during the swelling process. In this case, silk fibroin might start regenerating and encapsulating the agglomerates before the microgels can separate. The consequence is the formation of new and bigger aggregates and inhomogeneous distribution of silk fibroin, as highlighted in Fig 7.16. In particular, for some compositions such as $6S^2$ and $6S^5$, the gelation started almost immediately when the dry microgels were mixed with the silk fibroin solution. These samples were, therefore, not feasible for being shape in a mold.

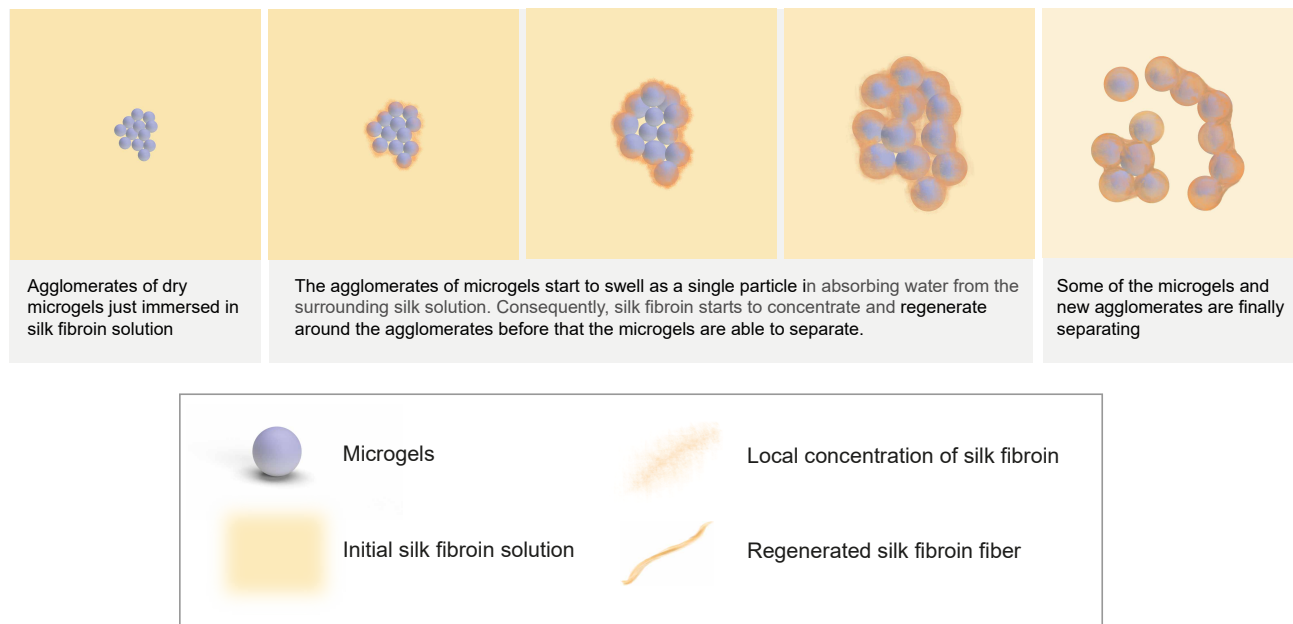


Figure 7.15: Illustration showing how silk fibroin regenerates around agglomerates of dry microgels.

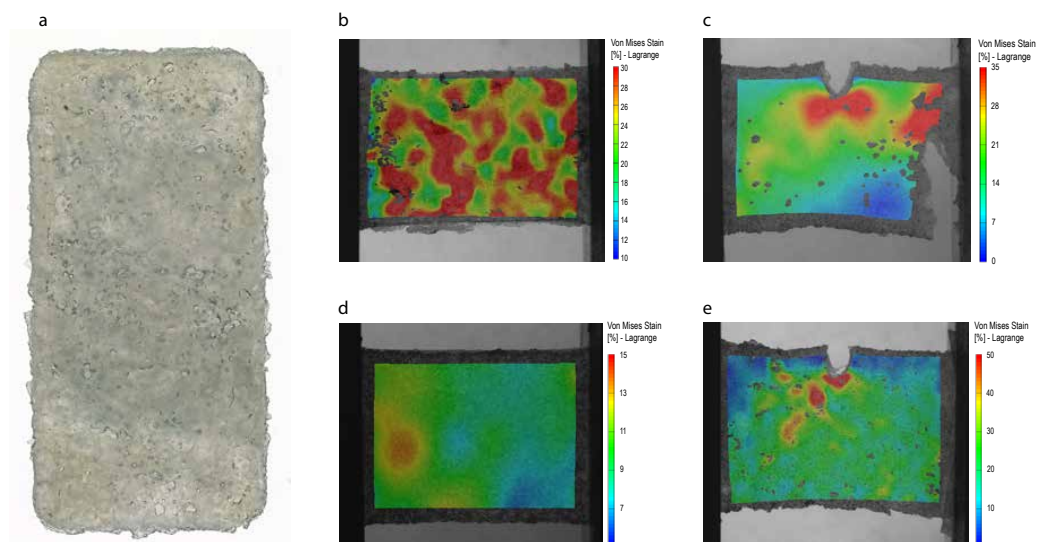


Figure 7.16: Sample quality of larger samples of silk granular hydrogels. (a) Image taken with a digital optical microscope, digital image correlation images highlighting (b-c) defective and homogeneous sample, (d-e) good samples.

Reducing agglomerates might be achieved by (i) slowing down the regeneration time of silk fibroin or (ii) by homogeneously pre-swelling the microgels in controlled relative humidity. Note that homogeneous pre-swelling of microgels is not straight forward, especially for polydispersed size distribution and dry microgels tightly in contact.

Qualitatively, the representative precursor $5S^5$ was injectable only through a large needle, as illustrated in Fig. 7.17. Nevertheless, it could easily be manipulated like a paste in a second step.

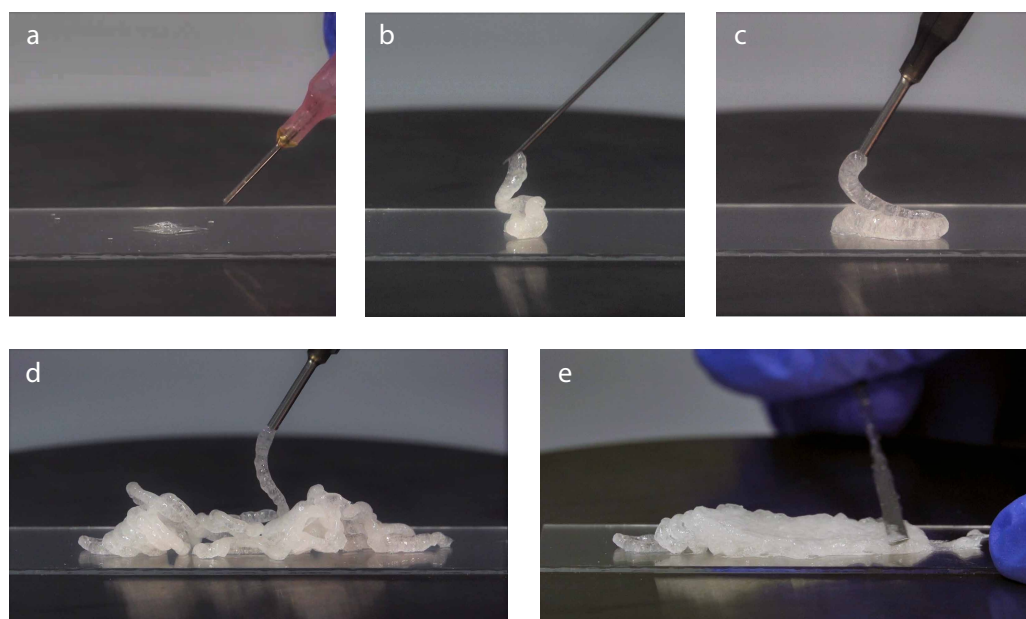


Figure 7.17: Injectability of a representative silk granular precursor $5S^5$, (a) aggregates are blocked in small needle, (b-d) the precursor is injectable (e) the precursors can be manipulate as a paste.

For future work, a quantitative characterization of the gelation time would help to better control the synthesis of silk granular hydrogels. This might be achieved by tracking the mechanical properties over time with a rheometer or an adapted *Vicat* test.

Direct contact test

The biocompatibility of silk granular hydrogels was rapidly assessed with a direct contact test for four days. The resulting images were taken with and inverted microscope (Nikon, Ti2) are presented in Fig. 7.18.

The brighter regions in Fig. 6.12 corresponds to the regions where the hydrogel had retracted during the staining process with Giemsa. The fibroblasts from the embryo of albino mice grew around and under the hydrogels for four days. However, silk granular hydrogel revealed some adverse effects on cell growth. Indeed, the fibroblasts proliferated better in composition with lower silk fibroin content. The differences were probably issued from the synthesis process of the silk fibroin solution. Therefore, more efforts on the cleaning and sterilization of the solution have to be performed.

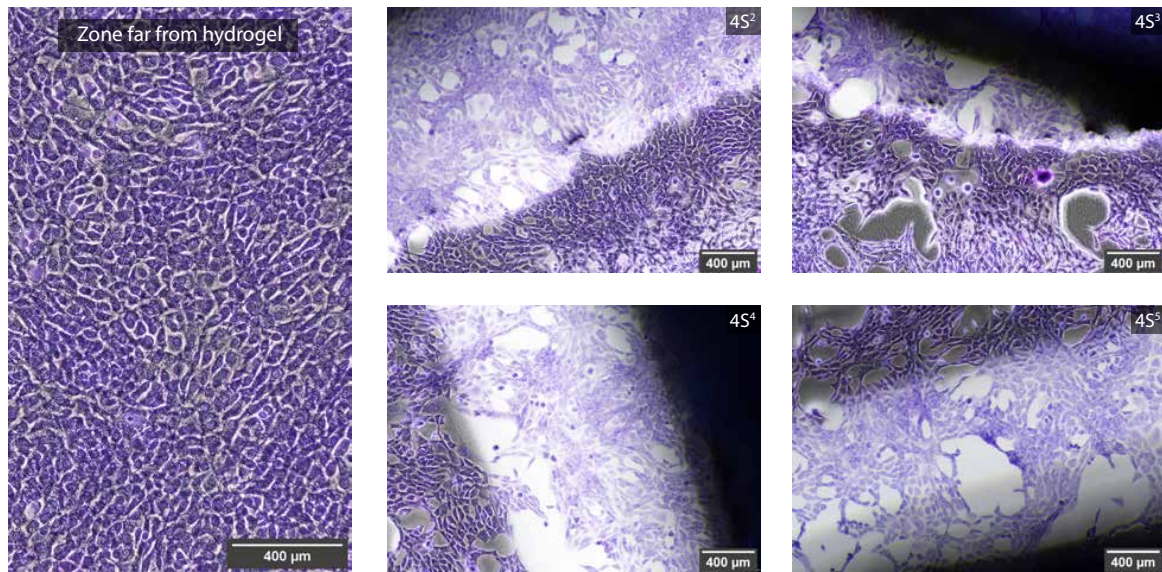


Figure 7.18: Direct contact test of silk granular hydrogels. Fibroblasts from embryo of albino mice were fixed with methanol after four days and stained with Giemsa procedure.

7.4 Conclusions

A new strategy was investigated to reinforce and maintain microgels together with a novel self-reinforced silk granular hydrogel composed of 20 kDa poly(ethylene glycol) dimethacrylate microgels and regenerated silk fibroin fibers. The principle is to locally concentrate and regenerate silk fibroin *in situ* using microgel swelling.

A study on 12 different hydrogel compositions showed that silk fibroin in most hydrogels was homogeneously distributed and had successfully regenerated *in situ* around microgels, maintaining them together in a network-like structure. FTIR analysis revealed the presence of amorphous and crystalline silk fibroin, where 50% of the secondary structures could be assigned to strong β -sheets.

Cyclic compression and tensile tests showed that silk granular hydrogels became softer after the first loading cycle and exhibited, therefore, similar characteristics to the *Mullins effect*. Moreover, the tensile moduli, *i.e.* 86-296 kPa, were significantly larger than compressive moduli, *i.e.* 58-136 kPa suggesting that microgels principally contribute to compressive modulus, while silk fibroin fibers mainly participate in the tensile properties. However, the strains measured at failure, *i.e.* 29-62% were probably limited by the maximal elongation of regenerated silk itself.

Silk granular hydrogels exhibited swelling ratios between 5 vol.% and 60 vol.%. Interestingly, the swelling of silk granular hydrogels increased proportionally with the microgel content suggesting that swelling is essentially governed by the microgels, which allowed us to estimate the final water content (WC) of microgels to around 97 wt.%.

In summary, silk granular hydrogel initially containing 4 wt.% of dry microgels swelled the less. However, those composed of 5 wt.% of dry microgels presented the best compromise between mechanical and swelling properties. Subsequently, we proposed a synthesis method for obtaining optimal silk granular hydrogels by choosing the right initial concentration of microgels.

The obtained silk granular hydrogel can be processed by injection with a large needle and/or casting in shape into a given volume. However, the spreading of the microgels and the pH level of all precursors need to be well controlled to extend the use of silk granular hydrogels further. Furthermore, more efforts on the cleaning and sterilizing of the silk fibroin solution have to be done because silk granular hydrogel revealed some adverse effects.

Nevertheless, the knowledge acquired from this study and the previous chapters enables the interpretation of adequate hydrogel materials for given applications.

Chapter 8

Tailoring hybrid hydrogels for load-bearing applications

How to select and combine hydrogels to better mimic the microstructures and functions of living tissues?

Tailoring individually mechanical and physical properties is essential for designing optimal customized implants. Therefore, to extend and apply the knowledge acquired from studying various structures, hybrid hydrogels, composed of stacked hydrogels, were designed for better targeting local properties or mimicking the morphology of native tissues. Mechanical gradients were successively processed in hybrid hydrogel through a sequential layering of hybrid or silk granular hydrogels. The surface strain field observed via digital image correlation revealed the created mechanical gradients with the silk or hybrid granular hydrogels. Hybrid granular hydrogels offered much more possible material combinations than silk granular hydrogels and were easier to process. However, the overall swelling ratios of about 90 vol.% was significantly higher than the one of silk-based hydrogels, which was less than 20 vol.%. In a second step, a hydrogel composite and a silk granular hydrogel based on gelatin hydrogels were synthesized to show the potential of the studied structures with other hydrogels and microgels. It was demonstrated that cellulose fibers could reinforce gelatin hydrogel similar to PEGDM hydrogels and that silk granular hydrogel based on gelatin microgels could successfully be synthesized. More specifically, the synthesis protocol developed for PEGDM microgels could be applied for gelatin microgels, while the synthesis method for determining the initial concentration of dry microgels in silk granular structures was validated. Moreover, stiff gelatin microgels significantly contributed to the compressive modulus. They limit, however, the lateral deformation of silk fibroin fibers during tensile loadings, reducing the hydrogel's maximal elongation. Therefore, softer gelatin microgels would be required to improve the strain at failure of gelatin-based silk granular hydrogels.

Keywords: material combination, gradients, gelatin, microgels, silk fibroin, composites.

8.1 Introduction

The ideal implant requirements differ according to the application, the patient, and the location, especially when the targeted tissues show some anisotropy. For example, as illustrated in Fig. 8.1, the properties of articular cartilages are highly depth-dependent. Besides, they vary a lot from person to person. Antons *and al.* reported serious variations up to 4 MPa, probably due to age, diseases, genetic or hormonal factors^[165]. Therefore, a broad understanding of how to tailor mechanical and physical properties individually is necessary to design an optimal customized implant. There are many ways to tailor the properties of hydrogels. Nevertheless, changing the components' concentration or microstructures in keeping the same basic materials is often preferred over chemical modifications. Indeed, chemical modifications influence almost all mechanical, physical, and biological properties and might induce new toxic reactions. Therefore, additional assessment is required, especially regarding biocompatibility, which can be very costly.

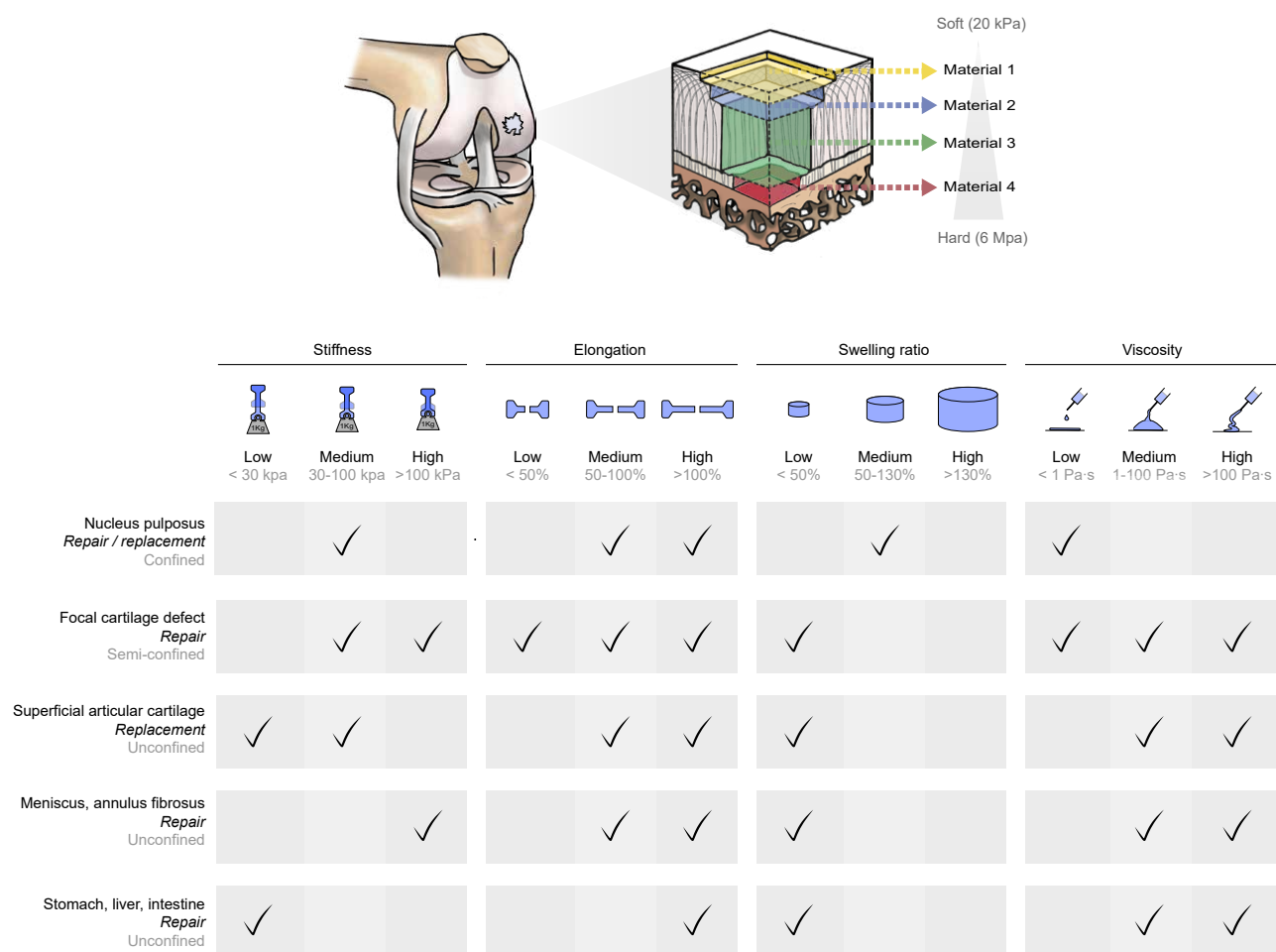


Figure 8.1: Examples of requirements for the ideal implant according to applications and the location^[1-6,165,338-344].

In previous chapters, an extensive parametric study on the composition and structure of hydrogels (Fig. 8.2) was performed for creating complete property charts that summarize mechanical, swelling, and rheological properties.








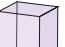
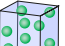

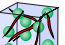

		Hydrogel components				
		 PEGDM Main network	 Alginate Second network	 Microgels	 NFC fiber	 Silk fibroin fiber
Neat - N		✓				
Composite - C		✓			✓	
Double network - DN		✓	✓			
Granular - G		✓		✓		
Composite double network - CDN		✓	✓		✓	
Hybrid granular - H		✓		✓	✓	
Silk granular - S				✓		✓

Figure 8.2: Components of studied hydrogel structures.

Fig. 8.3 summarizes the range of properties achieved for each structure. The precursors of neat hydrogel had the lowest viscosity, perfect for confined applications such as the replacement of nucleus pulposus^[1]. Microgels of similar composition can be added to the precursor to adapt and increase its viscosity for unconfined applications like the treatment of focal cartilage defects without using a membrane^[320], or 3D printing of complex unconfined structures^[7]. In parallel, adding cellulose fibers is a powerful way of increasing toughness. This method was more effective than creating a double network with alginate. Indeed, while the results were promising at the *as-prepared state*, alginate has lost almost all its benefits in the *swollen state*. Moreover, high-cycles fatigue tests revealed that hydrogel composites reinforced with nano-fibrillated cellulose fiber successfully survive 10 million loading cycles at 20% applied strain. However, after the first loading cycle, a softening behavior similar to the Mullins effect was observed. Therefore, we assessed how cyclic loading affects its fracture behavior, distribution of strain fields, and microstructure. The study showed that cyclic loading on hydrogel composites re-arrange the fiber network and do not seriously deteriorate the mechanical properties. Therefore, with their high fatigue resistance and their low precursor's viscosity, hydrogel composites were already proposed for replacing the nucleus pulposus^[1]. We also showed that combining composite and microgel approaches efficiently tailored hydrogels' swelling without significantly affecting elastic modulus, fracture energy, and deformation performance. Therefore, those hybrid granular hydrogels might be suitable for replacing the superficial layer of articular cartilage, where toughness is essential for limiting the propagation of cracks in the deeper and stiffer layers. Finally, the microgels can be swollen in silk fibroin solution for forming self-reinforced silk granular hydrogels, where around 50% of

the secondary structures could be assigned to strong β -sheets. Those hydrogels exhibit considerably higher stiffness. Although the maximal extension of regenerated silk fibroin fibers reduced the hydrogel's elongation capability, silk granular hydrogel is a potential candidate for repairing focal cartilage defects.



Figure 8.3: Range of properties of studied hydrogel structures.

Note that the range of elastic moduli achieved remains relatively low for load-bearing applications. Nevertheless, all samples were tested in an unconfined environment, which represents the worst case. Indeed, if a hydrogel with an elastic modulus of 50 kPa, is placed in a focal defect of stiffer cartilage, the hydrogel is semi-confined. Subsequently, the compressive modulus drastically increases because the water contained in the hydrogel act as an incompressible material. For example, hydrogel composite - $C_{10}^{0.5}$ was previously tested in a confined environment. The elastic modulus reached around 1 MPa at a loading rate of 10 N/s, while the swelling pressure was measured at 85 kPa^[1].

This chapter aims to extend and apply the knowledge acquired from previous chapters. Hybrid hydrogels, composed of stacked hydrogels, were designed for better targeting local properties or mimicking the morphology of native tissues. First, different hydrogel structures are combined in stacked layers to develop mechanical gradients in hydrogels. In a second step, we selected other hydrogels and microgels for shifting the overall properties in one or the other direction.

8.2 Materials and methods

8.2.1 Materials

20 kDa poly(ethylene glycol) dimethacrylate (PEGDM) was purchased from Polysciences (ref. 25406-25, Germany). Nano-fibrillated cellulose (NFC) fibers from bleached softwood pulp were provided by Weidmann (WMFC-Standard). The length of most fibers varies between 50-500 μm , while their diameters between 0.1-10 μm . *Bombyx mori* silk fibers were provided by swiss silk. 20 kDa poly(ethylene glycol) (CAS 25322-68-3), mineral oil (CAS 8042-47-5), and span 80 (CAS 1338-43-8) were supplied by Merck. Irgacure 2959 from BASF was used as a photoinitiator for PEGDM-based hydrogel, while lithium phenyl(2,4,6-trimethylbenzoyl)phosphinate (LAP, ref 6146), obtained from Tocris Bioscience, was used for gelatin-based hydrogel. Gelatin Type A from porcine skin (ref. G2500) and methacrylic anhydride (ref. 276685) was obtained from Sigma-Aldrich.

8.2.2 Synthesis of microgels

The synthesis of microgels, initially composed of 10 wt.% PEGDM, are described in Fig. 3.2 in *Chapter 3. Materials and methods*. The particle size distribution of microgels was measured with a digital particle size analyzer (Saturn DigiSizer II, micromeritics), where the refractive index was estimated at 1.334 with a tomographic microscope (3D Nanolive Cell Explorer) and the density at 1.01 g/cm³. As shown in Fig. 6.2 the size of particles varied from 20-160 μm .

8.2.3 Synthesis of silk fibroin

Silk fibroin was extracted from *Bombyx mori* silkworms. As illustrated in Fig. 3.3 in *Chapter 3. Materials and methods*, silk fibers were boiled in water containing 0.05 wt.% of sodium carbonate (Na_2CO_3) for 45 min and washed three times with pure water to remove sericin. After drying at 60°C for 4h, the remaining silk fibroin was dissolved in 80 wt.% 9.3M lithium bromide for 4h, before to be dialyzed for three days against pure water. The final concentration of silk fibroin was measured at 4.5 wt.%, while the pH was adjusted at 9.5 by adding ammonium at low concentration to avoid early crystallization^[327].

8.2.4 Synthesis of hydrogels

The full synthesis of the neat hydrogel, hydrogel composite, granular hydrogel, and hybrid granular hydrogels are described and illustrated in Fig. 3.4-3.8 in *Chapter 3. Materials and methods*.

Self-reinforced granular hydrogels were synthesis as shown in Fig. 3.9 on p. 44. The precursors were cast in acide polylactique (PLA) molds and cover with a microscopic glass before being placed in an incubator at 37°C for 12h. Table summarizes the dimension of casting molds 6.1.

The gelatin methacryloyl hydrogel (GelMa) was developed by Peyman Karami, from the laboratory of biomechanical orthopedics (LBO, EPFL), as previously reported methods^[345]. The precursors,

composed of 10-15 wt.% of gelatin methacryloyl, 0.02 wt.% LAP photoinitiator and phosphate and buffered saline (PBS) were vortexed at 37°C for homogenization. The hydrogels composite precursor was then mixed with the Ultra Turrax (IKA T25 digital, SN 25 10G) at 10'000 rpm for 5 min. The homogenized precursors were either cast in Teflon molds and covered with microscope slides or mixed with mineral oil and 5 wt.% Span 80 for synthesizing microgels. Both were cured for 2 min under UV-light irradiation at a wavelength of 405 nm and an intensity of 5 mW.cm⁻².

8.2.5 Swelling ratios

The volume of the samples was determined with Archimedes' principle. The samples were immersed in extra pure hexane (99+%, Fisher Chemical) with a density of $\rho = 0.659$ g/l. For reaching the equilibrium swelling state, the hydrogels were immersed in distilled water for at least 24h before measuring the swelling ratio (SR) with equation (3.3) on p.49. The average swelling ratios and their corresponding standard deviation errors were based on three different samples.

8.2.6 Compression and tensile test

Cyclic compression and tensile loadings were performed as previously described in section 3.4.4 on p. 50 on swollen hydrogels with a tensile machine (5 kN Zwick equipped with a 100 N load cell, Zwick Roell, Germany) presented in Fig. 3.14 on p. 51 at a constant displacement rate of 1 mm/s. For evaluating the real stress, it was considered that no change of volume occurs during loading time. Three samples were tested in the *swollen state* under cyclic loading-unloading compression loading. They were five different stages during the tests:

- Stage 1: 3 cycles between 0% and 30% applied strain
- Stage 2: 3 cycles between 0% and 50% applied strain
- Stage 3: 3 cycles between 0% and 70% applied strain
- Stage 4: 3 cycles between 0% and 90% applied strain
- Stage 5: loading up to rupture if the samples could sustain deformation up to 90%

The pre-loading was 0.05 N and 0.02 N for compression and tensile test respectively, The elastic moduli were then determined by linear regression between 10% and 15% applied strain during the first loading cycles. Note that for the tensile test, the strain was reordered with a virtual extensometer (VideoXtens, Zwick / Roell).

8.2.7 Digital image correlation analysis

Graphit 33 (Kontakt Chemie, Germany) was sprayed on samples' surface to make a fine, randomly, and homogeneously distributed speckles pattern. 3D DIC analysis was then performed with the test equipment illustrated in Fig. 3.19 provide by correlated solutions according to the test parameters presented in Table 3.4. The test equipment incorporates two cameras Grasshopper USB3 (monochrom,

5.0 Mpix, 75 fps), 70 mm lens, the software Vicsnap V.9 for the recording of images, and VIC3D V.8 for the analysis. The reference images were taken when the applied load reached 0.04 N.

8.2.8 Microstructures

The morphology and distribution of the regenerated silk fibroin were observed in swollen hydrogels with an inverted fluorescent confocal microscope (Zeiss LSM 700) equipped with a 20x lens and a laser of 555 nm. For enhancing fluorescence of silk fibroin fibers, the self-reinforced granular hydrogels were placed for at least 3 hours in 0.02 g/l Rhodamine B stain (Merck, CAS 81-88-9) before being placed in pure water for at least 2 hours .

8.3 Gradient in hydrogels

Hydrogels can currently not compete with some load-bearing tissues, such as meniscus or articular cartilage, mainly because it is difficult to mimic their highly hierarchical microstructures. Articular cartilage exhibits multiple mechanical gradients, for example. The stiffness progressively increases when approaching the subchondral bone and regions, which sustain and transfer higher loads. However, gradients are usually ignored in tissue engineering, mainly for practical reasons, despite their physiological functions. Creating gradients, especially multiple gradients, remains challenging and often requires special equipment and a complex synthesis process^[22]. Nevertheless, these last years, many techniques were established to create layered or continuous gradients in hydrogels as illustrated in Fig. 2.5 and described in Table 2.6 on p. 21^[22,167–174]. The choice of the synthesis process is based on different criteria such as the type of gradients (*i.e.* continuous or layered), type of precursors (*i.e.* low or high viscosity, crosslinking mechanism), freedom of geometries (*i.e.* film, cylinder, or complex 3D printed geometrie), or the number of gradients (*i.e.* gradient in one or different directions).

For example, as presented in Fig. 8.4, to obtain well-defined mechanical gradients through additive manufacturing, the stacked hydrogels require to have (i) different stiffnesses, (ii) similar swelling ratios to avoid dimensional distortion, (iii) sufficient adhesion between the layers and (iv) a viscous precursor with low diffusion rate of its components to avoid full homogenization across the layers before curing. Note that precursors with low viscosity can be employed as well. Nevertheless, curing must be done between each layer.

Different compositions of hybrid and silk granular hydrogels were selected that exhibited high precursors' viscosity, different elastic moduli, and similar swelling ratios to create hybrid hydrogels with gradients properties. The mechanical gradients were processed through sequential layering. This technique was favored over other techniques such as controlled fluid mixing or graded crosslinking because the process is simple, reproducible, and can be applied to different material systems^[22].

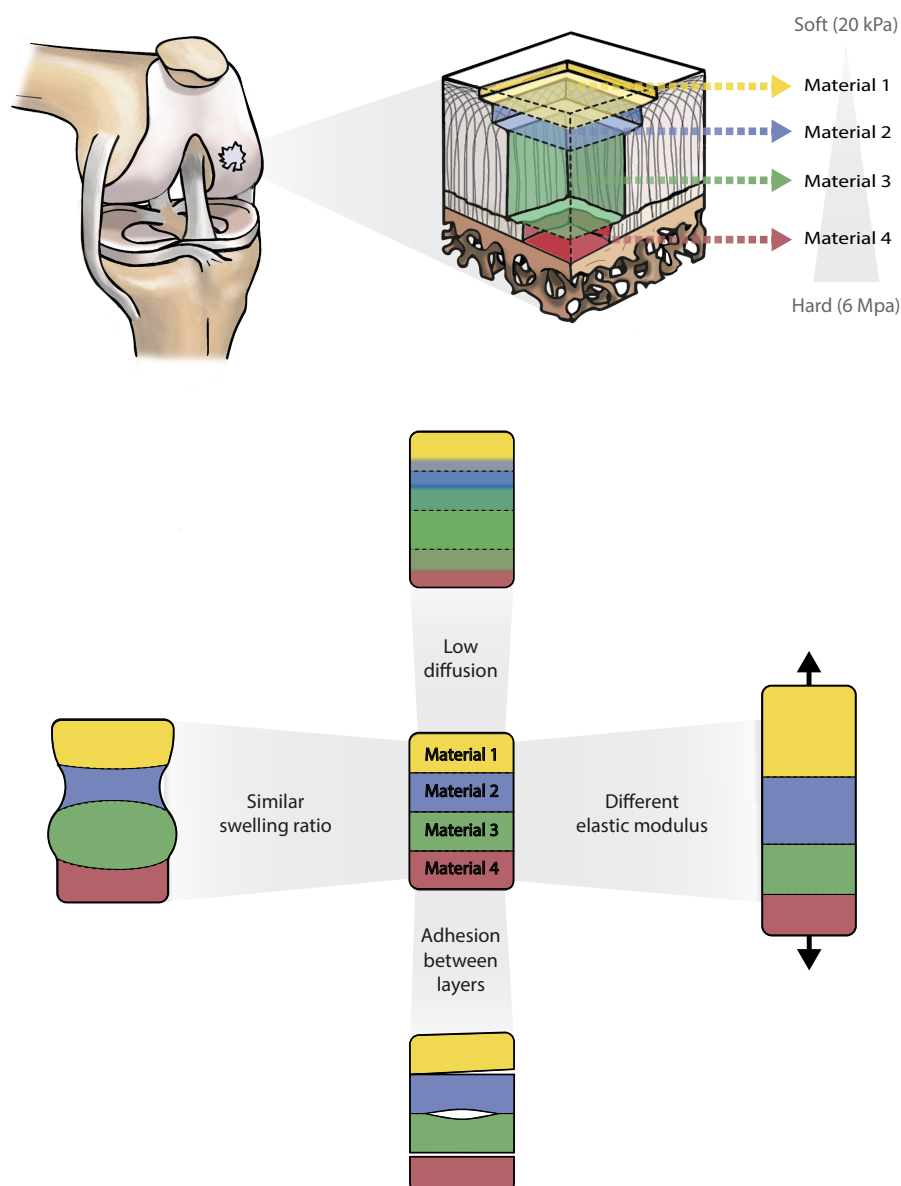


Figure 8.4: Requirements for developing mechanical gradients in hydrogels through sequential layering. The example illustrates the local replacement of osteochondral tissues exhibiting a mechanical gradient with four different materials.

8.3.1 Hybrid granular hydrogels

For designing hybrid hydrogels with gradient properties, the compositions specified in Table 8.2 were carefully chosen according to the property chart presented in Fig. 6.3 on p. 99 and Fig. 6.10 on p. 108 summarizing compressive modulus, the swelling ratio, and complex viscosity. Their precursors were placed side by side before curing. Fig. 8.5 presents the resulting hybrid hydrogel.

Fig. 8.5a shows hybrid hydrogels with a mechanical gradient in the *as-prepared state* and *swollen state*. Although the volume increase is consequent, the swelling of the hydrogels seems to be homogeneous. As observed in Fig. 8.5a, there is no significant difference in width between the layers.

Table 8.1: Selection of hybrid granular hydrogels for creating gradients through sequential layering.

Sample name	Compressive modulus [kPa]	Tensile modulus [kPa]	Fracture energy [$\text{kJ} \cdot \text{m}^{-2}$]	Swelling ratio [vol.%]	Complex viscosity [$\text{Pa} \cdot \text{s}$]
$5\text{H}_3^{0.1}$	15 ± 1	27 ± 3	28 ± 1	87 ± 1	247
$5\text{H}_4^{0.5}$	25 ± 1	41 ± 7	68 ± 21	91 ± 2	179
$6\text{H}_4^{0.5}$	42 ± 1	63 ± 4	68 ± 9	88 ± 4	1005
$4\text{H}_6^{0.5}$	53 ± 2	90 ± 3	163 ± 7	90 ± 4	362

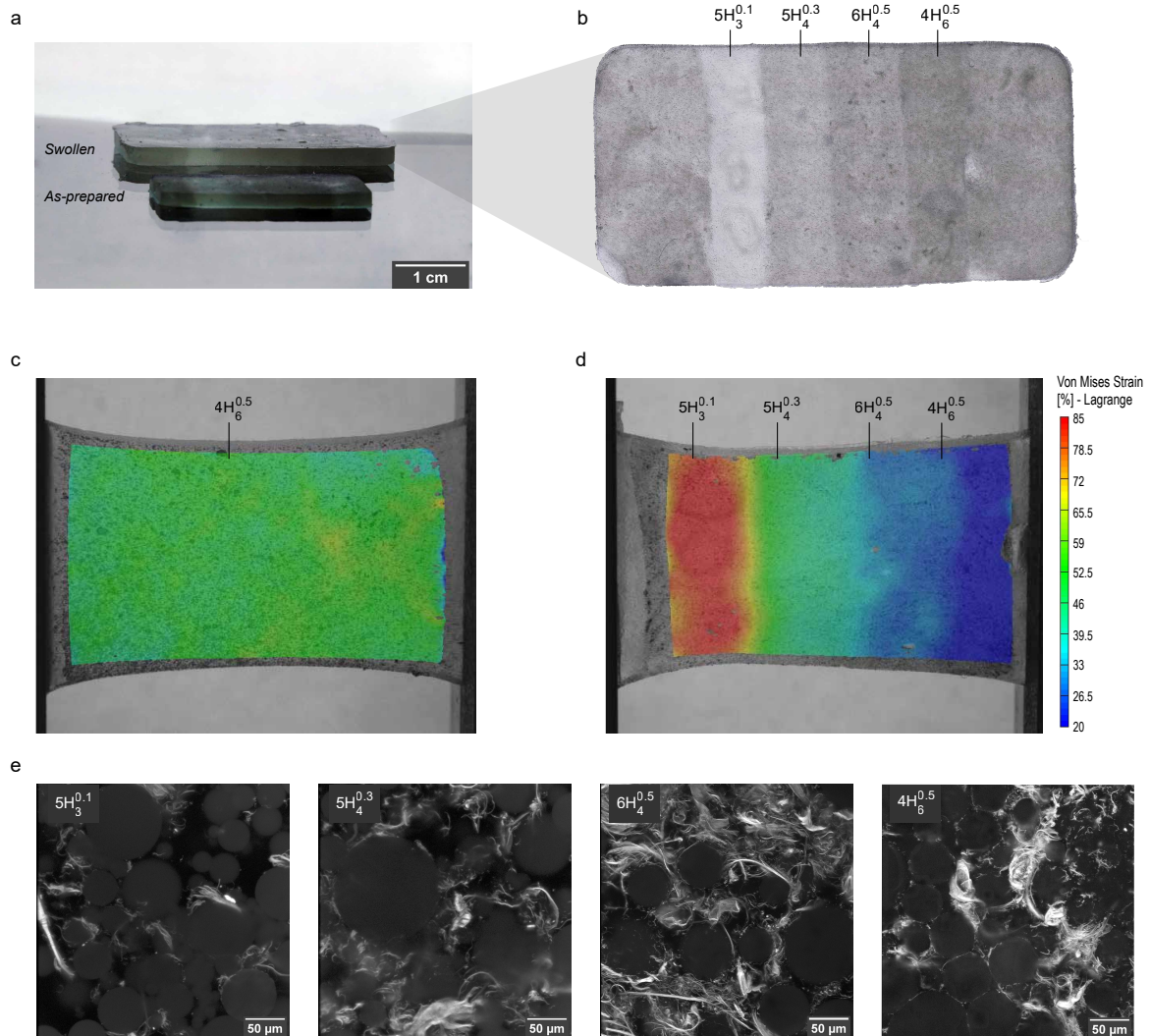


Figure 8.5: Gradient in hybrid hydrogels through sequential layering of hybrid granular hydrogels: (a) the swelling ratio of about 90 vol.% from *as-prepared state* to *swollen state* represents a consequent increase of volume, (b) swollen sample shows no dimensional distortion between layers of different composition. Digital image correlation showing strain field on the surface of representative hydrogel (c) without and (d) with a mechanical gradient. (e) Z-projections taken with fluorescence confocal microscopy showing the microstructures of hybrid granular hydrogels for each layer.

The surface strain field was measured via digital image correlation for observing the gradients in the hydrogel qualitatively. Fig. 8.5c shows a representative sample $4H_6^{0.5}$ without gradient that deformed homogeneously, while Fig. 8.5d presents a hydrogel made of layered precursors, which revealed a mechanical gradient.

This experience demonstrated that the layering of hybrid granular precursors effectively creates a mechanical gradient in hydrogels. However, the overall swelling ratios remained relatively large.

Hybrid hydrogels composed of two materials with different swelling ratios

For illustrating what happens when two materials with different swelling ratios are combined, the granular hydrogel $6G_4$ and hybrid granular hydrogel $5H_3^{0.3}$ were combined. They were selected according to the property chart presented in Fig. 6.3 on p. 99 and Fig. 6.10 on p. 108. Their precursors were either placed side by side or on top of each other before curing. Table 8.2 gives some of the properties, while the resulting hydrogels are presented in Fig. 8.6.

Table 8.2: Selection of hybrid granular hydrogels with different swelling ratios.

Sample name	Compressive modulus [kPa]	Swelling ratio [vol.%]	Complex viscosity [Pa · s]
$6G_4$	19 ± 1	137 ± 1	426
$5H_3^{0.3}$	20 ± 1	79 ± 3	291

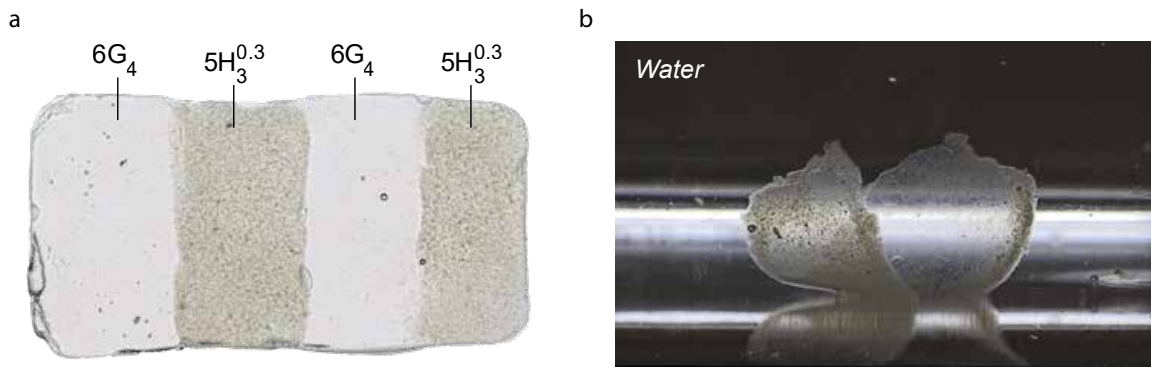


Figure 8.6: Layering of granular hydrogel $6G_4$ and hybrid granular hydrogel $5H_3^{0.3}$ with different swelling ratios (a) side by side or (b) on the top of each other.

This second experiment showed that layering of granular hydrogel and hybrid granular hydrogel with different swelling ratios is feasible and induces changes in geometries. The latter can present drawbacks or/and assets, depending on the applications. For example, directional swelling is used in 4D printing^[119,180,181] or in the development of biomimetic anisotropic actuators used for soft robotic, valves or artificial muscles^[175,182].

8.3.2 Silk granular hydrogels

For combining three silk granular hydrogels, the compositions specified in Table 8.3 were carefully chosen according to the property chart presented in Fig. 7.4 on p. 117. Their precursors were placed side by side before placing the hybrid hydrogels for 12h at 37°C and 100% HR.

Table 8.3: Selection of silk granular hydrogels for creating gradients through sequential layering.

Sample name	Compressive modulus [kPa]	Tensile modulus [kPa]	Elongation [%]	Swelling ratio [vol.%]
4S ³	79 ± 9	126 ± 9	29 ± 7	18 ± 3
4S ⁴	97 ± 5	161 ± 8	35 ± 6	19 ± 1
4S ⁵	124 ± 9	247 ± 15	32 ± 6	17 ± 1

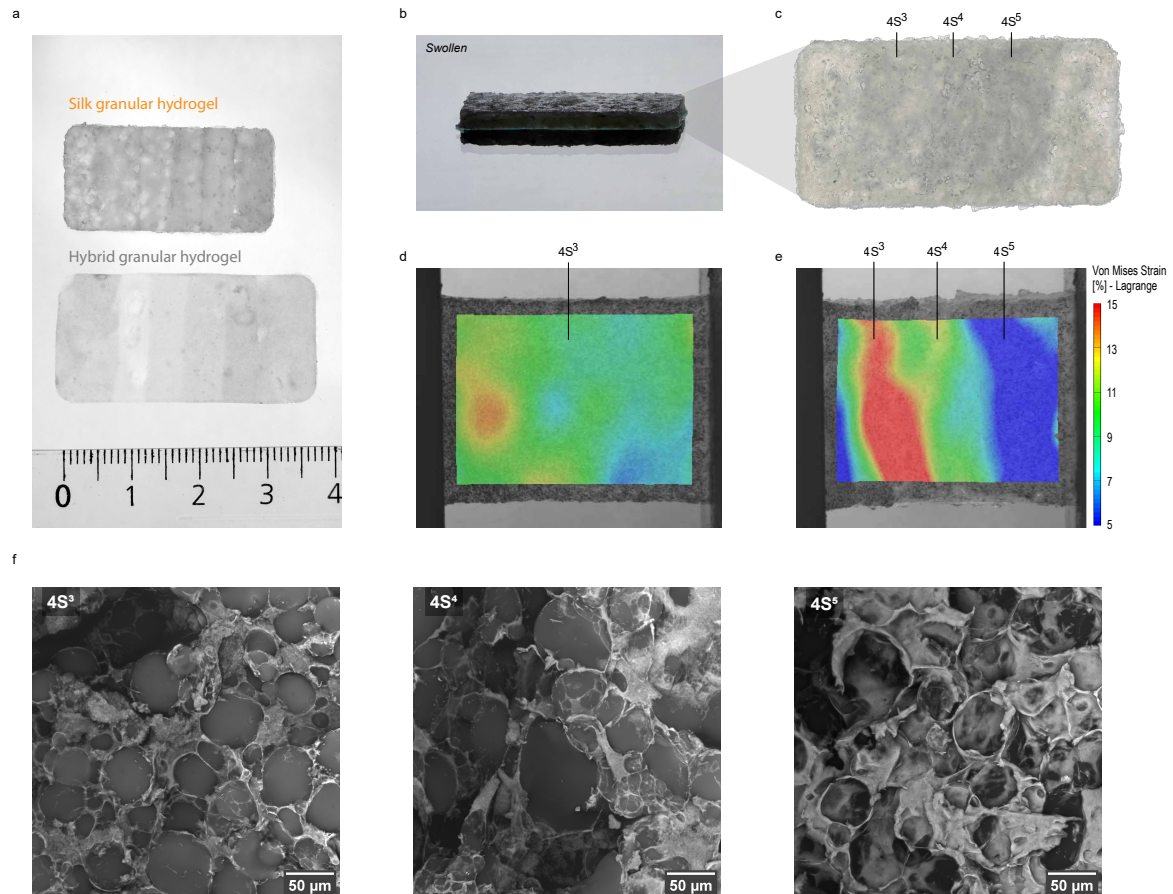


Figure 8.7: Gradient in hybrid hydrogels through sequential layering of silk granular hydrogels: (a) comparison between swollen hybrid and silk granular hydrogel, (b-c) swollen sample shows no dimensional distortion between layers of different composition, (d-e) digital image correlation showing strain field on the surface of representative hydrogel (d) without and (e) with a mechanical gradient. (f) Z-projections took with fluorescence confocal microscopy showing the microstructures of different silk granular hydrogels self-reinforced with regenerated silk fibroin fibers for each layer.

Fig. 8.7 presents the resulting hybrid hydrogels showing a gradient with layered silk granular hydrogels. As highlighted in Fig. 8.7a, silk granular hydrogels exhibited a notable lower volume increase due to swelling compared to hybrid granular hydrogels. The surface strain field was measured via digital image correlation for observing the gradients in the hydrogel qualitatively. Fig. 8.7d shows a representative sample $4S^3$ without gradient that deforms homogeneously, while Fig. 8.7e presents a hybrid hydrogel made of layered silk granular hydrogels, which revealed a mechanical gradient. However, the gradient was not as well defined as in hybrid hydrogels based on hybrid granular hydrogel, and the overall strain level was lower (*i.e.* 85% for stacked hybrid granular hydrogels and 15% for stacked the silk granular hydrogels). Indeed, the processing of silk granular hydrogels is more challenging than hybrid granular hydrogel, diminishing the quality of the mechanical gradients subsequently.

The third combination of hydrogels demonstrated that layering of silk granular precursors is feasible for creating gradient hydrogels.

8.4 Gelatin based hydrogels

Hydrogels based on 20kDa PEGDM present good mechanical properties, especially regarding elongation and fatigue resistance. However, the elastic moduli achieved remained low, and the swelling ratios relatively high for many load-bearing applications. Therefore, based on the knowledge developed with the first composites and silk granular hydrogels, the integration of other hydrogels, microgels, and fibers can be envisaged for shifting the overall properties to a new range of values. As an example, hydrogel composite and silk granular hydrogels were synthesized based on gelatin methacryloyl hydrogels. Gelatin methacryloyl (GelMa) is a biodegradable and photopolymerizable hydrogel synthesized by Peyman Karami at EPFL for its adhesion performance.

8.4.1 Hydrogel composites

Similar to the neat hydrogel - N_{10} and the hydrogel composites - $C_{10}^{0.5}$ based on PEGDM, a gelatin methacryloyl hydrogel containing initially 10 wt.% of polymer - Ge_{10} and gelatin hydrogel composite - $Ge_{10}^{0.5}$ were synthesized. The compressive and tensile modulus in *swollen state* as well as the swelling ratio are shown in Fig. 8.8.

Cellulose fibers reinforced GelMa hydrogel in a similar way than PEGDM based hydrogels. Indeed, composites had 45-48 kPa and 63-75 kPa higher compressive and tensile modulus, respectively, than their corresponding neat hydrogels. However, since the swelling ratio of GelMa - Ge_{10} is close to zero, the addition of fibers did not significantly influence the swelling ratio.

Therefore, a general trend showing fibers' effect on swelling cannot be achieved at this stage. Negative or zero swellings may not be ideal for some confined or semi-confined applications, where a pre-constrained implant helps fix it into the tissues. .

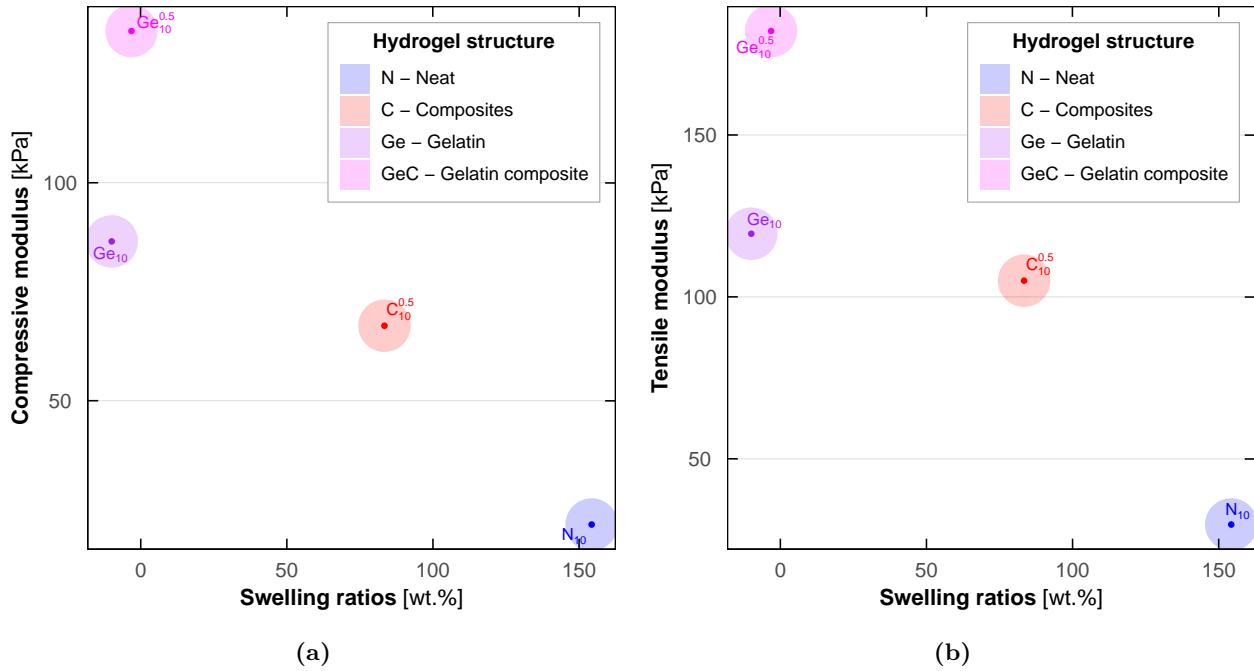


Figure 8.8: Property chart of neat and hydrogel composites based on PEGDM and gelatin showing the (a) compressive and (b) tensile modulus determined between 10 and 15% applied strain in compression as a function of the swelling ratio measured with Archimedes' principle with equation (3.3).

8.4.2 Silk granular hydrogel

The synthesis process for silk granular hydrogel based on PEGDM microgels was applied for gelatin-based microgels. The microgels, initially composed of 15 wt.% of GelMa, were synthesized as PEGDM microgels, which are described in Fig. 3.2 on p. 42. The only difference was that the gelatin precursor was heated up to 37 °C to reduce viscosity before creating the emulsion with the oil phase. According to the rule defined in Chapter 7. *Self-reinforced granular hydrogel with silk fibroin fibers* and explained in Fig. 7.10, the ideal initial concentration of dry microgels was fixed at 16 wt.%. Indeed, the final polymer content of swollen GelMa hydrogels is 15 wt.%, which added to 1 wt.% gives 16 wt.%. Moreover, the silk fibroin solution was dialyzed against PBS, and its pH was fixed to 8.5.

Fig. 8.9 shows that gelatin-based silk granular hydrogels could successfully be synthesized. Despite that gelatin has an affinity with the fluorescent dye, we could observe that silk fibroin regenerated around gelatin microgels in a network like structures, similarly to PEGDM based silk granular hydrogels.

Fig. 8.10 presents the compressive moduli and swelling ratios of the gelatin methacryloyl hydrogel - *Ge* and the silk granular hydrogel based on gelatin - *GeS*, which are compared with the structures studied in previous chapters. Both silk granular hydrogels showed similar swelling ratios suggesting that the synthesis protocol was reproducible and that microgel governed the hydrogels' swelling. However, the compressive modulus was slightly higher for gelatin-based silk granular hydrogels, probably due to the stiffer microgels. Indeed, gelatin hydrogel - *Ge*₁₅ had a compressive modulus of around 150 kPa,

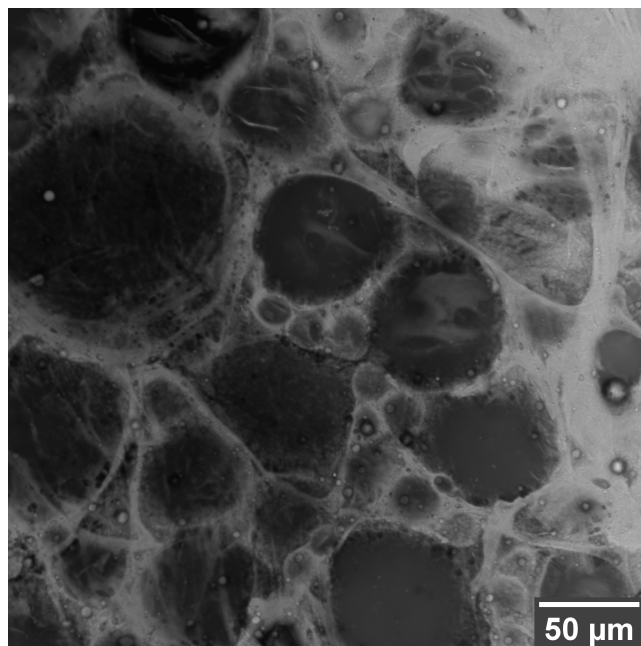


Figure 8.9: Z-stack projection taken with fluorescence confocal microscopy showing the microstructure of granular hydrogel based on gelatin reinforced with silk fibroin fibers.

significantly higher than the one of the neat PEGDM hydrogel - N_{10} (*i.e.* 20 kPa).

For completing the mechanical characterization, tensile properties were evaluated and presented in Fig. 8.11, which is a property chart that shows the tensile modulus determined between 10% and 15% applied strain as a function of the strain at failure. The tensile moduli of silk granular hydrogels (*i.e.* 85-300 kPa) were similar for both compositions. In contrast to compressive modulus, the stiff microgels could probably not contribute to increasing the tensile modulus. However, the measured average strains at failure were seriously smaller for hydrogel based on gelatin (*i.e.* 11-20%) than for the one based on PEGDM (*i.e.* 29-62%). In this case, the stiff microgels might alter the elongation potential of regenerated silk fibroin fibers because they avoid lateral deformation during tensile loadings. Therefore, softer gelatin microgels would be required to improve the strain at failure of gelatin-based silk granular hydrogels.

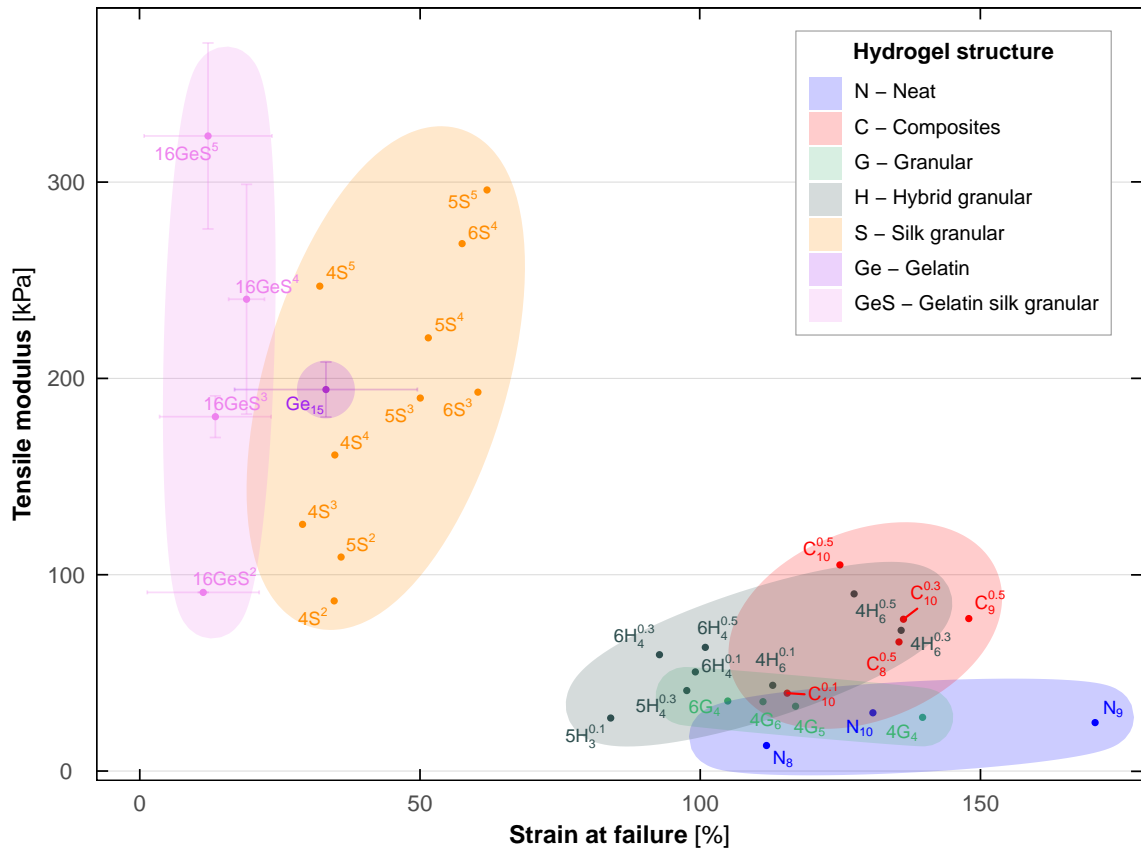


Figure 8.11: Property chart of seven different hydrogel structures with various compositions showing the tensile modulus determined between 10% and 15% applied strain as a function of the maximum deformation.

8.5 Conclusions

To extend and apply the knowledge acquired from studying various structures, hybrid hydrogels, composed of stacked hydrogels, were designed for better targeting local properties or mimicking the morphology of native tissues. Several silk and hybrid granular hydrogels were selected that exhibited high precursors' viscosity, different elastic moduli, and similar swelling ratios and were combined to create mechanical gradients. Gradients were processed through sequential layering, which was favored over other techniques because it is simple, reproducible, and applicable to different material systems.

The surface strain field observed via digital image correlation revealed the tailored mechanical gradients with silk or hybrid granular hydrogels. Nevertheless, both structures had their specificities. Hybrid granular hydrogels offered much more possible material combinations than silk granular hydrogels and were easier to process. However, the overall swelling ratios of about 90 vol.% was significantly higher than the one of silk-based hydrogels, which was less than 20 vol.%.

In a second step, a hydrogel composite and a silk granular hydrogel based on gelatin hydrogels were synthesized to highlight the potential of those structures when using other hydrogels and microgels.

Cellulose fibers could reinforce gelatin hydrogels in a similar way to PEGDM hydrogels. However, the initial low swelling ratio of gelatin hydrogel was not affected by the fibers.

Finally, silk granular hydrogel based on gelatin microgels could successfully be processed. We could apply the synthesis protocol developed for PEGDM microgels to gelatin microgels. Moreover, the method for determining the initial concentration of dry microgels in silk granular structures could be validated. Regarding the achieved mechanical properties, stiff gelatin microgels significantly contributed to the compressive modulus, while the tensile modulus mainly depended on the properties of the regenerated silk fibroin. However, the stiff microgels might alter the elongation potential of regenerated silk fibroin fibers because they avoid lateral deformation during tensile loadings. Therefore, softer gelatin microgels might be considered for applications where a less brittle behavior is required.

Chapter 9

Conclusions and perspectives

9.1 Conclusions

The study evaluates the processing and properties of different hydrogel microstructures made of well-known biomaterials. Various material systems were studied, from neat to self-reinforced granular structures.

In the first part, single and double network hydrogels and their composites were assessed according to load-bearing characteristics such as swelling ratio, adhesion, elastic modulus, toughness, or fatigue resistance. Four different hydrogel structures based on poly(ethylene glycol) dimethacrylate were tested: neat, composites, double network, and composite double network hydrogels. Composites were reinforced with nano-fibrillated cellulose fibers, while the second network was alginate. Adding cellulose fibers and/or a second network significantly improved mechanical and adhesion properties in the *as-prepared state*. Nevertheless, the double network hydrogel with alginate lost all profits in the *swollen state*. Indeed, compared to neat hydrogels, double network hydrogels had at least 30% higher swelling ratios and 25% lower elastic moduli. In contrast, the addition of 0.5 wt.% cellulose fibers to neat hydrogels reduced swelling by more than 30% without seriously affecting the processability or the long-term reliability. High-cycles fatigue tests revealed that hydrogel composites successfully survive 10 million loading cycles at 20% applied strain. However, it became softer after the first loading cycles and behaved similarly to the *Mullins effect*.

Subsequently, we assessed how cyclic loading affects the fracture behavior, the distribution of strain fields, and the microstructure of hydrogel composites. Surprisingly, we observed that preloading before creating a notch in the hydrogel composite increased the fracture strength of pre-notched samples while diminished the corresponding fracture energy. A digital image correlation analysis was conducted at the macro- and microscopic scale to understand this behavior and obtain local information on the strain field. Additionally, cellulose fibers' morphology was directly observed through fluorescence confocal microscopy before and after cyclic loading at different maximal applied strains. Microscopy results showed that cyclic loadings re-arranged the fiber network and relaxed local resid-

ual stresses in the hydrogel composite. The re-arrangement of the fiber network decreased the overall elastic modulus and correspondingly the fracture energy. However, it helped the hydrogel composite to accommodate larger strains before the crack starts to propagate, which subsequently improved the pre-notched sample's fracture strength. The study showed that cyclic loading on hydrogel composites do not deteriorate the mechanical properties. Small preloading strain might even be beneficial for reducing residual stresses. Hydrogel composite remains, therefore, a suitable candidate for load-bearing implants despite the large swelling ratio and low stiffness.

The next step was to control and understand better the relationships between mechanical, swelling, and rheological properties. Indeed developing hydrogels with optimal properties for specific applications is challenging as most of these properties, such as toughness, stiffness, swelling, or deformability, are interrelated. The improvement of one property usually comes at the cost of another. To decouple the interdependence between these properties and extend the range of material properties for hydrogels, we propose a strategy that combines composite and microgels approaches. The study focused first on tailoring the swelling performance of hydrogels while minimally affecting other properties. The underlying principle was to partially substitute some hydrogels with pre-swollen microgels composed of the same materials. Swelling reductions up to 45% were obtained. Those granular hydrogels were then reinforced with nano-fibrillated cellulose fibers obtaining hybrid granular materials to improve their toughness and further reduce their initial swelling. Four different structures of neat, granular, and composite hydrogels, including 63 different hydrogel compositions based on 20 kDa poly(ethylene glycol) dimethacrylate, showed that the swelling ratio could be tailored without significantly affecting elastic modulus and deformation performance. The results explain the role of the PEGDM precursors on the swelling of the microgels as well as the influence of the microgel and fiber contents on the final properties. All precursors were injectable and the one incorporating microgels and/or cellulose fibers showed apparent shear-thinning behavior required for advanced 3D printing. This opens a new horizon for processing in confined and unconfined environments and using these material systems when precise control of stiffness and minimum swelling is needed. Based on these first hybrid granular structures, the integration of hydrogels, microgels, and fibers could be envisaged. Indeed, the overall swelling ratios reported in this study remained quite large. Therefore, further research is required to better control and reduce swelling ratios for many unconfined or semi-confined applications. In particular, we observed that mainly the matrix surrounding the microgels swelled and significantly influenced the pre-swelling degree of microgels themselves.

To further reinforce and reduce swelling of granular hydrogels using the same microgels, a new strategy was proposed to modify the structure of the matrix material. A novel self-reinforced granular hydrogel was developed composed of 20 kDa poly(ethylene glycol) dimethacrylate microgels and self-assembled silk fibroin fibers. The principle is to locally concentrate and regenerate silk fibroin *in situ* through microgel swelling. We showed that silk fibroin in most compositions was homogeneously distributed and had successfully regenerated *in situ* around microgels, maintaining them together in a network-like structure. FTIR analysis revealed the presence of amorphous and crystalline silk fibroin, where

50% of the secondary structures could be assigned to strong β -sheets. Silk granular hydrogels exhibited swelling ratios between 5 vol.% and 60 vol.% and elastic moduli between 58 kPa and 296 kPa. Particularly, swelling of silk granular hydrogels increased proportionally with the microgel content suggesting that the microgels mainly governed swelling. In contrast, the elastic modulus increased almost linearly with silk fibroin content, and the enhancement was further pronounced at higher microgel content. Silk granular hydrogel initially composed of 5 wt.% of dry microgels presented the best compromise between mechanical and swelling properties. Subsequently, we proposed a synthesis method for obtaining optimal silk granular hydrogels by choosing the right initial concentration of microgels. Finally, we showed that the precursor silk granular hydrogel could be injected and cast it in shape into a given volume.

To extend and apply the knowledge acquired from studying various structures, hybrid hydrogels, composed of stacked hydrogels, were designed for better targeting local properties or mimicking the morphology of native tissues. Mechanical gradients were successively processed in hybrid hydrogel through a sequential layering of silk or hybrid granular hydrogels. The surface strains observed via digital image correlation clearly revealed the tailored mechanical gradients in both silk and hybrid granular hydrogel combinations. Hybrid granular hydrogels offered much more possible material combinations than silk granular hydrogels and were easier to process. However, the overall swelling ratios of about 90 vol.% was significantly higher than the one of silk-based hybrid hydrogels, which was less than 20 vol.%. In a second step, a hydrogel composite and a silk granular hydrogel based on gelatin hydrogels were synthesized to show those structures' potential when using other hydrogels and microgels. It was demonstrated that cellulose fibers could reinforce gelatin hydrogel similar to PEGDM hydrogels and that silk granular hydrogel based on gelatin microgels could successfully be synthesized. More specifically, the synthesis protocol developed for PEGDM microgels could be applied for gelatin microgels. Furthermore, the synthesis methods for determining the initial concentration of dry microgels in silk granular structures could be validated.

In summary, the following statements can be made:

1. The precursors of neat hydrogels had the lowest viscosity, perfect for confined applications such as the replacement of nucleus pulposus.
2. Microgels of similar composition than neat hydrogel can be added to the precursor to adapt and increase its viscosity for unconfined applications like repairing focal cartilage defects without using a membrane to 3D printed complex structures.
3. The addition of cellulose fibers is effective for increasing toughness. In particular, high-cycles fatigue tests revealed that hydrogel composites reinforced with nano-fibrillated cellulose fiber successfully survive 10 million loading cycles at 20% applied strain. Despite some softening after the first loading cycle similar to the *Mullins effect*, hydrogel composites, with their high fatigue resistance and low precursor's viscosity, were already proposed for replacing the nucleus pulposus.

4. Combining composite and microgel approaches can efficiently tailor hydrogels' swelling and viscosity without significantly affecting elastic modulus, fracture energy, and deformation performance. Therefore, those hybrid granular hydrogels, with their precursor of jammed microgels, might be appropriated for replacing the superficial layer of articular cartilage, where toughness is essential for limiting the propagation of cracks in the deeper and stiffer layers.
5. Microgels can be swollen in silk fibroin solution for forming self-reinforced silk granular hydrogels, which exhibit considerably higher stiffness and lower swelling as hybrid granular hydrogels. Despite their lower elongation performance, silk granular hydrogel represents a potential candidate for repairing focal cartilage defects.
6. Mechanical gradients can successively be processed in hybrid hydrogels through a sequential layering of silk or hybrid granular hydrogels for better mimicking the morphology of native tissues.
7. Other hydrogels and microgels, such as gelatin-based hydrogels, can be employed for shifting the overall properties to a new range of values.

9.2 Perspectives

9.2.1 Hybrid granular hydrogels

Hybrid granular hydrogels revealed their potentials offering similar properties to hydrogel composites and their possibility to tune swelling. Moreover, for exploring additional biological, physical, and mechanical properties, microgels with different sizes, composition, and/or drugs could be combined. Nevertheless, to complete their assessment, further study on the effect of cyclic loading on granular structures should be performed.

9.2.2 Silk granular hydrogels

Silk granular hydrogel showed promising results. The obtained self-reinforced material can be processed by injection with a needle and cast in shape into a given volume. However, the spreading of the microgels and the pH level of all precursors need to be well controlled to extend the use of silk granular hydrogels further.

Toughness

Compare to hydrogel composites and hybrid granular hydrogels, the surface strains were very concentrated around the crack tip, suggesting that the energy is not well distributed into the material. Subsequently, the fracture energy could significantly be improved if the silk granular hydrogel surrounding the crack would accommodate larger strains. This may be achieved by improving the quality of regenerated silk fibroin or the interface between silk fibroin and microgels, or incorporating larger silk or cellulose fibers. Indeed, composites of cellulose and silk fibroin may promote structural changes

by making covalent and hydrogen bonds as well as electrostatic interactions between cellulose and fibroin^[328].

Reduction of agglomerates

The processability of silk fibroin is challenging to characterize because the gelation of silk granular hydrogel varied from minutes to several hours. Moreover, the regeneration speed of silk fibroin is most probably not homogeneous in the hydrogel self. Indeed, depending on their size, microgels adsorb more or less water from silk solution, which creates a local gradient in silk fibroin concentration. Additionally, dry microgels often formed agglomerates. As illustrated in Fig. 7.15 in *Chapter 7. Self-reinforced granular hydrogel with silk fibroin fibers*, agglomerates might swell as a single large particle during the swelling process. In this case, silk fibroin might start regenerating and encapsulating the agglomerates before that the microgels can separate. It will result in new and bigger aggregates and inhomogeneous distribution of silk fibroin.

Reducing agglomerates might be achieved by (i) slowing down the regeneration time of silk fibroin or (ii) by homogeneously pre-swelling the microgels in controlled relative humidity. Nevertheless, homogeneous pre-swelling of microgels is not straight forward, especially for polydispersed size distribution and dry microgels tightly in contact.

Gelatin based silk granular hydrogels

Silk granular hydrogel based on gelatin microgels could successfully be synthesized. It was suggested that the stiff gelatin microgels significantly contribute to the compressive modulus regarding the achieved mechanical properties. In contrast, the tensile modulus mainly depends on the properties of the regenerated silk fibroin. However, the stiff microgels might alter the elongation potential of regenerated silk fibroin fibers because they avoid lateral deformation during tensile loadings. Therefore, softer gelatin microgels might be considered for applications where a less brittle behavior is required.

9.2.3 Hybrid silk granular hydrogels

The feasibility of hybrid granular hydrogels reinforced with regenerated silk fibroin was evaluated on eight compositions. This hydrogel was composed of pre-swollen PEGDM microgels and regenerated silk fibroin fibers embedded in a PEGDM matrix. The processability of those hydrogels is complicated. In particular, silk fibroin was not distributed homogeneously and formed large aggregates, probably due to the osmotic pressure induced by the PEGDM of the surrounding matrix^[156]. Therefore, for this material system and contrary to the previous self-reinforced granular hydrogel, silk fibroin fibers need to be regenerated before being added to the PEGDM matrix.

9.2.4 Additive manufacturing

The precursors of hybrid granular hydrogels are adapted for 3D printing. Therefore, complex geometries or multiple gradients can be envisaged in the future. Furthermore, silk granular hydrogels can

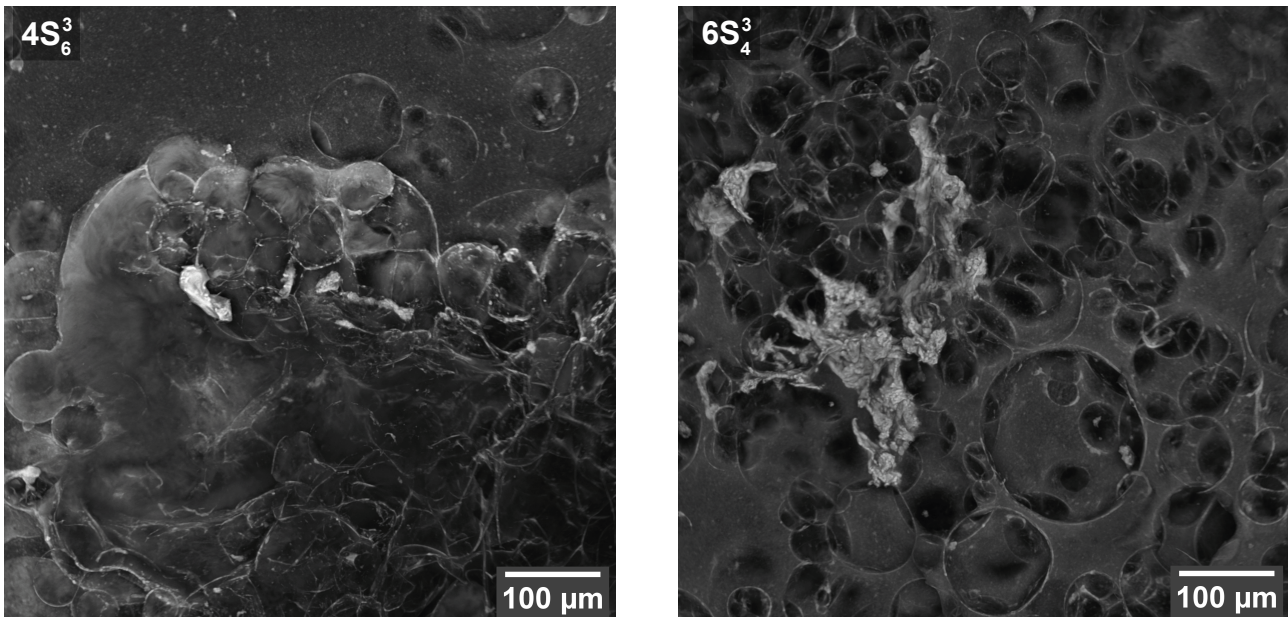


Figure 9.1: Hybrid granular hydrogel reinforced with self-assembled silk fibroin.

also be employed in 3D printing, as illustrated and explained in Fig.9.2a. When the process does not occur *in vivo*, some of the silk fibroin can be dissolved in formic acid for creating fibers of better quality. Fig. 9.2b shows such silk fibroin fibers regenerated inside a silk granular hydrogel through the phase and pH changes.

3D printing of silk fibroin fibers in granular hydrogel may be a very promising method for mimicking anisotropic tissues, such as the meniscus, deep or superficial layers of cartilage.

This example further illustrates the wide range of possibilities to combine the developed material systems to fulfill specific application requirements for the biomedical field, but also for soft robotics, sensing applications, or even food packaging.

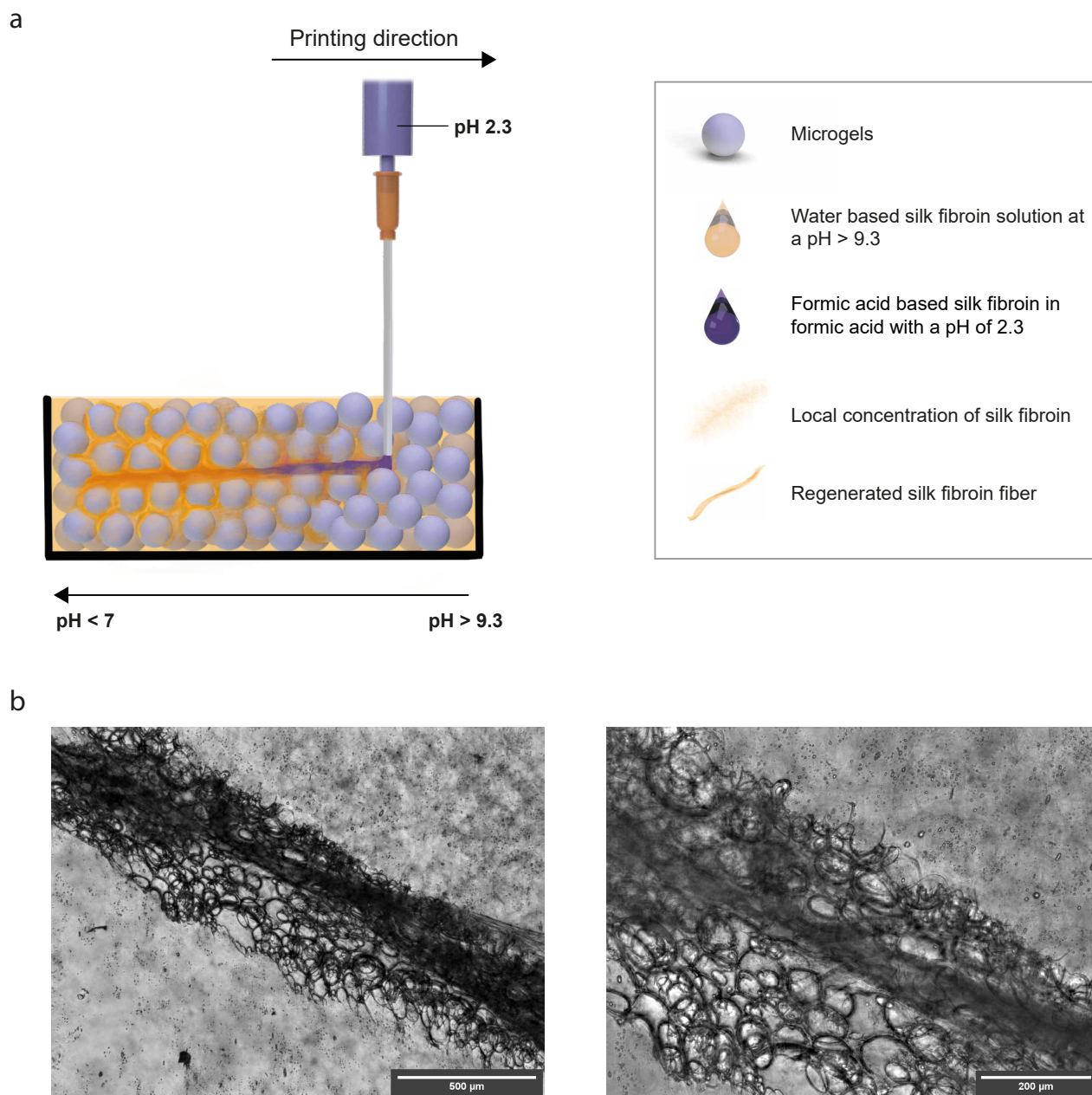


Figure 9.2: Potential 3D printing of anisotropic silk granular hydrogels. (a) Formic acid-based silk fibroin solution is placed with a needle in a granular medium containing a water-based silk fibroin solution. The mixing of both solutions changes the pH and induce the gelation of silk fibroin. In particular, silk fibroin from the acidic solution will form an oriented fiber along the printing direction, while silk fibroin from the medium regenerates around the microgels, maintaining them together. (b) Images were taken with an optical microscope showing an example of silk fibroin fibers regenerated in silk granular hydrogel. Silk fibroin dissolved in formic acid was manually deposited in silk granular hydrogel.

Chapter 10

Annexes

10.1 Annexes - State of the art

10.1.1 Adhesion theories

Many theories emerged, trying to understand and explain how adhesion occurs. The most common ones, summarized in Table 10.1, are based on energy and molecular interactions. All theories agree that high adhesion can only be reached if the interface is strong enough to allow dissipative forms of deformation^[212–215]. Nevertheless, the link between dissipation and adhesion is not yet clear.

Table 10.1: Common adhesion theories.

Adsorption theory or wettability theory	Absorption theory is based on attractive atomic and molecular interactions such as van der Waals (VDW) forces, weak hydrogen bonding, acid-base interactions and dispersion forces at the interface that give rise to interfacial adhesion. Good wetting properties and highly localized interactions are considered sufficient to give rise to high adhesion strength (length scale of interactions: 0.01-1000 nm) ^[80,346–348] .
Mechanical interlocking theory	Adhesion can be due to mechanical interlocking at the interface issued from penetration of the adhesive into pores, irregularities, or crevices. When the intimate contact between adhesive and substrate remains, higher roughness enhance the mechanical interlocking and the contact area exhibit better adhesion properties (length scale of interactions: 0.01-1000 μm) ^[80,346–348] .

Electrostatic theory	According to the electrostatic theory, adhesion is due to electrical interactions described by the Derjaguin, Landau, Verwey, and Overbeek (DLVO) theory involving van der Waals forces and the electric double layer forces at the interface. However, some estimations of the associated energy show that electrical interactions represent only a small contribution, compared to adhesion fracture energies for example (length scale of interactions: 0.1-1.0 μm) ^[80,346-348] .
Diffusion theory	Diffusion theory suggests that adhesion between substrate and adherend is issued from the dissolution of one into another. These two soluble materials form interphase exhibiting a gradient of physical properties. The major stress concentration at the interface is consequently reduced because of the improved load transfer (length scale of interactions: 10 nm-2.0 μm) ^[80,346-348] .
Chemical (covalent) bonding theory	Covalent bonding theory proposes that the durability of adhesion is improved with covalent bonding (shared electron pairs) at the interface (length scale of interactions: 0.1-0.2 nm) ^[80,348]
Acid-base theory	Acid-base theory refers to a polar interactions where a base, <i>i.e.</i> electron-donor, shares an electron-pair to an acid, <i>i.e.</i> electron-acceptor (length scale of interactions: 0.1-0.4 nm) ^[80,348] .
Weak boundary layers theory	Weak boundary layer is believed to be responsible for a premature failure of adhesion. It may be composed of impurities, air bubbles, or new materials (third body) next to a reaction between components at the interface. ^[80,348]

10.1.2 Photopolymerization

Table 10.2 presents the main steps for radical photopolymerization.

Table 10.2: Photopolymerization steps^[349].

Steps	Reaction	Description
Initiation	$PI + h\nu \rightarrow PI^*$	Photoinitiator (PI) is excited by irradiation of UV or visible light (ν : frequency, h : Planck constant $6.63 \cdot 10^{-34} \text{ J} \cdot \text{s}$).
	$PI^* \rightarrow R \cdot + R'$	The excited photoinitiator (PI^*) is decomposed to radicals ($R \cdot + R'$).
	$R \cdot + M \rightarrow M_1 \cdot$	Free radical ($R \cdot$) reacts with monomer (M), which forms in turn a free radical ($M_1 \cdot$).
Propagation	$M_n \cdot + M \rightarrow M_{n+1} \cdot$	The polymer growth by additions of large numbers of monomer molecules (M_n).
Termination	$M_n \cdot + M_m \cdot \rightarrow M_{n+m}$	The reaction end because of coupling.
	$M_n \cdot + M_m \cdot \rightarrow M_n + M_m$	The reaction end because of disproportion.

10.2 Annexes - Equipment

Table 10.3 describes the equipment used for the synthesis.

Table 10.3: Equipment for the material characterization.

Pos.	Description	Function	Comments
1	C-MAG HS 10 digital equipped with IKA ETS D5 (IKA-Werke, Staufen, Germany)	Heating magnetic stirrer.	Homogenise Irgacure solution at 80°C before using it for the hydrogel synthesis.
2	Heidolph stirrer	Mechanical stirrer.	Homogenise NFC solution before use for the hydrogel synthesis.
3	Mettler Toledo (readability: 0.1 mg - 1 mg)	Digital scale	Weight the PEGDM powder.
4	Pipetman micropipettes (Gilson)	Transfer liquid solution.	Micropipettes of 200 μ l and 1000 μ l.
5	MICROMAN micropipettes (Gilson)	Transfer viscous solution (e.g. hydrogel composite precursor).	Micropipettes of 1000 μ l.
6	BD Flacon conical tubes	Recipient	-
7	BD Flacon round-bottom tube	Recipient	Enable the use of Ultra Turrax for mixing the content.
8	Ultra Turrax IKA T25 digital	Mechanical stirrer	Disperse the NFC homogeneously in the hydrogel precursor.
9	Vacuubrand PC 2001 Vario	Vaccum pump combined with a desiccator.	Degassing the hydrogel precursor.
10	Eppendorf cup	Casting mold	Cylinder Ø8 mm x 4.5 mm.
11	Microscope slides (76 x 26 mm)	Mold cover	Avoid that the precursor enter in contact with air during curing and to obtain flat surfaces.
12	AxonLab	Monochromatic 365 nm ultra violet lamp.	Intensity 5 mW/cm ² Photo-polymerisation of the hydrogel.
13	Vortex Genie 2	Vortex	Mix hydrogel precursor.

Bibliography

- [1] Andreas Schmocker, Azadeh Khoushabi, Daniela A. Frauchiger, Benjamin Gantenbein, Constantin Schizas, Christophe Moser, Pierre-Etienne Bourban, and Dominique P. Pioletti. A photopolymerized composite hydrogel and surgical implanting tool for a nucleus pulposus replacement. 88:110–119, . ISSN 0142-9612. doi: 10.1016/j.biomaterials.2016.02.015. URL <http://www.sciencedirect.com/science/article/pii/S0142961216001290>.
- [2] W. Y. Gu, X. G. Mao, R. J. Foster, M. Weidenbaum, V. C. Mow, and B. A. Rawlins. The anisotropic hydraulic permeability of human lumbar annulus fibrosus: Influence of age, degeneration, direction, and water content. 24(23):2449. ISSN 0362-2436. URL https://journals.lww.com/spinejournal/Fulltext/1999/12010/The_Anisotropic_Hydraulic_Permability_of_Human.5.aspx.
- [3] S Lüssea, H Claassen, T Gehrke, J Hassenpflug, M Schünke, M Heller, and C. C Glüer. Evaluation of water content by spatially resolved transverse relaxation times of human articular cartilage. 18(4):423–430. ISSN 0730-725X. doi: 10.1016/S0730-725X(99)00144-7. URL <http://www.sciencedirect.com/science/article/pii/S0730725X99001447>.
- [4] J. S. Stephan, Jr RM McLaughlin, and G. Griffith. Water content and glycosaminoglycan disaccharide concentration of the canine meniscus. 59(2):213–216. ISSN 0002-9645. URL <http://europepmc.org/abstract/med/9492939>.
- [5] U. F. O. Themes. Meniscal transplantation. URL <https://musculoskeletalkey.com/meniscal-transplantation-2/>.
- [6] Lori Thein Brody. Knee osteoarthritis: Clinical connections to articular cartilage structure and function. 16(4):301–316. ISSN 1466-853X. doi: 10.1016/j.ptsp.2014.12.001. URL <http://www.sciencedirect.com/science/article/pii/S1466853X14001060>.
- [7] Ana M. S. Costa and João F. Mano. Extremely strong and tough hydrogels as prospective candidates for tissue repair – a review. 72:344–364. ISSN 0014-3057. doi: 10.1016/j.eurpolymj.2015.07.053. URL <http://www.sciencedirect.com/science/article/pii/S0014305715004012>.
- [8] Brian Amsden. Photo-crosslinking methods to design hydrogels. In *Gel Handbook: Fundamentals, Properties and Applications*, volume 1. Utkan Demirci, 2016 edition.
- [9] Charles W. Peak, Jonathan J. Wilker, and Gudrun Schmidt. A review on tough and sticky hydrogels. 291(9):2031–2047. ISSN 0303-402X, 1435-1536. doi: 10.1007/s00396-013-3021-y. URL <http://link.springer.com/article/10.1007/s00396-013-3021-y>.
- [10] Timothy M. Maul, Douglas W. Chew, Alejandro Nieponice, and David A. Vorp. Mechanical stimuli differentially control stem cell behavior: morphology, proliferation, and differentiation. 10(6):939–953. ISSN 1617-7959, 1617-7940. doi: 10.1007/s10237-010-0285-8. URL <https://link.springer.com/article/10.1007/s10237-010-0285-8>.
- [11] Greg Altman, Rebecca Horan, Ivan Martin, Jian Farhadi, Peter Stark, Vladimir Volloch, Gordana Vunjak-Novakovic, John Richmond, and David L. Kaplan. Cell differentiation by mechanical stress. 16(2):270–272. ISSN 0892-6638. doi: 10.1096/fj.01-0656fje. URL <https://www.fasebj.org/doi/abs/10.1096/fj.01-0656fje>.
- [12] Xin Xin Shao, Dietmar W. Hutmacher, Saey Tuan Ho, James C. H. Goh, and Eng Hin Lee. Evaluation of a hybrid scaffold/cell construct in repair of high-load-bearing osteochondral defects in rabbits. 27(7):1071–1080. ISSN 0142-9612. doi: 10.1016/j.biomaterials.2005.07.040. URL <http://www.sciencedirect.com/science/article/pii/S0142961205007003>.
- [13] Oju Jeon, Jung-Youn Shin, Robyn Marks, Mitchell Hopkins, Tae-Hee Kim, Hong-Hyun Park, and Eben Alsberg. Highly elastic and tough interpenetrating polymer network-structured hybrid hydrogels for cyclic mechanical loading-enhanced tissue engineering. 29(19):8425–8432, . ISSN 0897-4756. doi: 10.1021/acs.chemmater.7b02995. URL <https://doi.org/10.1021/acs.chemmater.7b02995>.

- [14] David L. Butler, Steven A. Goldstein, and Farshid Guilak. Functional tissue engineering: The role of biomechanics. 122(6): 570–575. ISSN 0148-0731. doi: 10.1115/1.1318906. URL <http://dx.doi.org/10.1115/1.1318906>.
- [15] Md. Anamul Haque, Takayuki Kurokawa, and Jian Ping Gong. Super tough double network hydrogels and their application as biomaterials. 53(9):1805–1822. . ISSN 0032-3861. doi: 10.1016/j.polymer.2012.03.013. URL <http://www.sciencedirect.com/science/article/pii/S0032386112002212>. Overview though hydrogel.
- [16] Peng Lin, Shuanhong Ma, Xiaolong Wang, and Feng Zhou. Molecularly engineered dual-crosslinked hydrogel with ultrahigh mechanical strength, toughness, and good self-recovery. 27(12):2054–2059. . ISSN 1521-4095. doi: 10.1002/adma.201405022. URL <http://onlinelibrary.wiley.com/doi/10.1002/adma.201405022/abstract>. Homogenous, recoverable, softening.
- [17] Koichi Mayumi, Jingyi Guo, Tetsuharu Narita, Chung Yuen Hui, and Costantino Creton. Fracture of dual crosslink gels with permanent and transient crosslinks. 6:52–59. ISSN 2352-4316. doi: 10.1016/j.eml.2015.12.002. URL <http://www.sciencedirect.com/science/article/pii/S2352431615300055>.
- [18] Jian Ping Gong. Why are double network hydrogels so tough? 6(12):2583–2590. ISSN 1744-6848. doi: 10.1039/B924290B. URL <http://pubs.rsc.org/en/content/articlelanding/2010/sm/b924290b>. DN-characterisation.
- [19] Ecaterina Stela Dragan. Design and applications of interpenetrating polymer network hydrogels. a review. 243:572–590. ISSN 1385-8947. doi: 10.1016/j.cej.2014.01.065. URL <http://www.sciencedirect.com/science/article/pii/S1385894714000904>.
- [20] Stefanie Utech and Aldo R. Boccaccini. A review of hydrogel-based composites for biomedical applications: enhancement of hydrogel properties by addition of rigid inorganic fillers. 51(1):271–310. ISSN 0022-2461, 1573-4803. doi: 10.1007/s10853-015-9382-5. URL <https://link.springer.com/article/10.1007/s10853-015-9382-5>.
- [21] Fuli Zhao, Dan Yao, Ruiwei Guo, Liandong Deng, Anjie Dong, and Jianhua Zhang. Composites of polymer hydrogels and nanoparticulate systems for biomedical and pharmaceutical applications. 5(4):2054–2130. doi: 10.3390/nano5042054. URL <http://www.mdpi.com/2079-4991/5/4/2054>.
- [22] Chunching Li, Liliang Ouyang, James P. K. Armstrong, and Molly M. Stevens. Advances in the fabrication of biomaterials for gradient tissue engineering. . ISSN 0167-7799. doi: 10.1016/j.tibtech.2020.06.005. URL <http://www.sciencedirect.com/science/article/pii/S0167779920301694>.
- [23] A. Khoushabi, A. Schmock, D. P. Pioletti, C. Moser, C. Schizas, J. A. Manson, and P. E. Bourban. Photo-polymerization, swelling and mechanical properties of cellulose fibre reinforced poly(ethylene glycol) hydrogels. 119:93–99. . ISSN 0266-3538. doi: 10.1016/j.compscitech.2015.10.002. URL <http://www.sciencedirect.com/science/article/pii/S0266353815300993>.
- [24] Johnna S. Temenoff, Kyriacos A. Athanasiou, Richard G. LeBaron, and Antonios G. Mikos. Effect of poly(ethylene glycol) molecular weight on tensile and swelling properties of oligo(poly(ethylene glycol) fumarate) hydrogels for cartilage tissue engineering. 59(3):429–437. ISSN 0021-9304. doi: 10.1002/jbm.1259.
- [25] E. O. Akala, P. Kopecková, and J. Kopecek. Novel pH-sensitive hydrogels with adjustable swelling kinetics. 19(11):1037–1047. ISSN 0142-9612. doi: 10.1016/s0142-9612(98)00023-4.
- [26] Lin Zhang, Jing Zhao, Jintang Zhu, Changcheng He, and Huiliang Wang. Anisotropic tough poly(vinyl alcohol) hydrogels. 8(40):10439–10447. . doi: 10.1039/C2SM26102B. URL <http://pubs.rsc.org/en/Content/ArticleLanding/2012/SM/C2SM26102B>.
- [27] Rebecca E. Webber, Costantino Creton, Hugh R. Brown, and Jian Ping Gong. Large strain hysteresis and mullins effect of tough double-network hydrogels. 40(8):2919–2927. ISSN 0024-9297. doi: 10.1021/ma062924y. URL <http://dx.doi.org/10.1021/ma062924y>. DN,mullins effect.
- [28] Jasna Djonlagić, Dragana Žugić, and Zoran Petrović. High strength thermoresponsive semi-IPN hydrogels reinforced with nanoclays. 124(4):3024–3036. ISSN 1097-4628. doi: 10.1002/app.35334. URL <http://onlinelibrary.wiley.com/doi/10.1002/app.35334/abstract>. semi-IPN, NC, mullins effect,elastic recovery?
- [29] M. Anamul Haque, Takayuki Kurokawa, Gen Kamita, and J. Ping Gong. Lamellar bilayers as reversible sacrificial bonds to toughen hydrogel: Hysteresis, self-recovery, fatigue resistance, and crack blunting. 44(22):8916–8924. . ISSN 0024-9297. doi: 10.1021/ma201653t. URL <http://pubs.acs.org/doi/abs/10.1021/ma201653t>. Anisotropic, recoverable.

- [30] Weifu Dong, Chiguang Huang, Yang Wang, Yujie Sun, Piming Ma, and Mingqing Chen. Superior mechanical properties of double-network hydrogels reinforced by carbon nanotubes without organic modification. 14(11):22380–22394. doi: 10.3390/ijms141122380. URL <http://www.mdpi.com/1422-0067/14/11/22380>. DN+NC, softening, Mullins.
- [31] A. Khoushabi, C. S. Wyss, B. Caglar, D. Pioletti, and P. E. Bourban. Tailoring swelling to control softening mechanisms during cyclic loading of PEG/cellulose hydrogel composites. 168:88–95. ISSN 0266-3538. doi: 10.1016/j.compscitech.2018.08.043. URL <http://www.sciencedirect.com/science/article/pii/S0266353818303427>.
- [32] Huachuan Du, Alice Cont, Mathias Steinacher, and Esther Amstad. Fabrication of hexagonal-prismatic granular hydrogel sheets. 34(11):3459–3466. ISSN 0743-7463. doi: 10.1021/acs.langmuir.7b04163. URL <https://doi.org/10.1021/acs.langmuir.7b04163>.
- [33] Lindsay Riley, Lucas Schirmer, and Tatiana Segura. Granular hydrogels: emergent properties of jammed hydrogel microparticles and their applications in tissue repair and regeneration. 60:1–8. ISSN 0958-1669. doi: 10.1016/j.copbio.2018.11.001. URL <http://www.sciencedirect.com/science/article/pii/S095816691830137X>.
- [34] Joshua E. Mealy, Jennifer J. Chung, Heon-Ho Jeong, David Issadore, Daeyeon Lee, Pavan Atluri, and Jason A. Burdick. Injectable granular hydrogels with multifunctional properties for biomedical applications. 30(20):1705912. ISSN 1521-4095. doi: 10.1002/adma.201705912. URL <https://onlinelibrary.wiley.com/doi/abs/10.1002/adma.201705912>.
- [35] Minna H. Chen, Jennifer J. Chung, Joshua E. Mealy, Samir Zaman, Elizabeth C. Li, Maria F. Arisi, Pavan Atluri, and Jason A. Burdick. Injectable supramolecular hydrogel/microgel composites for therapeutic delivery. 0(0):1800248. ISSN 1616-5195. doi: 10.1002/mabi.201800248. URL <https://onlinelibrary.wiley.com/doi/abs/10.1002/mabi.201800248>.
- [36] Donald R. Griffin, Westbrook M. Weaver, Philip O. Scumpia, Dino Di Carlo, and Tatiana Segura. Accelerated wound healing by injectable microporous gel scaffolds assembled from annealed building blocks. 14(7):737–744. ISSN 1476-4660. doi: 10.1038/nmat4294. URL <https://www.nature.com/articles/nmat4294>.
- [37] Lorenzo Moroni, Jason A. Burdick, Christopher Highley, Sang Jin Lee, Yuya Morimoto, Shoji Takeuchi, and James J. Yoo. Biofabrication strategies for 3d in vitro models and regenerative medicine. 3:21–37. ISSN 2058-8437. doi: 10.1038/s41578-018-0006-y. URL <http://adsabs.harvard.edu/abs/2018NatRM...3...21M>.
- [38] Shangjing Xin, David Chimene, Jay E. Garza, Akhilesh K. Gaharwar, and Daniel L. Alge. Clickable PEG hydrogel microspheres as building blocks for 3d bioprinting. 7(3):1179–1187. doi: 10.1039/C8BM01286E. URL <https://pubs.rsc.org/en/content/articlelanding/2019/bm/c8bm01286e>.
- [39] Christopher B. Highley, Kwang Hoon Song, Andrew C. Daly, and Jason A. Burdick. Jammed microgel inks for 3d printing applications. 6(1):1801076. ISSN 2198-3844. doi: 10.1002/advs.201801076. URL <https://onlinelibrary.wiley.com/doi/abs/10.1002/advs.201801076>.
- [40] A. Sivashanmugam, R. Arun Kumar, M. Vishnu Priya, Shantikumar V. Nair, and R. Jayakumar. An overview of injectable polymeric hydrogels for tissue engineering. 72:543–565. ISSN 0014-3057. doi: 10.1016/j.eurpolymj.2015.05.014. URL <http://www.sciencedirect.com/science/article/pii/S0014305715002785>.
- [41] Kuen Yong Lee and David J. Mooney. Hydrogels for tissue engineering. 101(7):1869–1880. ISSN 0009-2665. doi: 10.1021/cr000108x. URL <http://dx.doi.org/10.1021/cr000108x>.
- [42] Soohwan An, Eun Je Jeon, Jihoon Jeon, and Seung-Woo Cho. A serotonin-modified hyaluronic acid hydrogel for multifunctional hemostatic adhesives inspired by a platelet coagulation mediator. 6(6):1169–1178. ISSN 2051-6355. doi: 10.1039/C9MH00157C. URL <https://pubs.rsc.org/en/content/articlelanding/2019/mh/c9mh00157c>.
- [43] Todd R. Hoare and Daniel S. Kohane. Hydrogels in drug delivery: Progress and challenges. 49(8):1993–2007. ISSN 0032-3861. doi: 10.1016/j.polymer.2008.01.027. URL <http://www.sciencedirect.com/science/article/pii/S0032386108000487>.
- [44] Jianyu Li and David J. Mooney. Designing hydrogels for controlled drug delivery. 1(12):16071. ISSN 2058-8437. doi: 10.1038/natrevmats.2016.71. URL <https://www.nature.com/articles/natrevmats201671>.
- [45] Gang He, Sheng Chen, Yunjun Xu, Zhaohua Miao, Yan Ma, Haisheng Qian, Yang Lu, and Zhengbao Zha. Charge reversal induced colloidal hydrogel acts as a multi-stimuli responsive drug delivery platform for synergistic cancer therapy. 6(4):711–716. ISSN 2051-6355. doi: 10.1039/C9MH00020H. URL <https://pubs.rsc.org/en/content/articlelanding/2019/mh/c9mh00020h>.

- [46] Daehoon Han, Cindy Farino, Chen Yang, Tracy Scott, Daniel Browe, Wonjoon Choi, Joseph W. Freeman, and Howon Lee. Soft robotic manipulation and locomotion with a 3d printed electroactive hydrogel. 10(21):17512–17518, . ISSN 1944-8244. doi: 10.1021/acsami.8b04250. URL <https://doi.org/10.1021/acsami.8b04250>.
- [47] Wen Jiang Zheng, Ning An, Jian Hai Yang, Jinxiong Zhou, and Yong Mei Chen. Tough al-alginate/poly(n-isopropylacrylamide) hydrogel with tunable LCST for soft robotics. 7(3):1758–1764. ISSN 1944-8244. doi: 10.1021/am507339r. URL <https://doi.org/10.1021/am507339r>.
- [48] Lin Jing, Kerui Li, Haitao Yang, and Po-Yen Chen. Recent advances in integration of 2d materials with soft matter for multifunctional robotic materials. 7(1):54–70. ISSN 2051-6355. doi: 10.1039/C9MH01139K. URL <https://pubs.rsc.org/en/content/articlelanding/2020/mh/c9mh01139k>.
- [49] Takayuki Hiratani, Osamu Kose, Wadood Y. Hamad, and Mark J. MacLachlan. Stable and sensitive stimuli-responsive anisotropic hydrogels for sensing ionic strength and pressure. 5(6):1076–1081. ISSN 2051-6355. doi: 10.1039/C8MH00586A. URL <https://pubs.rsc.org/en/content/articlelanding/2018/mh/c8mh00586a>.
- [50] Daniel Buenger, Fuat Topuz, and Juergen Groll. Hydrogels in sensing applications. 37(12):1678–1719. ISSN 0079-6700. doi: 10.1016/j.progpolymsci.2012.09.001. URL <http://www.sciencedirect.com/science/article/pii/S007967001200086X>.
- [51] Rejane Andrade Batista, Paula Judith Perez Espitia, Jullyana de Souza Siqueira Quintans, Mayanna Machado Freitas, Miguel Ângelo Cerqueira, José Antônio Teixeira, and Juliana Cordeiro Cardoso. Hydrogel as an alternative structure for food packaging systems. 205:106–116. ISSN 0144-8617. doi: 10.1016/j.carbpol.2018.10.006. URL <http://www.sciencedirect.com/science/article/pii/S0144861718311822>.
- [52] Dario Fassini, Ana Rita C. Duarte, Rui L. Reis, and Tiago H. Silva. Bioinspiring chondrosia reniformis (nardo, 1847) collagen-based hydrogel: A new extraction method to obtain a sticky and self-healing collagenous material. 15(12):380. doi: 10.3390/md15120380. URL <https://www.mdpi.com/1660-3397/15/12/380>.
- [53] Nesrin Hasirci, Cemile Kilic, Aylin Kömez, Gökhan Bahcecioglu, and Vasif Hasirci. Hydrogels in regenerative medicine. In *Gel Handbook: Applications of Hydrogels in Regenerative Medicine*, volume 2. Utkan Demirci, 2016 edition.
- [54] Shangyou Tee. Natural hydrogels. In *Gel Handbook: Fundamentals, Properties and Applications*, volume 1. Utkan Demirci, 2016 edition.
- [55] Anne S. van Oosten, Peter A. Galie, and Paul A. Janmey. Mechanical properties of hydrogels. In *Gel Handbook: Fundamentals, Properties and Applications*, volume 1. Utkan Demirci, 2016 edition.
- [56] Kuen Yong Lee and David J. Mooney. Alginate: properties and biomedical applications. 37(1):106–126, . ISSN 0079-6700. doi: 10.1016/j.progpolymsci.2011.06.003. URL <http://www.ncbi.nlm.nih.gov/pmc/articles/PMC3223967/>.
- [57] J. Berger, M. Reist, J. M. Mayer, O. Felt, N. A. Peppas, and R. Gurny. Structure and interactions in covalently and ionically crosslinked chitosan hydrogels for biomedical applications. 57(1):19–34. ISSN 0939-6411. doi: 10.1016/S0939-6411(03)00161-9. URL <http://www.sciencedirect.com/science/article/pii/S0939641103001619>.
- [58] Hiroyuki Kono, Ikuo Oeda, and Taichi Nakamura. The preparation, swelling characteristics, and albumin adsorption and release behaviors of a novel chitosan-based polyampholyte hydrogel. 73(1):97–107. ISSN 1381-5148. doi: 10.1016/j.reactfunctpolym.2012.08.016. URL <http://www.sciencedirect.com/science/article/pii/S1381514812002398>.
- [59] Jin Woo Lee, So Yeon Kim, Seong Soo Kim, Young Moo Lee, Kwang Hyun Lee, and Seon Jeong Kim. Synthesis and characteristics of interpenetrating polymer network hydrogel composed of chitosan and poly(acrylic acid). 73(1): 113–120, . ISSN 1097-4628. doi: 10.1002/(SICI)1097-4628(19990705)73:1<113::AID-APP13>3.0.CO;2-D. URL [http://onlinelibrary.wiley.com/doi/10.1002/\(SICI\)1097-4628\(19990705\)73:1<113::AID-APP13>3.0.CO;2-D/abstract](http://onlinelibrary.wiley.com/doi/10.1002/(SICI)1097-4628(19990705)73:1<113::AID-APP13>3.0.CO;2-D/abstract).
- [60] Marguerite Rinaudo. Chitin and chitosan: Properties and applications. 31(7):603–632. ISSN 0079-6700. doi: 10.1016/j.progpolymsci.2006.06.001. URL <http://www.sciencedirect.com/science/article/pii/S0079670006000530>.
- [61] Yun Lin Guan, Lei Shao, and Kang De Yao. State of water in the pH-sensitive chitosan-polyether semi-IPN hydrogel. 61(2):393–400. ISSN 1097-4628. doi: 10.1002/app.1996.070610224. URL <http://onlinelibrary.wiley.com/doi/10.1002/app.1996.070610224/abstract>.

- [62] J. F. Mano, G. A. Silva, H. S. Azevedo, P. B. Malafaya, R. A. Sousa, S. S. Silva, L. F. Boesel, J. M. Oliveira, T. C. Santos, A. P. Marques, N. M. Neves, and R. L. Reis. Natural origin biodegradable systems in tissue engineering and regenerative medicine: present status and some moving trends. 4(17):999–1030. ISSN 1742-5689, 1742-5662. doi: 10.1098/rsif.2007.0220. URL <http://rsif.royalsocietypublishing.org/content/4/17/999>.
- [63] Edward M. Petrie. Cyanoacrylate adhesives in surgical applications. 2(3):253–310. ISSN 21680965. doi: 10.7569/RAA.2014.097306. URL <http://openurl.ingenta.com/content/xref?genre=article&issn=2168-0965&volume=2&issue=3&page=253>.
- [64] Mark D. Brigham, Alexander Bick, Edward Lo, Amel Bendali, Jason A. Burdick, and Ali Khademhosseini. Mechanically robust and bioadhesive collagen and photocrosslinkable hyaluronic acid semi-interpenetrating networks. 15(7):1645–1653. ISSN 1937-3341. doi: 10.1089/ten.tea.2008.0441. URL <http://online.liebertpub.com/doi/abs/10.1089/ten.tea.2008.0441>.
- [65] Jason A. Burdick and Glenn D. Prestwich. Hyaluronic acid hydrogels for biomedical applications. 23(12):H41–H56. ISSN 1521-4095. doi: 10.1002/adma.201003963. URL <http://onlinelibrary.wiley.com/doi/10.1002/adma.201003963/abstract>.
- [66] Iris L. Kim, Robert L. Mauck, and Jason A. Burdick. Hydrogel design for cartilage tissue engineering: A case study with hyaluronic acid. 32(34):8771–8782, . ISSN 0142-9612. doi: 10.1016/j.biomaterials.2011.08.073. URL <http://www.sciencedirect.com/science/article/pii/S0142961211010210>.
- [67] Annada Rajbhandary and Bradley L. Nilsson. Self-assembling hydrogels. In *Gel Handbook: Fundamentals, Properties and Applications*, volume 1. Utkan Demirci, 2016 edition.
- [68] Ung-Jin Kim, Jaehyung Park, Chunmei Li, Hyoung-Joon Jin, Regina Valluzzi, and David L. Kaplan. Structure and properties of silk hydrogels. 5(3):786–792, . ISSN 1525-7797. doi: 10.1021/bm0345460. URL <http://dx.doi.org/10.1021/bm0345460>.
- [69] Naresh Kasoju, Nicholas Hawkins, Ognen Pop-Georgievski, Dana Kubies, and Fritz Vollrath. Silk fibroin gelation via non-solvent induced phase separation. 4(3):460–473. doi: 10.1039/C5BM00471C. URL <http://pubs.rsc.org/en/Content/ArticleLanding/2016/BM/C5BM00471C>.
- [70] Zhenming Wang, Chen Li, Jielong Xu, Kefeng Wang, Xiong Lu, Hongping Zhang, Shuxin Qu, Guanming Zhen, and Fuzeng Ren. Bioadhesive microporous architectures by self-assembling polydopamine microcapsules for biomedical applications. 27(3):848–856, . ISSN 0897-4756. doi: 10.1021/cm5038765. URL <http://dx.doi.org/10.1021/cm5038765>.
- [71] Monica A. Serban, Bruce Panilaitis, and David L. Kaplan. Silk fibroin and polyethylene glycol-based biocompatible tissue adhesives. 98A(4):567–575. ISSN 1552-4965. doi: 10.1002/jbm.a.33149. URL <http://onlinelibrary.wiley.com/doi/10.1002/jbm.a.33149/abstract>.
- [72] Yashi Jin, Banani Kundu, Yurong Cai, Subhas C. Kundu, and Juming Yao. Bio-inspired mineralization of hydroxyapatite in 3d silk fibroin hydrogel for bone tissue engineering. 134:339–345. ISSN 0927-7765. doi: 10.1016/j.colsurfb.2015.07.015. URL <https://www.sciencedirect.com/science/article/pii/S0927776515300461>.
- [73] John Garner and Kinam Park. Types and chemistry of synthetic hydrogels. In *Gel Handbook: Fundamentals, Properties and Applications*, volume 1. Utkan Demirci, 2016 edition.
- [74] Silvia Petrova. Tailoring hydrogel adhesiveness to cells, proteins, and bacteria. In *Gel Handbook: Fundamentals, Properties and Applications*, volume 1. Utkan Demirci, 2016 edition.
- [75] Deniz C. Tuncaboylu, Murat Sari, Wilhelm Oppermann, and Oguz Okay. Tough and self-healing hydrogels formed via hydrophobic interactions. 44(12):4997–5005. ISSN 0024-9297. doi: 10.1021/ma200579v. URL <http://dx.doi.org/10.1021/ma200579v>.
- [76] Jeong-Yun Sun, Xuanhe Zhao, Widusha R. K. Illeperuma, Ovijit Chaudhuri, Kyu Hwan Oh, David J. Mooney, Joost J. Vlassak, and Zhigang Suo. Highly stretchable and tough hydrogels. 489(7414):133–136, . ISSN 0028-0836. doi: 10.1038/nature11409. URL <http://www.nature.com/nature/journal/v489/n7414/abs/nature11409.html>. hybrid,(IPN), softening, recoverable.
- [77] Mathew Patenaude, Niels M. B. Smeets, and Todd Hoare. Designing injectable, covalently cross-linked hydrogels for biomedical applications. 35(6):598–617. ISSN 1521-3927. doi: 10.1002/marc.201300818. URL <https://onlinelibrary.wiley.com/doi/abs/10.1002/marc.201300818>. [_eprint: https://onlinelibrary.wiley.com/doi/pdf/10.1002/marc.201300818](https://onlinelibrary.wiley.com/doi/pdf/10.1002/marc.201300818).
- [78] Angela Babin. Adhesives and toxicity. URL <http://www.nontoxichub.com/>.

- [79] M. C. Sabater, M. A. Martínez, and R. Font. Toxicity and hazardous properties of solvent base adhesive wastes. 19(5): 442–449. ISSN 0734-242X. doi: 10.1177/0734242X0101900509.
- [80] K. L. Mittal. *Progress in Adhesion and Adhesives*. John Wiley & Sons. ISBN 978-1-119-16232-2. Google-Books-ID: 8kdECgAAQBAJ.
- [81] A. San Juan, A. Montembault, D. Gillet, J. P. Say, S. Rouif, T. Bouet, I. Royaud, and L. David. Degradation of chitosan-based materials after different sterilization treatments. 31:012007. ISSN 1757-899X. doi: 10.1088/1757-899X/31/1/012007. URL <https://doi.org/10.1088/1757-899X/31/1/012007>.
- [82] Pariksha J. Kondiah, Yahya E. Choonara, Pierre P. D. Kondiah, Thashree Marimuthu, Pradeep Kumar, Lisa C. du Toit, and Viness Pillay. A review of injectable polymeric hydrogel systems for application in bone tissue engineering. 21(11):1580. doi: 10.3390/molecules21111580. URL <http://www.mdpi.com/1420-3049/21/11/1580>.
- [83] Jamie L. Ifkovits and Jason A. Burdick. Review: Photopolymerizable and degradable biomaterials for tissue engineering applications. 13(10):2369–2385. ISSN 1076-3279. doi: 10.1089/ten.2007.0093. URL <https://www.liebertpub.com/doi/abs/10.1089/ten.2007.0093>.
- [84] Vladimir P. Torchilin. Multifunctional, stimuli-sensitive nanoparticulate systems for drug delivery. 13(11):813–827. ISSN 1474-1784. doi: 10.1038/nrd4333. URL <https://www.nature.com/articles/nrd4333>.
- [85] Kytai Truong Nguyen and Jennifer L. West. Photopolymerizable hydrogels for tissue engineering applications. 23(22):4307–4314. ISSN 0142-9612. doi: 10.1016/S0142-9612(02)00175-8. URL <http://www.sciencedirect.com/science/article/pii/S0142961202001758>.
- [86] Iris Mironi-Harpaz, Dennis Yingquan Wang, Subbu Venkatraman, and Dror Seliktar. Photopolymerization of cell-encapsulating hydrogels: Crosslinking efficiency versus cytotoxicity. 8(5):1838–1848. ISSN 1742-7061. doi: 10.1016/j.actbio.2011.12.034. URL <http://www.sciencedirect.com/science/article/pii/S1742706112000050>.
- [87] Janine Jansen, Abdul Ghaffar, Thomas N. S. van der Horst, George Mihov, Sjoerd van der Wal, Jan Feijen, and Dirk W. Grijpma. Controlling the kinetic chain length of the crosslinks in photo-polymerized biodegradable networks. 24(4):877–888. ISSN 0957-4530, 1573-4838. doi: 10.1007/s10856-013-4873-x. URL <https://link.springer.com/article/10.1007/s10856-013-4873-x>.
- [88] L. Tytgat, S. Baudis, H. Ottevaere, R. Liska, H. Thienpont, P. Dubruel, and S. Van Vlierberghe. Photopolymerizable materials for cell encapsulation. In *3D Printing and Biofabrication*, Reference Series in Biomedical Engineering, pages 1–43. Springer, Cham. ISBN 978-3-319-40498-1. doi: 10.1007/978-3-319-40498-1_15-1. URL https://link.springer.com/referenceworkentry/10.1007/978-3-319-40498-1_15-1.
- [89] Hironobu Ikehata and Tetsuya Ono. The mechanisms of UV mutagenesis. 52(2):115–125. ISSN 0449-3060, 1349-9157. doi: 10.1269/jrr.10175. URL https://www.jstage.jst.go.jp/article/jrr/52/2/52_10175/_article/-char/ja/.
- [90] Xiaohong Hu and Changyou Gao. Photoinitiating polymerization to prepare biocompatible chitosan hydrogels. 110(2):1059–1067. ISSN 1097-4628. doi: 10.1002/app.28704. URL <https://onlinelibrary.wiley.com/doi/abs/10.1002/app.28704>.
- [91] Junli Hu, Yaping Hou, Hyejin Park, Bogyu Choi, Siying Hou, Amy Chung, and Min Lee. Visible light crosslinkable chitosan hydrogels for tissue engineering. 8(5):1730–1738. ISSN 1742-7061. doi: 10.1016/j.actbio.2012.01.029. URL <http://www.sciencedirect.com/science/article/pii/S1742706112000451>.
- [92] Ciba. Ciba IRGACURE 2959. pages 2.4.98, Basle.
- [93] Herman Bergwerf. MolView. URL <http://molview.org/>.
- [94] Rafael Turra Alarcon, Caroline Gaglieri, Bruno Henrique Sacoman Torquato da Silva, Luiz Carlos da Silva Filho, and Gilbert Bannach. New fluorescein dye derivatives and their use as an efficient photoinitiator using blue light LED. 343: 112–118. ISSN 1010-6030. doi: 10.1016/j.jphotochem.2017.04.027. URL <http://www.sciencedirect.com/science/article/pii/S1010603017301752>.
- [95] Carine T. W. Meereis, Fernanda B. Leal, Giana S. Lima, Rodrigo V. de Carvalho, Evandro Piva, and Fabrício A. Ogliari. BAPO as an alternative photoinitiator for the radical polymerization of dental resins. 30(9):945–953. ISSN 0109-5641, 1879-0097. doi: 10.1016/j.dental.2014.05.020. URL [https://www.demajournal.com/article/S0109-5641\(14\)00152-3/abstract](https://www.demajournal.com/article/S0109-5641(14)00152-3/abstract).

- [96] Benjamin D. Fairbanks, Michael P. Schwartz, Christopher N. Bowman, and Kristi S. Anseth. Photoinitiated polymerization of PEG-diacrylate with lithium phenyl-2,4,6-trimethylbenzoylphosphinate: polymerization rate and cytocompatibility. 30 (35):6702–6707. ISSN 0142-9612. doi: 10.1016/j.biomaterials.2009.08.055. URL <http://www.sciencedirect.com/science/article/pii/S0142961209009041>.
- [97] Phenylbis(2,4,6-trimethylbenzoyl)phosphine oxide | sigma-aldrich, . URL <https://www.sigmaaldrich.com/catalog/substance/phenylbis246trimethylbenzoylphosphineoxide4184616288126711?lang=fr®ion=CH>.
- [98] John J. Florio and Daniel J. Miller. *Handbook Of Coating Additives*. CRC Press. ISBN 978-0-8247-5626-0. Google-Books-ID: vlq0UzebgG4C.
- [99] Julian G. Leprince, William M. Palin, Mohammed A. Hadis, Jacques Devaux, and Gaetane Leloup. Progress in dimethacrylate-based dental composite technology and curing efficiency. 29(2):139–156. ISSN 0109-5641. doi: 10.1016/j.dental.2012.11.005. URL <http://www.sciencedirect.com/science/article/pii/S0109564112004629>.
- [100] Eiichi Yoshii. Cytotoxic effects of acrylates and methacrylates: Relationships of monomer structures and cytotoxicity. 37(4):517–524. ISSN 1097-4636. doi: 10.1002/(SICI)1097-4636(19971215)37:4<517::AID-JBM10>3.0.CO;2-5. URL <https://onlinelibrary.wiley.com/doi/abs/10.1002/%28SICI%291097-4636%2819971215%2937%3A4%3C517%3A%3AAID-JBM10%3E3.0.CO%3B2-5>.
- [101] Jason A Burdick, Alan J Peterson, and Kristi S Anseth. Conversion and temperature profiles during the photoinitiated polymerization of thick orthopaedic biomaterials. 22(13):1779–1786, . ISSN 0142-9612. doi: 10.1016/S0142-9612(00)00347-1. URL <http://www.sciencedirect.com/science/article/pii/S0142961200003471>.
- [102] Silvana Asmusen, Gustavo Arenas, Wayne D. Cook, and Claudia Vallo. Photobleaching of camphorquinone during polymerization of dimethacrylate-based resins. 25(12):1603–1611. ISSN 0109-5641. doi: 10.1016/j.dental.2009.08.010. URL <http://www.sciencedirect.com/science/article/pii/S0109564109002851>.
- [103] Andreas Schmocker, Azadeh Khoushabi, Constantin Schizas, Pierre-Etienne Bourban, Dominique P. Pioletti, and Christophe Moser. Miniature probe for the delivery and monitoring of a photopolymerizable material. 20(12):127001–127001, . ISSN 1083-3668. doi: 10.1117/1.JBO.20.12.127001. URL <http://dx.doi.org/10.1117/1.JBO.20.12.127001>.
- [104] Sina Naficy, Hugh R. Brown, Joselito M. Razal, Geoffrey M. Spinks, and Philip G. Whitten. Progress toward robust polymer hydrogels. 64(8):1007–1025. ISSN 1445-0038. doi: 10.1071/CH11156. URL <http://dx.doi.org/10.1071/CH11156>.
- [105] Tao Lin Sun, Takayuki Kurokawa, Shinya Kuroda, Abu Bin Ihsan, Taigo Akasaki, Koshiro Sato, Md Anamul Haque, Tasuku Nakajima, and Jian Ping Gong. Physical hydrogels composed of polyampholytes demonstrate high toughness and viscoelasticity. 12(10):932–937, . ISSN 1476-1122. doi: 10.1038/nmat3713. URL <http://www.nature.com/nmat/journal/v12/n10/abs/nmat3713.html>. polyampholyte, softening, recoverable.
- [106] Xueyu Li, Kunpeng Cui, Tao Lin Sun, Lingpu Meng, Chengtao Yu, Liangbin Li, Costantino Creton, Takayuki Kurokawa, and Jian Ping Gong. Mesoscale bicontinuous networks in self-healing hydrogels delay fatigue fracture. 117(14):7606–7612, . ISSN 0027-8424, 1091-6490. doi: 10.1073/pnas.2000189117. URL <https://www.pnas.org/content/117/14/7606>. Publisher: National Academy of Sciences Section: Physical Sciences.
- [107] Mingyu Guo, Louis M. Pitet, Hans M. Wyss, Matthijn Vos, Patricia Y. W. Dankers, and E. W. Meijer. Tough stimuli-responsive supramolecular hydrogels with hydrogen-bonding network junctions. 136(19):6969–6977, . ISSN 0002-7863. doi: 10.1021/ja500205v. URL <http://dx.doi.org/10.1021/ja500205v>. Supramolecule, h-bond, softening, PEG.
- [108] Xuanhe Zhao. A theory for large deformation and damage of interpenetrating polymer networks. 60(2):319–332, . ISSN 0022-5096. doi: 10.1016/j.jmps.2011.10.005. URL <http://www.sciencedirect.com/science/article/pii/S0022509611001980>. IPN model, mullins effect.
- [109] Shannon E. Bakarich, Geoffrey C. Pidcock, Paul Balding, Leo Stevens, Paul Calvert, and Marc in het Panhuis. Recovery from applied strain in interpenetrating polymer network hydrogels with ionic and covalent cross-links. 8(39):9985–9988. doi: 10.1039/C2SM26745D. URL <http://pubs.rsc.org/en/Content/ArticleLanding/2012/SM/C2SM26745D>. IPN, softening, ionic+covalent bond, recoverable.
- [110] Abhijeet Joshi, Garland Fussell, Jonathan Thomas, Andrew Hsuan, Anthony Lowman, Andrew Karduna, Ed Vresilovic, and Michele Marcolongo. Functional compressive mechanics of a PVA/PVP nucleus pulposus replacement. 27(2):176–184. ISSN 0142-9612. doi: 10.1016/j.biomaterials.2005.06.003. URL <http://www.sciencedirect.com/science/article/pii/S0142961205005715>. NP, no softening, IPN, hydrogen bond.

- [111] Ana M. S. Costa and João F. Mano. Highly robust hydrogels via a fast, simple and cytocompatible dual crosslinking-based process. 51(86):15673–15676. doi: 10.1039/C5CC05564D. URL <http://pubs.rsc.org/en/Content/ArticleLanding/2015/CC/C5CC05564D>. DN, Mullins, recoverable.
- [112] Jian Hu, Takayuki Kurokawa, Tasuku Nakajima, Tao Lin Sun, Tiffany Suekama, Zi Liang Wu, Song Miao Liang, and Jian Ping Gong. High fracture efficiency and stress concentration phenomenon for microgel-reinforced hydrogels based on double-network principle. 45(23):9445–9451, . ISSN 0024-9297. doi: 10.1021/ma301933x. URL <http://dx.doi.org/10.1021/ma301933x>. comparison between DN,NC and convential.
- [113] Xuanhe Zhao. Multi-scale multi-mechanism design of tough hydrogels: building dissipation into stretchy networks. 10(5): 672–687, . doi: 10.1039/C3SM52272E. URL <http://pubs.rsc.org/en/Content/ArticleLanding/2014/SM/C3SM52272E>.
- [114] Hai-Wei Liang, Qing-Fang Guan, Li-Feng Chen, Zhu Zhu, Wen-Jun Zhang, and Shu-Hong Yu. Macroscopic-scale template synthesis of robust carbonaceous nanofiber hydrogels and aerogels and their applications. 51(21):5101–5105. ISSN 1521-3773. doi: 10.1002/anie.201200710. URL <http://onlinelibrary.wiley.com/doi/10.1002/anie.201200710/abstract>. NC, softening, no mullins.
- [115] Huai-Ping Cong, Ping Wang, and Shu-Hong Yu. Highly elastic and superstretchable graphene oxide/polyacrylamide hydrogels. 10(3):448–453. ISSN 1613-6829. doi: 10.1002/sml.201301591. URL <http://onlinelibrary.wiley.com/doi/10.1002/sml.201301591/abstract>. hybrid-NC, No softening.
- [116] Ming Zhong, Yi-Tao Liu, and Xu-Ming Xie. Self-healable, super tough graphene oxide–poly(acrylic acid) nanocomposite hydrogels facilitated by dual cross-linking effects through dynamic ionic interactions. 3(19):4001–4008, . doi: 10.1039/C5TB00075K. URL <http://pubs.rsc.org/en/Content/ArticleLanding/2015/TB/C5TB00075K>. NC, softening, partially recoverable.
- [117] F. Duc, P. E. Bourban, and J. A. E. Månson. The role of twist and crimp on the vibration behaviour of flax fibre composites. 102:94–99. ISSN 0266-3538. doi: 10.1016/j.compscitech.2014.07.004. URL <http://www.sciencedirect.com/science/article/pii/S0266353814002346>.
- [118] Leming Sun, Sijia Yi, Yongzhong Wang, Kang Pan, Qixin Zhong, and Mingjun Zhang. A bio-inspired approach for in situ synthesis of tunable adhesive. 9(1):016005, . ISSN 1748-3190. doi: 10.1088/1748-3182/9/1/016005. URL <http://stacks.iop.org/1748-3190/9/i=1/a=016005>.
- [119] A. Sydney Gladman, Elisabetta A. Matsumoto, Ralph G. Nuzzo, L. Mahadevan, and Jennifer A. Lewis. Biomimetic 4d printing. 15(4):413–418. ISSN 1476-1122. doi: 10.1038/nmat4544. URL <http://www.nature.com/nmat/journal/v15/n4/full/nmat4544.html>.
- [120] Mokit Chau, Kevin J. De France, Bernd Kopera, Vanessa R. Machado, Sabine Rosenfeldt, Laura Reyes, Katelyn J. W. Chan, Stephan Förster, Emily D. Cranston, Todd Hoare, and Eugenia Kumacheva. Composite hydrogels with tunable anisotropic morphologies and mechanical properties. 28(10):3406–3415. ISSN 0897-4756. doi: 10.1021/acs.chemmater.6b00792. URL <http://dx.doi.org/10.1021/acs.chemmater.6b00792>.
- [121] Kevin J. De France, Emily D. Cranston, and Todd Hoare. Mechanically reinforced injectable hydrogels. 2(3):1016–1030, . doi: 10.1021/acsapm.9b00981. URL <https://doi.org/10.1021/acsapm.9b00981>. Publisher: American Chemical Society.
- [122] Scott Brice Campbell and Todd Hoare. Externally addressable hydrogel nanocomposites for biomedical applications. 4: 1–10. ISSN 2211-3398. doi: 10.1016/j.coche.2013.12.003. URL <http://www.sciencedirect.com/science/article/pii/S2211339813001196>.
- [123] Jeffrey P. Maranchi, Morgana M. Trexler, Qiongyu Guo, and Jennifer H. Elisseeff. Fibre-reinforced hydrogels with high optical transparency. 59(5):264–296. ISSN 0950-6608. doi: 10.1179/1743280414Y.0000000032. URL <http://dx.doi.org/10.1179/1743280414Y.0000000032>.
- [124] Lanti Yang, Carel F. C. Fitié, Kees O. van der Werf, Martin L. Bennink, Pieter J. Dijkstra, and Jan Feijen. Mechanical properties of single electrospun collagen type i fibers. 29(8):955–962, . ISSN 0142-9612. doi: 10.1016/j.biomaterials.2007.10.058. URL <http://www.sciencedirect.com/science/article/pii/S0142961207008666>.
- [125] Xuan Yang, Emilia Bakaic, Todd Hoare, and Emily D. Cranston. Injectable polysaccharide hydrogels reinforced with cellulose nanocrystals: Morphology, rheology, degradation, and cytotoxicity. 14(12):4447–4455, . ISSN 1525-7797. doi: 10.1021/bm401364z. URL <http://pubs.acs.org/doi/abs/10.1021/bm401364z>.

- [126] Jingjing Yao, Shiyen Chen, Ye Chen, Baoxiu Wang, Qibing Pei, and Huaping Wang. Macrofibers with high mechanical performance based on aligned bacterial cellulose nanofibers. ISSN 1944-8244. doi: 10.1021/acsami.6b14650. URL <http://dx.doi.org/10.1021/acsami.6b14650>.
- [127] S. J. Eichhorn, A. Dufresne, M. Aranguren, N. E. Marcovich, J. R. Capadona, S. J. Rowan, C. Weder, W. Thielemans, M. Roman, S. Renneckar, W. Gindl, S. Veigel, J. Keckes, H. Yano, K. Abe, M. Nogi, A. N. Nakagaito, A. Mangalam, J. Simonsen, A. S. Benight, A. Bismarck, L. A. Berglund, and T. Peijs. Review: current international research into cellulose nanofibres and nanocomposites. 45(1):1. ISSN 0022-2461, 1573-4803. doi: 10.1007/s10853-009-3874-0. URL <http://link.springer.com/article/10.1007/s10853-009-3874-0>.
- [128] Karim Missoum, Mohamed Naceur Belgacem, and Julien Bras. Nanofibrillated cellulose surface modification: A review. 6(5):1745–1766. doi: 10.3390/ma6051745. URL <http://www.mdpi.com/1996-1944/6/5/1745>.
- [129] Rui M. A. Domingues, Manuela E. Gomes, and Rui L. Reis. The potential of cellulose nanocrystals in tissue engineering strategies. 15(7):2327–2346. ISSN 1525-7797. doi: 10.1021/bm500524s. URL <http://dx.doi.org/10.1021/bm500524s>.
- [130] Chengjun Zhou and Qinglin Wu. A novel polyacrylamide nanocomposite hydrogel reinforced with natural chitosan nanofibers. 84(1):155–162. ISSN 0927-7765. doi: 10.1016/j.colsurfb.2010.12.030. URL <http://www.sciencedirect.com/science/article/pii/S0927776511000051>.
- [131] Ngesa Ezekiel Mushi. Chitin nanofibers, networks and composites : Preparation, structure and mechanical properties. URL <http://www.diva-portal.org/smash/record.jsf?pid=diva2:761483>.
- [132] Jun Araki, Yuta Yamanaka, and Kousaku Ohkawa. Chitin-chitosan nanocomposite gels: reinforcement of chitosan hydrogels with rod-like chitin nanowhiskers. 44(7):713–717. ISSN 0032-3896. doi: 10.1038/pj.2012.11. URL <http://www.nature.com/pj/journal/v44/n7/abs/pj201211a.html>.
- [133] Shinsuke Ifuku and Hiroyuki Saimoto. Chitin nanofibers: preparations, modifications, and applications. 4(11):3308–3318. doi: 10.1039/C2NR30383C. URL <http://pubs.rsc.org/en/Content/ArticleLanding/2012/NR/C2NR30383C>.
- [134] Fereshteh Mirahmadi, Mohammad Tafazzoli-Shadpour, Mohammad Ali Shokrgozar, and Shahin Bonakdar. Enhanced mechanical properties of thermosensitive chitosan hydrogel by silk fibers for cartilage tissue engineering. 33(8):4786–4794. ISSN 0928-4931. doi: 10.1016/j.jmsec.2013.07.043. URL <http://www.sciencedirect.com/science/article/pii/S0928493113004591>.
- [135] Supansa Yodmuang, Stephanie L. McNamara, Adam B. Nover, Biman B. Mandal, Monica Agarwal, Terri-Ann N. Kelly, Penhsu Grace Chao, Clark Hung, David L. Kaplan, and Gordana Vunjak-Novakovic. Silk microfiber-reinforced silk hydrogel composites for functional cartilage tissue repair. 11:27–36. ISSN 1742-7061. doi: 10.1016/j.actbio.2014.09.032. URL <http://www.sciencedirect.com/science/article/pii/S174270611400422X>.
- [136] Kevin J. De France, Todd Hoare, and Emily D. Cranston. Review of hydrogels and aerogels containing nanocellulose. 29(11):4609–4631. ISSN 0897-4756. doi: 10.1021/acs.chemmater.7b00531. URL <https://doi.org/10.1021/acs.chemmater.7b00531>. Publisher: American Chemical Society.
- [137] Wolfgang Gindl, Gerhard Emsenhuber, Günther Maier, and Jozef Keckes. Cellulose in never-dried gel oriented by an AC electric field. 10(5):1315–1318. ISSN 1525-7797. doi: 10.1021/bm801508e. URL <http://dx.doi.org/10.1021/bm801508e>.
- [138] Damien Bordel, Jean-Luc Putaux, and Laurent Heux. Orientation of native cellulose in an electric field. 22(11):4899–4901. ISSN 0743-7463. doi: 10.1021/la0600402. URL <http://dx.doi.org/10.1021/la0600402>.
- [139] E. D. Cranston and D. G. Gray. Formation of cellulose-based electrostatic layer-by-layer films in a magnetic field. 7(4):319–321. ISSN 1468-6996. doi: 10.1016/j.stam.2006.02.007. URL <http://www.sciencedirect.com/science/article/pii/S1468699606000519>.
- [140] Kevin J. De France, Kevin G. Yager, Todd Hoare, and Emily D. Cranston. Cooperative ordering and kinetics of cellulose nanocrystal alignment in a magnetic field. 32(30):7564–7571. ISSN 0743-7463. doi: 10.1021/acs.langmuir.6b01827. URL <https://doi.org/10.1021/acs.langmuir.6b01827>. Publisher: American Chemical Society.
- [141] Tanja Zimmermann, Nicolae Bordeanu, and Esther Strub. Properties of nanofibrillated cellulose from different raw materials and its reinforcement potential. 79(4):1086–1093. ISSN 0144-8617. doi: 10.1016/j.carbpol.2009.10.045. URL <http://www.sciencedirect.com/science/article/pii/S0144861709005992>.

- [142] Sinke H. Osong, Sven Norgren, and Per Engstrand. Processing of wood-based microfibrillated cellulose and nanofibrillated cellulose, and applications relating to papermaking: a review. 23(1):93–123. ISSN 1572-882X. doi: 10.1007/s10570-015-0798-5. URL <https://doi.org/10.1007/s10570-015-0798-5>.
- [143] Alaa Raheem Kazim. Production, optimization, and characterization of cellulose produced from pseudomonas spp. Vol. 3, No. 2:89–93.
- [144] Guilherme Fadel Picheth, Cleverton Luiz Pirich, Maria Rita Sierakowski, Marco Aurélio Woehl, Caroline Novak Sakakibara, Clayton Fernandes de Souza, Andressa Amado Martin, Renata da Silva, and Rilton Alves de Freitas. Bacterial cellulose in biomedical applications: A review. 104:97–106. ISSN 0141-8130. doi: 10.1016/j.ijbiomac.2017.05.171. URL <http://www.sciencedirect.com/science/article/pii/S0141813017313375>.
- [145] Rui F. P. Pereira, Maria M. Silva, and Verónica de Zea Bermudez. Bombyx mori silk fibers: An outstanding family of materials. 300(12):1171–1198. ISSN 1439-2054. doi: 10.1002/mame.201400276. URL <https://onlinelibrary.wiley.com/doi/abs/10.1002/mame.201400276>.
- [146] Chris Holland, Keiji Numata, Jelena Rnjak-Kovacina, and F. Philipp Seib. The biomedical use of silk: Past, present, future. page 1800465. ISSN 0006-3525. doi: 10.1002/adhm.201800465@10.1002/(ISSN)1097-0282.Biopolymers2019. URL [https://onlinelibrary.wiley.com/doi/abs/10.1002/adhm.201800465@10.1002/\(ISSN\)1097-0282.Biopolymers2019](https://onlinelibrary.wiley.com/doi/abs/10.1002/adhm.201800465@10.1002/(ISSN)1097-0282.Biopolymers2019).
- [147] Charu Vepari and David L. Kaplan. Silk as a biomaterial. 32(8):991–1007. ISSN 0079-6700. doi: 10.1016/j.progpolymsci.2007.05.013. URL <http://www.sciencedirect.com/science/article/pii/S0079670007000731>.
- [148] Daniela Angelika Frauchiger, Adel Tekari, Michael Wöltje, Giuseppino Fortunato, Lorin Michael Benneker, and Benjamin Gantenbein. A review of the application of reinforced hydrogels and silk as biomaterials for intervertebral disc repair. 34: 271–290. ISSN 1473-2262. doi: info:doi:10.22203/eCM.v034a17. URL <https://boris.unibe.ch/106570/>.
- [149] Keiji Numata, Takuya Katashima, and Takamasa Sakai. State of water, molecular structure, and cytotoxicity of silk hydrogels. 12(6):2137–2144. ISSN 1525-7797. doi: 10.1021/bm200221u. URL <https://doi.org/10.1021/bm200221u>.
- [150] Danielle N. Rockwood, Rucsanda C. Preda, Tuna Yücel, Xiaoqin Wang, Michael L. Lovett, and David L. Kaplan. Materials fabrication from *Bombyx mori* silk fibroin. 6(10):1612–1631. ISSN 1750-2799. doi: 10.1038/nprot.2011.379. URL <https://www.nature.com/articles/nprot.2011.379>.
- [151] Amanda R. Murphy and David L. Kaplan. Biomedical applications of chemically-modified silk fibroin. 19(36):6443–6450. doi: 10.1039/B905802H. URL <http://pubs.rsc.org/en/Content/ArticleLanding/2009/JM/B905802H>.
- [152] Fengxuan Han, Chen Shi, Huilin Yang, and Bin Li. Calcium phosphate-silk fibroin composites: Bone cement and beyond. In Changsheng Liu and Hongyan He, editors, *Developments and Applications of Calcium Phosphate Bone Cements*, Springer Series in Biomaterials Science and Engineering, pages 449–472. Springer Singapore, . ISBN 978-981-10-5975-9. doi: 10.1007/978-981-10-5975-9_10. URL https://doi.org/10.1007/978-981-10-5975-9_10.
- [153] Jinfa Ming, Mengmeng Li, Yuhui Han, Ying Chen, Han Li, Baoqi Zuo, and Fukui Pan. Novel two-step method to form silk fibroin fibrous hydrogel. 59:185–192. ISSN 0928-4931. doi: 10.1016/j.msec.2015.10.013. URL <http://www.sciencedirect.com/science/article/pii/S0928493115304446>.
- [154] Tuna Yucel, Nikola Kojic, Gary G. Leisk, Tim J. Lo, and David L. Kaplan. Non-equilibrium silk fibroin adhesives. 170 (2):406–412. ISSN 1047-8477. doi: 10.1016/j.jsb.2009.12.012. URL <http://www.sciencedirect.com/science/article/pii/S1047847709003396>.
- [155] Xiaoqin Wang, Benjamin Partlow, Jian Liu, Zhaozhu Zheng, Bo Su, Yansong Wang, and David L. Kaplan. Injectable silk-polyethylene glycol hydrogels. 12:51–61, . ISSN 1742-7061. doi: 10.1016/j.actbio.2014.10.027. URL <http://www.sciencedirect.com/science/article/pii/S1742706114004693>.
- [156] Sungkyun Sohn, Helmut H. Strey, and Samuel P. Gido. Phase behavior and hydration of silk fibroin. 5(3):751–757. ISSN 1525-7797. doi: 10.1021/bm0343693. URL <http://dx.doi.org/10.1021/bm0343693>.
- [157] Feng Zhang, Xinran You, Hao Dou, Zhi Liu, Baoqi Zuo, and Xueguang Zhang. Facile fabrication of robust silk nanofibril films via direct dissolution of silk in CaCl₂-formic acid solution. 7(5):3352–3361, . ISSN 1944-8244. doi: 10.1021/am508319h. URL <https://doi.org/10.1021/am508319h>.

- [158] Feng Zhang, Qiang Lu, Jinfa Ming, Hao Dou, Zhi Liu, Baoqi Zuo, Mingde Qin, Fang Li, David L. Kaplan, and Xueguang Zhang. Silk dissolution and regeneration at the nanofibril scale. 2(24):3879–3885, . doi: 10.1039/C3TB21582B. URL <https://pubs.rsc.org/en/content/articlelanding/2014/tb/c3tb21582b>.
- [159] Shiyu Bie, Jinfa Ming, Yan Zhou, Tianyi Zhong, Feng Zhang, and Baoqi Zuo. Rapid formation of flexible silk fibroin gel-like films. 132(15). ISSN 1097-4628. doi: 10.1002/app.41842. URL <https://onlinelibrary.wiley.com/doi/abs/10.1002/app.41842>.
- [160] Feng Zhang, Qiang Lu, Xiaoxiao Yue, Baoqi Zuo, Mingde Qin, Fang Li, David L. Kaplan, and Xueguang Zhang. Regeneration of high-quality silk fibroin fiber by wet spinning from CaCl₂-formic acid solvent. 12:139–145, . ISSN 1742-7061. doi: 10.1016/j.actbio.2014.09.045. URL <http://www.sciencedirect.com/science/article/pii/S1742706114004371>.
- [161] Feng Zhang, Bao Q. Zuo, and Lun Bai. Study on the structure of SF fiber mats electrospun with HFIP and FA and cells behavior. 44(20):5682–5687, . ISSN 1573-4803. doi: 10.1007/s10853-009-3800-5. URL <https://doi.org/10.1007/s10853-009-3800-5>.
- [162] Julianne L. Holloway, Anthony M. Lowman, Mark R. VanLandingham, and Giuseppe R. Palmese. Chemical grafting for improved interfacial shear strength in UHMWPE/PVA-hydrogel fiber-based composites used as soft fibrous tissue replacements. 85:118–125. ISSN 0266-3538. doi: 10.1016/j.compscitech.2013.06.007. URL <http://www.sciencedirect.com/science/article/pii/S0266353813002388>.
- [163] Vijay Kumar Thakur, Manju Kumari Thakur, and Raju Kumar Gupta. Graft copolymers of natural fibers for green composites. 104:87–93. ISSN 0144-8617. doi: 10.1016/j.carbpol.2014.01.016. URL <http://www.sciencedirect.com/science/article/pii/S0144861714000186>.
- [164] Janak Sapkota, Mehdi Jorfi, Christoph Weder, and Earl Johan Foster. Reinforcing poly(ethylene) with cellulose nanocrystals. 35(20):1747–1753. ISSN 1521-3927. doi: 10.1002/marc.201400382. URL <http://onlinelibrary.wiley.com/doi/10.1002/marc.201400382/abstract>.
- [165] J. Antons, M. G. M. Marascio, J. Nohava, R. Martin, L. A. Applegate, P. E. Bourban, and D. P. Pioletti. Zone-dependent mechanical properties of human articular cartilage obtained by indentation measurements. 29(5):57. ISSN 1573-4838. doi: 10.1007/s10856-018-6066-0. URL <https://doi.org/10.1007/s10856-018-6066-0>.
- [166] Sajedeh Khorshidi and Akbar Karkhaneh. A review on gradient hydrogel/fiber scaffolds for osteochondral regeneration. 12(4):e1974–e1990. ISSN 1932-7005. doi: 10.1002/term.2628. URL <https://onlinelibrary.wiley.com/doi/abs/10.1002/term.2628>. __eprint: <https://onlinelibrary.wiley.com/doi/pdf/10.1002/term.2628>.
- [167] Jingyi Guo, Mincong Liu, Alan T. Zehnder, Jingwen Zhao, Tetsuhara Narita, Costantino Creton, and Chung-Yuen Hui. Fracture mechanics of a self-healing hydrogel with covalent and physical crosslinks: A numerical study. . ISSN 0022-5096. doi: 10.1016/j.jmps.2018.03.009. URL <http://www.sciencedirect.com/science/article/pii/S0022509617308037>.
- [168] Shannon E. Bakarich, Robert Gorkin, Reece Gately, Sina Naficy, Marc in het Panhuis, and Geoffrey M. Spinks. 3d printing of tough hydrogel composites with spatially varying materials properties. 14:24–30. ISSN 2214-8604. doi: 10.1016/j.addma.2016.12.003. URL <http://www.sciencedirect.com/science/article/pii/S221486041630361X>.
- [169] Lauren M. Cross, Kunal Shah, Sowmiya Palani, Charles W. Peak, and Akhilesh K. Gaharwar. Gradient nanocomposite hydrogels for interface tissue engineering. 14(7):2465–2474. ISSN 1549-9634. doi: 10.1016/j.nano.2017.02.022. URL <http://www.sciencedirect.com/science/article/pii/S1549963417300874>.
- [170] Shangjing Xin, Jing Dai, Carl A. Gregory, Arum Han, and Daniel L. Alge. Creating physicochemical gradients in modular microporous annealed particle hydrogels via a microfluidic method. 30(6):1907102, . ISSN 1616-3028. doi: 10.1002/adfm.201907102. URL <https://onlinelibrary.wiley.com/doi/abs/10.1002/adfm.201907102>. __eprint: <https://onlinelibrary.wiley.com/doi/pdf/10.1002/adfm.201907102>.
- [171] Jiankang He, Ting Qin, Yaxiong Liu, Xiang Li, Dichen Li, and Zhongmin Jin. Electrospinning of nanofibrous scaffolds with continuous structure and material gradients. 137:393–397, . ISSN 0167-577X. doi: 10.1016/j.matlet.2014.09.045. URL <http://www.sciencedirect.com/science/article/pii/S0167577X14016796>.
- [172] Gang Xu, Zhaozhao Ding, Qiang Lu, Xiaoyi Zhang, Xiaozhong Zhou, Liying Xiao, Guozhong Lu, and David L. Kaplan. Electric field-driven building blocks for introducing multiple gradients to hydrogels. 11(4):267–285, . ISSN 1674-8018. doi: 10.1007/s13238-020-00692-z. URL <https://doi.org/10.1007/s13238-020-00692-z>.

- [173] Tae Ho Kim, Dan Bi An, Se Heang Oh, Min Kwan Kang, Hyun Hoon Song, and Jin Ho Lee. Creating stiffness gradient polyvinyl alcohol hydrogel using a simple gradual freezing–thawing method to investigate stem cell differentiation behaviors. 40:51–60, . ISSN 0142-9612. doi: 10.1016/j.biomaterials.2014.11.017. URL <http://www.sciencedirect.com/science/article/pii/S0142961214011776>.
- [174] Luke G. Major, Andrew W. Holle, Jennifer L. Young, Matt S. Hepburn, Kwanghee Jeong, Ian L. Chin, Rowan W. Sanderson, Ji Hoon Jeong, Zachary M. Aman, Brendan F. Kennedy, Yongsung Hwang, Dong-Wook Han, Hyun Woo Park, Kun-Liang Guan, Joachim P. Spatz, and Yu Suk Choi. Volume adaptation controls stem cell mechanotransduction. 11(49):45520–45530. ISSN 1944-8244. doi: 10.1021/acsami.9b19770. URL <https://doi.org/10.1021/acsami.9b19770>. Publisher: American Chemical Society.
- [175] Xiaoxia Le, Wei Lu, Jiawei Zhang, and Tao Chen. Recent progress in biomimetic anisotropic hydrogel actuators. 6(5):1801584. ISSN 2198-3844. doi: 10.1002/advs.201801584. URL <https://onlinelibrary.wiley.com/doi/abs/10.1002/advs.201801584>. _eprint: <https://onlinelibrary.wiley.com/doi/pdf/10.1002/advs.201801584>.
- [176] Koki Sano, Yasuhiro Ishida, and Takuzo Aida. Synthesis of anisotropic hydrogels and their applications. 57(10):2532–2543. ISSN 1521-3773. doi: 10.1002/anie.201708196. URL <https://onlinelibrary.wiley.com/doi/abs/10.1002/anie.201708196>. _eprint: <https://onlinelibrary.wiley.com/doi/pdf/10.1002/anie.201708196>.
- [177] Elisabeth Prince, Moien Alizadehgiashi, Melissa Campbell, Nancy Khuu, Alexandra Albulescu, Kevin De France, Dimitrije Ratkov, Yunfeng Li, Todd Hoare, and Eugenia Kumacheva. Patterning of structurally anisotropic composite hydrogel sheets. 19(4):1276–1284. ISSN 1525-7797. doi: 10.1021/acs.biomac.8b00100. URL <https://doi.org/10.1021/acs.biomac.8b00100>. Publisher: American Chemical Society.
- [178] Kevin J. De France, Kevin G. Yager, Katelyn J. W. Chan, Brandon Corbett, Emily D. Cranston, and Todd Hoare. Injectable anisotropic nanocomposite hydrogels direct in situ growth and alignment of myotubes. 17(10):6487–6495, . ISSN 1530-6984. doi: 10.1021/acs.nanolett.7b03600. URL <https://doi.org/10.1021/acs.nanolett.7b03600>. Publisher: American Chemical Society.
- [179] Brett G. Compton and Jennifer A. Lewis. 3d-printing of lightweight cellular composites. 26(34):5930–5935. ISSN 1521-4095. doi: 10.1002/adma.201401804. URL <http://onlinelibrary.wiley.com/doi/10.1002/adma.201401804/abstract>.
- [180] Bin Gao, Qingzhen Yang, Xin Zhao, Guorui Jin, Yufei Ma, and Feng Xu. 4d bioprinting for biomedical applications. 34(9): 746–756. ISSN 0167-7799. doi: 10.1016/j.tibtech.2016.03.004. URL <http://www.sciencedirect.com/science/article/pii/S0167779916000664>.
- [181] Jérémy Odent, Sophie Vanderstappen, Antoniya Toncheva, Enzo Pichon, Thomas J. Wallin, Kaiyang Wang, Robert F. Shepherd, Philippe Dubois, and Jean-Marie Raquez. Hierarchical chemomechanical encoding of multi-responsive hydrogel actuators via 3d printing. 7(25):15395–15403. doi: 10.1039/C9TA03547H. URL <https://pubs.rsc.org/en/content/articlelanding/2019/ta/c9ta03547h>. Publisher: Royal Society of Chemistry.
- [182] Chunxin Ma, Wei Lu, Xuxu Yang, Jiang He, Xiaoxia Le, Li Wang, Jiawei Zhang, Michael J. Serpe, Youju Huang, and Tao Chen. Bioinspired anisotropic hydrogel actuators with on–off switchable and color-tunable fluorescence behaviors. 28(7): 1704568. ISSN 1616-3028. doi: 10.1002/adfm.201704568. URL <https://onlinelibrary.wiley.com/doi/abs/10.1002/adfm.201704568>. _eprint: <https://onlinelibrary.wiley.com/doi/pdf/10.1002/adfm.201704568>.
- [183] Chien-Chi Lin and Kristi S. Anseth. PEG hydrogels for the controlled release of biomolecules in regenerative medicine. 26(3):631–643. ISSN 1573-904X. doi: 10.1007/s11095-008-9801-2. URL <https://doi.org/10.1007/s11095-008-9801-2>.
- [184] Ján Kruželák, Richard Sýkora, and Ivan Hudec. Sulphur and peroxide vulcanisation of rubber compounds — overview. 70(12):1533–1555. ISSN 1336-9075. doi: 10.1515/chempap-2016-0093. URL <https://doi.org/10.1515/chempap-2016-0093>.
- [185] Lauren N. Russell and Kyle J. Lampe. Oligodendrocyte precursor cell viability, proliferation, and morphology is dependent on mesh size and storage modulus in 3d poly(ethylene glycol)-based hydrogels. 3(12):3459–3468. doi: 10.1021/acsbiomaterials.7b00374. URL <https://doi.org/10.1021/acsbiomaterials.7b00374>.
- [186] Susan Lin, Nivedita Sangaj, Tojo Razafiarison, Chao Zhang, and Shyni Varghese. Influence of physical properties of biomaterials on cellular behavior. 28(6):1422–1430, . ISSN 1573-904X. doi: 10.1007/s11095-011-0378-9. URL <https://doi.org/10.1007/s11095-011-0378-9>.

- [187] Steven R. Caliri and Jason A. Burdick. A practical guide to hydrogels for cell culture. 13(5):405–414. ISSN 1548-7091. doi: 10.1038/nmeth.3839. URL <https://www.ncbi.nlm.nih.gov/pmc/articles/PMC5800304/>.
- [188] Fan Yang, Christopher G. Williams, Dong-an Wang, Hyukjin Lee, Paul N. Manson, and Jennifer Elisseeff. The effect of incorporating RGD adhesive peptide in polyethylene glycol diacrylate hydrogel on osteogenesis of bone marrow stromal cells. 26(30):5991–5998. . ISSN 0142-9612. doi: 10.1016/j.biomaterials.2005.03.018. URL <http://www.sciencedirect.com/science/article/pii/S0142961205002346>.
- [189] Thamarasee Jeewandara. Semi-flexible model-based analysis of cell adhesion to hydrogels. URL <https://phys.org/news/2019-02-semi-flexible-model-based-analysis-cell-adhesion.html>.
- [190] Ramses Ayala, Chao Zhang, Darren Yang, Yongsung Hwang, Aereas Aung, Sumeet S. Shroff, Fernando T. Arce, Ratnesh Lal, Gaurav Arya, and Shyni Varghese. Engineering the cell–material interface for controlling stem cell adhesion, migration, and differentiation. 32(15):3700–3711. ISSN 0142-9612. doi: 10.1016/j.biomaterials.2011.02.004. URL <http://www.sciencedirect.com/science/article/pii/S014296121100127X>.
- [191] Naser Nasrollahzadeh, Peyman Karami, and Dominique P. Pioletti. Control of dissipation sources: A central aspect for enhancing the mechanical and mechanobiological performances of hydrogels. 11(43):39662–39671. . ISSN 1944-8244. doi: 10.1021/acsami.9b15450. URL <https://doi.org/10.1021/acsami.9b15450>.
- [192] Kevin J. De France, Fei Xu, and Todd Hoare. Structured macroporous hydrogels: Progress, challenges, and opportunities. 7(1):1700927. ISSN 2192-2659. doi: 10.1002/adhm.201700927. URL <https://onlinelibrary.wiley.com/doi/abs/10.1002/adhm.201700927>. _eprint: <https://onlinelibrary.wiley.com/doi/pdf/10.1002/adhm.201700927>.
- [193] Yin Chen, Lu Huang, Xin Dai, Qian Tian, Miao Yu, Maria Agheb, Ho Nam Chan, Ellen Poon, Zhihong Guo, Kenneth Richard Boheler, and Hongkai Wu. Facile formation of a microporous chitosan hydrogel based on self-crosslinking. 5(47):9291–9299. . ISSN 2050-7518. doi: 10.1039/C7TB02736B. URL <https://pubs.rsc.org/en/content/articlelanding/2017/tb/c7tb02736b>.
- [194] Naser Nasrollahzadeh, Lee Ann Applegate, and Dominique P. Pioletti. Development of an effective cell seeding technique: Simulation, implementation, and analysis of contributing factors. 23(8):485–496. . ISSN 1937-3384. doi: 10.1089/ten.tec.2017.0108. URL <https://www.liebertpub.com/doi/10.1089/ten.tec.2017.0108>.
- [195] Fu You, Xia Wu, and Xiongbiao Chen. 3d printing of porous alginate/gelatin hydrogel scaffolds and their mechanical property characterization. 66(6):299–306. ISSN 0091-4037. doi: 10.1080/00914037.2016.1201830. URL <https://doi.org/10.1080/00914037.2016.1201830>.
- [196] Jonas C. Rose, David B. Gehlen, Tamás Haraszti, Jens Köhler, Christopher J. Licht, and Laura De Laporte. Biofunctionalized aligned microgels provide 3d cell guidance to mimic complex tissue matrices. 163:128–141. . ISSN 0142-9612. doi: 10.1016/j.biomaterials.2018.02.001. URL <http://www.sciencedirect.com/science/article/pii/S0142961218300796>.
- [197] Penggang Ren, Hua Zhang, Zhong Dai, Fang Ren, Yidong Wu, Ruixia Hou, Yabin Zhu, and Jun Fu. Stiff micelle-crosslinked hyaluronate hydrogels with low swelling for potential cartilage repair. 7(36):5490–5501. doi: 10.1039/C9TB01155B. URL <https://pubs.rsc.org/en/content/articlelanding/2019/tb/c9tb01155b>.
- [198] Romain Marcombe, Shengqiang Cai, Wei Hong, Xuanhe Zhao, Yuri Lapusta, and Zhigang Suo. A theory of constrained swelling of a pH-sensitive hydrogel. 6(4):784–793. doi: 10.1039/B917211D. URL <https://pubs.rsc.org/en/content/articlelanding/2010/sm/b917211d>.
- [199] Qiang Chen, Xiaoqiang Yan, Lin Zhu, Hong Chen, Bing Jiang, Dandan Wei, Lina Huang, Jia Yang, Baozhong Liu, and Jie Zheng. Improvement of mechanical strength and fatigue resistance of double network hydrogels by ionic coordination interactions. 28(16):5710–5720. . ISSN 0897-4756. doi: 10.1021/acs.chemmater.6b01920. URL <https://doi.org/10.1021/acs.chemmater.6b01920>.
- [200] Peyman Karami, Céline Samira Wyss, Azadeh Khoushabi, Andreas Schmock, Martin Broome, Christophe Moser, Pierre-Etienne Bourban, and Dominique P. Pioletti. Composite double-network hydrogels to improve adhesion on biological surfaces. 10(45):38692–38699. ISSN 1944-8244. doi: 10.1021/acsami.8b10735. URL <https://doi.org/10.1021/acsami.8b10735>.
- [201] Eva Klok. Polymer physical chemistry and materials properties.

- [202] Devin G. Barrett, Grace G. Bushnell, and Phillip B. Messersmith. Mechanically robust, negative-swelling, mussel-inspired tissue adhesives. 2(5):745–755. ISSN 2192-2659. doi: 10.1002/adhm.201200316. URL <http://onlinelibrary.wiley.com/doi/10.1002/adhm.201200316/abstract>.
- [203] Kun Xu, Ying Tan, Qiang Chen, Huiyong An, Wenbo Li, Lisong Dong, and Pixin Wang. A novel multi-responsive polyampholyte composite hydrogel with excellent mechanical strength and rapid shrinking rate. 345(2):360–368, . ISSN 0021-9797. doi: 10.1016/j.jcis.2010.01.058. URL <http://www.sciencedirect.com/science/article/pii/S0021979710001074>.
- [204] Neha Dhar, Seyedeh Parinaz Akhlaghi, and Kam C. Tam. Biodegradable and biocompatible polyampholyte microgels derived from chitosan, carboxymethyl cellulose and modified methyl cellulose. 87(1):101–109. ISSN 0144-8617. doi: 10.1016/j.carbpol.2011.07.022. URL <http://www.sciencedirect.com/science/article/pii/S0144861711005984>.
- [205] S. K. De, N. R. Aluru, B. Johnson, W. C. Crone, D. J. Beebe, and J. Moore. Equilibrium swelling and kinetics of pH-responsive hydrogels: models, experiments, and simulations. 11(5):544–555. ISSN 1057-7157. doi: 10.1109/JMEMS.2002.803281.
- [206] B. D Johnson, D. J Beebe, and W. C Crone. Effects of swelling on the mechanical properties of a pH-sensitive hydrogel for use in microfluidic devices. 24(4):575–581. ISSN 0928-4931. doi: 10.1016/j.msec.2003.11.002. URL <http://www.sciencedirect.com/science/article/pii/S0928493103002947>. conventional, softer when swollen, poisson ratio.
- [207] Kuen Yong Lee, Jon A. Rowley, Petra Eiselt, Erick M. Moy, Kamal H. Bouhadir, and David J. Mooney. Controlling mechanical and swelling properties of alginate hydrogels independently by cross-linker type and cross-linking density. 33(11):4291–4294, . ISSN 0024-9297. doi: 10.1021/ma9921347. URL <http://dx.doi.org/10.1021/ma9921347>.
- [208] Nicholas Guziewicz, Annie Best, Bernardo Perez-Ramirez, and David L. Kaplan. Lyophilized silk fibroin hydrogels for the sustained local delivery of therapeutic monoclonal antibodies. 32(10):2642–2650. ISSN 0142-9612. doi: 10.1016/j.biomaterials.2010.12.023. URL <http://www.sciencedirect.com/science/article/pii/S0142961210015838>.
- [209] Haiwei Wang, Pengchong Li, Kun Xu, Ying Tan, Cuige Lu, Yangling Li, Xuechen Liang, and Pixin Wang. Synthesis and characterization of multi-sensitive microgel-based polyampholyte hydrogels with high mechanical strength. 294(2):367–380, . ISSN 1435-1536. doi: 10.1007/s00396-015-3792-4. URL <https://doi.org/10.1007/s00396-015-3792-4>.
- [210] Hua Zhang, Penggang Ren, Yanling Jin, and Fang Ren. Injectable, strongly compressible hyaluronic acid hydrogels via incorporation of pluronic f127 diacrylate nanomicelles. 243:112–115, . ISSN 0167-577X. doi: 10.1016/j.matlet.2019.01.159. URL <http://www.sciencedirect.com/science/article/pii/S0167577X19302125>.
- [211] Lucas F. M. da Silva, Andreas Öchsner, and Robert D. Adams. Introduction to adhesive bonding technology. In Lucas F. M. da Silva, Andreas Öchsner, and Robert D. Adams, editors, *Handbook of Adhesion Technology*, pages 1–7. Springer Berlin Heidelberg. ISBN 978-3-642-01168-9 978-3-642-01169-6. doi: 10.1007/978-3-642-01169-6_1. URL http://link.springer.com/referenceworkentry/10.1007/978-3-642-01169-6_1.
- [212] Dr Pr Maurice Brogly. Forces involved in adhesion. In Lucas F. M. da Silva, Andreas Öchsner, and Robert D. Adams, editors, *Handbook of Adhesion Technology*, pages 39–63. Springer Berlin Heidelberg. ISBN 978-3-642-01168-9 978-3-642-01169-6. doi: 10.1007/978-3-642-01169-6_3. URL http://link.springer.com/referenceworkentry/10.1007/978-3-642-01169-6_3.
- [213] J. R. Torres, G. D. Jay, K.-S. Kim, and G. D. Bothun. Adhesion in hydrogel contacts. 472(2189):20150892. ISSN 1364-5021, 1471-2946. doi: 10.1098/rspa.2015.0892. URL <http://rspa.royalsocietypublishing.org/content/472/2189/20150892>.
- [214] Liliane Léger and Costantino Creton. Adhesion mechanisms at soft polymer interfaces. 366(1869):1425–1442. ISSN 1364-503X, 1471-2962. doi: 10.1098/rsta.2007.2166. URL <http://rsta.royalsocietypublishing.org/content/366/1869/1425>.
- [215] Steven Abbott. Adhesion science | DEStech publishing. URL <http://www.destechpub.com/product/adhesion-science/>.
- [216] Jessica Blume and Willi Schwotzer. Medical products and their application range. pages 213–224. doi: 10.1007/978-3-7091-0286-2_14. URL http://link.springer.com/chapter/10.1007/978-3-7091-0286-2_14.
- [217] Allan S. Hoffman. Hydrogels for biomedical applications. 64, Supplement:18–23. ISSN 0169-409X. doi: 10.1016/j.addr.2012.09.010. URL <http://www.sciencedirect.com/science/article/pii/S0169409X12002700>.
- [218] Mohammadreza Mehdizadeh and Jian Yang. Design strategies and applications of tissue bioadhesives. 13(3):271–288. ISSN 1616-5195. doi: 10.1002/mabi.201200332. URL <http://onlinelibrary.wiley.com/doi/10.1002/mabi.201200332/abstract>.

- [219] Nasim Annabi, Ali Tamayol, Su Ryon Shin, Amir M. Ghaemmaghami, Nicholas A. Peppas, and Ali Khademhosseini. Surgical materials: Current challenges and nano-enabled solutions. 9(5):574–589. ISSN 1748-0132. doi: 10.1016/j.nantod.2014.09.006. URL <http://www.sciencedirect.com/science/article/pii/S1748013214001315>.
- [220] Petra J. M. Bouten, Marleen Zonjee, Johan Bender, Simon T. K. Yauw, Harry van Goor, Jan C. M. van Hest, and Richard Hoogenboom. The chemistry of tissue adhesive materials. 39(7):1375–1405. ISSN 0079-6700. doi: 10.1016/j.progpolymsci.2014.02.001. URL <http://www.sciencedirect.com/science/article/pii/S0079670014000215>.
- [221] Seung Yun Yang, Eoin D. O’Cearbhaill, Geoffroy C. Sisk, Kyeng Min Park, Woo Kyung Cho, Martin Villiger, Brett E. Bouma, Bohdan Pomahac, and Jeffrey M. Karp. A bio-inspired swellable microneedle adhesive for mechanical interlocking with tissue. 4:1702, . doi: 10.1038/ncomms2715. URL <http://www.nature.com/ncomms/journal/v4/n4/abs/ncomms2715.html>.
- [222] Enrica Caló and Vitaliy V. Khutoryanskiy. Biomedical applications of hydrogels: A review of patents and commercial products. 65:252–267. ISSN 0014-3057. doi: 10.1016/j.eurpolymj.2014.11.024. URL <http://www.sciencedirect.com/science/article/pii/S0014305714004091>.
- [223] Akhilesh K. Gaharwar, Nicholas A. Peppas, and Ali Khademhosseini. Nanocomposite hydrogels for biomedical applications. 111(3):441–453. ISSN 1097-0290. doi: 10.1002/bit.25160. URL <http://onlinelibrary.wiley.com/doi/10.1002/bit.25160/abstract>.
- [224] Pelagie M. Favi, Sijia Yi, Scott C. Lenaghan, Lijin Xia, and Mingjun Zhang. Inspiration from the natural world: from bio-adhesives to bio-inspired adhesives. 28(3):290–319. ISSN 0169-4243. doi: 10.1080/01694243.2012.691809. URL <http://dx.doi.org/10.1080/01694243.2012.691809>.
- [225] Luigi Petrone, Akshita Kumar, Clarinda N. Sutanto, Navinkumar J. Patil, Srinivasaraghavan Kannan, Alagappan Palaniappan, Shahrouz Amini, Bruno Zappone, Chandra Verma, and Ali Miserez. Mussel adhesion is dictated by time-regulated secretion and molecular conformation of mussel adhesive proteins. 6:8737. ISSN 2041-1723. doi: 10.1038/ncomms9737. URL <http://www.nature.com/ncomms/2015/151028/ncomms9737/full/ncomms9737.html>.
- [226] Carrie E. Brubaker, Hermann Kissler, Ling-Jia Wang, Dixon B. Kaufman, and Phillip B. Messersmith. Biological performance of mussel-inspired adhesive in extrahepatic islet transplantation. 31(3):420–427. ISSN 0142-9612. doi: 10.1016/j.biomaterials.2009.09.062. URL <http://www.sciencedirect.com/science/article/pii/S0142961209009946>.
- [227] Haeshin Lee, Shara M. Dellatore, William M. Miller, and Phillip B. Messersmith. Mussel-inspired surface chemistry for multifunctional coatings. 318(5849):426–430, . ISSN 0036-8075, 1095-9203. doi: 10.1126/science.1147241. URL <http://science.sciencemag.org/content/318/5849/426>.
- [228] Hong Zhang, Lgia P. Br , Tianyu Zhao, Yu Zheng, Ben Newland, and Wenxin Wang. Mussel-inspired hyperbranched poly(amino ester) polymer as strong wet tissue adhesive. 35(2):711–719, . ISSN 0142-9612. doi: 10.1016/j.biomaterials.2013.10.017. URL <http://www.sciencedirect.com/science/article/pii/S0142961213012283>.
- [229] Haeshin Lee, Bruce P. Lee, and Phillip B. Messersmith. A reversible wet/dry adhesive inspired by mussels and geckos. 448(7151):338–341, . ISSN 0028-0836. doi: 10.1038/nature05968. URL <http://www.nature.com/nature/journal/v448/n7151/abs/nature05968.html>.
- [230] Hilary Hurd. Thorny-headed worms make shrimps lose their sense to smell fish predators. URL <https://blogs.biomedcentral.com/bugbitten/2015/01/27/thorny-headed-worms-make-shrimps-lose-their-sense-to-smell-fish-predators/>.
- [231] Yong Doo Park, Nicola Tirelli, and Jeffrey A. Hubbell. Photopolymerized hyaluronic acid-based hydrogels and interpenetrating networks. 24(6):893–900. ISSN 0142-9612. doi: 10.1016/S0142-9612(02)00420-9. URL <http://www.sciencedirect.com/science/article/pii/S0142961202004209>.
- [232] Daniel R. King, Michael D. Bartlett, Casey A. Gilman, Duncan J. Irschick, and Alfred J. Crosby. Creating gecko-like adhesives for “real world” surfaces. 26(25):4345–4351. ISSN 1521-4095. doi: 10.1002/adma.201306259. URL <http://onlinelibrary.wiley.com/doi/10.1002/adma.201306259/abstract>.
- [233] Leming Sun, Yujian Huang, Zehua Bian, Jennifer Petrosino, Zhen Fan, Yongzhong Wang, Ki Ho Park, Tao Yue, Michael Schmidt, Scott Galster, Jianjie Ma, Hua Zhu, and Mingjun Zhang. Sundew-inspired adhesive hydrogels combined with adipose-derived stem cells for wound healing. 8(3):2423–2434, . ISSN 1944-8244, 1944-8252. doi: 10.1021/acsami.5b11811. URL <http://pubs.acs.org/doi/abs/10.1021/acsami.5b11811>.

- [234] S. C. Lenaghan, K. Serpersu, L. Xia, W. He, and M. Zhang. A naturally occurring nanomaterial from the sundew (*drosera*) for tissue engineering. 6(4):046009. ISSN 1748-3190. doi: 10.1088/1748-3182/6/4/046009. URL <http://stacks.iop.org/1748-3190/6/i=4/a=046009>.
- [235] Laurence Gaume and Yoel Forterre. A viscoelastic deadly fluid in carnivorous pitcher plants. 2(11):e1185. ISSN 1932-6203. doi: 10.1371/journal.pone.0001185. URL <http://journals.plos.org/plosone/article?id=10.1371/journal.pone.0001185>.
- [236] Mingjun Zhang, Scott C. Lenaghan, Lijin Xia, Lixin Dong, Wei He, William R. Henson, and Xudong Fan. Nanofibers and nanoparticles from the insect-capturing adhesive of the sundew (*drosera*) for cell attachment. 8:20, . ISSN 1477-3155. doi: 10.1186/1477-3155-8-20. URL <http://dx.doi.org/10.1186/1477-3155-8-20>.
- [237] Yujian Huang, Yongzhong Wang, Leming Sun, Richa Agrawal, and Mingjun Zhang. Sundew adhesive: a naturally occurring hydrogel. 12(107):20150226. ISSN 1742-5689, 1742-5662. doi: 10.1098/rsif.2015.0226. URL <http://rsif.royalsocietypublishing.org/content/12/107/20150226>.
- [238] Vrushali Bhagat, Emily O'Brien, Jinjun Zhou, and Matthew L. Becker. Caddisfly inspired phosphorylated poly(ester urea)-based degradable bone adhesives. 17(9):3016–3024. ISSN 1525-7797. doi: 10.1021/acs.biomac.6b00875. URL <https://doi.org/10.1021/acs.biomac.6b00875>.
- [239] Nicholas Nathan Ashton. The adhesive silk of the aquatic caddisfly larva: Structure, mechanics, and fiber spinning. URL <https://search.proquest.com/docview/1875567094/abstract/FCCD3DF5D0EE4841PQ/1>.
- [240] Mengkui Cui, Susu Ren, Shicao Wei, Chengjun Sun, and Chao Zhong. Natural and bio-inspired underwater adhesives: Current progress and new perspectives. 5(11):116102. doi: 10.1063/1.4985756. URL <https://aip.scitation.org/doi/full/10.1063/1.4985756>.
- [241] Rosta Kracík. English: *Drosera capensis*. URL https://commons.wikimedia.org/wiki/File:Drosera_capensis_3_Darwiniana.jpg.
- [242] Nicholas N. Ashton and Russell J. Stewart. Aquatic caddisworm silk is solidified by environmental metal ions during the natural fiber-spinning process. 33(1):572–583. ISSN 0892-6638. doi: 10.1096/fj.201801029R. URL <https://www.fasebj.org/doi/full/10.1096/fj.201801029R>.
- [243] Feng Yu, Xiaodong Cao, Yuli Li, Lei Zeng, Bo Yuan, and Xiaofeng Chen. An injectable hyaluronic acid/PEG hydrogel for cartilage tissue engineering formed by integrating enzymatic crosslinking and diels–alder “click chemistry”. 5(3):1082–1090, . doi: 10.1039/C3PY00869J. URL <http://pubs.rsc.org/en/Content/ArticleLanding/2014/PY/C3PY00869J>. Conventional hydrogel, recoverable, low softening.
- [244] Mattia Bacca, Costantino Creton, and Robert M. McMeeking. A model for the mullins effect in multinet network elastomers. 84(12). ISSN 0021-8936. doi: 10.1115/1.4037881. URL <https://asmedigitalcollection.asme.org/appliedmechanics/article/84/12/121009/421977/A-Model-for-the-Mullins-Effect-in-Multinet>. Publisher: American Society of Mechanical Engineers Digital Collection.
- [245] Gaolai Du, Guorong Gao, Ruixia Hou, Yajun Cheng, Tao Chen, Jun Fu, and Bin Fei. Tough and fatigue resistant biomimetic hydrogels of interlaced self-assembled conjugated polymer belts with a polyelectrolyte network. 26(11):3522–3529, . ISSN 0897-4756. doi: 10.1021/cm501095s. URL <http://dx.doi.org/10.1021/cm501095s>. DN, mullins, softening.
- [246] Julie Diani, Bruno Fayolle, and Pierre Gilormini. A review on the mullins effect. 45(3):601–612. ISSN 0014-3057. doi: 10.1016/j.eurpolymj.2008.11.017. URL <http://www.sciencedirect.com/science/article/pii/S0014305708006332>.
- [247] A. F. Blanchard and D. Parkinson. Breakage of carbon-rubber networks by applied stress. 44(4):799–812. ISSN 0019-7866. doi: 10.1021/ie50508a034. URL <http://dx.doi.org/10.1021/ie50508a034>.
- [248] F. Bueche. Molecular basis for the mullins effect. 4(10):107–114. ISSN 1097-4628. doi: 10.1002/app.1960.070041017. URL <http://onlinelibrary.wiley.com/doi/10.1002/app.1960.070041017/abstract>. Mullins-bondbreak.
- [249] G. Kraus, C. W. Childers, and K. W. Rollmann. Stress softening in carbon black reinforced vulcanizates. strain rate and temperature effects. 39(5):1530–1543. ISSN 0035-9475. doi: 10.5254/1.3547068. URL <http://www.rubberchemtechnol.org/doi/abs/10.5254/1.3547068>. Mullins+filler rupture.
- [250] R. Houwink. Slipping of molecules during the deformation of reinforced rubber. 29(3):888–893. ISSN 0035-9475. doi: 10.5254/1.3542602. URL <http://www.rubberchemtechnol.org/doi/abs/10.5254/1.3542602>. Mullins-slipping molecule.

- [251] David E. Hanson, Marilyn Hawley, Robert Houlton, Kiran Chitanvis, Philip Rae, E. Bruce Orler, and Debra A. Wroblewski. Stress softening experiments in silica-filled polydimethylsiloxane provide insight into a mechanism for the mullins effect. 46 (24):10989–10995. ISSN 0032-3861. doi: 10.1016/j.polymer.2005.09.039. URL <http://www.sciencedirect.com/science/article/pii/S0032386105013637>. Mullins-distanglement.
- [252] Kara L. Spiller, Suzanne A. Maher, and Anthony M. Lowman. Hydrogels for the repair of articular cartilage defects. 17 (4):281–299. ISSN 1937-3368. doi: 10.1089/ten.teb.2011.0077. URL <http://online.liebertpub.com/doi/abs/10.1089/ten.teb.2011.0077>.
- [253] D. M. Kirchmayer, R. Gorkin Iii, and M. in het Panhuis. An overview of the suitability of hydrogel-forming polymers for extrusion-based 3d-printing. 3(20):4105–4117. ISSN 2050-7518. doi: 10.1039/C5TB00393H. URL <http://pubs.rsc.org/en/content/articlelanding/2015/tb/c5tb00393h>.
- [254] Valentin Dhote, Stacey Skaalure, Umut Akalp, Justine Roberts, Stephanie J. Bryant, and Franck J. Vernerey. On the role of hydrogel structure and degradation in controlling the transport of cell-secreted matrix molecules for engineered cartilage. 19:61–74. ISSN 1751-6161. doi: 10.1016/j.jmbbm.2012.10.016. URL <http://www.sciencedirect.com/science/article/pii/S1751616112002779>.
- [255] Iossif Strehin, Zayna Nahas, Karun Arora, Thao Nguyen, and Jennifer Elisseeff. A versatile pH sensitive chondroitin sulfate–PEG tissue adhesive and hydrogel. 31(10):2788–2797. ISSN 0142-9612. doi: 10.1016/j.biomaterials.2009.12.033. URL <http://www.sciencedirect.com/science/article/pii/S0142961209014203>.
- [256] Oju Jeon, Julia E. Samorezov, and Eben Alsberg. Single and dual crosslinked oxidized methacrylated alginate/PEG hydrogels for bioadhesive applications. 10(1):47–55, . ISSN 1742-7061. doi: 10.1016/j.actbio.2013.09.004. URL <http://www.sciencedirect.com/science/article/pii/S1742706113004522>.
- [257] Jason A. Burdick, Cindy Chung, Xinqiao Jia, Mark A. Randolph, and Robert Langer. Controlled degradation and mechanical behavior of photopolymerized hyaluronic acid networks. 6(1):386–391, . ISSN 1525-7797. doi: 10.1021/bm049508a. URL <http://dx.doi.org/10.1021/bm049508a>.
- [258] Nathaniel Huebsch, Michele Gilbert, and Kevin E. Healy. Analysis of sterilization protocols for peptide-modified hydrogels. 74B(1):440–447. ISSN 1552-4981. doi: 10.1002/jbm.b.30155. URL <http://onlinelibrary.wiley.com/doi/10.1002/jbm.b.30155/abstract>.
- [259] Tao Bai, Peng Zhang, Yanjiao Han, Yuan Liu, Wenguang Liu, Xiaoli Zhao, and William Lu. Construction of an ultrahigh strength hydrogel with excellent fatigue resistance based on strong dipole–dipole interaction. 7(6):2825–2831, . doi: 10.1039/C0SM01108H. URL <http://pubs.rsc.org/en/Content/ArticleLanding/2011/SM/C0SM01108H>. Dipole-dipole interactions, no softening, conventional hydrogel.
- [260] Changcheng He, Zhiwei Zheng, Di Zhao, Jiaqi Liu, Jin Ouyang, and Huiliang Wang. Tough and super-resilient hydrogels synthesized by using peroxidized polymer chains as polyfunctional initiating and cross-linking centers. 9(10):2837–2844, . doi: 10.1039/C2SM27605D. URL <http://pubs.rsc.org/en/Content/ArticleLanding/2013/SM/C2SM27605D>. PFC.
- [261] Jinlong Zhang, Ning Wang, Wenguang Liu, Xiaoli Zhao, and William Lu. Intermolecular hydrogen bonding strategy to fabricate mechanically strong hydrogels with high elasticity and fatigue resistance. 9(27):6331–6337, . doi: 10.1039/C3SM50866H. URL <http://pubs.rsc.org/en/Content/ArticleLanding/2013/SM/C3SM50866H>. Conventional, no softening.
- [262] Linqing Li and Kristi L. Kiick. Transient dynamic mechanical properties of resilin-based elastomeric hydrogels. 2:21. doi: 10.3389/fchem.2014.00021. URL <http://journal.frontiersin.org/article/10.3389/fchem.2014.00021/full>. Conventional, no softening.
- [263] Silvia Kull, Ilaria Martinelli, Enrica Briganti, Paola Losi, Dario Spiller, Sara Tonlorenzi, and Giorgio Soldani. Glubran2 surgical glue: In vitro evaluation of adhesive and mechanical properties. 157(1):e15–e21. ISSN 0022-4804. doi: 10.1016/j.jss.2009.01.034. URL <http://www.sciencedirect.com/science/article/pii/S0022480409000432>.
- [264] Jacob A. Simson, Iossif A. Strehin, Brian W. Allen, and Jennifer H. Elisseeff. Bonding and fusion of meniscus fibrocartilage using a novel chondroitin sulfate bone marrow tissue adhesive. 19(15):1843–1851. ISSN 1937-3341. doi: 10.1089/ten.tea.2012.0578. URL <http://online.liebertpub.com/doi/abs/10.1089/ten.TEA.2012.0578>.
- [265] Jason A. Burdick and Kristi S. Anseth. Photoencapsulation of osteoblasts in injectable RGD-modified PEG hydrogels for bone tissue engineering. 23(22):4315–4323. ISSN 0142-9612. doi: 10.1016/S0142-9612(02)00176-X. URL <http://www.sciencedirect.com/science/article/pii/S014296120200176X>.

- [266] Jisoo Shin, Jung Seung Lee, Changhyun Lee, Hyun-Ji Park, Kisuk Yang, Yoonhee Jin, Ji Hyun Ryu, Ki Sung Hong, Sung-Hwan Moon, Hyung-Min Chung, Hee Seok Yang, Soong Ho Um, Jong-Won Oh, Dong-Ik Kim, Haeshin Lee, and Seung-Woo Cho. Tissue adhesive catechol-modified hyaluronic acid hydrogel for effective, minimally invasive cell therapy. 25(25): 3814–3824. ISSN 1616-3028. doi: 10.1002/adfm.201500006. URL <http://onlinelibrary.wiley.com/doi/10.1002/adfm.201500006/abstract>.
- [267] Yalin Zhou, Wei Nie, Jin Zhao, and Xiaoyan Yuan. Rapidly in situ forming adhesive hydrogel based on a PEG-maleimide modified polypeptide through michael addition. 24(10):2277–2286. ISSN 0957-4530, 1573-4838. doi: 10.1007/s10856-013-4987-1. URL <http://link.springer.com/article/10.1007/s10856-013-4987-1>.
- [268] Wei Nie, Xiaoyan Yuan, Jin Zhao, Yalin Zhou, and Huijing Bao. Rapidly in situ forming chitosan/e-polylysine hydrogels for adhesive sealants and hemostatic materials. 96(1):342–348. ISSN 0144-8617. doi: 10.1016/j.carbpol.2013.04.008. URL <http://www.sciencedirect.com/science/article/pii/S0144861713003615>.
- [269] Biji Balakrishnan, Nitin Joshi, Athipettah Jayakrishnan, and Rinti Banerjee. Self-crosslinked oxidized alginate/gelatin hydrogel as injectable, adhesive biomimetic scaffolds for cartilage regeneration. 10(8):3650–3663. ISSN 1742-7061. doi: 10.1016/j.actbio.2014.04.031. URL <http://www.sciencedirect.com/science/article/pii/S1742706114002001>.
- [270] Michael C. Giano, Zuhair Ibrahim, Scott H. Medina, Karim A. Sarhane, Joani M. Christensen, Yuji Yamada, Gerald Brandacher, and Joel P. Schneider. Injectable bioadhesive hydrogels with innate antibacterial properties. 5:4095. doi: 10.1038/ncomms5095. URL http://www.nature.com/ncomms/2014/140624/ncomms5095/full/ncomms5095.html?WT.ec_id=NCOMMS-20140625.
- [271] Sungwon Lee, Yusuke Inoue, Dongmin Kim, Amir Reuveny, Kazunori Kuribara, Tomoyuki Yokota, Jonathan Reeder, Masaki Sekino, Tsuyoshi Sekitani, Yusuke Abe, and Takao Someya. A strain-absorbing design for tissue-machine interfaces using a tunable adhesive gel. 5:5898. doi: 10.1038/ncomms6898. URL http://www.nature.com/ncomms/2014/141219/ncomms6898/full/ncomms6898.html?WT.ec_id=NCOMMS-20141224.
- [272] Hong Zhang, Lígia Bré, Tianyu Zhao, Ben Newland, Mark Da Costa, and Wenxin Wang. A biomimetic hyperbranched poly(amino ester)-based nanocomposite as a tunable bone adhesive for sternal closure. 2(26):4067–4071. doi: 10.1039/C4TB00155A. URL <http://pubs.rsc.org/en/Content/ArticleLanding/2014/TB/C4TB00155A>. READ.
- [273] J. Vernengo, G. W. Fussell, N. G. Smith, and A. M. Lowman. Synthesis and characterization of injectable bioadhesive hydrogels for nucleus pulposus replacement and repair of the damaged intervertebral disc. 93B(2):309–317. ISSN 1552-4981. doi: 10.1002/jbm.b.31547. URL <http://onlinelibrary.wiley.com/doi/10.1002/jbm.b.31547/abstract>.
- [274] Yoshimi Tanaka, Rikimaru Kuwabara, Yang-Ho Na, Takayuki Kurokawa, Jian Ping Gong, and Yoshihito Osada. Determination of fracture energy of high strength double network hydrogels. 109(23):11559–11562. ISSN 1520-6106. doi: 10.1021/jp0500790. URL <http://dx.doi.org/10.1021/jp0500790>.
- [275] Qiu Ming Yu, Yoshimi Tanaka, Hidemitsu Furukawa, Takayuki Kurokawa, and Jian Ping Gong. Direct observation of damage zone around crack tips in double-network gels. 42(12):3852–3855. ISSN 0024-9297. doi: 10.1021/ma900622s. URL <http://dx.doi.org/10.1021/ma900622s>.
- [276] Tristan Baumberger, Christiane Caroli, and David Martina. Solvent control of crack dynamics in a reversible hydrogel. 5(7): 552–555. ISSN 1476-1122. doi: 10.1038/nmat1666. URL <http://www.nature.com/nmat/journal/v5/n7/abs/nmat1666.html>.
- [277] T. Baumberger, C. Caroli, D. Martina, and O. Ronsin. Magic angles and cross-hatching instability in hydrogel fracture. 100(17):178303. doi: 10.1103/PhysRevLett.100.178303. URL <http://link.aps.org/doi/10.1103/PhysRevLett.100.178303>.
- [278] T. Baumberger and O. Ronsin. A convective instability mechanism for quasistatic crack branching in a hydrogel. 31(1): 51–58. ISSN 1292-8941, 1292-895X. doi: 10.1140/epje/i2010-10546-x. URL <http://link.springer.com/article/10.1140/epje/i2010-10546-x>.
- [279] Etienne Ducrot, Yulan Chen, Markus Bulters, Rint P. Sijbesma, and Costantino Creton. Toughening elastomers with sacrificial bonds and watching them break. 344(6180):186–189. ISSN 0036-8075, 1095-9203. doi: 10.1126/science.1248494. URL <http://science.sciencemag.org/content/344/6180/186>.
- [280] Wei-Chun Lin, Wei Fan, Alba Marcellan, Dominique Hourdet, and Costantino Creton. Large strain and fracture properties of poly(dimethylacrylamide)/silica hybrid hydrogels. 43(5):2554–2563. ISSN 0024-9297. doi: 10.1021/ma901937r. URL <http://dx.doi.org/10.1021/ma901937r>.

- [281] F. Pizzocolo, J. M. Huyghe, and K. Ito. Mode I crack propagation in hydrogels is step wise. 97:72–79. ISSN 0013-7944. doi: 10.1016/j.engfracmech.2012.10.018. URL <http://www.sciencedirect.com/science/article/pii/S0013794412004158>.
- [282] Feng Luo, Tao Lin Sun, Tasuku Nakajima, Takayuki Kurokawa, Yu Zhao, Abu Bin Ihsan, Hong Lei Guo, Xu Feng Li, and Jian Ping Gong. Crack blunting and advancing behaviors of tough and self-healing polyampholyte hydrogel. 47(17): 6037–6046. ISSN 0024-9297. doi: 10.1021/ma5009447. URL <http://dx.doi.org/10.1021/ma5009447>.
- [283] Francesco Baldi, Fabio Bignotti, Isabella Peroni, Silvia Agnelli, and Theonis Riccò. On the measurement of the fracture resistance of polyacrylamide hydrogels by wire cutting tests. 31(3):455–465. ISSN 0142-9418. doi: 10.1016/j.polymertesting.2012.01.009. URL <http://www.sciencedirect.com/science/article/pii/S0142941812000232>.
- [284] A. E. Forte, F. D’Amico, M. N. Charalambides, D. Dini, and J. G. Williams. Modelling and experimental characterisation of the rate dependent fracture properties of gelatine gels. 46:180–190. ISSN 0268-005X. doi: 10.1016/j.foodhyd.2014.12.028. URL <http://www.sciencedirect.com/science/article/pii/S0268005X14004706>.
- [285] Widusha R. K. Illeperuma, Jeong-Yun Sun, Zhigang Suo, and Joost J. Vlassak. Fiber-reinforced tough hydrogels. 1: 90–96. ISSN 2352-4316. doi: 10.1016/j.eml.2014.11.001. URL <http://www.sciencedirect.com/science/article/pii/S2352431614000042>.
- [286] Jun Yang, Chun-Rui Han, Xue-Ming Zhang, Feng Xu, and Run-Cang Sun. Cellulose nanocrystals mechanical reinforcement in composite hydrogels with multiple cross-links: Correlations between dissipation properties and deformation mechanisms. 47(12):4077–4086, . ISSN 0024-9297. doi: 10.1021/ma500729q. URL <http://dx.doi.org/10.1021/ma500729q>.
- [287] Yuhan Lee, Hyun Jung Chung, Sangho Yeo, Cheol-Hee Ahn, Haeshin Lee, Phillip B. Messersmith, and Tae Gwan Park. Thermo-sensitive, injectable, and tissue adhesive sol–gel transition hyaluronic acid /pluronic composite hydrogels prepared from bio-inspired catechol - thiol reaction. 6(5):977–983, . doi: 10.1039/B919944F. URL <http://pubs.rsc.org/en/Content/ArticleLanding/2010/SM/B919944F>.
- [288] Craig Wiltsey, Pamela Kubinski, Thomas Christiani, Katelynn Toomer, Joseph Sheehan, Amanda Branda, Jennifer Kadowec, Cristina Iftode, and Jennifer Vernengo. Characterization of injectable hydrogels based on poly(n-isopropylacrylamide)-g-chondroitin sulfate with adhesive properties for nucleus pulposus tissue engineering. 24(4):837–847. ISSN 0957-4530, 1573-4838. doi: 10.1007/s10856-013-4857-x. URL <https://link.springer.com/article/10.1007/s10856-013-4857-x>.
- [289] Bum Jin Kim, Dongyeop X. Oh, Sangsik Kim, Jeong Hyun Seo, Dong Soo Hwang, Admir Masic, Dong Keun Han, and Hyung Joon Cha. Mussel-mimetic protein-based adhesive hydrogel. 15(5):1579–1585, . ISSN 1525-7797. doi: 10.1021/bm4017308. URL <http://dx.doi.org/10.1021/bm4017308>.
- [290] Séverine Rose, Alexandre PrevotEAU, Paul Elzière, Dominique Hourdet, Alba Marcellan, and Ludwik Leibler. Nanoparticle solutions as adhesives for gels and biological tissues. 505(7483):382–385, . ISSN 0028-0836. doi: 10.1038/nature12806. URL <http://www.nature.com/nature/journal/v505/n7483/full/nature12806.html>.
- [291] Eugene Lih, Jung Seok Lee, Kyung Min Park, and Ki Dong Park. Rapidly curable chitosan-PEG hydrogels as tissue adhesives for hemostasis and wound healing. 8(9):3261–3269. ISSN 1742-7061. doi: 10.1016/j.actbio.2012.05.001. URL <http://www.sciencedirect.com/science/article/pii/S174270611200205X>.
- [292] Antonio Feula, Xuegang Tang, Ioannis Giannakopoulos, Ann M. Chippindale, Ian W. Hamley, Francesca Greco, C. Paul Buckley, Clive R. Siviour, and Wayne Hayes. An adhesive elastomeric supramolecular polyurethane healable at body temperature. 7(7):4291–4300. doi: 10.1039/C5SC04864H. URL <http://pubs.rsc.org/en/Content/ArticleLanding/2016/SC/C5SC04864H>.
- [293] Paula Rulf Marreco, Patrícia da Luz Moreira, Selma Candelária Genari, and Ângela Maria Moraes. Effects of different sterilization methods on the morphology, mechanical properties, and cytotoxicity of chitosan membranes used as wound dressings. 71B(2):268–277. ISSN 1552-4981. doi: 10.1002/jbm.b.30081. URL <http://onlinelibrary.wiley.com/doi/10.1002/jbm.b.30081/abstract>.
- [294] Jennifer L. Belelie. Photoinitiator functionalized with alkoxy groups. URL <http://www.google.com/patents/US7705065>. U.S. Classification 522/37, 522/42, 568/337, 568/14, 522/53, 568/331, 568/42, 522/64; International Classification C08F2/50, C07C321/22, C07F9/00, C07C49/00; Cooperative Classification C07C69/712, C08F2/50, C08F2/48; European Classification C07C69/712, C08F2/48, C08F2/50.
- [295] Mladen Marković and Branimir Cucic. Transformer lifetime management through solid and liquid insulation assessment.

- [296] Zhijun Shi, Shanshan Zang, Fan Jiang, Long Huang, Dan Lu, Yuguang Ma, and Guang Yang. In situ nano- assembly of bacterial cellulose– polyaniline composites. 2(3):1040–1046. doi: 10.1039/C1RA00719J. URL <http://pubs.rsc.org/en/Content/ArticleLanding/2012/RA/C1RA00719J>.
- [297] Poly(ethylene glycol) dimethacrylate average mn 550, contains 270-330 ppm BHT as inhibitor, 80-120 ppm MEHQ as inhibitor | sigma-aldrich, . URL <http://www.sigmaaldrich.com/catalog/product/aldrich/409510?lang=fr®ion=CH>.
- [298] M. Fazley Elahi, Guoping Guan, Lu Wang, and Martin W. King. Influence of layer-by-layer polyelectrolyte deposition and EDC/NHS activated heparin immobilization onto silk fibroin fabric. 7(4):2956–2977. doi: 10.3390/ma7042956. URL <http://www.mdpi.com/1996-1944/7/4/2956>.
- [299] Span[®] 80 840123, . URL <https://www.sigmaaldrich.com/catalog/product/mm/840123>.
- [300] Span 80, sorbitan oleate, emulsifier s80., . URL <https://www.irochemical.com/product/Surfactants/Span-80.htm>.
- [301] Frank Dieterle, Alfred Ross, Götz Schlotterbeck, and Hans Senn. Probabilistic quotient normalization as robust method to account for dilution of complex biological mixtures. application in 1h NMR metabonomics. 78(13):4281–4290. ISSN 0003-2700. doi: 10.1021/ac051632c. URL <https://doi.org/10.1021/ac051632c>. Publisher: American Chemical Society.
- [302] My Y. Truong, Naba K. Dutta, Namita R. Choudhury, Misook Kim, Christopher M. Elvin, Kate M. Nairn, and Anita J. Hill. The effect of hydration on molecular chain mobility and the viscoelastic behavior of resilin-mimetic protein-based hydrogels. 32(33):8462–8473. ISSN 0142-9612. doi: 10.1016/j.biomaterials.2011.07.064. URL <http://www.sciencedirect.com/science/article/pii/S0142961211008611>. softer when swell.
- [303] Tao Lin Sun, Feng Luo, Takayuki Kurokawa, Sadia Nazneen Karobi, Tasuku Nakajima, and Jian Ping Gong. Molecular structure of self-healing polyampholyte hydrogels analyzed from tensile behaviors. 11(48):9355–9366. doi: 10.1039/C5SM01423A. URL <http://pubs.rsc.org/en/Content/ArticleLanding/2015/SM/C5SM01423A>. stiffer.
- [304] S. P. Marra, K. T. Ramesh, and A. S. Douglas. Characterization and modeling of compliant active materials. 51(9):1723–1743. ISSN 0022-5096. doi: 10.1016/S0022-5096(03)00055-3. URL <http://www.sciencedirect.com/science/article/pii/S0022509603000553>. Conventional, thin film, stiffer when swollen.
- [305] Aleksandr B. Stefaniak, Mohindar S. Seehra, Natalie R. Fix, and Stephen S. Leonard. Lung biodurability and free radical production of cellulose nanomaterials. 26(12):733–749. ISSN 0895-8378. doi: 10.3109/08958378.2014.948650. URL <https://doi.org/10.3109/08958378.2014.948650>.
- [306] Céline Samira Wyss, Peyman Karami, Pierre-Etienne Bourban, and Dominique P. Pioletti. Cyclic loading of a cellulose/hydrogel composite increases its fracture strength. 24:66–74. ISSN 2352-4316. doi: 10.1016/j.eml.2018.09.002. URL <http://www.sciencedirect.com/science/article/pii/S2352431618301615>.
- [307] Yunwei Mao, Shaoting Lin, Xuanhe Zhao, and Lallit Anand. A large deformation viscoelastic model for double-network hydrogels. 100:103–130. ISSN 0022-5096. doi: 10.1016/j.jmps.2016.12.011. URL <http://www.sciencedirect.com/science/article/pii/S0022509616308389>.
- [308] Teng Zhang, Shaoting Lin, Hyunwoo Yuk, and Xuanhe Zhao. Predicting fracture energies and crack-tip fields of soft tough materials. 4:1–8, . ISSN 2352-4316. doi: 10.1016/j.eml.2015.07.007. URL <http://www.sciencedirect.com/science/article/pii/S2352431615000899>.
- [309] Jingda Tang, Jianyu Li, Joost J. Vlassak, and Zhigang Suo. Fatigue fracture of hydrogels. 10:24–31. ISSN 2352-4316. doi: 10.1016/j.eml.2016.09.010. URL <http://www.sciencedirect.com/science/article/pii/S2352431616301626>.
- [310] Wenlei Zhang, Xiao Liu, Jikun Wang, Jingda Tang, Jian Hu, Tongqing Lu, and Zhigang Suo. Fatigue of double-network hydrogels. 187:74–93, . ISSN 0013-7944. doi: 10.1016/j.engfracmech.2017.10.018. URL <http://www.sciencedirect.com/science/article/pii/S0013794417309499>.
- [311] Ruobing Bai, Quansan Yang, Jingda Tang, Xavier P. Morelle, Joost Vlassak, and Zhigang Suo. Fatigue fracture of tough hydrogels. 15:91–96, . ISSN 2352-4316. doi: 10.1016/j.eml.2017.07.002. URL <http://www.sciencedirect.com/science/article/pii/S2352431617300731>.
- [312] Ruobing Bai, Jiawei Yang, Xavier P. Morelle, Canhui Yang, and Zhigang Suo. Fatigue fracture of self-recovery hydrogels. 7(3):312–317, . doi: 10.1021/acsmacrolett.8b00045. URL <https://doi.org/10.1021/acsmacrolett.8b00045>.

- [313] Chao Chen, Zhengjin Wang, and Zhigang Suo. Flaw sensitivity of highly stretchable materials. 10:50–57, . ISSN 2352-4316. doi: 10.1016/j.eml.2016.10.002. URL <http://www.sciencedirect.com/science/article/pii/S2352431616301523>.
- [314] Matt Pharr, Jeong-Yun Sun, and Zhigang Suo. Rupture of a highly stretchable acrylic dielectric elastomer. 111(10):104114. ISSN 0021-8979. doi: 10.1063/1.4721777. URL <https://aip.scitation.org/doi/abs/10.1063/1.4721777>.
- [315] Khaow Tonsomboon, Annabel L. Butcher, and Michelle L. Oyen. Strong and tough nanofibrous hydrogel composites based on biomimetic principles. 72:220–227. ISSN 0928-4931. doi: 10.1016/j.msec.2016.11.025. URL <http://www.sciencedirect.com/science/article/pii/S092849311630875X>.
- [316] Sungmin Hong, Dalton Sycks, Hon Fai Chan, Shaoting Lin, Gabriel P. Lopez, Farshid Guilak, Kam W. Leong, and Xuanhe Zhao. 3d printing of highly stretchable and tough hydrogels into complex, cellularized structures. 27(27):4035–4040. ISSN 1521-4095. doi: 10.1002/adma.201501099. URL <http://onlinelibrary.wiley.com/doi/10.1002/adma.201501099/abstract>.
- [317] Mark A. Gonzalez, Joseph R. Simon, Ali Ghoorchian, Zachary Scholl, Shaoting Lin, Michael Rubinstein, Piotr Marszałek, Ashutosh Chilkoti, Gabriel P. López, and Xuanhe Zhao. Strong, tough, stretchable, and self-adhesive hydrogels from intrinsically unstructured proteins. 29(10):1604743. ISSN 1521-4095. doi: 10.1002/adma.201604743. URL <https://onlinelibrary.wiley.com/doi/abs/10.1002/adma.201604743>.
- [318] Mahoor Mehdikhani, Mohammadali Aravand, Baris Sabuncuoglu, Michaël G. Callens, Stepan V. Lomov, and Larissa Gorbatikh. Full-field strain measurements at the micro-scale in fiber-reinforced composites using digital image correlation. 140:192–201. ISSN 0263-8223. doi: 10.1016/j.compstruct.2015.12.020. URL <http://www.sciencedirect.com/science/article/pii/S0263822315011101>.
- [319] Céline Samira Wyss, Peyman Karami, Pierre-Etienne Bourban, and Dominique P. Pioletti. Hybrid granular hydrogels: combining composites and microgels for extended ranges of material properties. 16(15):3769–3778. doi: 10.1039/D0SM00213E. URL <https://pubs.rsc.org/en/content/articlelanding/2020/sm/d0sm00213e>.
- [320] Mazen Falah, Gabreil Nierenberg, Michael Soudry, Morris Hayden, and Gershon Volpin. Treatment of articular cartilage lesions of the knee. 34(5):621–630. ISSN 0341-2695. doi: 10.1007/s00264-010-0959-y. URL <https://www.ncbi.nlm.nih.gov/pmc/articles/PMC2903160/>.
- [321] David Chimene, Roland Kaunas, and Akhilesh K. Gaharwar. Hydrogel bioink reinforcement for additive manufacturing: A focused review of emerging strategies. n/a:1902026. ISSN 1521-4095. doi: 10.1002/adma.201902026. URL <https://onlinelibrary.wiley.com/doi/abs/10.1002/adma.201902026>.
- [322] Francois Barthelat and Reza Rabiei. Toughness amplification in natural composites. 59(4):829–840. ISSN 0022-5096. doi: 10.1016/j.jmps.2011.01.001. URL <http://www.sciencedirect.com/science/article/pii/S0022509611000020>.
- [323] Apostolos A. Karanastasis, Yongdeng Zhang, Gopal S. Kenath, Mark D. Lessard, Joerg Bewersdorf, and Chaitanya K. Ullal. 3d mapping of nanoscale crosslink heterogeneities in microgels. 5(6):1130–1136. ISSN 2051-6355. doi: 10.1039/C8MH00644J. URL <https://pubs.rsc.org/en/content/articlelanding/2018/mh/c8mh00644j>.
- [324] Andrew C. Daly, Lindsay Riley, Tatiana Segura, and Jason A. Burdick. Hydrogel microparticles for biomedical applications. 5(1):20–43. ISSN 2058-8437. doi: 10.1038/s41578-019-0148-6. URL <https://www.nature.com/articles/s41578-019-0148-6>. Number: 1 Publisher: Nature Publishing Group.
- [325] Frank Scheffold. Pathways and challenges towards a complete characterization of microgels. 11(1):4315. ISSN 2041-1723. doi: 10.1038/s41467-020-17774-5. URL <https://www.nature.com/articles/s41467-020-17774-5>. Number: 1 Publisher: Nature Publishing Group.
- [326] Hai-Yan Wang and Yu-Qing Zhang. Processing silk hydrogel and its applications in biomedical materials. 31(3):630–640, . ISSN 1520-6033. doi: 10.1002/btpr.2058. URL <https://aiche.onlinelibrary.wiley.com/doi/abs/10.1002/btpr.2058>.
- [327] Tsunenori Kameda. Influence of pH, temperature, and concentration on stabilization of aqueous hornet silk solution and fabrication of salt-free materials. 103(1):41–52. ISSN 1097-0282. doi: 10.1002/bip.22562. URL <https://onlinelibrary.wiley.com/doi/abs/10.1002/bip.22562>.
- [328] David Chelazzi, Diego Badillo-Sanchez, Rodorico Giorgi, Alessandra Cincinelli, and Piero Baglioni. Self-regenerated silk fibroin with controlled crystallinity for the reinforcement of silk. 576:230–240. ISSN 0021-9797. doi: 10.1016/j.jcis.2020.04.114. URL <http://www.sciencedirect.com/science/article/pii/S0021979720305786>.

- [329] Hai-Yan Wang and Yu-Qing Zhang. Effect of regeneration of liquid silk fibroin on its structure and characterization. 9(1): 138–145, . doi: 10.1039/C2SM26945G. URL <https://pubs.rsc.org/en/content/articlelanding/2013/sm/c2sm26945g>.
- [330] Jian Zhong, Mengjia Ma, Wenying Li, Juan Zhou, Zhiqiang Yan, and Dannong He. Self-assembly of regenerated silk fibroin from random coil nanostructures to antiparallel beta-sheet nanostructures. 101(12):1181–1192, . ISSN 1097-0282. doi: 10.1002/bip.22532. URL <https://onlinelibrary.wiley.com/doi/abs/10.1002/bip.22532>.
- [331] N. Drnovšek, R. Kocen, A. Gantar, M. Drobnič-Košorok, A. Leonardi, I. Križaj, A. Rečnik, and S. Novak. Size of silk fibroin beta-sheet domains affected by ca 2+. 4(40):6597–6608. doi: 10.1039/C6TB01101B. URL <https://pubs.rsc.org/en/content/articlelanding/2016/tb/c6tb01101b>.
- [332] Xu Wu, Xiaodong Wu, Min Shao, and Bin Yang. Structural changes of bombyx mori fibroin from silk gland to fiber as evidenced by terahertz spectroscopy and other methods. 102:1202–1210. ISSN 0141-8130. doi: 10.1016/j.ijbiomac.2017.05.011. URL <http://www.sciencedirect.com/science/article/pii/S0141813017311303>.
- [333] Yaowalak Srisuwan, Prasong Srihanam, and Yodthong Baimark. Preparation of silk fibroin microspheres and its application to protein adsorption. 46(5):521–525. ISSN 1060-1325. doi: 10.1080/10601320902797780. URL <https://doi.org/10.1080/10601320902797780>.
- [334] Natalia Jaramillo-Quiceno, Catalina Álvarez López, and Adriana Restrepo-Osorio. Structural and thermal properties of silk fibroin films obtained from cocoon and waste silk fibers as raw materials. 200:384–388. ISSN 1877-7058. doi: 10.1016/j.proeng.2017.07.054. URL <http://www.sciencedirect.com/science/article/pii/S1877705817328886>.
- [335] Akira Matsumoto, Jingsong Chen, Adam L. Collette, Ung-Jin Kim, Gregory H. Altman, Peggy Cebe, and David L. Kaplan. Mechanisms of silk fibroin sol-gel transitions. 110(43):21630–21638. ISSN 1520-6106. doi: 10.1021/jp056350v. URL <https://doi.org/10.1021/jp056350v>.
- [336] C. Wong Po Foo, E. Bini, J. Hensman, D.P. Knight, R.V. Lewis, and D.L. Kaplan. Role of pH and charge on silk protein assembly in insects and spiders. 82(2):223–233. ISSN 1432-0630. doi: 10.1007/s00339-005-3426-7. URL <https://doi.org/10.1007/s00339-005-3426-7>.
- [337] Ann E. Terry, David P. Knight, David Porter, and Fritz Vollrath. pH induced changes in the rheology of silk fibroin solution from the middle division of bombyx mori silkworm. 5(3):768–772. ISSN 1525-7797. doi: 10.1021/bm034381v. URL <https://doi.org/10.1021/bm034381v>.
- [338] Jihye Baek, Sujata Sovani, Wonchul Choi, Sungho Jin, Shawn P. Grogan, and Darryl D. D’Lima. Meniscal tissue engineering using aligned collagen fibrous scaffolds: Comparison of different human cell sources. 24(1):81–93. ISSN 1937-3341. doi: 10.1089/ten.tea.2016.0205. URL <https://www.liebertpub.com/doi/full/10.1089/ten.TEA.2016.0205>. Publisher: Mary Ann Liebert, Inc., publishers.
- [339] Diane E. Gregory and Jack P. Callaghan. A comparison of uniaxial and biaxial mechanical properties of the annulus fibrosus: A porcine model. 133(2). ISSN 0148-0731. doi: 10.1115/1.4003327. URL <https://asmedigitalcollection.asme.org/biomechanical/article/133/2/024503/383547/A-Comparison-of-Uniaxial-and-Biaxial-Mechanical>. Publisher: American Society of Mechanical Engineers Digital Collection.
- [340] Naama T. Lewis, Mohammad A. Hussain, and Jeremy J. Mao. Investigation of nano-mechanical properties of annulus fibrosus using atomic force microscopy. 39(7):1008–1019. ISSN 0968-4328. doi: 10.1016/j.micron.2007.08.009. URL <http://www.sciencedirect.com/science/article/pii/S0968432807001382>.
- [341] Javad Tavakoli, Dawn M. Elliott, and John J. Costi. Structure and mechanical function of the inter-lamellar matrix of the annulus fibrosus in the disc. 34(8):1307–1315. ISSN 1554-527X. doi: 10.1002/jor.23306. URL <https://onlinelibrary.wiley.com/doi/abs/10.1002/jor.23306>. _eprint: <https://onlinelibrary.wiley.com/doi/pdf/10.1002/jor.23306>.
- [342] Giorgio Mattei and Arti Ahluwalia. Sample, testing and analysis variables affecting liver mechanical properties: A review. 45:60–71. ISSN 1742-7061. doi: 10.1016/j.actbio.2016.08.055. URL <http://www.sciencedirect.com/science/article/pii/S1742706116304603>.
- [343] R. C. Aydin, S. Brandstaeter, F. A. Braeu, M. Steigenberger, R. P. Marcus, K. Nikolaou, M. Notohamiprodjo, and C. J. Cyron. Experimental characterization of the biaxial mechanical properties of porcine gastric tissue. 74:499–506. ISSN 1751-6161. doi: 10.1016/j.jmbbm.2017.07.028. URL <http://www.sciencedirect.com/science/article/pii/S1751616117303144>.

-
- [344] Alekya B., Sanjay Rao, and Hardik J. Pandya. Engineering approaches for characterizing soft tissue mechanical properties: A review. 69:127–140. ISSN 0268-0033. doi: 10.1016/j.clinbiomech.2019.07.016. URL <http://www.sciencedirect.com/science/article/pii/S0268003318310696>.
- [345] Mengxiang Zhu, Yingying Wang, Gaia Ferracci, Jing Zheng, Nam-Joon Cho, and Bae Hoon Lee. Gelatin methacryloyl and its hydrogels with an exceptional degree of controllability and batch-to-batch consistency. 9(1):6863. ISSN 2045-2322. doi: 10.1038/s41598-019-42186-x. URL <https://www.nature.com/articles/s41598-019-42186-x>. Number: 1 Publisher: Nature Publishing Group.
- [346] Prof Dr Wulff Possart and Dr Martin E. R. Shanahan. Thermodynamics of adhesion. In Lucas F. M. da Silva, Andreas Öchsner, and Robert D. Adams, editors, *Handbook of Adhesion Technology*, pages 105–116. Springer Berlin Heidelberg. ISBN 978-3-642-01168-9 978-3-642-01169-6. doi: 10.1007/978-3-642-01169-6_6. URL http://link.springer.com/referenceworkentry/10.1007/978-3-642-01169-6_6.
- [347] David E. Packham. Theories of fundamental adhesion. In Lucas F. M. da Silva, Andreas Öchsner, and Robert D. Adams, editors, *Handbook of Adhesion Technology*, pages 9–38. Springer Berlin Heidelberg. ISBN 978-3-642-01168-9 978-3-642-01169-6. doi: 10.1007/978-3-642-01169-6_2. URL http://link.springer.com/referenceworkentry/10.1007/978-3-642-01169-6_2.
- [348] Douglas J. Gardner, Melanie Blumentritt, Lu Wang, and Nadir Yildirim. Adhesion theories in wood adhesive bonding. 2 (2):127–172. ISSN 21680965. doi: 10.7569/RAA.2014.097304. URL <http://openurl.ingenta.com/content/xref?genre=article&issn=2168-0965&volume=2&issue=2&spage=127>.
- [349] George Odian. *Principles of Polymerization*. John Wiley & Sons. ISBN 978-0-471-27400-1. Google-Books-ID: GbLrBgAAQBAJ.



CÉLINE WYSS

PH.D. IN MATERIAL SCIENCE

✉ wyss.celine@gmail.com

☎ +41 79 603 89 23

🏠 Swiss nationality



WORK EXPERIENCE

ÉCOLE POLYTECHNIQUE FÉDÉRALE DE LAUSANNE - EPFL, CH

LABORATORY FOR PROCESSING OF ADVANCED COMPOSITE - LPAC

LABORATORY OF BIOMECHANICAL ORTHOPEDICS - LBO

2016 - 2020
(4.5 years)

PH.D. ASSISTANT

Objective: Design new robust implants containing more than 90% water to treat load-bearing tissues, such as articular cartilage or meniscus.

Main activities:

- Multidisciplinary research, project management, laboratory work, data analysis, and communication results in scientific journals.
- Teaching assistant and supervision of students (6 semester students and 6 groups of 4-5 students).
- Present research in simple terms to specialists and the general public in French, English, and Swiss German.
- Responsible for the chemistry laboratory (safety and orders) and waste management.
- Train new users for using material characterization equipment.

Achievements: 4 publications, 4 oral presentations, 2 awards

2016
(4 months)

MASTER THESIS INTERN

Objective: Study fatigue behavior of implants to replace the core of the intervertebral disc.

Achievements: 1 publication.

STRYKER, SELZACH CH, A MEDICAL TECHNOLOGY COMPANY

2015 - 2016
(6 months)

BIOMECHANICS INTERN, R&D

Role: Test and evaluate the quality of new products according to requirements.



EDUCATION

ÉCOLE POLYTECHNIQUE FÉDÉRALE DE LAUSANNE - EPFL, CH

2011 - 2016
(5 years)

BACHELOR AND MASTER STUDENT

Material science and engineering

Specialization: Materials for biotechnological and medical applications.



CONTINUOUS LEARNING

EPFL EXTENSION SCHOOL

2020 | FOUNDATIONS OF DATA SCIENCE (150h)

EXPERTISES

- Material science
- Applied research
- Communication
- Data analysis
- Polymers
- Hydrogels
- Soft composites
- Cellulose, silk fibroin fibers
- Emulsion, microgels
- Material characterization
- Fracture mechanics
- 3D printing

TECHNICAL SKILLS

MATERIAL CHARACTERIZATION

- Mechanical testing
- Microscopy
- Rheology
- FTIR
- Particle size analyzer
- Digital image correlation

SOFTWARE

- R / Matlab
- Image J
- Photoshop / Illustrator
- Microsoft Office
- LaTeX
- Solidworks / Fusion 360
- Comsol

LANGUAGES

- French - mother tongue
- Swiss German - mother tongue
- German - fluent
- English - fluent

ACTIVITIES





PUBLICATIONS

- 2020 | HYBRID GRANULAR HYDROGELS: COMBINING COMPOSITES AND MICROGELS FOR EXTENDED RANGES OF MATERIAL PROPERTIES, *Soft Matter*
C.S. Wyss, P. Karami, P-E. Bourban, D.P. Pioletti
- 2018 | COMPOSITE DOUBLE-NETWORK HYDROGELS TO IMPROVE ADHESION ON BIOLOGICAL SURFACES, *ACS Applied Materials & Interfaces*
P. Karami*, C.S. Wyss*, A. Khoushabi, A. Schmocker, M. Broome, C. Moser, P-E. Bourban, D.P. Pioletti
*same contribution
- 2018 | CYCLIC LOADING OF A CELLULOSE/HYDROGEL COMPOSITE INCREASES ITS FRACTURE STRENGTH, *Extreme Mechanics Letter*
C.S. Wyss, P. Karami, P-E. Bourban, D.P. Pioletti
- 2018 | TAILORING SWELLING TO CONTROL SOFTENING MECHANISMS DURING CYCLIC LOADING OF PEG/CELLULOSE HYDROGEL COMPOSITES, *Composites Science and Technology*
A. Khoushabi, C.S. Wyss, B. Caglar, D.P. Pioletti, P-E. Bourban



CONFERENCES

- 2020 | 11TH WORLD BIOMATERIALS CONGRESS - WBC 2020 VIRTUAL, *Oral presentation*
- 2019 | 6TH INTERNATIONAL CONFERENCE ON MULTIFUNCTIONAL, HYBRID AND NANOMATERIALS - HYBRID 2019
Sitges, ES, *Poster*
- 2018 | ANNUAL MEETING OF THE EUROPEAN SOCIETY FOR BIOMATERIALS – ESB 2018
Maastricht, NL, *Oral presentation*
- 2018 | SWISS SOCIETY FOR BIOMATERIALS AND REGENERATIVE MEDICINE - SSBRM 2018
Fribourg, CH, *Oral presentation*
- 2016 | SWISS SOCIETY FOR BIOMATERIALS AND REGENERATIVE MEDICINE - SSBRM 2016
Zurich, CH, *Poster*



AWARDS

- 2018 | **BEST ORAL PRESENTATION**
DOCTORAL PROGRAM IN MATERIALS SCIENCE AND ENGINEERING - EDMX Research Day 2018
- 2018 | **BEST STUDENT ORAL PRESENTATION**
SWISS SOCIETY FOR BIOMATERIALS AND REGENERATIVE MEDICINE - SSBRM 2018